THE CALORIMETRY OF HIGH ENERGY PHOTON AND ELECTRON BEAMS

by

Brian M. Tedman, B.Sc.

Thesis presented for the Degree of Doctor of Philosophy of the University of Edinburgh, January 1975.

C O N T E N T S

A B S T R A C T

The past two decades have seen a very dramatic rise in the production of megavoltage X-ray and electron accelerators for use in therapeutic medicine. Concomitant with this increase has been the need to develop accurate and reliable methods for measuring the deposition of radiation energy within the irradiated medium. Frequently, the ionometric methods used for assessing the absorbed dose in materials irradiated by X-ray beams generated at a few hundreds of kV have been extended to the megavoltage region, but, whilst the precision and reliability of such methods have generally been unaffected by this extension, the interpretation of such measurements and their relationship to the absorbed dose has become extremely complex. In this situation the technique of calorimetry offers the only direct and unambiguous approach for measuring the absorbed dose and this thesis deals with the design, construction and operation of such an instrument with the particular intention of calibrating a number of secondary dosimeters.

The production of a stable temperature environment, which enables the small temperature changes encountered in calorimetry to be measured accurately, is discussed and it was concluded that a multi-jacket system, operated in the quasi-adiabatic mode, was the most suitable. The actual temperature measurements were made with a Wheatstone Bridge Network, using a thermistor transducer, and it is shown that if a particular criterion is adopted for the sensitivity of the system then the bridge can be so designed to maximise this sensitivity. The practical construction of a bridge system using a phase sensitive detector and capable of a temperature resolution of 2×10^{-5} K is also described.

Carbon was chosen as the calorimetric material on the grounds of its thermal conductivity, low heat-defect and tissue equivalent radiation properties. The design and construction of a calorimeter composed of this material are fully discussed, particular attention being devoted to the balance between the theoretical requirements of a small, isolated homogeneous absorbing element with a localised point of measurement and the practical difficulties of thermal isolation, calibration and construction.

An analysis of the effect of temperature gradients within the calorimeter and the absence of true quasi-adiabatic conditions during electrical calibration is presented. The results of this analysis, which were verified experimentally, showed that, whilst the ratio of heat dissipation in the absorber to that in the jacket was not critical, the calibration period should not exceed 5 minutes and a residual correction for the existence of temperature gradients was necessary.

The design of a carbon-walled air ionization chamber is presented in Chapter 6 and includes a description of the circuitry necessary to measure the small amount of charge produced in the chamber during irradiation.

Measurements were made on a 4 MV X-ray beam using this chamber in conjunction with the calorimeter and a value of 1.016 ± 0.026 was obtained for the carbon/air mass stopping power ratio. This result is in close agreement with the previously determined experimental and theoretical values. An analysis of the experiment showed that one of the major sources of uncertainty was the variation of the beam profile produced by the accelerator. Possible solutions to this problem and others relating to the intercomparison of the various dosimetric systems are discussed.

More extensive measurements were made on electron beams with three different energies in the range up to 11 MeV. These included calorimetric calibrations of three secondary dosimetric systems, the carbon-walled ionization chamber, a Farmer-Baldwin chamber and a ferrous sulphate dosimeter, yielding carbon/air mass stopping power ratios, C_E values and G values respectively. The water/air C_E values derived from the above results are in close agreement with those previously determined and provide confirmation of the routinely employed values. The carbon/air mass stopping power ratios did not provide definitive confirmation of the existing theoretical estimates and served to underline the considerable amount of disagreement shown by other experimental determinations. As a result of the sharply contrasting irradiation geometries of the calorimeter and the ferrous sulphate vessels and the limited number of results, particular significance cannot be attached to the G value results. Nevertheless the results do reflect the trend towards lower G values when using a calorimeter as the reference instrument.

In conclusion, it may be stated that, whilst many more results will be required to reduce the present levels of uncertainty in the calibration factors, such as C_E and G, the present work does substantiate much of the currently available data. More particularly, the present work serves to highlight many of the problems involved in the design and operation of calorimeters, and the results presented demonstrate the influence of extraneous factors, such as environmental temperature stability and beam profile variation, on the results attainable by this method of dosimetry.

CHAPTER 1

CONCEPTS AND METHODS OF ABSORBED DOSE MEASUREMENTS

1.1 INTRODUCTION

One of the basic properties of directly and indirectly ionizing radiations is their ability to penetrate a condensed medium and interact with the atoms comprising this medium, the nett result of these interactions being a transfer of energy from the beam to the medium. This deposition of energy within the material may be quantitatively expressed by the absorbed dose, D. This quantity has been defined by the International Commission on Radiation Units and Measurements (I.C.R.U.) as the quotient of the mean energy imparted by ionizing radiations, $\Delta \bar{\varepsilon}$, in a volume element, Δv, by the mass of this volume, Δm, as this mass approaches zero. Stated mathematically this is

$$D = \frac{\Delta \bar{\varepsilon}}{\Delta m} \quad (\text{limit} \quad \Delta m \rightarrow 0) \qquad 1.1$$

$$\text{or} \quad D = \frac{d\bar{\varepsilon}}{dm} \qquad 1.2$$

This quantity will obviously be of fundamental importance in a rigorous discussion of the physical or biological effects of radiation.

In the case of high energy electron or photon beams impinging upon a material comprised of low atomic number elements ($Z < 26$), the predominant interactions concern the extra-nuclear electrons only (Araya, 1966). Such interactions have been extensively studied and are now quite well understood (Segrè, 1953). In particular, the irradiation of water or carbon media by a beam of high energy electrons has received considerable attention. A number of authors

(Spencer, 1955; Kessaris, 1964, 1966; Berger, 1965) have solved the appropriate electron transport equations, or performed a Monte Carlo calculation, to derive the energy deposition in a medium as a function of the depth below the entry point of the radiation. Unfortunately, many of the numerical values which must be substituted into these equations are not well known, and the theoretical predictions do not always agree with the experimental depth dose curves (Lillicrap and Rosenbloom, 1972).

The measurement of absorbed dose and the resultant construction of a depth dose curve is of central importance in radiotherapeutic practice, and, historically, considerable effort has been expended in the experimental determination of this quantity. Many of the earliest measurements in this field used small air ionization chambers or the yield of a radiochemical reaction, but, from the outset, it was realised that all such dosimeters required a calibration factor to convert their response into the required absorbed dose. Many of these calibration factors have been determined from theoretical considerations, and it has already been stated that the numerical substitutions involved in these factors are rather imprecise.

The only absolute method capable of measuring the absorbed dose is calorimetry, but, because of the technical difficulties involved and the lack of sensitivity, this method cannot be used for routine investigations. Nevertheless, this technique affords the only valid experimental determination of the aforementioned conversion factors, and the bulk of this thesis is concerned with the design, construction and operation of an absorbed dose calorimeter.

1.2 DEFINITION OF ABSORBED DOSE

One of the earliest units employed to define a radiation beam was the roentgen, and it served for many years not only as an indication of the photon intensity, but also as a basis for determining the energy absorbed per unit mass of air, or materials of similar atomic number. However, it was not until 1962 that the I.C.R.U. made the roentgen the unit of a rigorously defined quantity called the X-ray exposure. The strict application of this definition to experimental measurements requires that all charged particles, liberated by the photon flux at the point of measurement, are completely stopped and the ions which these charged particles produce are all collected. For photon beams generated by accelerating potentials in the range 5 kV to 500 kV this can normally be achieved by creating secondary electron equilibrium at the boundaries of the sensitive volume. When generating potentials in excess of 500 kV are employed, the ranges of the secondary electrons produced by the photon beam become comparable with the mean free path of the initial photons. In these circumstances the determination of exposure, and its relationship to the absorbed dose, becomes exceedingly complex. Perhaps the most serious limitation imposed by the definition of exposure though, is that it is limited solely to photon beams. To overcome these difficulties the I.C.R.U. published a report (National Bureau of Standards, 1962) setting out a detailed series of definitions for use in radiation practice. These definitions drew a clear distinction between quantities used to characterise a radiation beam, such as energy fluence, and the parameters used to specify the interaction of the beam with matter, such as the absorbed dose.

The original definition of the absorbed dose involved the use of an elementary volume, of mass Δm, such that the absorbed dose, D, was given by

$$D = \frac{\Delta E}{\Delta m}$$

where ΔE was the radiation energy locally imparted to the mass Δm. This equation requires that D is a macroscopic quantity, defined over the volume occupied by Δm, and any attempt to specify D at a point requires that the mass, Δm, approaches zero. In this situation the absorbed dose becomes a discontinuous quantity in time and space, due to the discreet and random nature of particle interactions. This inability to specify D at a point invalidated any attempts to differentiate the absorbed dose, and terms such as the absorbed dose rate, dD/dt, or the absorbed dose gradient dD/dx became meaningless.

This dilemma was resolved by the I.C.R.U. in 1971, who introduced the stochastic quantity, ε, defined as the radiation energy imparted to a volume ΔV. As this volume, ΔV, approaches zero, the imparted energy will be subject to very large fluctuations, however, the expectation value of the imparted energy, $\bar{\varepsilon}$, defined by the equation

$$\bar{\varepsilon} = \int_0^\infty \varepsilon . f(\varepsilon) d\varepsilon$$

where $f(\varepsilon)$ is the probability density of ε such that $\int_0^\infty f(\varepsilon)d\varepsilon = 1$, is not subject to random variations, and will converge smoothly to zero as the volume ΔV approaches zero. In this situation the absorbed dose can be defined in terms of the non-stochastic quantity $d\bar{\varepsilon}$, as the quotient of $d\bar{\varepsilon}$ by dm:

$$D = \frac{d\bar{\varepsilon}}{dm} \qquad 1.2$$

The special unit of absorbed dose is termed the rad, which is equal to 10^{-2} J/kg.

1.3 METHODS OF ABSORBED DOSE MEASUREMENT

1.3.1 Cavity Theory

In radiotherapy, as in most other applications, it is normally required to measure the absorbed dose, D_m, at a point of interest, P, in an extended medium, m. This measurement can be conveniently performed by inserting a probe of radiation sensitive material, i, in the vicinity of the point P. The signal generated by this probe material can then be related to the absorbed dose, D_m, which would have been produced in a homogeneous region of the material, m, at the point P. The general relationship between the signal developed by a probe, of any given size and composition, and the absorbed dose, D_m, is the domain of cavity theory. Historically, this theory was deduced for gas filled probes in condensed materials, hence the term cavity, but it is generally applicable to all probe materials and incident radiations. Many articles have been published on this theory and a broad synopsis, with particular reference to photon beams, has been given by Burlin (1968, 1970). The particular application of this technique to electron irradiation has been discussed by Burlin et al. (1969) and Harder (1968), but, because of the central importance of this aspect of the theory to the present work, a brief account, based on that presented by the I.C.R.U. (1972), will be given here.

Consider the situation depicted by Figure 1.1, where a probe

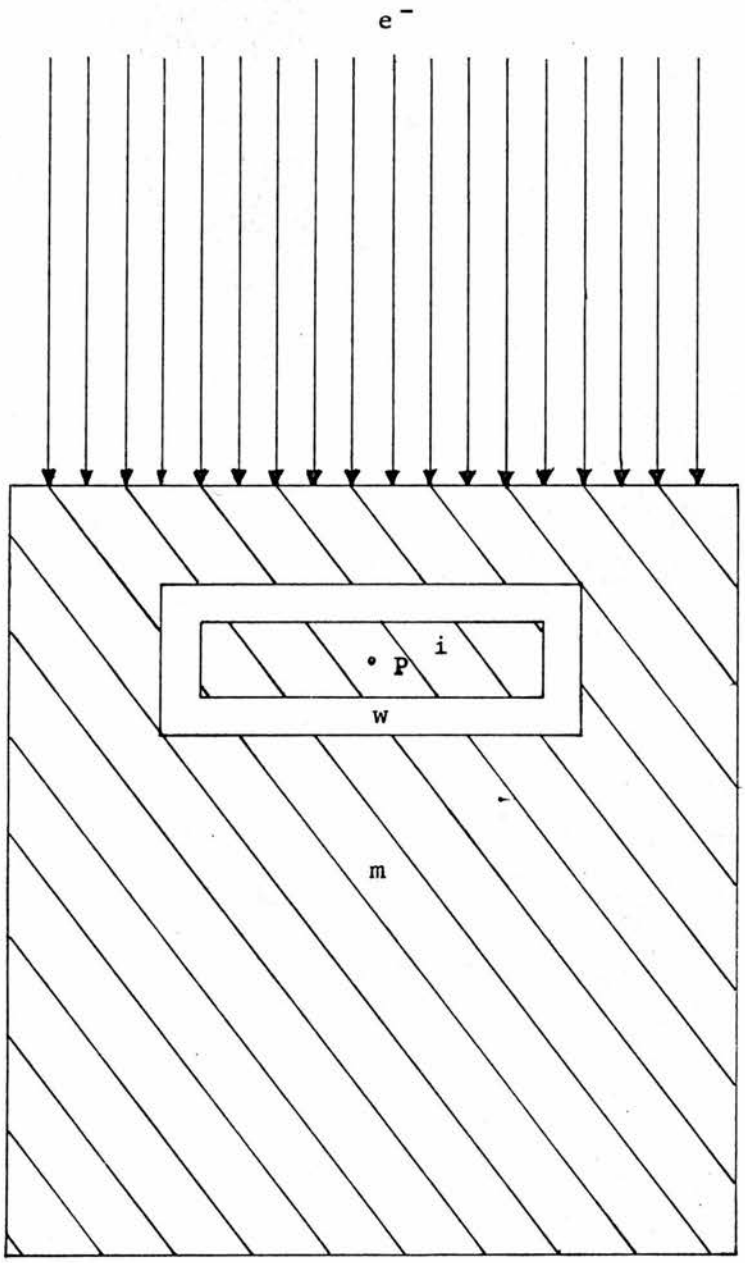

FIGURE 1.1 PROBE OF MATERIAL i IN MEDIUM m, AT POINT, P, IRRADIATED BY ELECTRON BEAM, e^-

of material,i, surrounded by a wall of material,w, is irradiated by a beam of high energy electrons, $\bar{e}$. If the extent of the probe and wall material is small when compared with the range of the primary electrons traversing the probe, then the dose, D_m, at the point P will be given by the Bragg-Gray relation:

$$D_m = D_i s_{m,i} \qquad 1.2$$

where D_i is the absorbed dose in the probe material and $s_{m,i}$ is the ratio of the mass collision stopping powers of the medium, m, to the sensitive material, i, integrated over the whole of the electron spectrum present in the probe. Using the idealised assumption that the electrons dissipate their energy continuously, and that the electron spectrum at the point P is not distorted by the presence of the probe, $s_{m,i}$ is given by

$$s_{m,i} = \frac{\int_o^{E_o} (\Phi_E)_m \cdot (\frac{S}{\rho})_{COLL,m} \cdot dE}{\int_o^{E_o} (\Phi_E)_m \cdot (\frac{S}{\rho})_{COLL,i} \cdot dE} \qquad 1.3$$

where (Φ_E) is the electron fluence spectrum in the medium, m, in the vicinity of P, having a maximum electron energy E_o, and $(\frac{S}{\rho})_{COLL}$ refers to the mass collision stopping power in the energy range E to E + dE.

In practice the existence of the probe and wall material does produce a slight perturbation of the electron spectrum in the region of P, and a factor $p_{m,i}$ must be introduced into equation 1.2 to account for this effect. Therefore equation 1.2 becomes

$$D_m = D_i \, s_{m,i} \, P_{m,i} \qquad 1.4$$

The perturbation factor defined here should not be confused with a similar factor, $p_{m,i}$, which is often included to account for the non-realization of secondary electron equilibrium at the point P,

when the medium is undisturbed by the inclusion of the probe.

The determination of the absorbed dose in the probe material, D_i, depends on the choice of this material, and normally an effect such as the ionization produced in a gaseous probe, or the yield of a radiochemical reaction in a liquid probe, is used to calculate D_i.

Equation 1.3 indicates that a precise knowledge of the electron spectrum traversing the probe will be required for a correct evaluation of $s_{m,i}$. It has been stated (I.C.R.U., 1972) that as much as 25% of the absorbed dose may be contributed by the low energy tail of the electron spectrum below 0.1 MeV, thus it will be necessary to consider all parts of the spectrum. However, under conditions of secondary electron equilibrium at the boundaries of the sensitive volume, the energy transport across the boundaries by these secondary electrons will exactly cancel, and, in this situation, it is permissible to neglect all electrons with energies below a value Δ, related to the dimensions of the probe. In this event the calculation of the mass stopping power ratio becomes

$$s_{m,i} = \frac{\int_{\Delta}^{E_o} (\Phi_E)_m \cdot (\frac{s}{\rho})_{COLL\ \Delta,m} \cdot dE}{\int_{\Delta}^{E_o} (\Phi_E)_m \cdot (\frac{s}{\rho})_{COLL\ \Delta,i} \cdot dE} \qquad 1.5$$

where the symbol $(\frac{s}{\rho})_{COLL,\Delta,m}$ refers to the restricted mass stopping power of an electron at energy, E, with a cut-off energy, Δ, for the secondary electrons. The whole term relates to the medium m. Furthermore, this argument can be extended to include all electron energies, by postulating that electronic equilibrium exists up to

the most energetic electrons, E_o, at the depth of interest. Then, if a linear relationship exists between $(\frac{s}{\rho})_{COLL}$ and the energies in the region of the peak of the primary electron spectrum at the point of interest, equation 1.5 reduces to

$$s_{m,i} = \frac{(\frac{s}{\rho})_{COLL,\bar{E},m}}{(\frac{s}{\rho})_{COLL,\bar{E},m}} \qquad 1.6$$

where $\bar{E}$ is the mean electron energy at the point of interest, weighted by a function to account for the spectral distribution (Harder, 1965). It has also been shown (Harder, 1966) that for beams of narrow spectral width, this mean electron energy, $\bar{E}$, decreases linearly with depth. The evaluation of equations 1.3, 1.5 and 1.6 can be performed with the aid of tables of mass stopping power ratios published by Berger and Seltzer (1964, 1966) and the rather scant data for the energy spectrum of electron beams in water and carbon, Kessaris (1966, 1970a), Harder (1966) and Berger and Seltzer (1969).

If the probe and wall material, i and w respectively, are similar to that of the irradiated medium, m, then the value of the perturbation coefficient, $p_{m,i}$, will be close to unity, and may, in some cases, be neglected. Alternatively, the value of $p_{m,i}$ can be determined by extrapolating the probe size to zero (Rase and Pohlit, 1962) and for a few simple geometries a theoretical evaluation can be made (Harder, 1968).

1.3.2 The Absolute Determination of Absorbed Dose

A considerable simplification of equation 1.4 can be achieved if the probe material has the same composition and density as the surrounding medium. The value of $s_{m,i}$ then becomes unity and,

apart from a small perturbation correction for the wall material, the value of $p_{m,i}$ is also unity. If all the energy locally imparted to the medium, m, is degraded into heat, and none of this energy is allowed to escape to the surroundings, then it is possible to estimate the absorbed dose in the medium directly. Stated mathematically this means that

$$D_m = \frac{dE}{dm} = \frac{dE_h}{dm} + \frac{dE_s}{dm} \qquad 1.7$$

where dE_h is the energy appearing as heat, and dE_s signifies any heat loss or defect, which, to fulfil the above condition, must be equal to zero. Equation 1.7 defines, in essence, the principles of calorimetry and is of prime importance.

Unfortunately however, the theoretical advantages of this approach are considerably offset by the practical difficulties involved. As an example consider the requirement that $dE_s = 0$. This constraint requires that all the energy deposited by the beam appears as heat, and, since few materials which exist in a chemically combined state exhibit a zero heat defect, it is not possible to estimate directly the absorbed dose in water, soft tissue, bone or other materials of particular biological interest. The major disadvantage of this method however, lies in the necessity to measure the extremely small quantities of heat evolved. If no change of state occurs in the absorber, then, for a material of constant specific heat, C_p, the temperature change is given by

$$\frac{dE_h}{dm} = C_p \Delta T$$

For an absorbed dose of a few hundred rads, commonly encountered in radiotherapy, ΔT would be a few milli kelvin, which, for an accuracy

of 1%, requires a temperature detection system capable of discriminating to the micro kelvin level. The complexity of the equipment necessary to isolate and detect such small temperature changes does not allow this approach to be used for routine measurements.

1.3.3. Secondary Dosimetric Systems

Traditionally, the use of a gas-filled cavity as the probe and the collection of the charged ions produced during irradiation has served as the simplest and most direct method of absorbed dose measurement. Substitution of the mass stopping power ratio into equations 1.3, 1.4 and 1.5, when these equations are applied to a gas-filled probe traversed by a relativistic particle beam, is complicated by the presence of the density effect (Sternheimer 1952, 1956). Briefly, this effect states that, at relativistic particle energies, the mass stopping power of a condensed medium is less than the mass stopping power for the same medium in a gaseous state, the effect increasing with the particle energy. Although this complication can be allowed for in calculations of the mass stopping power ratio, $s_{m,i}$, the nett result is to increase the dependence of this function on the electron spectrum within the cavity. In particular, if the probe is used to estimate the dose throughout an extended medium, as in radiotherapy depth dose curves, the calibration factor becomes a continuously varying function of depth, since the radiation spectrum changes with its passage through the medium. In addition, if a large cavity of much less dense material (i.e. gas) is present in the medium, a quite different electron fluence will be produced inside the cavity compared to the fluence which would have been present had the cavity been replaced by the homogeneous medium (Harder, 1968). As a result, the perturbation factor can diverge

quite markedly from its optimum value of unity.

The complications of the density effect can be eliminated by utilising a solid or liquid probe material, and considerable research has been devoted to the investigation of liquid chemical dosimeters for this application. Of these, probably the most widely used is the Fricke, or ferrous sulphate, dosimeter, which employs the radiochemical oxidation of ferrous to ferric ions to estimate the absorbed dose (Fricke and Morse, 1927; Shalek and Smith, 1969). If this dosimeter is used to measure the absorbed dose in a water medium, the aqueous nature of the probe material (96% water I.C.R.U., 1972) means that not only is the perturbation factor very nearly unity, but also the stopping power ratio is approximately unity and shows very little dependence on electron energy. The disadvantage of this system however, is the rather poor sensitivity, a series of ten readings each of 10 k rads is required to yield an uncertainty of 0.4% (95% confidence limit) under ideal conditions (I.C.R.U., 1972). Also, the need for meticulous care in the preparation and handling of the dosimeter constituents and their containing vessels adds a further unfortunate complication.

In recent years many solid state probe materials have been produced, which are reputed to yield an approximately linear response to absorbed dose, and are suitable for measurements in biological systems. In particular, thermoluminescent crystals (T.L.D's) such as lithium fluoride, which has a mass number similar to that of water, and solid state ionization chambers, such as semiconductor p-n junctions, have shown considerable promise.

Nevertheless, all the dosimetric systems mentioned in this

section constitute a probe of foreign material in the irradiated medium, and must therefore rely on cavity theory, as expressed by equations 1.3 to 1.6, to evaluate the absorbed dose in the extended medium. In this respect all these systems must be regarded as secondary dosimeters since they require an experimental or theoretical factor to convert their response into the desired parameter.

1.4 AIMS OF THE PROJECT

At present ionization chambers, and to a lesser extent ferrous sulphate ampoules, are still widely used in the routine assessment of absorbed dose for radiotherapy applications and, until the reliability, or otherwise, of the new generation of solid state dosimeters is proven, these systems will provide the mainstay of dosimetric measurements.

The relevant conversion factors for these two systems when irradiated by megavoltage X-ray beams have been reviewed by the I.C.R.U. (1969). As noted above many of these factors have been derived from theoretical considerations, and,whilst extensive experimental confirmation is still lacking, the few published experimental results indicate a substantial degree of support for the accepted values (Bewley, 1963; Almond, 1968; Engelke and Hohlfeld, 1971a).

The situation with regard to high energy electron dosimetry is rather less satisfactory, since most of the experimental conversion factors for ionization chambers have been determined by reference to a ferrous sulphate dosimeter (Svensson and Pettersson, 1967; Svensson, 1971; Loevinger et al., 1961). As yet no national

standardising laboratory has produced a calorimetric standard for either type of radiation, although considerable efforts are being made in this direction (Kemp, 1971; Domen, 1969, 1970; Engelke and Hohl feld, 1971a; Sakata, 1972).

The aim of the work reported here is to construct a calorimeter, specifically for use with high energy electrons, to act as an absolute standard of absorbed dose. Then, using this instrument, the routinely employed secondary dosimeters can be directly calibrated, yielding an experimental check of the theoretically derived conversion factors.

CHAPTER 2.

C A L O R I M E T R Y

2.1 PRINCIPLES OF CALORIMETRY

The basic principles of calorimetry, which were outlined in section 1.3.2., can be summarised by the equations given there

$$D = \frac{dE}{dm} = \frac{dE}{dm}_h + \frac{dE}{dm}_s \qquad 1.7$$

$$\frac{dE}{dm}_h = C_p . \Delta T \qquad 1.8$$

This chapter discusses the implications of these equations and the practical methods by which they can be realised. A short section reviewing the experimental aspects of calorimetry, with special reference to absorbed dose measurements, has also been included to indicate the capabilities of the method.

2.1.1 Absorber Size and Geometry

The strict application of the definition of absorbed dose (Chapter 1.) requires the evaluation of the stochastic quantity $\bar{\varepsilon}$ in a vanishingly small volume element. For all practical purposes this is a mathematical abstraction since, experimentally, the mean energy absorbed in a finite volume of mass Δ m will always be measured. However, to avoid the possibility of a dose gradient occurring within the sample volume it is desirable to keep this volume small. In calorimetric measurements though, two other competing factors set a lower limit to the size of the absorbing element. Firstly, to measure the temperature and evaluate the thermal capacity of the absorber, it is necessary to introduce a certain amount of foreign material into this component. To reduce any perturbing effect that these materials might produce the mass

of the absorber should be as large as possible. Secondly, a very small volume would have an insignificant thermal capacity and consequently would be very susceptible to thermal shocks, thereby masking the desired signal. In practice a compromise must be reached such that the chosen volume is large enough to satisfy the experimental requirements whilst minimising the absorbed dose gradient within this volume. Normally this volume is also sufficiently large to include a great many interactions, thus the problem of the random deposition of energy does not arise.

The design of absorbing element most commonly employed in radiation calorimeters is that of a disc, orientated with its plane faces perpendicular to the axis of the incident beam. This geometry affords a well defined depth of measurement, whilst allowing the mass of the element to be increased at will by extending the radial dimensions to the limits of the uniform radiation field. The surface to volume ratio of this design is rather poor, resulting in an undesirable increase in the heat leakage modulus (Chapter 3). To counteract this failing Petree and Ward (1962) constructed a calorimeter employing a spherical absorbing body. This geometry has the advantage of an optimum surface to volume ratio, resulting in a minimal heat leakage modulus. Unfortunately though, this design does not readily lend itself to the introduction of a calibration heater and the possibility of creating severe temperature gradients, due to an eccentrically located heater, detracts from this approach.

The present calorimeter design was originally based on a disc or coin-shaped geometry, but, for constructional reasons, this was later altered to a cylindrical or rod-shaped geometry, where the axis of the cylinder was orientated perpendicular to the direction

of the incident beam.

2.1.2 Heat Defect

The possibility of an incomplete degradation of the radiation energy into heat was accounted for in equation 1.7 by the inclusion of the term dE_s, which is normally referred to as the 'heat defect'. An incomplete energy conversion is usually associated with the presence of radio-chemical reactions. This effect occurs most readily in chemical compounds, where the breaking and reforming of chemical bonds can result in a large positive or negative energy change. This defect is particularly marked in polymers due to their large numbers of cross-links and chains, but, because of their tissue equivalent properties, a number of studies have been carried out using these materials. An early experimental demonstration of the heat defect was reported by Milvy and his colleagues (Milvy et al., 1958), who noted an endothermic defect of 3% in a polytheylene/carbon mixture when irradiated with ^{60}Co gamma rays. In a similar investigation Fleming and Glass (1969) used a Shonka type tissue equivalent plastic (T.E.P.) (Shonka et al., 1958) irradiated with 1.7 MeV protons and observed an endothermic defect varying from 4.17% to 3.6%, the precise value depending on the cumulative dose received by the material. A subsequent determination of the defect in this material, when irradiated by the lower L.E.T. ^{60}Co gamma rays, indicated a defect of -3% (Fleming, 1970). The most recent assessment of the defect in T.E.P. irradiated with ^{60}Co gamma rays indicated an initial exothermic defect of 10%, which progressed to an endothermic defect of 4% after a cumulative dose of 100 krad (Bewley et al., 1971). A similar variation was reported by Major (1973) who used a polyethylene absorber irradiated with

^{60}Co gamma rays and noted a change from an initial value of + 2.5% to a steady state value -2.3%. The explanation of the deviation of these values from the expected endothermic effect was suggested by Ebert (Bewley et al., 1971) to be the result of an initial radiochemical reaction between the material and any absorbed oxygen, which, as a combustion process, would liberate a considerable amount of energy.

The substantial variation and uncertainty in these figures does not recommend the use of chemically combined compounds in absolute calorimetric systems, and, unless there is some overriding reason for their use such as in neutron dosimetry, recourse must normally be sought to materials composed of pure elements. Nevertheless, even in these materials the possibility of stored energy in the crystal lattice (Dienes and Vineyard, 1957; Billington and Crawford, 1961) and radiochemical reactions with absorbed gases, such as atmospheric oxygen, demand careful consideration before a reliable estimate of the absorbed dose can be derived.

2.1.3 Selection of Calorimeter Material

The prime objective of the present investigation is to construct a calorimetric system to calibrate secondary dosimeters for use in biological applications. This condition requires that the calorimetric material has an atomic number and electron density close to that of water or soft tissue and, for a minimal heat defect, it must also be a pure element. Inspection of the periodic table shows that the only solid elements with the desired atomic number are carbon, magnesium and aluminium. Of these magnesium is less readily available than the other two and is rather reactive, especially in humid conditions. Although at least one calorimeter has been constructed

of this material (Keene and Law, 1963) it has not gained a wide acceptance as a calorimetric medium. A further interesting possibility is the construction of a magnesium-beryllium, or an aluminium-beryllium, alloy with a mean electron density identical to that of water, but, since berryllium is a rather toxic substance which has to be machined in special workshops, this does not offer an attractive alternative. A further consideration in the selection of a calorimetric material is the thermal conductivity, since the use of a poor thermal conductivity material may produce severe temperature gradients within the absorber, especially during calibration if the source of electrical energy is a discreet heater. In this situation the measured temperature becomes a function of position and any corrections may be subject to a large error. In this respect both carbon and aluminium are sufficiently good thermal conductors to reduce such problems to a minimum.

2.1.4 Calibration

In most calorimeters the estimation of the heat deposited by the passage of a radiation beam is performed by observing the resultant temperature rise, and then simulating an equivalent temperature change by injecting a known amount of electrical energy. Provided that the point of measurement and the temperature gradients are the same during the radiation and calibration experiments, the energy deposited may be represented as

$$W_{RAD} = W_{ELEC} \frac{\Delta T_{RAD}}{\Delta T_{ELEC}} \qquad 2.1$$

The passage of a radiation beam through a homogeneous medium results in a regular deposition of energy, yielding a bulk heating effect, and the major problem in calibration experiments is to recreate this

uniform heat distribution. The most common approach to this problem has been to distribute a resistance wire, or thin film heater, as evenly as possible throughout the absorber and then to estimate a correction for any ensuing temperature gradients. Several attempts have been made to simulate a bulk heating effect using the electrical resistance of the absorbing medium as its own heating element (Milvy et al., 1955; Genna et al., 1963). Unfortunately though, the difficulty of providing good electrical contacts to these materials and the high proportion of polymers normally present, with a subsequent heat defect, detract from the advantages of this method. Of particular interest in this respect though, is the use of pyrolytic graphite in an absorbed dose calorimeter under development at the National Physical Laboratory (Kemp, 1971). This substance is anistropic and has the particular merit of exhibiting a high electrical resistance in one direction, which has been utilised to provide a bulk heating effect. Also, since the material is a pure element, it does not show a significant heat defect.

2.1.5 Temperature Stabilising Systems

It was observed in Chapter 1 that the main reason for regarding calorimetry as a specialised research or calibration instrument was the necessity to determine very small temperature changes, 10^{-3}K, to a high degree of precision. The techniques available for measuring such small temperature changes are fully discussed in Chapter 4, but it is perhaps pertinent to mention here some of the techniques which can be used to provide a stable thermal environment capable of suppressing any external temperature variations. Probably the simplest and most straightforward method is to immerse

the calorimeter in an ice-water bath, such as the type described by Dove and Cole (1962). This technique was also initially adopted by Redpath (1967) but, because one face of the calorimeter, which constituted the thin entry window for the radiation beam, was exposed to the external environment, the temperature regulation of the actual absorber was very poor and the design had to be abandoned. It is probable that with a very carefully designed system this difficulty could be substantially reduced. However, the problem of achieving a stable thermodynamic equilibrium is more difficult to solve and therefore this technique of temperature stability is seldom used.

A variation of the ice-water bath approach is the use of a thermostatically controlled fluid bath. Calorimeters employing this system have been described by Myers et al. (1961), Kruglov and Lopatin (1963) and Laughlin and Beattie (1951). However, to achieve a stable temperature control (3×10^{-4}K, Myers) a large volume of coolant liquid is required (200 gallons, Myers). Less bulky thermostatically controlled environments can be produced by utilising a solid shield, containing a controlled heating element, to surround the calorimeter absorber and jacket (Milvy et al., 1955). Unfortunately though, all these approaches require the provision of a sophisticated feedback and control circuit which adds an extra constructional burden. Also, if this device is incorrectly adjusted it can lead to excessive "hunting".

A simpler approach is the use of a 'twin' absorber system where a dummy absorber, with identical physical properties, is situated adjacent to the true absorber but shielded from any radiation input.

In this situation both absorbers experience similar thermal environments and any temperature fluctuations will occur equally in either element. If the temperature measuring system is carefully designed these variations can be made to cancel out, leaving a signal derived solely from the radiation or electrical heat input to one absorber. The stringent temperature regulations normally demanded by radiation calorimeters can then be considerably relaxed, obviating the need for a carefully regulated thermal environment.

Another solution to the temperature stability problem, and the one used here, which avoids the need for a complicated feedback system or the construction of a twin absorber, is the multijacket principle. The origin of this method has been attributed to Tian (1922)(Laughlin and Genna, 1966) and practical adaptations have been described by Linacre and Thomas (1965) and Domen (1969). Basically, the design consists of a central absorber surrounded by a series of high thermal conductivity elements, each element totally enclosing the preceding one but remaining thermally isolated from it. Once this system has attained thermal equilibrium any thermal shock, applied via the outermost element, will be absorbed by this element and result in an even temperature change throughout this first element. (This situation is analogous to the distribution of an added charge over the surface of a hollow electrostatic conductor.) This change in temperature results in a small, but fairly even, heat flow towards the next internal element which smooths out any remaining temperature inhomogenities. This operation may be repeated indefinitely by increasing the number of elements, but, in practice, the rapidly

increasing complexity of construction and the large number of voids or discontinuities produced by a multijacket system, limit the number of elements to two, or possibly three, jackets surrounding the central absorber. The nett result of such an arrangement is that any temperature fluctuations, with a time constant much less than that of the system, are not transmitted to the absorber and, although long term temperature changes are recorded by this element, the large thermal capacity of the surrounding shields and the long time constants involved reduce these changes to an acceptably small temperature drift rate in the central absorber.

2.2 MODES OF CALORIMETER OPERATION

The basic design of an absorbed dose calorimeter is very similar to the requirements expressed by Figure 1.1. In its simplest form the calorimeter consists of an element, or absorber, surrounded by a bulk of similar material referred to as the jacket. In this situation the temperature behaviour of the system, in the absence of external heating, may be represented by equation 2.2:

$$\frac{dT}{dt}A = -K_A (T_A - T_J) \qquad 2.2$$

where T_A is the absorber temperature at a time t, T_J is the jacket temperature, also at the time t, and K_A is the absorber heat leakage modulus, defined as the quotient of the total heat leakage coefficient, h_A, by the thermal capacity of the absorber, $m_A c_A$, m_A being the mass and c_A the specific heat of the absorber. If the rate of energy deposition in the absorber is W_A then the temperature time relationship becomes

$$\frac{dT}{dt}A = \frac{W_A}{m_A c_A} - K_A (T_A - T_J) \qquad 2.3$$

where 2.2 and 2.3 both assume a linear relationship between temperature difference and the rate of cooling. This is sometimes referred to as Newton's Law of Cooling. In fact this nomenclature is incorrect in this application, since Newton's law relates to a state of free or forced convection whilst most calorimeters are designed to operate under conditions of zero convection. Nevertheless, for the small temperature differences encountered in radiation calorimetry the modes of heat transfer (i.e. conduction and radiation) do approximate very closely to a linear relationship (Chapter 3). A further assumption implicit in these two equations is the existence of a uniform temperature distribution throughout the jacket and absorber. For the case of calibration heating this is rarely true and a fuller description of the temperature distribution and heat flow, such as that given by West (1963), should be used. For the purposes of the present discussion though, equations 2.2 and 2.3 will suffice and the deviations from ideal conditions will be reviewed elsewhere (Chapter 5). In principle, equations 2.2 and 2.3 can be applied in a number of ways to estimate the total heat evolved, but it will be convenient here to classify these methods into three groups - namely Isothermal, Heat Flow and Adiabatic.

2.2.1 Isothermal

In this design the whole system is constrained to remain at one fixed temperature and the heat developed is measured by the change of state in one of the constituents of the absorber. Most examples of this method are based upon Bunsen's ice calorimeter, such as the experiments described by Ginnings et al. (1953) who used this technique to measure the half life of Polonium. Other examples of this method have been reviewed by Laughlin and Genna (1966) who noted that unless

very high dose rates (> 1,400 rads/min) were used to mask the spontaneous changes in volume, due to lack of thermodynamic equilibrium, appreciable errors could ensue. Since this technique can usually only be applied to radionuclide measurements, when the sample can be completely enclosed in the calorimeter thereby preventing any heat loss, it is inapplicable in the present situation.

2.2.2 Heat Flow Calorimetry

If the jacket temperature, T_J, is held constant at a value T_O by a thermostatic control system or the freezing point of a eutectic mixture, then equation 2.3 becomes

$$\frac{dT}{dt}_A = \frac{W_A}{m_A c_A} - K_A (T_A - T_O) \qquad 2.4$$

which when integrated with respect to 't' gives

$$T_A = T_A' \exp(-k_A t) + \left[T_O + \frac{W_A}{K_A m_A c_A} \right] \left[1 - \exp(-K_A t) \right] \qquad 2.5$$

where T_A' is the absolute temperature at time t = O. The most straightforward application of this equation is to allow the system to reach equilibrium, when the exponential factors disappear and equation 2.5 reduces to

$$T_A - T_O = \frac{W_A}{K_A m_A c_A}$$

The equilibrium temperature difference is then directly proportional to the rate of heat input. The disadvantages of this method are the need for an accurate evaluation of K_A and the considerable lengths of time required to achieve equilibrium. The latter objection can be substantially reduced by employing the kinetic method developed by Radak and Marković (1962). This approach consists of plotting

the absorber temperature as a function of $\exp(-K_A t)$ and then extrapolating the straight line obtained to the zero value of this function (i.e. $t = \infty$), which yields the final equilibrium temperature. A further refinement of the isothermal technique was provided by Dove and Cole (1962) who deduced a method of measurement which eliminated a knowledge of the leakage modulus K_A whilst still retaining a short observation period. Briefly, the method consists of heating the absorber from a temperature T_1 to a temperature T_2 (T_1 & $T_2 > T_0$) in a period t_1, the absorber is then allowed to regain the initial temperature, T_1, in a time t_2. Substitution of these values in equation 2.5 yields, on rearrangement,

$$\frac{W_A}{m_A c_A} = \frac{K_A}{2} (T_2 - T_1) \left[\coth \left(\frac{K_A t_1}{2}\right) + \coth \left(\frac{K_A t_2}{2}\right) \right]$$

which, if t_1 and $t_2 \ll K_A^{-1}$, gives

$$W_A = m_A c_A (T_2 - T_1) \left[\frac{1}{t_1} + \frac{1}{t_2} \right]$$

Another interesting variation of the isothermal method is the use of a differential heat flow technique, such as the example reported by Fleming (1970). This calorimeter consisted of two T.E.P. absorbers, one solid the other hollow, both exposed to a ^{60}Co γ-ray beam. These absorbers had identical external dimensions and surface coatings (Al) which resulted in identical heat transfer coefficients, but, because of the different masses, the heat leakage moduli were substantially different. Although the power developed per unit mass during irradiation is the same in each absorber, neglecting attenuation effects, the equilibrium temperature of the solid absorber (which has the lower K_A value) is higher than that of the hollow absorber. This calorimeter could then be calibrated directly during irradiation

by introducing just enough electrical energy into the hollow absorber to annul the temperature difference between the absorbers. This energy is exactly equal to the radiation energy deposited in the extra mass of the solid absorber. Unfortunately, the simplicity of the method was devalued by the use of a heat defect material. A slightly modified differential technique was used by Fregene (1967) to calibrate ferrous sulphate dosimeters exposed to ^{3}H and ^{32}P β rays, but the method was less elegant than that of Fleming (1970). Whilst the technique of thermal cycling has been successfully applied to low energy X-ray beams generated by a stabilised X-ray tube (Redpath, 1967) the isothermal method is more useful for constant flux sources, such as those encountered in atomic piles or the decay of long lived radionuclides, since all approaches require a very stable value of the heat input, W_A. Most clinical linacs have rather unstable outputs and are not designed for long periods of continuous operation. Thus the use of an isothermal method is inapplicable in the present situation.

2.2.3 Adiabatic and Quasi-adiabatic Calorimetry

This approach requires that the temperature difference $T_A - T_J$ is constrained to be zero throughout the experiment. Equation 2.3 then reduces to

$$\frac{dT}{dt}A = \frac{W_A}{m_A c_A} \qquad 2.6$$

which on integration yields a linear relationship between the temperature rise and the absorbed energy. The factor $m_A c_A$ can be determined from weighings and the relevant value of c_A, or, more usually, by the method of calibration outlined in section 2.1.4 since tabulations of specific heats are rarely precise enough for

accurate evaluation. In most instances it is impossible to maintain zero heat transfer, even with the aid of heaters coupled to thermometric feedback systems (Fleming and Glass, 1969), and a more realistic approach is to correct for the small residual heat leakage between the absorber and the jacket. The precise calculation of this correction has been described by Genna et al. (1963) and will be further discussed in Chapter 5, but, basically, it consists of an observation of the temperature history before and after the application of a heat input. Normally this correction is quite small and, in the case of radiation heating, may be zero. This is a result of the bulk heating effect which does not disturb the temperature differences within the calorimeter. A particular advantage of this method is the elimination of the heat leakage modulus, K_A, from the defining equation 2.6, the only restriction being that K_A is small allowing the heat loss correction to remain valid. A further benefit of this approach is that it can be applied to radiation beams of variable intensity existing for only a short duration. Such beams are often generated by clinical linacs. The severe limitations of all the other methods described in this section leave this technique as the only suitable alternative in the present situation.

2.3 CALORIMETRY : A REVIEW

The scope of radiation calorimetry is prodigious and a complete review of the whole subject would be inappropriate in this thesis. Instead, a brief mention of some of the applications of calorimetry will be made followed by a more detailed study of absorbed dose calorimeters. Two very comprehensive reviews covering most aspects

of calorimetry have been published by Gunn (1964, 1970), whilst the I.C.R.U. have published reports outlining absorbed dose calorimetry for X rays (1968) and electrons (1972). More general treatments of the subject, covering the various modes of operation, temperature measurements etc., have been published by Radak and Marković (1970) and Laughlin and Genna (1966). The latter authors reviewed some of the earlier calorimeters (Curie and Laborde, 1904; Rump, 1927) which were used as total photon absorption instruments. Similar techniques, with the refinements of sophisticated temperature measuring systems and corrections for energy loss due to transmission or scattering, are still used today and form a large branch of calorimetry. A number of authors (Laughlin and Beattie, 1951; Goodwin, 1959; Pruitt and Domen, 1962; Kruglov and Lopatin, 1962; Redpath, 1967) have used this total absorption method to measure X-ray fluence, whilst Myers et al. (1961) have used the technique to estimate the activity of ^{60}Co and Radium sources and Ginnings et al. (1953) determined the half life of a polonium sample by this method. One of the most recent applications of radiation calorimeters is the development of atomic reactor 'in-pile' calorimeters (Kott, 1967; Linacre and Thomas, 1965) where the extremely high flux rates often make calorimetry the system of choice. In addition, the selection of different absorbing elements, such as graphite, heavy water and light water (Radak and Marković, 1962), can yield valuable information about the reactor (particle) spectrum due to the differing absorption properties of these materials for neturons and X rays.

2.3.1 Absorbed Dose Calorimeters

The perfection of the thermistor as a highly sensitive temperature

transducer in the 1950's, and the coincident proliferation of high energy linear accelerators for clinical and industrial use, allowed the first serious attempts to be made in the construction of absorbed dose calorimeters. One of the earliest descriptions of this generation of calorimeters was given by Laughlin and his colleagues (Laughlin et al., 1956; Milvy et al., 1958) who used a polyethylene-carbon matrix as the absorbing medium which also acted as its own self heating resistance. The calorimeter was operated in the quasi-adiabatic mode with a thermostatically controlled mantle and the system was used to derive the G value for the ferrous sulphate dosimeter at ^{60}Co energies. A similar calorimeter, constructed of tissue equivalent plastic (Shonka et al., 1958), for use with high energy X rays was described by Genna (1963) but no details of irradiation results were included. Since both these calorimeters exhibited heat defects a further calorimeter, based on Laughlin's design, was developed by Geisselsoder and her colleagues (1963) which employed carbon as the absorbing medium . This calorimeter was used to calibrate commercial thimble ionization chambers as well as a ferrous sulphate dosimeter at 10 and 20 MeV electron energies.

Another North American group headed by Johns described some initial work with aluminium alloy and Carbon calorimeters designed to operate with 22 MV X rays and ^{60}Co γ rays. The initial construction (Skarsgard et al., 1957) was rather crude and lacked any jacket or mantle calibration heaters to simulate the quasi-adiabatic conditions encountered during irradiation. This deficiency was rectified in a later model (Reid and Johns, 1961) who determined the $\overline{W}$ value for air at ^{60}Co and ^{137}Cs γ-ray energies, but, because of

the rather involved calculations and corrections, these values were not well received (Bewley, 1963).

Two other calorimeters, which were designed for use with high energy electron beams have been described by Almond (1967) and Pinkerton (1969). Almond's calorimeter was a rather simple design, consisting of a single aluminium disc with a calibration heating wire wound around the circumference and a single thermistor placed at the centre. The absorber was surrounded by an inner and outer jacket, of which only the latter contained a heating element for thermostatic control. Although a quasi-adiabatic analysis was adopted the absence of a calibration heater in the inner jacket and the rather poor geometry of the absorber heater could give rise to substantial errors. Pinkerton's calorimeter was of a more standard design. The single carbon absorber was surrounded by two jackets, both containing heating elements, and the whole assembly was placed in a large thermostatically controlled block. This calorimeter was used to calibrate a number of secondary dosimeters including T.L.D.'s and a semiconductor diode.

Apart from some early work by Goodwin (1960, 1963) who employed a composite wax-aluminium absorber irradiated by 250 kV X rays, one of the first calorimetric determinations of absorbed dose in this country was by Bewley (1963). This calorimeter, fabricated from graphite, used a twin absorber arrangement and was operated in a quasi-adiabatic mode. Calibration of a carbon-walled ionization chamber was performed which yielded mass stopping power ratios for carbon to air for X rays produced at various accelerating potentials between 4 and 20 MV, as well as ^{60}Co γ- rays. A similar design was subsequently used by Bradshaw (1965) to derive the carbon to air

mass stopping power ratio for 14 MeV electrons.

Several calorimeters have been specifically designed to calibrate ferrous sulphate dosimeters of which those by Keene and Law (1963) and Dove and Cole (1962) have already been mentioned. Although both of these calorimeters employed solid absorbing media, considerable interest has been shown in the use of aqueous absorbing elements in this particular application. One of the earliest reports of this approach was given by Hochanadel and Ghormley (1953) who used a small (2.54 cm dia.) silvered pyrex glass bulb to contain the aqueous absorbing medium. This bulb was enclosed by a heated copper jacket which was adjusted manually to maintain adiabatic conditions. The whole assembly was placed in an array of ^{60}Co sources which yielded a minimum exposure rate of 25 R/s (Authors' Nomenclature). This resulted in a temperature rise of better than 1 K/h which was measured by a thermocouple. No electrical calibration was used and the energy deposition was determined from a theoretical estimate of the heat capacity of the compound absorber. Other aqueous calorimeters have been described by Fregene (1967) who used a twin adiabatic system irradiated by 14 MV X rays and ^{60}Co γ rays, and Anderson (1962) who employed a very simple adiabatic device at very high electron dose rates, 10^8 rad/s. Probably the most refined example of this technique is the apparatus described by Pettersson (1967) who used a water filled dewar flask as the absorbing element and surrounded this with a constant temperature water bath. Instead of an electrical calibration he calculated the temperature rise by noting the expansion of the absorber fluid along a graduated capillary tube and the tabulated coefficients of expansion for water and glass. Strictly speaking none of this group

is a true absorbed dose calorimeter since the composite nature of the absorber and jacket do not conform to an extended homogeneous medium, and, in the cases of Pettersson and Anderson, a total beam absorption label would not be inappropriate. Nevertheless, the method does appear to yield consistent results and, despite the large corrections for the additional heat developed in the container walls during irradiation, it is capable of a high precision.

The advantages of using a calorimetric system as a national and international standard were noted by Reid and Johns in 1961. This statement precipitated the first of a series of reports published by a group working at the National Bureau of Standards in the U.S.A. (Petree and Ward, 1962; Petree and Lamperti, 1967; Domen, Petree and Lamperti, 1970). The initial design was based on a spherical absorber which, as observed earlier in this chapter, gave an optimum surface to volume ratio. However, the existence of a temperature gradient due to the location of the calibration heater caused considerable problems and a number of corrections had to be evaluated. In particular, one correction for the heat loss, determined by extrapolating measurements at atmospheric pressure and very low pressures to zero pressure, must be regarded with considerable suspicion, since the heat transfer mechanisms in gases are markedly different at these pressures. The problems generated by the heat leakage corrections culminated in 1969 with the publication of Domen's Heat Loss Compensated Calorimeter (Domen, 1969). In this design an extra thermal jacket surrounds the absorber, the purpose of this jacket being to trap any heat lost by the absorber during calibration due to lack of perfect adibatic conditions created by the temperature gradients. The temperature

measuring system was designed to add this residual heat leak directly to the main signal. Apart from a brief report in 1970 (Domen, 1970) which noted a reversion to the popular disc geometry, no further details appear to have been published. Another national standard calorimeter has been described by a group working at the Physikalisch-Techische Bundesanstalt (P.T.B.) in Germany (F.R.G.) (Engelke and Hohlfeld, 1971a). This calorimeter, constructed from graphite, had a single disc shaped absorber which was equipped with a conductive glue heater and four thermistors. An inner jacket, containing another glue heater to provide adiabatic conditions, and a thermostatically controlled outer jacket, which provided a stable environment, were also included. The whole assembly was placed in a massive carbon shield which was also thermally stabilised by a water jacket. The system was used to calibrate a carbon-walled air ionization chamber and yielded an excellent value of $\overline{W}$ (see Table 2.1). In a separate paper (Engelke and Hohlfeld, 1971b) a careful examination of the temperature gradients created during electrical heating was performed. This examination indicated that a correction of 0.2% should be included in the calculations. One of the most recent publications by a national laboratory appears to be that of a Japanese group (Sakata, 1972) who have described a twin calorimeter again operated in a quasi-adiabatic mode. This calorimeter was designed for electron irradiation and has yielded a number of mass stopping power ratios for carbon to air at energies between 15 and 25 MeV.

Before concluding this chapter it is perhaps worthwhile to note the enormous simplification that can be achieved with absorbed dose calorimeters when very high dose rates are employed. Bewley (1969)

TABLE 2.1

AUTHOR	$\overline{W}$	$s \frac{\text{CARBON}}{\text{AIR}}$
Reid and Johns (1961)	33.98 ± 0.3	1.005
Bewley (1963)	33.97 ± 0.21	1.004
Petree and Lamperti (1967)	33.59 ± 0.14	1.004
Engelke and Hohlfeld (1971)	33.72 ± 0.17	1.014

TABLE 2.2

AUTHOR	G	M of H_2SO_4
Hochanadel and Ghormley (1953)	15.6 ± 0.3	0.4
Keene and Law (1963)	15.42 ± 0.04	0.4
Fregene (1967)	15.5 ± 0.2	0.1
Pettersson (1967)	15.57 ± 0.14	0.4

and Goodwin (1969) have both described extremely simple calorimeters which consisted of little more than a carbon block, containing a thermistor and calibration heater, embedded in an insulating material. Dose rates of the order of 10^5 rads/min were used resulting in a temperature rise of 1 K/min. Unfortunately, for safety reasons dose rates of this magnitude are unacceptable in clinical practice and, since it is required to calibrate the secondary dosimeter under the particular conditions of operation, it is still necessary to retain the absorbed dose micro-calorimeter.

A summary of some of the results obtained with carbon calorimeters irradiated by ^{60}Co beams is presented in Table 2.1. Since the usual endpoint of a calorimetric calibration is an evaluation of $\overline{W}$ (the mean energy expended in the formation of one ion pair in air) these values have been tabulated as indicative of the precision of the calorimetric method. A small allowance should be deducted from these uncertainties since they include ionometric uncertainties, but these are usually considerably less than the calorimetric uncertainties. The invariable result of a calibration is the product $\overline{W}.s_{CARBON/AIR}$ and the estimates of the mass stopping power ratio used to evaluate $\overline{W}$ have been quoted in column 3. No attempt was made to assign an uncertainty to $s_{C/AIR}$ thus the uncertainties in column 2 represent experimental values only. Some representative calorimetric determinations of the ferrous sulphate G value (yield of Fe^{3+} ions/100 eV) have been tabulated in Table 2.2, again at ^{60}Co γ-ray energies. As mentioned earlier most of these results do not stem from absorbed dose calorimeters. In addition, the uncertainties quoted in column 3 may include a significant contribution from the ferrous sulphate measurements and cannot,

therefore, be regarded as indicative of the precision of the calorimeter. Results of electron irradiation experiments have not been included here since they are discussed elsewhere in this thesis.

CHAPTER 3.

DESIGN AND CONSTRUCTION OF THE CALORIMETER

3.1 INTRODUCTION

Chapter 2 discussed the principal requirements of an absorbed dose calorimeter and the techniques available for the observation of the minute quantities of heat deposited by the passage of a radiation beam. It was concluded that a calorimeter, composed of either carbon or aluminium and operated in the quasi-adiabatic mode, should be constructed for the purposes of the present investigation. This chapter presents an account of the design and construction of such a calorimeter.

Initially, considerable effort was devoted to the realisation of two theoretical requirements, namely, localisation of the point of measurement and a homogeneous absorbing medium. It will be shown that the practical difficulties created by this approach were so overwhelming that the original design had to be abandoned. Subsequently, a second design was proposed which relaxed the severity of the initial requirements to achieve a simpler construction. To complete the description of the calorimeter a brief summary of the electrical calibration circuit has also been included.

The chapter concludes with a short discussion of the vacuum system illustrating some of the pitfalls in the art of vacuum engineering.

3.2 THE FIRST CALORIMETER

Graphite has a density, ρ, equal to 1.7 g/cm^3 which is considerably lower than the density of aluminium, ρ = 2.7 g/cm^3, and is, therefore, a closer approximation to the density of water or soft tissue. Since graphite may also be readily obtained in a very

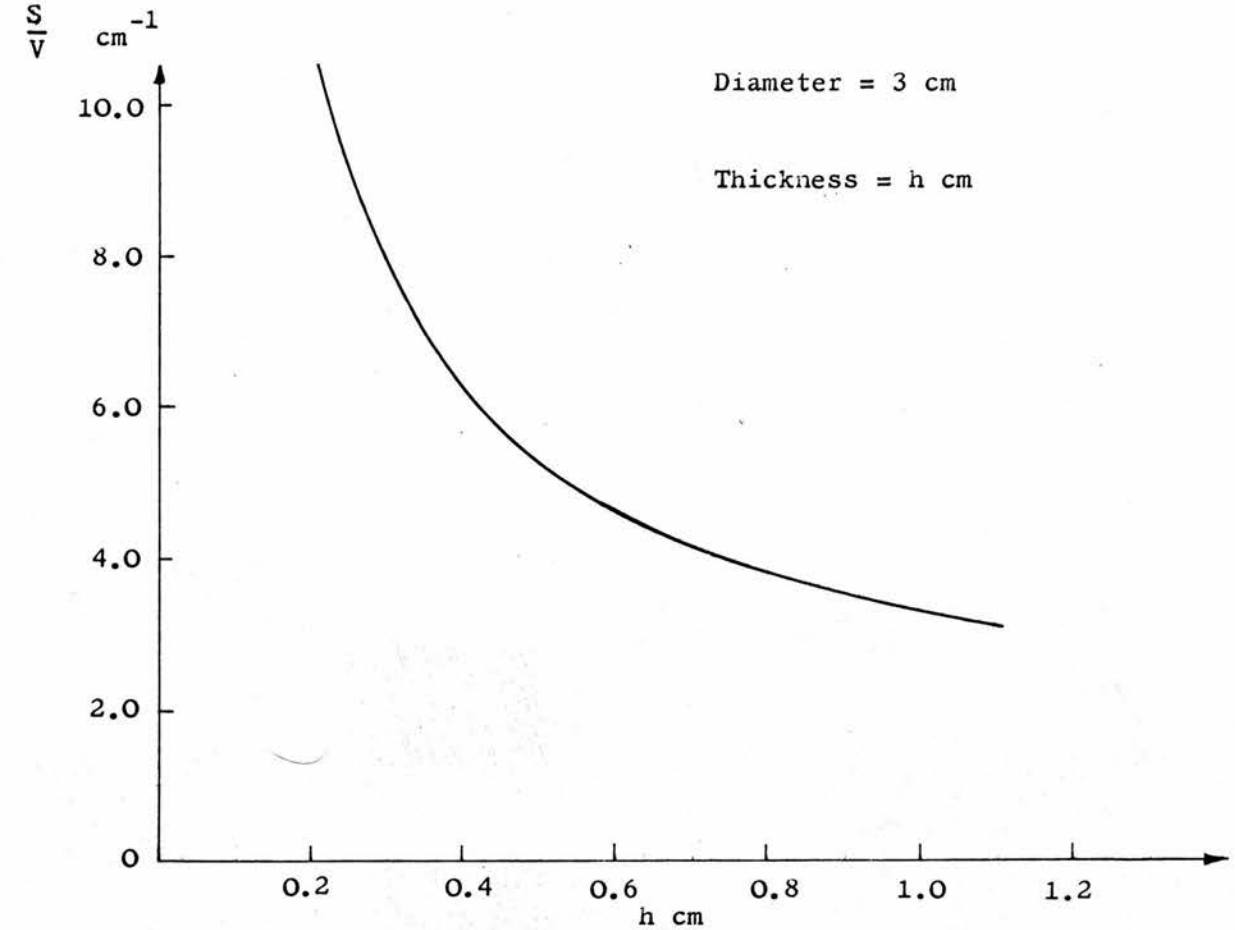

FIGURE 3.1. SURFACE TO VOLUME RATIO FOR DISC

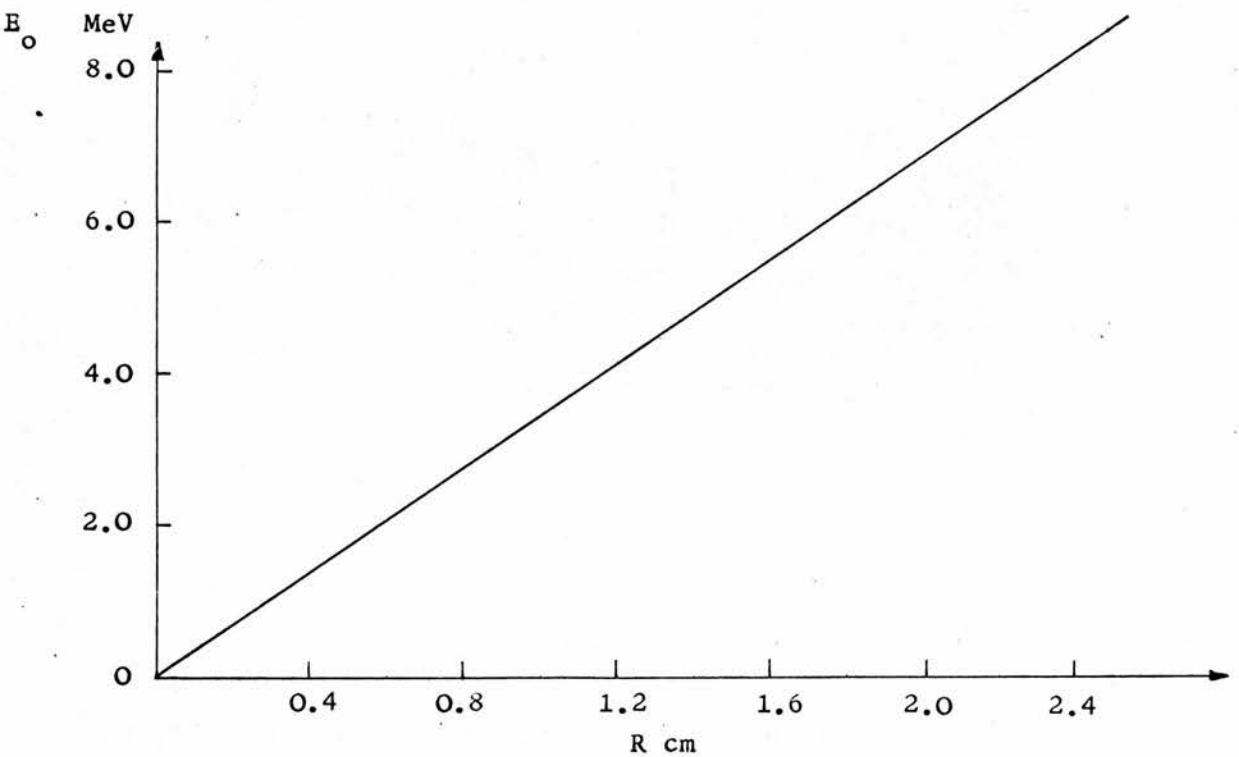

FIGURE 3.2 ENERGY-RANGE RELATIONSHIP FOR ELECTRONS

pure state (> 99.9% graphite) it was chosen as the calorimetric material. The discussion of section 2.1.1 concluded that, for a uniform radiation beam, the optimum design of the absorber was that of a disc, with its plane faces orientated perpendicular to the direction of the incident beam. This geometry was adopted in the first calorimeter.

The extent of the radial dimension of the disc is basically determined by the beam uniformity which is a specific characteristic of each linear accelerator. Nevertheless, most machines should be capable of yielding a reproducible beam profile in the immediate vicinity of the central axis. It was considered that a radius of 1.5 cm was the minimum absorber radius compatible with engineering and constructional requirements. A disc absorber of this size should not extend into the region of beam inhomogenities and the design was therefore based on a disc of 3 cm diameter.

The choice of the absorber thickness is less arbitrary, being dependent upon the range of electrons in the absorber and the heat loss characteristics of the absorber geometry. Ideally, the absorber should be as thin as possible to localise the point of measurement, but, as Figure 3.1 indicates, the surface to volume ratio, and therefore the heat leakage modulus, is very poor for a thin disc.

For a fixed radial dimension of the disc the surface to volume ratio falls with increasing thickness, indicating that this dimension should be maximised. An upper limit to the absorber thickness may be conveniently set by consideration of Figure 3.2, which shows the range-energy relationship for electrons in a material of density 1.7 g/cm^3. This graph is actually based on an empirical relationship

derived from the effective range of electrons in aluminium (Katz and Penfold, 1952), but it will suffice for the purposes of the present discussion. The present calorimeter is intended to measure the locally deposited absorbed dose rather than the total energy of the radiation beam. Therefore, the electron flux must not only be able to reach the sensitive absorbing element but must also be capable of traversing this element. Inspection of Figure 3.2 shows that a 4 MeV electron beam will just be able to penetrate a 0.4 cm thick absorber covered by a further 0.8 cm of graphite. Returning to Figure 3.1, it can be seen that a considerably greater thickness than 0.4 cm would be needed to substantially reduce the surface to volume ratio, whereas reducing the thickness below this value would dramatically increase the surface to volume ratio.

In addition, a thickness of 0.4 cm would be the minimum value compatible with the design of the absorber described later in this chapter. Therefore, a thickness of 0.4 cm was chosen as the best compromise in the conflicting circumstances and the overlying thickness was restricted to 0.8 cm, making 4 MeV the minimum possible incident electron energy.

To produce a negligible disturbance of the radiation spectrum within the calorimeter, the physical separation between the absorber and its surrounding jacket should be reduced to a minimum. The use of a multi-jacket temperature stabilising system and a quasi-adiabatic mode of operation both require a minimum heat leakage modulus for efficient performance. With the exception of radiative heat transfer, the heat flow between two bodies rapidly decreases with their increasing separation, thus a minimal heat leakage modulus is incompatible with a negligible absorber-jacket separation, α ,

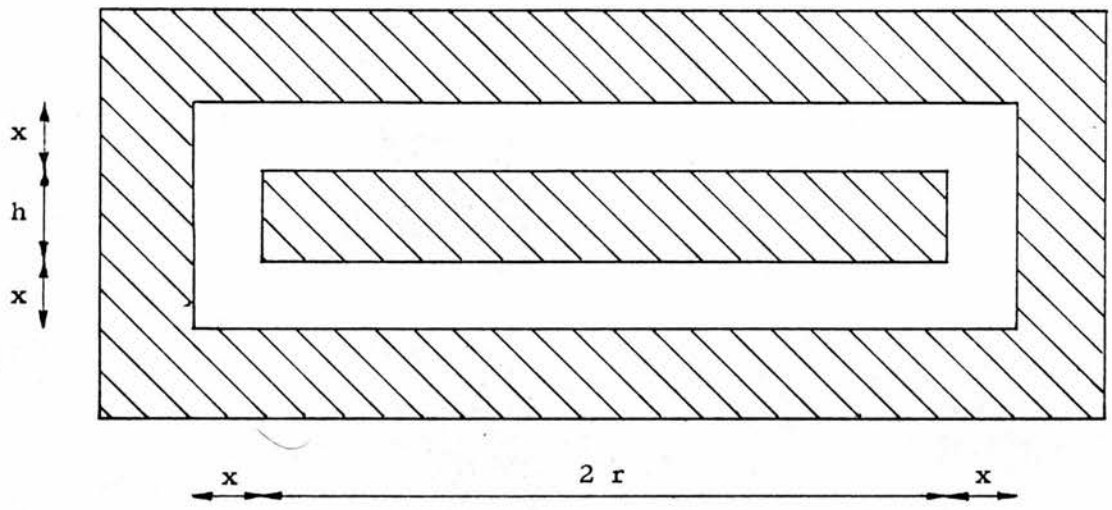

FIGURE 3.3 DEFINITION OF x

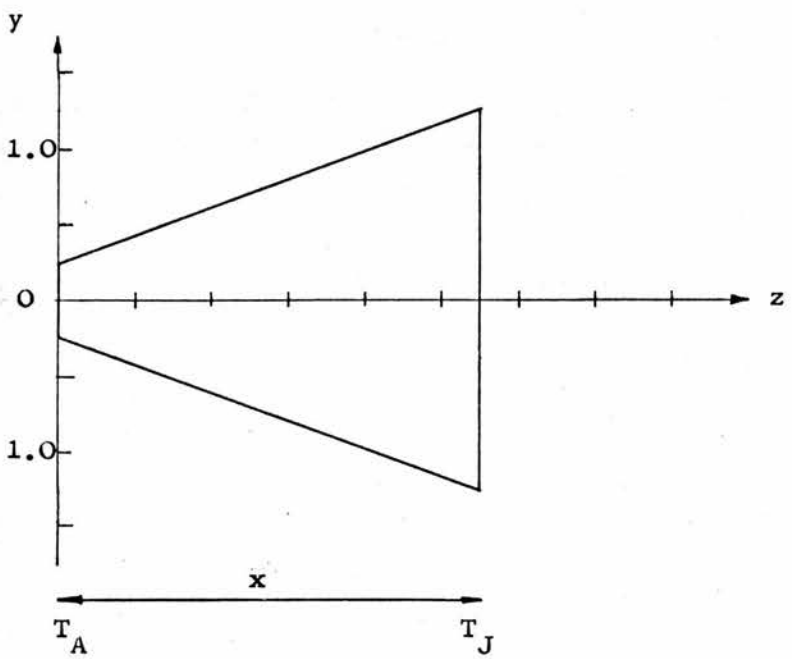

FIGURE 3.4 ABSORBER SUPPORTS

(defined by Figure 3.3). To ascertain if an optimum value of this separation exists it will be necessary to study each mode of heat transfer; convection, conduction and radiation as a function of $\propto$.

3.2.1 Convection

Bosworth (1952) has reported that convection currents cease if the value of the Rayleigh number, R, is less than 1620. For the case of a parallel plate geometry this constant may be given by equation 3.1:

$$R = \alpha d^3 (T_A - T_J) \qquad 3.1$$

where d is the plate separation between two isothermal surfaces with temperatures T_A and T_J and 'α' is the gas convection modulus, which is proportional to the square of the gas pressure. For air at normal atmospheric pressure and 300 K 'α' has a value of approximately 100 $K^{-1}cm^{-3}$. Substituting this value into equation 3.1 shows that a difference of 0.162 K would be necessary to initiate convection between two surfaces 0.1 cm apart. For reasons which will be explained in the next section, the gas pressure inside the calorimeter will be many orders of magnitude below atmospheric pressure. Therefore the temperature required to initiate convection will be very much greater than 0.162 K. Since the temperature stability of the calorimeter will be many orders of magnitude below such values, convection may be neglected as a mode of heat transfer within the system.

3.2.2 Conduction

Heat may be conducted to, or from, the absorber via three possible pathways, namely, (a) the gas (air) trapped in the cavity between the absorber and jacket, (b) the electrical connections between the absorber and the external instrumentation, which must inevitable pass

through the jacket, and (c) the pins used to support the absorber in the jacket cavity.

(a) Air Conduction

The thermal conductivity of air at s.t.p. is 2.44×10^{-4} W/cm.K. This value remains fairly constant as the pressure is decreased until the mean free path (m.f.p.) of the gas molecules exceeds the separation between the conducting surfaces. Under these conditions the heat transfer is no longer a function of the absorber-jacket separation but depends solely on the pressure, P. The heat transfer may then be approximated by the expression

$$\left(\frac{dQ}{dt}\right)_{c,AIR} = s_A \left[\frac{b(\gamma + 1)}{2(2 - b)} \frac{C_V P}{(2\pi RT)^{\frac{1}{2}}}\right] (T_A - T_J) \qquad 3.2$$

Kennard (1938), where s_A is the absorber surface area in cm^2 ($= 2\pi r(r + h)$), C_V is the specific heat of air at constant volume ($= 7.88 \times 10^{-1}$ J/g.K), γ is the ratio of specific heats for air at 300 K (= 1.4), P is the pressure in N/cm^2, R is the gas constant for 1 g of air ($= 2.89 \times 10^{-1}$ J/g.K) and b is a factor indicating the energy loss per collision between the gas molecule and the wall, referred to as the accommodation coefficient, (b = 3/4 for air). (N.B. all values from Kaye and Laby, 1966, except b, Laughlin and Genna, 1966). Substitution of these values in equation 3.2 yields

$$\left(\frac{dQ}{dt}\right)_{c,AIR} = 9.2 \times 10^{-3} \cdot s_A \cdot P \cdot (T_A - T_J)$$

where P is now in torr (= 1 mm Hg). For air at 10^{-3} torr the m.f.p. is 4.5 cm, which is considerably in excess of the likely separation between the various components of the calorimeter. Thus, for a value of $s_A = 17.91\ cm^2$ the heat transfer due to the air, at a pressure of 10^{-3} torr and a temperature difference $T_A - T_J = 1$ K, is 16.5 μW. Strictly, equations 3.1 and 3.2 apply only to parallel

geometries but, since the majority (79%) of the absorber surface, s_A, approximates to this condition and the correction factors for the cylindrical surfaces are very small, their use is permissible.

(b) Wire Conduction

The general heat conduction equation

$$\frac{dQ}{dt} = -\chi . dA . \frac{dT}{dx} \qquad 3.3$$

may be used to evaluate the heat flow along the electrical wires running between the absorber and the jacket. The value of the heat transfer via this pathway has been recorded in Table 3.1 under the heating $(\frac{dQ}{dt})_{c, WIRE}$. The calculations were based on values of χ = 0.152 W/cm.K and r = 5 x 10^{-4} cm for the two "Evanohm" heater wires, and χ = 0.73 W/cm.K and r = 1.25 x 10^{-3} for the four platinum thermistor wires.

(c) Insulator Conduction

The conical pins supporting the absorber were manufactured from P.T.F.E. and, ideally, they should not conduct any heat owing to their point of contact with the absorber. Unfortunately though, since graphite is a soft material, the pins inevitable embed themselves into the absorber resulting in a finite area of contact. The evaluation of heat conduction via these supports can be made by reference to Figure 3.4, which indicates the possible cross-section of one of the supports. Assuming thatall the heat flow is parallel to the z axis, and that therefore all planes parallel to the y axis are isothermal, the heat flow may be determined by the heat flow equation

$$(\frac{dQ}{dt})_{c,INS} = \chi . dA . \frac{dT}{dz}$$

where $dA = \pi y^2 = \pi(0.25 + 1.25 \frac{z}{x})^2 \times 10^{-2}$. (N.B. for the purposes of this equation x may be regarded as a constant.) Setting χ = 2.51 x 10^{-3} W/cm.K for P.T.F.E. this equation becomes

TABLE 3.1

x	$\left(\frac{dQ}{dt}\right)_C$ μW			$\left(\frac{dQ}{dt}\right)_R$ μW		TOTAL μW
m.m	AIR	WIRE	INSUL.	CARBON	ALUMINIUM	ALUMINIUM
0.5	16.5	291	4140	7687	1886	6334
1.0	16.5	146	2070	7781	1957	4190
1.5	16.5	97	1380	7861	2029	3523
2.0	16.5	73	1035	7922	2091	3216
2.5	16.5	58	828	7984	2152	3055
3.0	16.5	49	690	8046	2203	2959
4.0	16.5	36	518	8128	2296	2867
5.0	16.5	29	414	8210	2318	2838
∞	-	-	-	8722	3074	3074

$$\left(\frac{dQ}{dt}\right)_{c,INS} = 2.51 \times 10^{-5} \pi (0.25 + 1.25 \frac{z}{\alpha})^2 \frac{dT}{dz}$$

In the steady state $\frac{dQ}{dt}$ will be constant, thus, if $dT = T_A - T_J = 1K$, one obtains

$$\left(\frac{dQ}{dt}\right)_{c,INS} \times \frac{1}{\pi . 2.51 \times 10^{-5}} \int_0^{\alpha} \frac{dz}{(0.25 + 1.25 . z . \alpha^{-1})^2} = - \int_{T_A}^{T_J} dT$$

which yields on integration and subsequent reduction

$$\left(\frac{dQ}{dt}\right)_{c,INS} = \frac{2.96 \times 10^{-3}}{\alpha} \quad \mu W$$

where α is in cm. The numerical value of this function for a total of seven pins and a few values of α has been tabulated in column 4 of Table 3.1.

3.2.3 Radiation

Radiative heat transfer between the absorber and jacket is proportional to the fourth power of their absolute temperatures and may be expressed by equation 3.5:

$$\left(\frac{dQ}{dt}\right)_{RAD} = s_A \sigma F (T_A^4 - T_J^4) \qquad 3.5$$

where σ is Stefan's constant ($= 5.67 \times 10^{-2}$ W/cm^{2}K^4) and F is a factor to account for the emission and multiple scattering of the heat quanta from the absorber and jacket surfaces. The precise evaluation of F involves a double integration over both radiating surfaces, but, for the present purpose, an approximation given by McAdam (1942) for one body totally enclosed by another, will suffice:

$$F = (\varepsilon_A^{-1} + (s_A/s_J) [\varepsilon_J^{-1} - 1])^{-1} \qquad 3.6$$

where ε_A and ε_J refer to the emissivities of the absorber and jacket surfaces respectively. The value of the radiative heat transfer has been recorded in column 5 of Table 3.1 assuming a value of 0.85 for the emissivity of carbon, $T_A =$ 294 K and $T_J =$ 293 K.

Inspection of columns 2 to five of Table 3.1 shows that, unless the separation α is very small indeed, the predominant mode of heat transfer is by radiation. Consideration of equation 3.5 shows that this is mainly the result of a T^4 dependence. Therefore, the most obvious method of reducing the radiative heat transfer is to substantially lower the operating temperature. Although there have been some reports of calorimeters operated at liquid nitrogen temperatures (Schleiger and Goldstein, 1964; Goldstein, 1968) the extra constructional complexity resulting from such measures is a severe handicap. In addition, there is also the possibility of an increase in the heat defect, since the annealing of radiation induced damage to the crystal lattice is very much slower at very low temperatures (Billington and Crawford, 1961). In the case of graphite, which is almost a perfect black body absorber/radiator, a simpler and more practical approach is to reduce the spectral emissivity of the surface. Referring again to equation 3.6 a little consideration will show that a substantial reduction in the value of F can be achieved by treating only one surface with a low emissivity material. Thus, by coating the inner jacket surface only, it should be possible to reduce the heat transfer without increasing the foreign material content of the absorber.

Examination of a table of spectral emissivities shows that gold or silver would provide ideal coating materials, but their high atomic number and density preclude their use in this situation. Instead, aluminium offers a suitable alternative and a number of attempts were made to vacuum deposit a film of aluminium onto the graphite surface. Unfortunately, the powdery nature of this surface resulted in a very poor adhesion of the aluminium film, and it became obvious that to

achieve an effective result both surfaces would have to be coated with a fairly thick film. Eventually, after considerable polishing of the graphite surface prior to deposition, an acceptable covering was obtained with a 1 μm layer of aluminium. This thickness represented an increase in the mass of the absorber of less than 0.1%.

It is perhaps pertinent here to note a beneficial side effect of this process. Since the thermal conductivity of aluminium is almost five times greater than that of graphite, the deposition of a surface layer effectively forms an isothermal surface at the boundary of the absorber. This fact is of particular importance when positioning the temperature transducer so as to avoid errors due to temperature gradient effects. This isothermal boundary also removes some of the uncertainty in the correction for the heat lost due to non-adiabatic conditions. This latter consideration was one of the main reasons why an aluminium foil was not glued to the graphite surface, since, in this case, the glue layer would form a thermal barrier between the carbon and the aluminium, whereas an intimate thermal contact is formed between the two materials by vapour deposition of the aluminium. The other reason was that all adhesives are very inefficient in bonding graphite to other materials.

Initially, it had been hoped to utilise the very low spectral emissivity of pure aluminium but the rapid oxidation of the surface prevented this possibility. Values of the radiative transfer for an oxidised aluminium surface are therefore shown in column 6 of Table 3.1, which again demonstrates that, except for very small absorber-jacket separations, radiation is still the dominant mode of heat transfer. It is worthwhile to note that the figures in column 4, for the conductive heat transfer via the insulator, are only very

approximate and probably represent an upper limit.

Perhaps the most interesting result to emerge from Table 3.1 is that it demonstrates that, because radiative transfer increases at larger absorber-jacket separations, a value of α must exist for which the heat transfer is a minimum. However, as the table shows, such a value of the absorber-jacket separation will be well beyond the range considered as acceptable on homogeneity grounds and little effect would be gained by increasing the absorber separation beyond 1 mm. This value was eventually chosen as a reasonable compromise.

3.3 CALIBRATION HEATER

Considerable emphasis has already been attached to the possibility of errors arising from the temperature gradients created during electrical calibration. The various approaches and difficulties involved in the practical solution of this problem will now be discussed.

The bulk electrical resistivity of pure graphite is rather low, and any attempt to utilise its inherent electrical resistance for the purposes of calibration heating would require the manipulation of massive currents. This is obviously not a feasible proposition and recourse is normally made to the discreet heating element. Reference has already been made to several calorimeters constructed with glue heaters, but the technical difficulties involved in producing a uniform resistance element (Petree and Ward, 1962) and low resistance contacts to the absorber do not recommend this method.

The most commonly encountered solution to this problem is to employ a resistance wire spread as evenly as possible throughout the absorber. Inevitably, the length of wire which can be incorporated into the absorber volume is limited. This causes particular

difficulties in the accurate measurements of low power dissipations in the absorber, since, if W_A $(= \frac{V^2}{R_A})$ and R_A, the absorber resistance, are both small, V, the applied voltage,will be very small. The precise measurement of the power, W_A, is then dependent on the accurate determination of very small d.c. voltages. A further problem which is discussed more fully in section 3.4.2 is the fact that a significant "end effect" correction may be necessary for the resistance wire not actually forming part of the absorber heater. The first objection may be substantially reduced by the use of a fine wire, with a resultant high resistance per unit length, which has the additional benefit of introducing a minimum amount of foreign material into the absorber.

The introduction of the wire heater into the absorber was governed by two considerations. Firstly, the wire should be distributed as evenly as possible without crossing and recrossing its path. The necessity for the latter requirement was that the considerable localised heating produced at the intersection of two wires could cause the enamel coating of the wire to disintegrate. If a number of such insulation breakdown points occurred, there exists the distinct possibility that the highly conducting absorber substrate could provide a low resistance pathway between two of these points. In this situation the intervening portion of wire between the breakdown points would be short circuited leaving a "cold spot" in the absorber. Secondly, it was felt that the heater wire should be embedded below the surface of the absorber at all points. The reason for this requirement was that a surface heater could radiate a significant amount of its energy directly to the jacket, resulting in an incorrect assessment of the heat applied

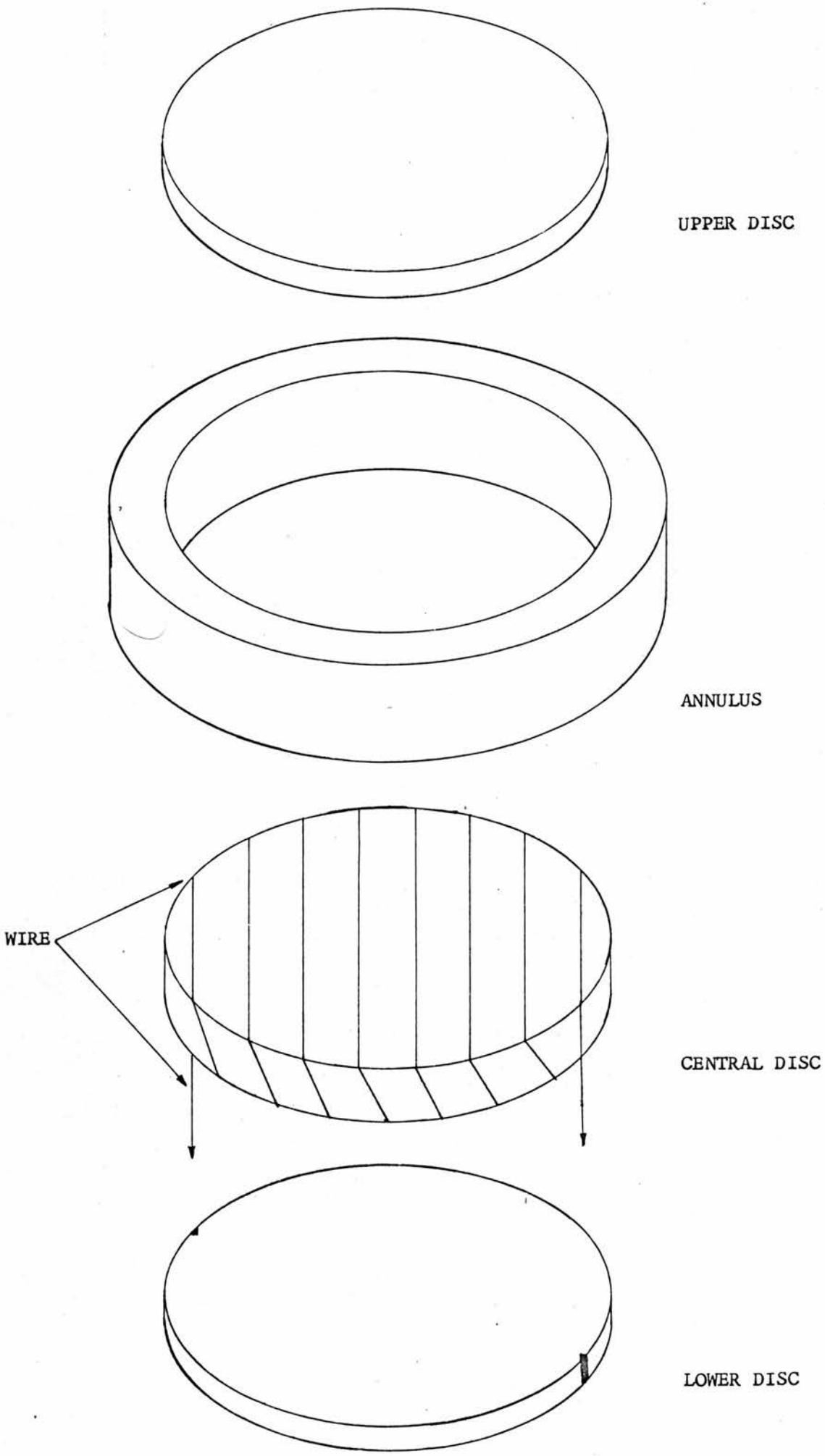

FIGURE 3.5 EXPLODED VIEW OF MK I ABSORBER

to the absorber. The solution employed, which conformed to these two requirements, is shown in Figure 3.5. The design basically consists of three discs with a surrounding annulus, the central disc being twice as thick, 2 mm, as the outer discs, 1 mm. In order to produce a uniform heat dissipation it was proposed that the wire should traverse each face of the central disc by a series of parallel chords, each chord being connected to the succeeding traverse, on the opposite face, by a locating groove cut in the radial surface of the disc. The annulus could then be placed in position around the central disc without damaging the wire's insulation. The upper and lower discs could then be pressed into place, the whole system having been engineered on a push fit principle. With this arrangement, if each traverse was 2 mm apart, every point within the absorber would be less than 1 mm from the heating element.

A schematic section of the absorber and jacket is shown in Figure 3.6, which indicates the composite nature of both the jacket and absorber. The position of some of the seven pins supporting the absorber are also illustrated by the dotted region

3.4 CONSTRUCTION AND FAILURE OF THE MARK I CALORIMETER

The first major setback encountered in the construction of the calorimeter was due to the design of the absorber heating element. The comments of the preceding section indicated that this heater should be fabricated from a very fine resistance wire and a spool of "Evanohm" wire, with a diameter of 10 μm and an insulation coating of 5 μm, was purchased for this purpose. The extreme fragility of this wire, and its almost negligible tensile strength

meant that a considerable number of attempts were required before a single, uninterrupted, coil could be wound upon the absorber. A far more serious problem however, was that the measured resistance of the coil fell well below the expected value. This value had previously been calculated from a measurement of the resistance per unit length of the wire and the length used in the construction of the heater. It was suspected that the thin enamel coating of the wire had become detached, causing a series of "cold spots" as explained above. In an attempt to demonstrate the existence of these regions and identify the source of the trouble, a series of infra-red photographs was taken. Unfortunately, the maximum value of current that the wire could withstand required exposures of 24 or 48 hours to achieve a detectable image of the resultant low level of heat dissipation. The fogging that resulted from such lengthy exposures meant that little detailed information could be gained by this technique, which was therefore abandoned.

The most obvious points for a possible breakdown were at the edges of the disc, where the wire encountered a ninety degree change of direction. To remove this possibility a liberal coating of polyurethane varnish was applied to the edges of the absorber. Eventually, an acceptable value of the coil resistance was achieved, demonstrating that this was the probable cause of the breakdown. The construction of the absorber could then proceed to the next stage.

Two thermistors were embedded 0.5 mm deep in the surface of the absorber, one in the centre of the upper surface, the other at the lower edge of the annulus. These two thermistors were affixed to the absorber by a small portion of varnish, which also served as a thermal connection between the two components. Since the platinum

FIGURE 3.6 SECTION THROUGH MK I CALORIMETER (SCALE:- 4 TIMES FULL SIZE)

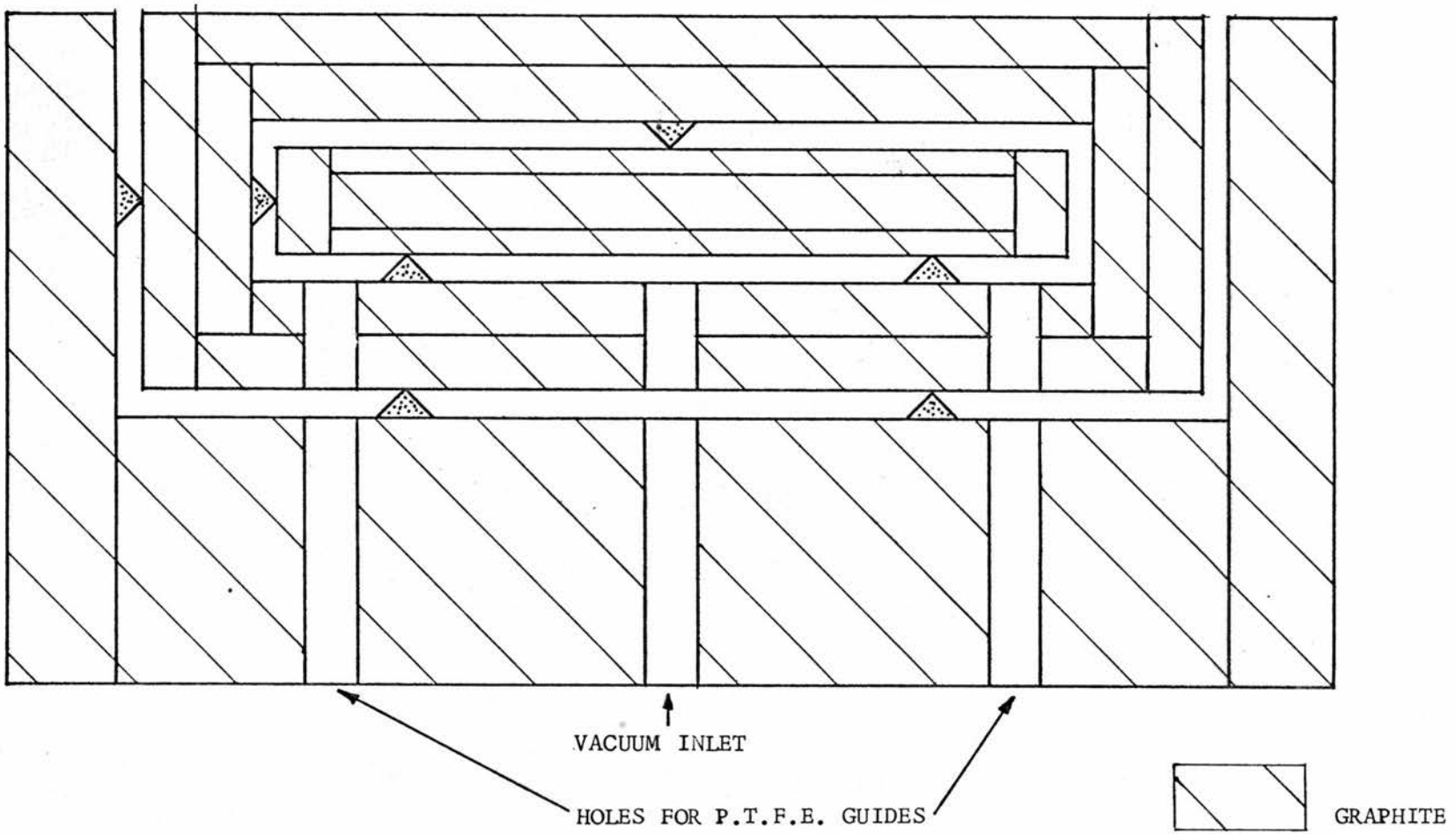

wires attached to the thermistor were not provided with an insulative coating, it was also necessary to varnish a section of the absorber surface and then affix the wires to this region. To facilitate the connection of the various wires to the external electrical circuitry two P.T.F.E. cylinders, each pierced by five fine holes, were to be used to guide the wires to a tag board placed below the calorimeter (Figure 3.6).

For similar reasons to those quoted above for the absorber heater, it was decided to bury the jacket heater in the centre of this component. Consideration of Figure 3.6 shows that, to accommodate this requirement, the jacket was formed from 2 annuli and 4 discs, again machined to form a push-fit construction. The result of this design meant that the absorber, complete with thermistors and heater, was the first component to be constructed and formed the corner-stone for the building of the rest of the calorimeter.

The first stage of the construction was duly completed and the second stage of construction, which required the winding of the heater wire on the surface of the inner jacket elements, was commenced. The considerable amount of handling necessary to perform this operation inevitably damaged the fine wires emerging from the P.T.F.E. cylinders. The nett result was that, each time an absorber wire fractured, the whole assembly had to be dismantled to replace the relevant component and reconstruction then had to start from the beginning again. It soon became apparent that the difficulties encountered in the construction were inherent in the design and a simpler approach, using an assembly of prefabricated units, was required. Two photographs of the Mark I calorimeter,

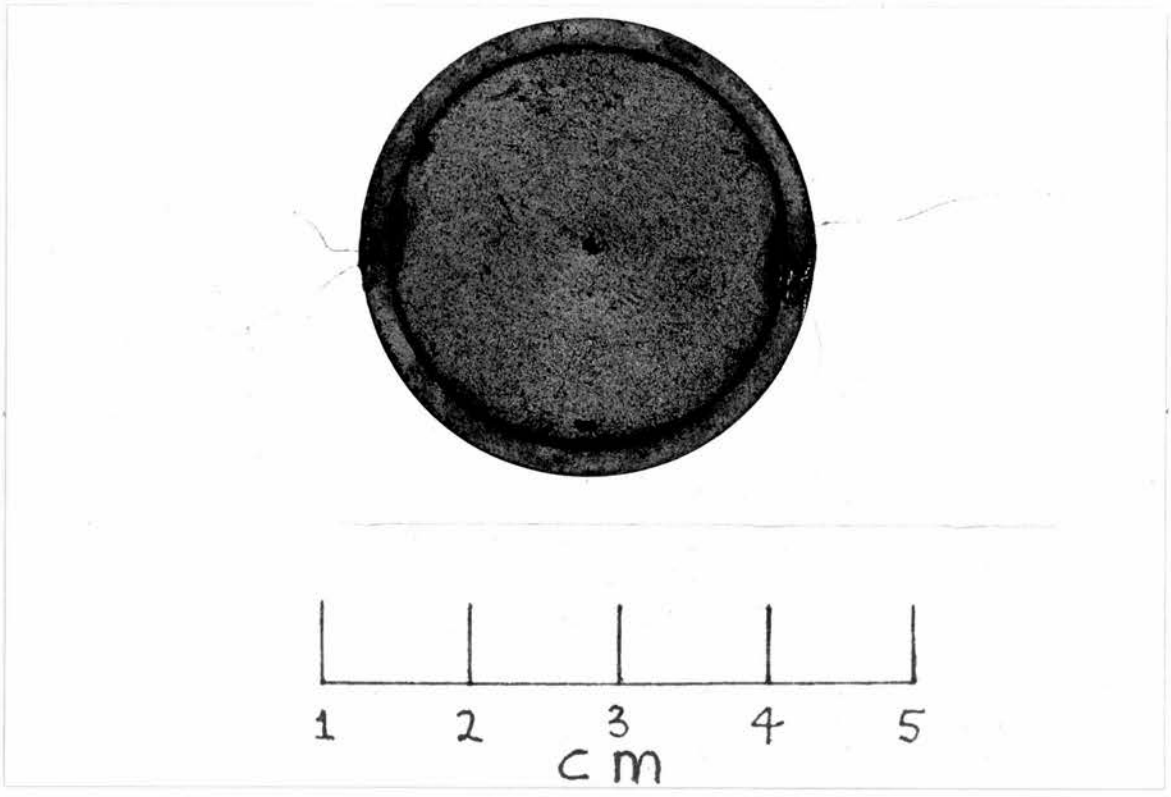

FIGURE 3.7a MK I ABSORBER

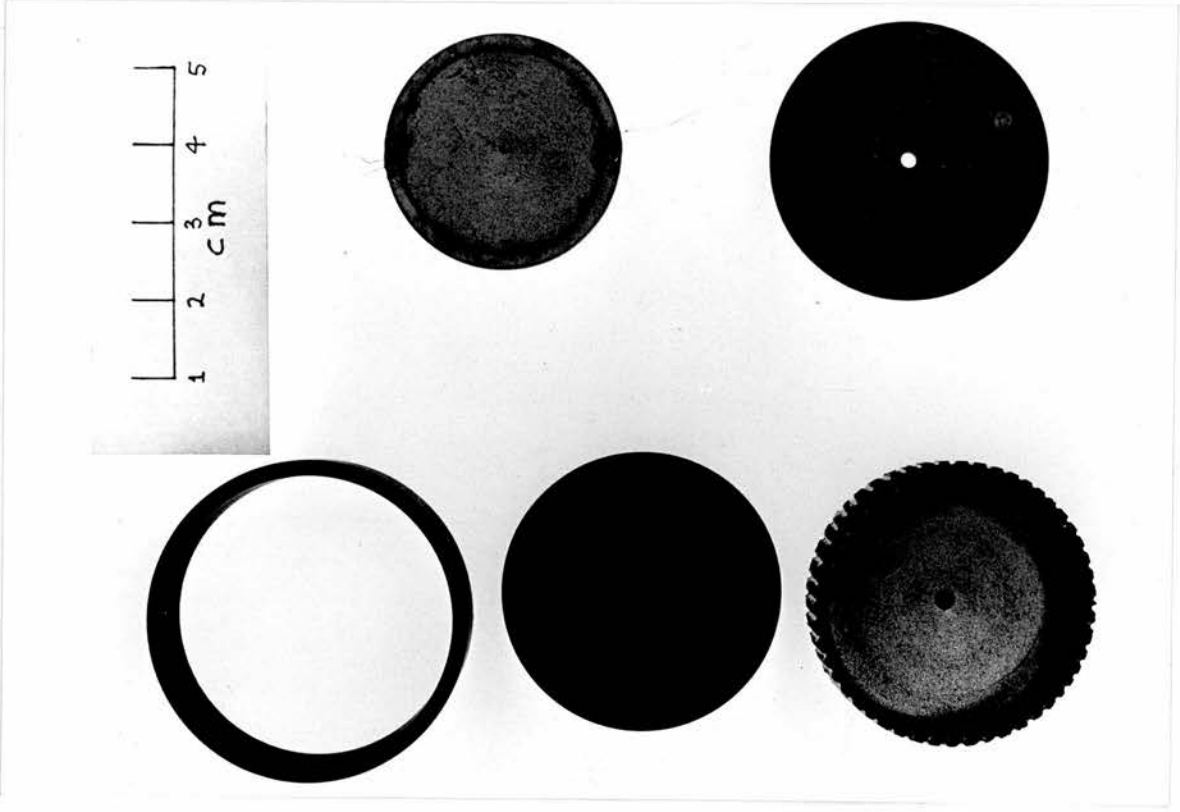

FIGURE 3.7b MK I ABSORBER AND JACKET COMPONENTS

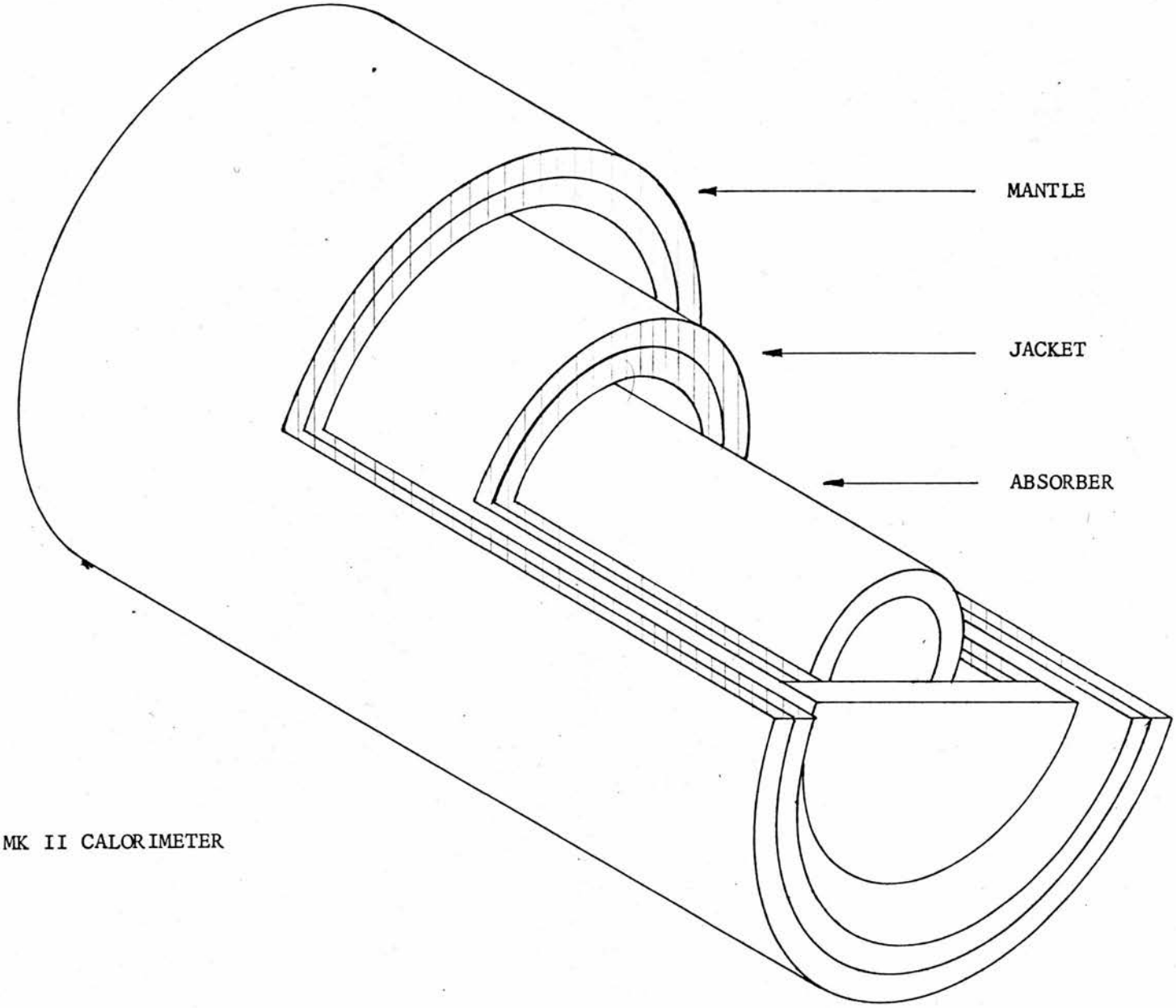

FIGURE 3.8

CUT-AWAY VIEW OF MK II CALORIMETER

at various stages in the construction, have been included in Figures 3.7a and 3.7b to indicate the physical scale of this problem.

3.5 THE SECOND CALORIMETER

3.5.1 Design

An analysis of the problems associated with the first calorimeter shows that, apart from the necessity for a prefabricated assembly, a particular difficulty was the breakdown of the heater wire's insulation. This breakdown was primarily caused by the sharp bends encountered by the wire as it traversed the disc. After careful consideration it was concluded that the simple fabrication of a uniform heating coil, based on a disc geometry, would be impossible without recourse to sharp changes in direction or a succession of crossed heating wires. In addition, if the jacket was to be prefabricated as a number of separate units, each containing its own heater, a dramatic increase in the number of fine wires requiring connection would result. As a consequence of these two factors it was decided to reject the coin shaped geometry in favour of a rod shaped geometry.

The design of the second calorimeter is illustrated by the diagram of Figure 3.8, which shows a general view of the three coaxial cylinders which form the absorber, jacket and mantle respectively. The choice of a cylindrical construction has two particular merits. In the first instance, a spiral groove, or thread, may be cut into the surface of the cylinder. This allows the positive location of the heater wire in a regular and dense pattern without creating any kinks or sharp discontinuities. In addition, if the groove is of a sufficient depth, the wire will not protrude above the surface of the cylinder and a covering sleeve

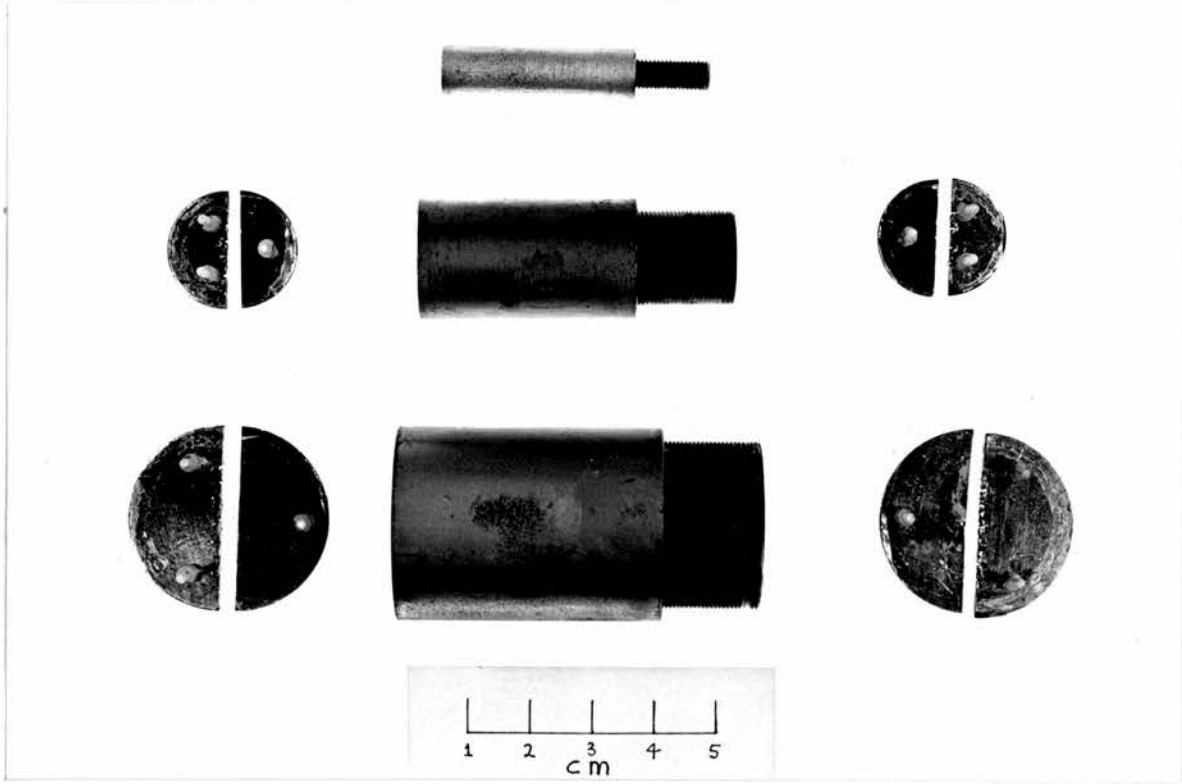

FIGURE 3.9 MK II CALORIMETER COMPONENTS

may be readily slipped over this cylinder without eroding the surface insulation of the wire. This construction is shown in Figure 3.9. The second advantage is that, by using three open ended cylinders, each element of the calorimeter, absorber, jacket and mantle, can be individually constructed and then the whole system can be assembled from these prefabricated units. A further difficulty encountered in the initial design was the necessity to thread the flimsy thermistor and heater wires through a number of very fine holes in a P.T.F.E. guide. This problem was also removed in the design of the second calorimeter and will be explained in the section describing the construction of the Mark II calorimeter.

3.5.2 Physical Data

Before proceeding with a description of the practical construction of the Mark II design, a similar analysis of the physical size and heat transfer characteristics to the one conducted for the Mark I calorimeter will be given. The length of the absorber cylinder was limited to 31 mm, partly by beam inhomogeneity considerations, but mainly because long thin cylinders have very poor surface to volume ratios. Unfortunately the rod shaped absorber geometry has a rather less well defined depth of measurement than a coin geometry. Also, to achieve mechanical strength and a low surface to volume ratio the diameter should be as large as possible. Obviously, a very large diameter would give an unacceptably high attenuation of the radiation beam, and a total diameter of 8 mm was chosen as the most satisfactory compromise. This total diameter comprised a 5 mm diameter inner element, which was considered to be the minimum diameter on which a thread could easily be cut, and a 1.5 mm thick covering sleeve, again the minimum thickness compatible with engineering

TABLE 3.2

MATERIAL	MASS	%
Carbon	2.4895	99.11
Aluminium	0.0023	0.09
Evanohm	0.0008	0.03
Thermistor	0.0019	0.08
Polyurethane	0.0173	0.69
TOTAL	2.5118 ± 0.0001 (SEOM)	100 %

problems. Although the extent of the absorber in the direction of the incident beam was greater than had been originally desired, due to the rod shaped design, this geometry is very similar to that of a commercial thimble ionization chamber. Since it was intended to calibrate such instruments with the calorimeter, it was felt that the uncertainty in the point of measurement was considerably reduced in this application.

A similar analysis of the heat transfer coefficient, as a function of the absorber-jacket separation, again showed that, for a graphite surface, the dominant mode of heat transfer was by radiation, except at exceedingly small separations. As a result, the graphite surface was again coated with a layer of vacuum deposited aluminium. The original separation between the various elements was again set at 1 mm, but, due to engineering difficulties with the special pins (described in the next section), the gap was later expanded to a 1.5 mm separation. A simple approximation for the heat flow through these pins showed that the total conductive transfer via this pathway was 1700 $\mu W.K^{-1}$. This figure should again be treated as an upper estimate, but it does indicate the possibility that, for low emissivity surfaces, conduction could become the dominant mode of heat transfer. Similar calculations to those in section 3.2 indicated that the other conduction losses are 81 $\mu W.K^{-1}$ for air at a pressure of 10^{-3} torr, 97 $\mu W.K^{-1}$ for the electrical connections and the radiative loss, for an oxidised aluminium surface, is 1043 $\mu W.K^{-1}$. This yields a total heat transfer coefficient of 2921 $\mu W.K^{-1}$.

The masses of the various components of the absorber are recorded in Table 3.2. This table shows that the only significant

foreign mass in the absorber was the polyurethane varnish (0.69%). This material is predominantly composed of carbon and nitrogen and does not contain any heavy elements. Thus, the radiation scattering and absorption properties of the varnish will not be significantly different from those of pure graphite. The heavy metal content, contributed by the heater wire and thermistors, amounted to 0.11%. At electron energies of a few MeV the mass stopping power for heavy elements is not markedly different from the equivalent values for carbon, and this level of impurity is therefore unlikely to result in a significant increase in the absorption, or scattering, of the radiation within the absorber.

3.5.3 Construction

The various components of the absorber, jacket and mantle were first machined to the appropriate sizes and fine threads were cut on the required surfaces. The exposed surfaces of the absorber and jacket were then coated with a 1 μm layer of vacuum deposited aluminium. The heating coils were wound onto their respective formers by rotating the threaded cylinder and wire spool in unison. This provided a much simpler method of coil fabrication and resulted in a much tauter coil being produced on the cylinder. In the case of the jacket and mantle a slightly thicker wire (49 s.w.g.), which was more easily manipulated, was used since the foreign material content was not critical in these two elements. (The inclusion of a heater in the mantle was a precautionary measure and was not material to the actual calibration of the absorber. The theory behind this inclusion was that if temperature stability inside the calorimeter proved to be a severe problem, then the mantle heater and thermistor, together with a feedback network, could act as a

FIGURE 3.10 TUBULAR SPACER

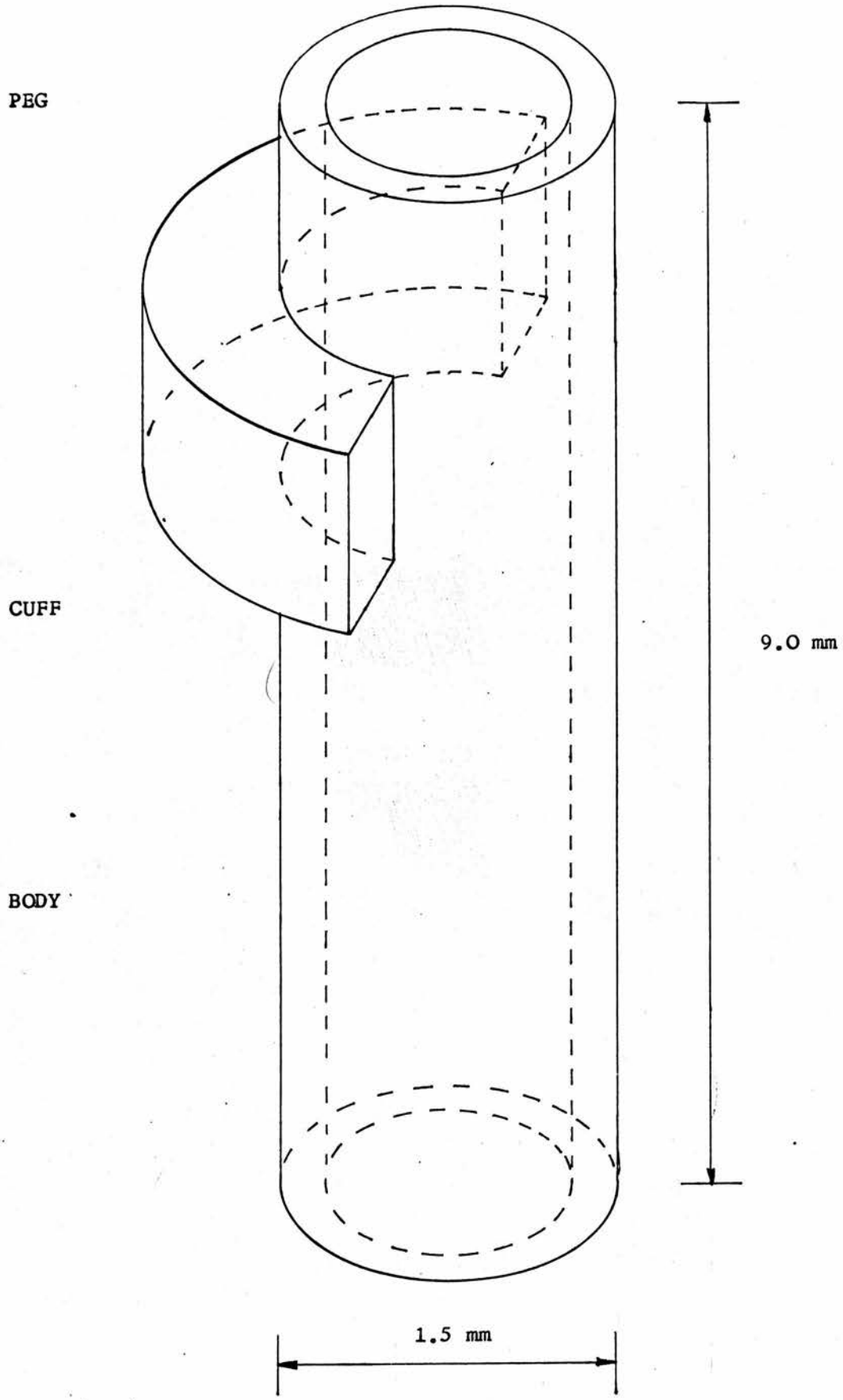

thermostatically controlled shield. Fortunately this added complication never proved necessary.)

Two thermistors were then affixed to the absorber, one being placed in a small cavity on the upper surface of the outer sleeve and the other on the plane end face of the cylinder. A coating of polyurethane varnish was again used to provide a thermal contact and to secure the thermistor and its uninsulated connecting wires. To check adiabatic conditions two further thermistors were added to the jacket and mantle respectively. The completion of these preliminary tasks left the various units ready for final assembly.

The suspension of the absorber within the hollow cylinder, which formed the major part of the jacket, was conveniently achieved by two sets of three tubular spacers placed symmetrically at each end of the absorber. The design of these spacers is shown in Figure 3.10. The construction was such that they performed the dual function of separating the absorber from the jacket with a minimum of thermal contact whilst the short peg, which protruded from each spacer, was used to locate the four "Dee" shaped end faces of the jacket (Figures 3.8, 3.11). A partial cuff was also included below the peg to separate these end faces from the absorber. All the spacers, constructed from P.T.P.E., had a central bore to reduce thermal conduction and provide a vacuum pathway to the absorber-jacket cavity. The two "Dees" which formed the lower halves of the jacket end faces were then located on their respective pegs. Each of these "Dees" contained a number of shallow varnished grooves along the central straight edge of the "Dee". The wires issuing from the various thermistors and heaters were then placed in these grooves and secured with a small portion of varnish. Particular care was taken not to

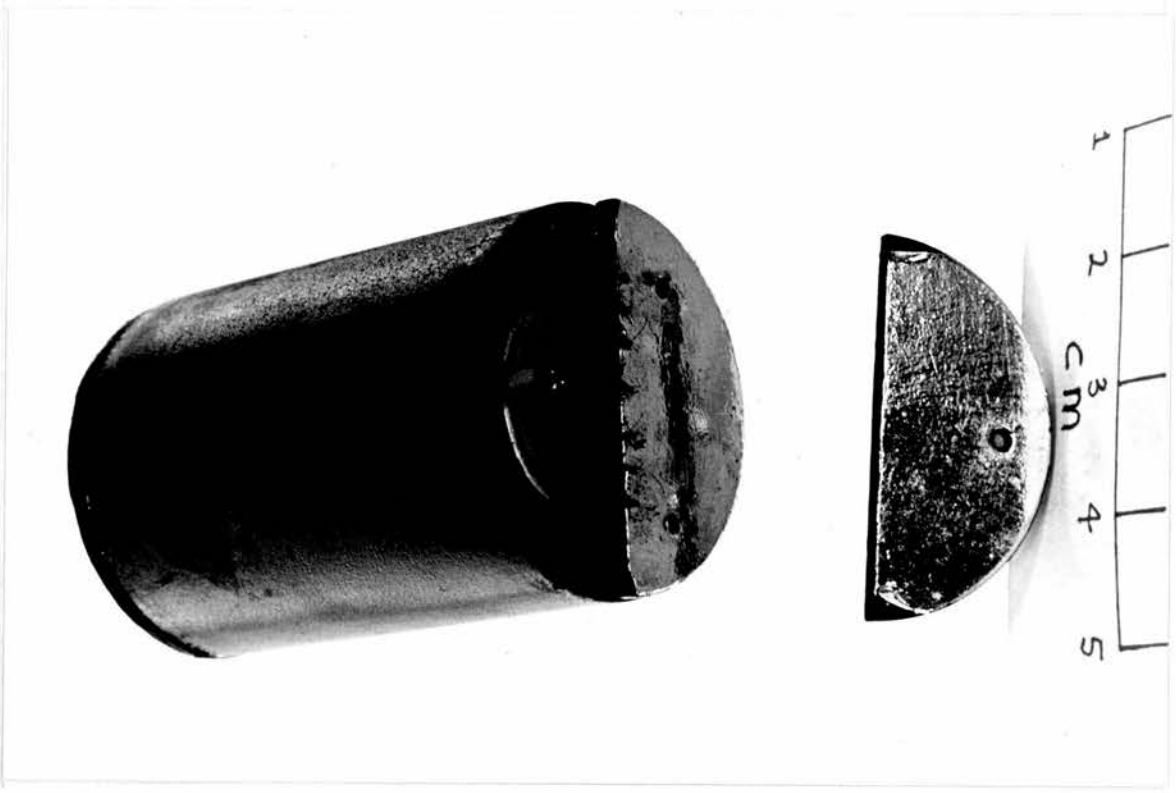

FIGURE 3.11 MANTLE ASSEMBLY WITH 1 DEE REMOVED

tension these wires, thereby allowing for a slight relative movement between the various components. In addition, the extra length of the slack wires reduced the heat transfer via this pathway. Once the varnish in the grooves had hardened the two remaining jacket "Dees" were pressed into place. This final step created an extremely robust unit which could withstand all but the most severe mechanical shocks.

Initially it had been intended to include a few loops of the jacket heater wire on the outside face of the "Dees". However, the area of these plane faces exposed to the absorber amounted to only 16% of the total internal surface area of the jacket, and it was felt that the extra technical difficulties involved in producing these loops did not justify their inclusion.

The incorporation of the jacket-absorber unit into the mantle cylinder followed an identical pattern to the assembly just described. The completed mantle, with 1"Dee"removed, is shown in Figure 3.11. This whole unit was then placed inside a circular cradle which presented a plane upper surface to the incident radiation. Six short hollow rods were used to separate the sensitive unit from the cradle using a similar principle to the one described above for the location of the absorber within the jacket.

3.5.4 Electrical Connection

Electrical connections to the fourteen wires emerging from the split circular ends of the mantle were facilitated by the use of two specially designed printed circuit boards. These boards were secured to the ends of the cradle by the six short rods which protruded from the mantle-cradle gap in a similar fashion to the location of the "Dee" end faces. The free ends of the wires issuing from the calorimeter

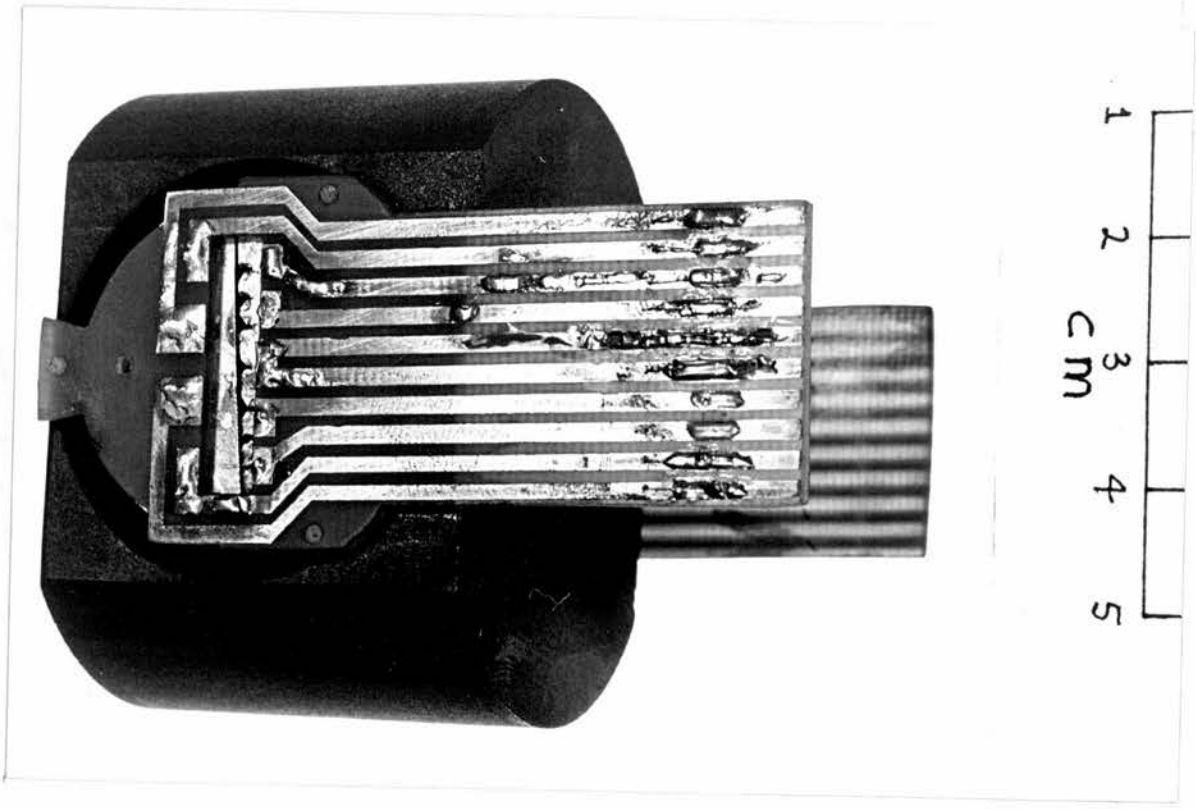

FIGURE 3.12 MANTLE/CRADLE ASSEMBLY WITH PRINTED CIRCUIT BOARDS ATTACHED

FIGURE 3.13 PRINTED CIRCUIT BOARD CONNECTIONS AND TAG BOARD

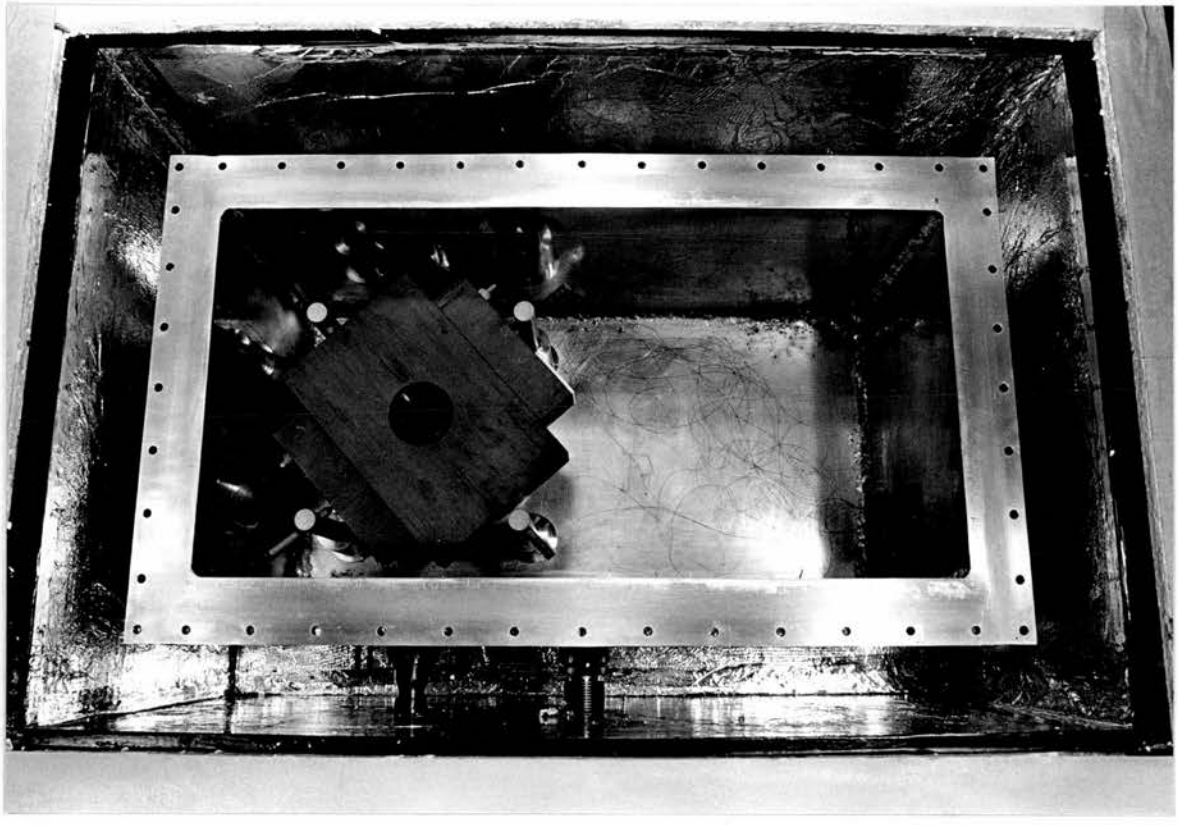

FIGURE 3.14a CALORIMETER POSITIONED INSIDE VACUUM TANK

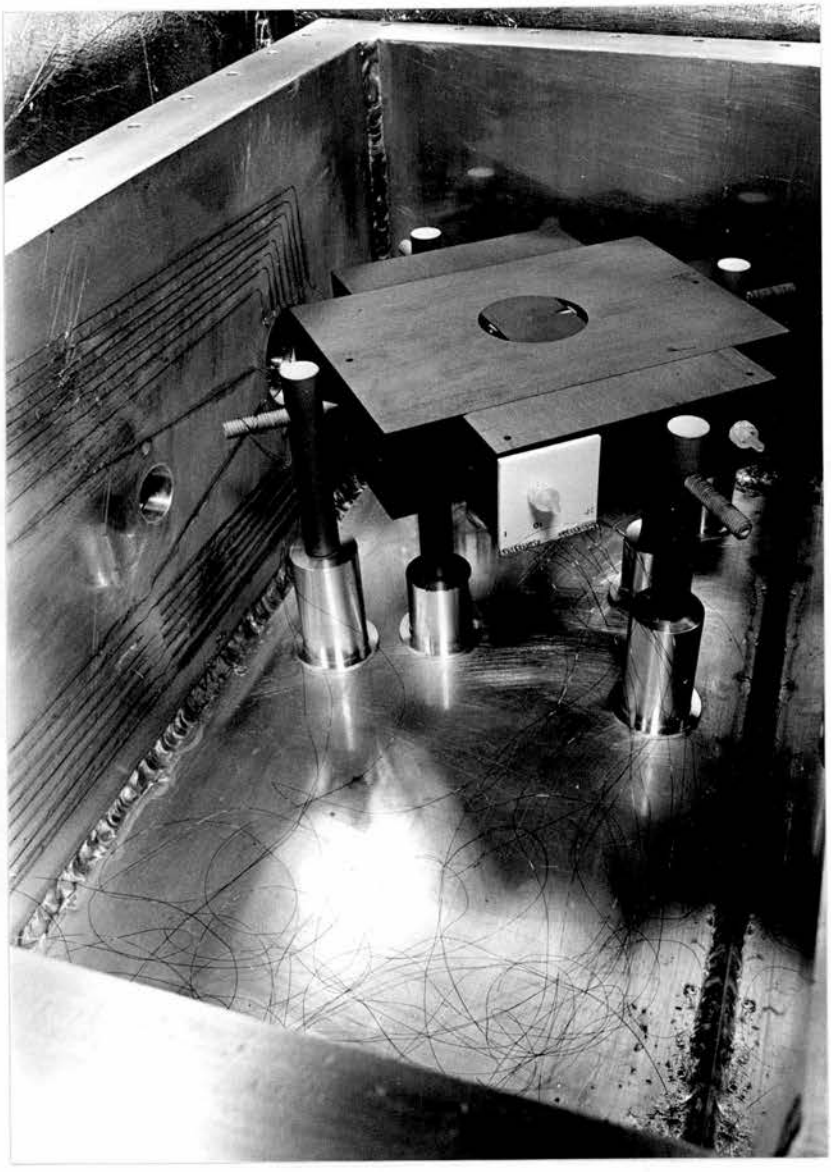

FIGURE 3.14b CALORIMETER POSITIONED INSIDE VACUUM TANK

were then soldered to an appropriate copper segment on the circuit board (Figure 3.12). Finally the whole assembly was mounted in a tightly fitting cavity in a large graphite block which formed the extended irradiated medium. Two slots had been cut in the lower surface of this cavity to allow the printed circuit boards to emerge from the underside of the block. These slots also served to locate the cradle in a fixed orientation within the block. Fine, insulated, copper wires (40 s.w.g.) were attached to the free ends of the copper strips on the printed circuit boards and the other ends of these wires were secured to a tag board on the side of the graphite block (Figure 3.13). The whole block was then rigidly located by seven P.T.F.E. supports inside the large aluminium tank which comprised the vacuum vessel (Figures 3.14 a and b).

Fourteen two metre lengths of 40 s.w.g. copper wire were then used to connect the tag board, on the edge of the calorimeter, to the heavy duty, vacuum sealed, multiway connector located in one of the vertical walls of the tank. To eliminate a direct thermal connection between the multiway connector, which was not thermally stabilised, and the heat sensitive central elements of the absorber, the initial 20 cm of each wire was araldited to the inner wall of the vacuum vessel. This provided a good thermal heat sink for the wire. The remaining 1.8 m of each wire was suspended in the bulk of the vessel, thus providing long thermal pathway between the heat sink and the calorimeter, further reducing any heat transfer to the sensitive elements.

3.6 ELECTRICAL CALIBRATION CIRCUIT

The fabrication of the calibration heater was described in

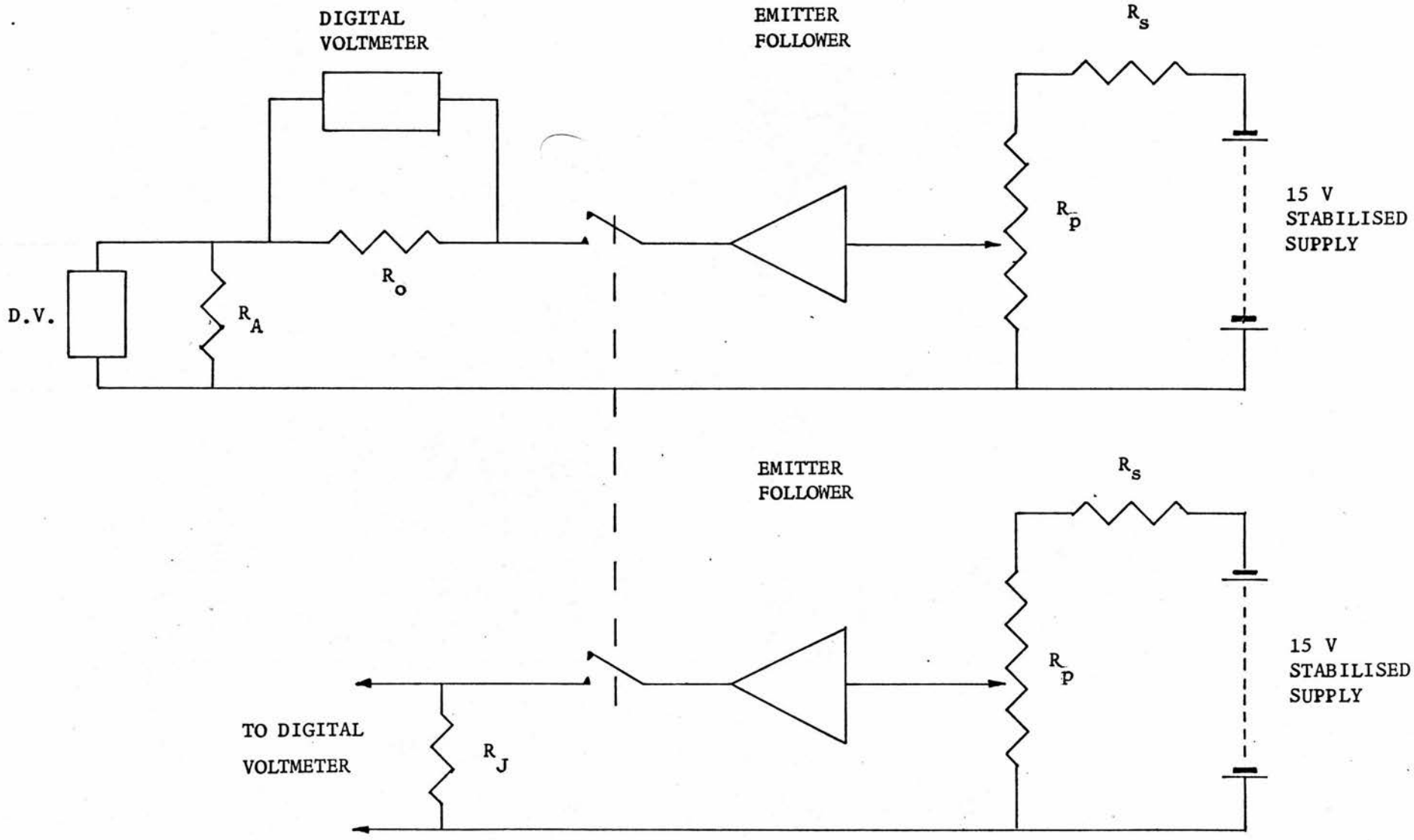

FIGURE 3.15 POWER SUPPLY UNITS

sections 3.3 and 3.5. This section outlines the measurement and supply of electrical power to the absorber and jacket heaters.

The measured resistance of the heater coil was 7.447 $\pm$ 0.005 kΩ, measured at a frequency of 1592 Hz. An approximate calculation shows that to quantitatively simulate a radiation heating rate of 100 rads/min in 2.5 g of carbon, using a heater resistance of 7.447 kΩ, requires a power supply capable of giving a stable output voltage in the region of 0.6 volts. The current drawn from such a supply would be less than 100 μA and, although dry cell batteries exist which could accommodate these requirements, it was felt that a stabilised voltage supply, coupled to a potential divider network, would provide a more flexible alternative. The accurate measurement of voltage levels of a few hundred millivolts can be readily achieved by potentiometric techniques or by a high impedance, precision voltmeter. The direct measurement of small d.c. currents in the range of a few tens of micro-amperes is rather more difficult, but an indirect method of observation, utilising the voltage developed across a precision, high value resistor, affords a useful alternative. This technique was adopted in practice and is illustrated by the schematic diagram in Figure 3.15. Two digital voltmeters, marked D.V. in the diagram, with a range of $\pm$ 3.9999 volts and an input impedance of 10^9Ω, were employed to measure the voltage developed across the heater resistance, R_A, and the precision resistor, R_O. The latter resistor had a value of 10 kΩ (± 0.01%). The digital voltmeters were quoted as being accurate to $\pm$ 1 on the last digit, which, for a voltage measurement of 1 v, yields an accuracy of $\pm$ 0.02%, including an error of $\pm$ 1 on the last digit of the zero reading.

Errors due to the voltage drop along the current leads connecting

R_A to the supply were partially eliminated by the use of two potential leads attached to the printed circuit boards at their junction with the fine "Evanohm" heater wires. A small end effect correction remained; this accounted for the potential developed along the short lengths of heater wire connecting the printed circuit board to the heater wire actually in contact with the absorber. This correction amounted to $2.50 \pm 0.5\%$. The systematic uncertainty associated with this correction was the dominant uncertainty in the electrical calibration and was primarily due to the difficulty in assessing the amount of slack wire between the various "Dees".

Figure 3.15 also shows the circuit which supplied electrical energy to the jacket heater R_J. This power supply unit was identical to that of the absorber, but, since an accurate determination of power dissipated in the jacket was not required, the equivalent resistance to R_O was omitted. Facilities for measuring the approximate voltage drop across R_J were provided, as indicated in Figure 3.15.

To simulate the same total temperature rise during calibration, as well as the rate of change, would require a total energy of 12.5 m J (= 500 rads deposited in the mass of the graphite absorber) which, for a dissipation of 42 μW, requires a heating period of 5 minutes. Assuming that the greatest error in the use of a stopwatch is the reaction time of the operator, it is still possible to measure periods of 5 minutes to an accuracy of better than 0.1% with this instrument. Therefore, no attempt was made to time the heating period electronically. Nevertheless, to eliminate any time lag between the response of the absorber and jacket heaters, the simple

precaution of ganging together the two relevant switches was taken (indicated by the broken line in Figure 3.15).

One final point, which deserves a brief mention, is the inclusion of the two emitter-followers in the heater circuits. The resistance of the potential divider circuits used in the network was only 10 kΩ, and, since both heater circuits had similar resistances, a severe loading effect could occur. To remove this possibility the emitter-followers were included to give an output voltage, regulated by the potential divider, with an almost zero output resistance. The source of the stabilised voltages were two transistor power supplies, Farnell type S.T.A., whose performance was more than adequate for this application.

3.7 THE VACUUM SYSTEM

The calculation of the heat losses in sections 3.3 and 3.5 assumed a pressure of 10^{-3} torr. During the planning and design stage the achievement of such a low pressure was not considered to be a major problem. However, for a variety of reasons, which will be discussed in this section, the production of such low pressures proved to be a major undertaking.

One of the original intentions of the work described in this thesis was to perform calorimetric measurements on a number of accelerators at various different radiotherapy centres. To achieve this aim the whole calorimetric system was designed to be easily portable. This condition formed the first constraint in the design of the vacuum system. Initially, it had been hoped to mount the tank containing the calorimeter and the pumping equipment on a single trolley, but it soon became apparent that the size of this trolley

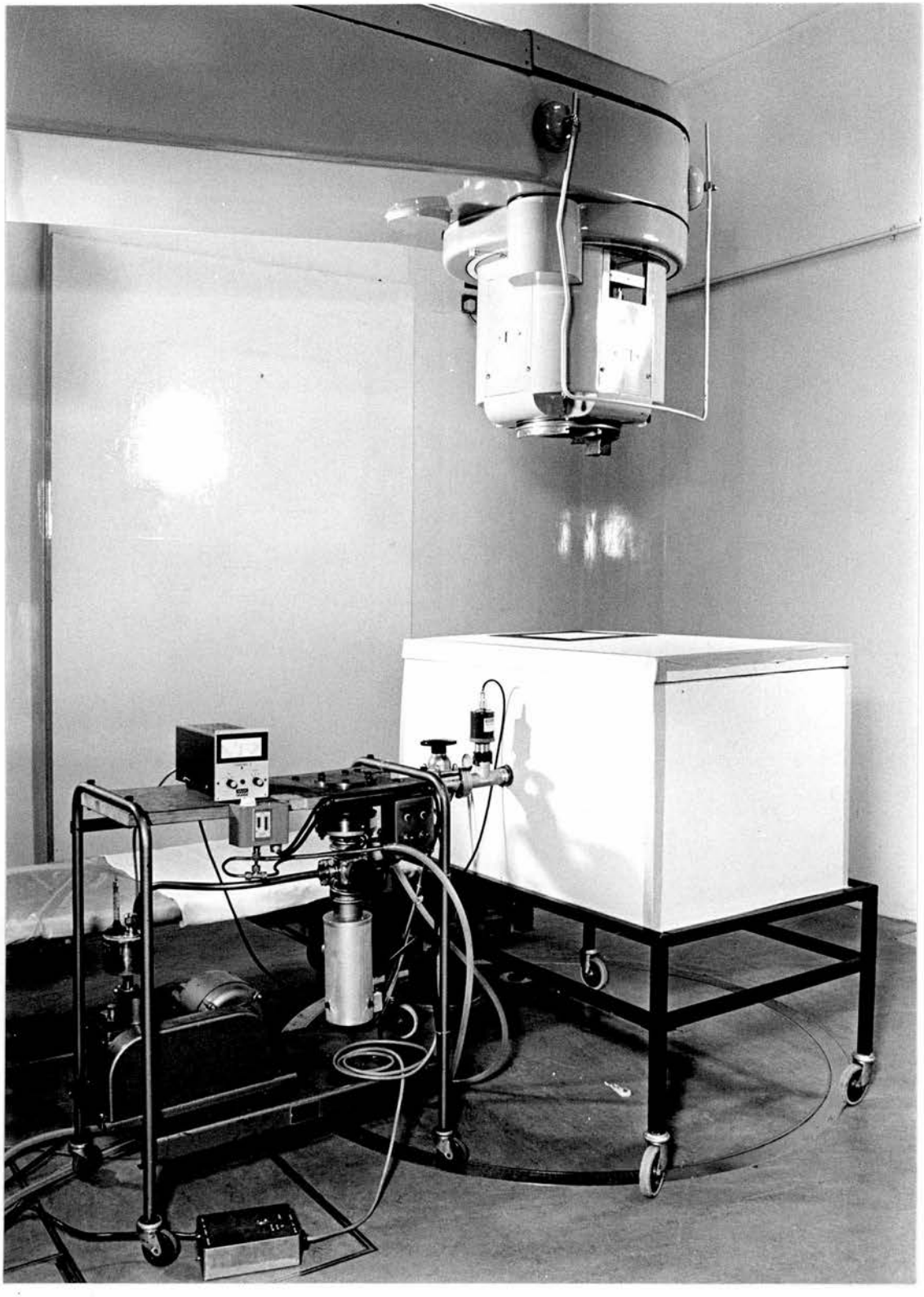

FIGURE 3.16 CALORIMETER, HEAT SHIELD AND VACUUM TROLLEY IN POSITION BENEATH LINEAR ACCELERATOR

would be prohibitively large, and it would not be possible to manoeuvre the equipment in a confined space, such as a treatment room maze. To solve this problem the pumping system was mounted on a separate trolley and attached to the vacuum tank via a flexible hose (Figure 3.16).

The vessel constructed to house the calorimeter was approximately 80 cm x 40 cm x 40 cm and was fabricated from 1.2 cm thick aluminium alloy. The reason for building the vessel from such thick plate was that, under vacuum, the walls of this vessel would have to withstand a force in excess of 2000 kg. Aluminium alloy was chosen in preference to steel for weight reasons, and the walls were duly argon arc-welded to ensure a vacuum tight seal. Access to the vessel was achieved via a detachable lid which could be secured in position by 72 bolts placed at 3 cm intervals around the outer edge. A vacuum seal was provided by an 'O' ring partially recessed in a channel cut in the flange which formed the rim of the vessel. A circular flange was also affixed to a hole in the side of the vessel to allow connection to the flexible hose attached to the pumping trolley.

One of the particular problems with radiation beam calorimeters designed to operate inside a vacuum vessel is the provision of a thin entrance window which does not disturb or attenuate the incident beam. The calorimeter had been designed to utilise a 15 cm diameter beam, thus the entry port was required to have a diameter slightly in excess of this value. Calculation shows that this window must withstand a force of approximately 320 kg when under vacuum. A series of experiments with thin melinex foils indicated that, although severely distorted, a thickness of 10^{-2} cm of foil should suffice.

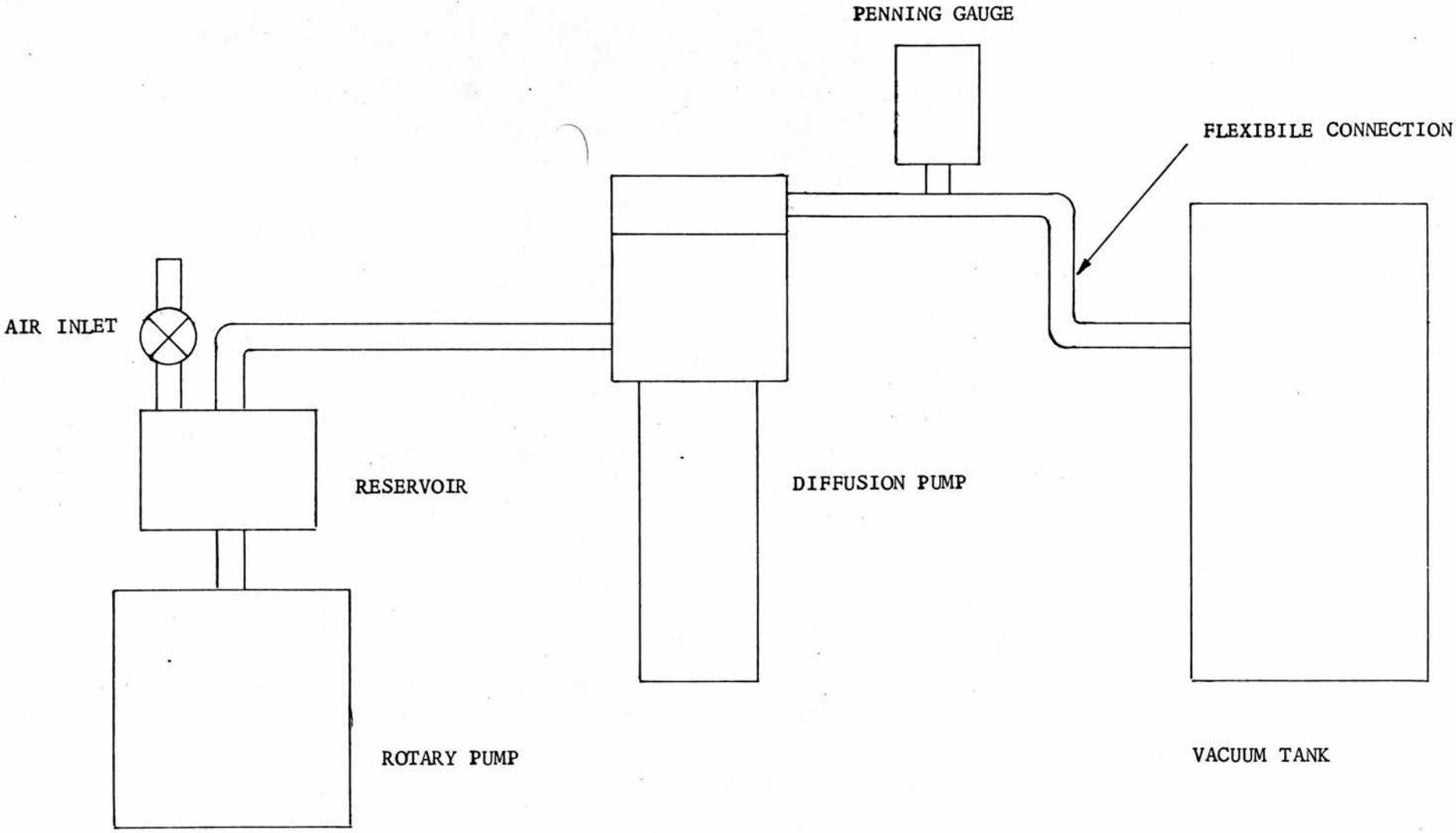

FIGURE 3.17 SCHEMATIC DIAGRAM OF VACUUM SYSTEM

A more extensive series of tests showed that the foil underwent a rapid ageing process after a number of cycles of evacuation and repressurisation and could suddenly rupture without warning. Such a rapid decompression inside the vessel could have catastrophic consequences if an oil diffusion pump was being used to evacuate the chamber. Therefore it was felt desirable to use a minimum window thickness of 5×10^{-2} cm to avoid this possibility.

Although only a maximum pressure of 10^{-3} torr was required inside the calorimeter, it was thought desirable for two reasons to operate with a maximum pressure of 10^{-4} torr. Firstly, the vacuum connections between the various cavities inside the calorimeter were exceedingly small and appreciable pressure gradients could therefore build up inside the calorimeter. Secondly, to reduce the heat transfer between the walls of the container and the calorimeter block, the mean free path of the gas molecules should exceed the maximum separation between these walls and the block. Since this maximum separation was in the region of 40 cm the maximum permissible pressure would be 10^{-4} torr.

Conventional multi-stage rotary pumps are not capable of supplying such a vacuum unaided and must be coupled to a diffusion or ion pump, as shown in the diagram of Figure 3.17. Initially, a roughing out by-pass system was included in the pumping system to allow the water cooled, oil diffusion pump to continue operation whilst repressurising the vacuum tank. This system was later removed though, to reduce the possible number of sites at which leakages could occur.

It became obvious at an early stage in the development of the calorimeter that the residual leakage in the vacuum system would

require the continuous operation of the pumping system. This requirement necessitated the introduction of a number of fail-safe devices to allow the operation of the pumps without continuous surveillance. To protect the diffusion pump from overheating due to a diminution, or cessation, of the coolant fluid flow, a pressure operated relay was included in the heater circuit to act as a cut-out. In the event of an electrical power failure the system was protected against a regurgitation of oil from the rotary pump by the provision of a reservoir, placed immediately above the entrance aperture to this pump. This particular fault occurred on a number of occasions and it was observed that if a sufficient amount of oil was allowed to seep into the rotary pump chamber this pump would jam. If this occurred, and the electrical supply was then resumed without prior drainage of the chamber, the electric motor which drove the pump could burn out. To prevent this predicament a circuit breaker relay, which had to be manually reset in the event of a power failure, was included in the main electrical supply to the pumping trolley.

After numerous difficulties with vacuum leaks and 'O' ring seals it was possible to attain a pressure of 10^{-5} torr inside the empty tank. This pressure was recorded by a Penning Gauge head affixed to the flexible connector joining the pumping system to the vessel. An unfortunate feature of the design of the system was that the large volume of the tank had to be evacuated via a small bore tube. This resulted in extremely long pumping times before achieving the required vacuum. However, the ultimate pressure attainable was not affected.

Introduction of the calorimeter and its supporting structure

into the vacuum vessel resulted in a marked increase in the lowest pressure attainable. Investigation indicated that the cause of the problem was the large P.T.F.E. insulating supports. The occurence of a poor vacuum could be due to two possible reasons. Either, a considerable amount of absorbed gas, or water, is present in the P.T.F.E., which is slowly released under vacuum, the effect being known as "out-gassing", or, the P. T.F.E. has a solid vapour pressure above 10^{-5} torr whereby it would continually sublimate into the vessel.

To avoid either of these effects the P.T.F.E. supports were replaced by a ceramic material, which had previously been vacuum baked for 24 hours at 1300 K before it was introduced into the calorimeter. The system could then achieve a pressure of 10^{-5} torr after 48 hours pumping and an ultimate pressure of 10^{-6} torr was normally attained. Apart from the initial development problems, and the occasional operation of the fail-safe devices, the system performed exceptionally well.

CHAPTER 4.

THE MEASUREMENT OF SMALL TEMPERATURE CHANGES

4.1 INTRODUCTION

The ultimate sensitivity of the calorimeter will be critically dependent on the choice of temperature measuring system, and the following chapter illustrates the design, construction and performance of this system. The first section examines the decision to employ a thermistor as the temperature sensor. Consideration is then given to the design of a Wheatstone Bridge network capable of measuring and recording small resistance changes. The latter half of the chapter is devoted to a description of the construction and performance of a temperature measuring system with an ultimate resolution of 2×10^{-5}K.

4.2 THE CHOICE OF TEMPERATURE SENSORS

The ideal temperature transducer, for use in radiation calorimeters, should combine the following properties:

i) A high temperature sensitivity.

ii) It should produce a signal, linearly related to the temperature, which is readily processed and recorded.

iii) It should have a small physical size, thereby introducing a negligible amount of foreign material into the absorber.

iv) It should maintain intimate thermal contact with the absorber, thus preventing time lag effects.

v) The transducer, by virtue of its mode of operation, should not introduce a significant amount of heat into the absorber, nor should it allow energy to flow into, or out of, the absorber by virtue of

its connections to the external environment.

v) Finally, it should not be susceptible to radiation damage or other deleterious radiation effects.

Thermocouples have a small physical size and can be readily incorporated into potentiometer circuit, thus ensuring a negligible power dissipation at the sensing junction. Unfortunately the sensitivity of even the best thermocouple materials only approaches 70 μV/K (Laughlin and Genna, 1966). Consequently, a system with the ability to detect and accurately process signals of a few nanovolts d.c. would be required for the present conditions. The sensitivity of thermocouple systems can be greatly increased by employing multi-junction thermocouples or thermopiles, and this configuration has been employed in several non-adiabatic calorimeters (Calvet and Duquense, 1964; Pruitt and Domen, 1962). Unfortunately, this method is not applicable to quasi-adiabatic calorimeters due to the vastly increased heat leakage created by the large number of thermocouple wires attached to the absorber. It is now technically possible to amplify very small d.c. voltages but the difficulties involved are still formidable. Coupled with this the high probability of spurious d.c. voltages being detected by such a system, make the method rather unattractive.

Thermistors can be readily obtained in a conveniently small size and with a minimum of vitreous coating, ensuring a rapid thermal response of the sensitive element. In addition, since thermistors only require two very fine connecting wires, the heat transfer to, or from, the absorber is kept to a minimum. The resistive behaviour of a negative temperature coefficient (N.T.C.) thermistor is shown

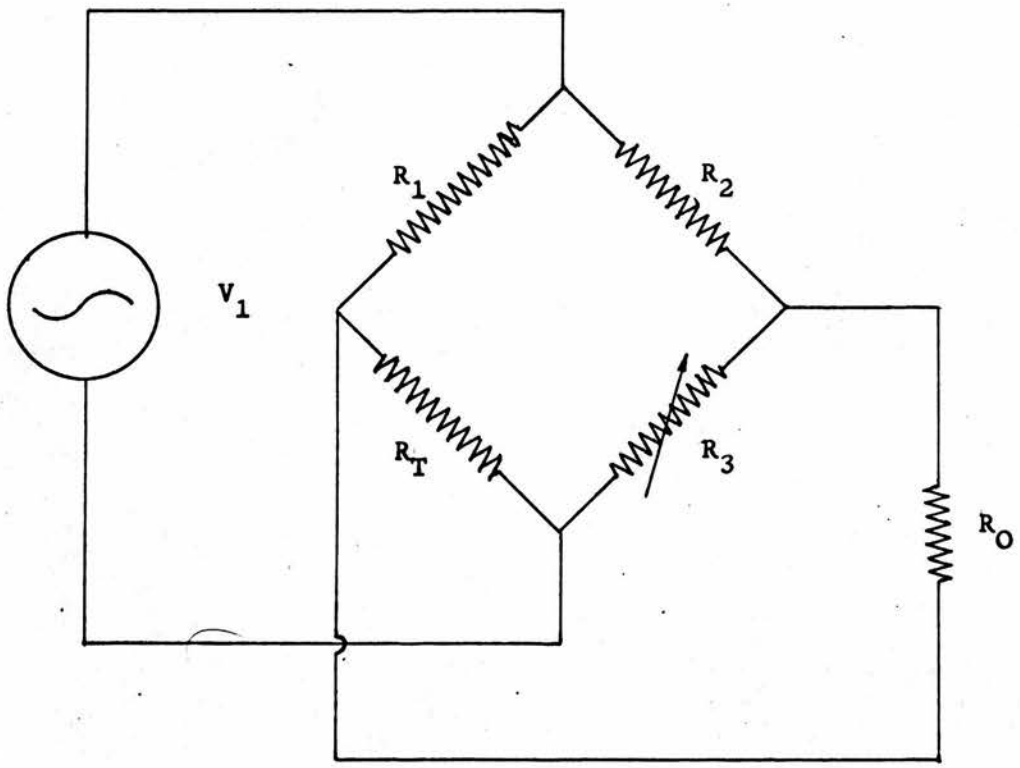

FIGURE 4.1 WHEATSTONE BRIDGE CIRCUIT

in equation 4.1

$$R_T = R_O \exp\left(\frac{B}{T} - \frac{B}{T_O}\right) \qquad 4.1$$

Where R_T = resistance at T(K) and R_O, B and T_O are constants. For a N.T.C. thermistor the value of B is typically 4000 K, thus the sensitivity at room temperature is approximately - 4%/K. Domen (1970) and Hyde (1971) have described positive temperature coefficient thermistors with sensitivities varying from 9 to 15%/K. Unfortunately though, these devices are considerably larger than the N.T.C. thermistors and are reportedly rather erratic in performance.

Inspection of equation 4.1 shows that the thermistor is an inherently non-linear device, but, it will be shown in Chapter 5, that, for the small temperature changes encountered in radiation calorimetry, non-linearity of response is not a severe problem.

The small changes in resistance can be conveniently measured by an a.c. or d.c. Wheatstone Bridge system. The only major disadvantage with this method of resistance measurement is that some energy is necessarily dissipated in the thermistor, thereby creating an additional heat source within the absorber. This point is fully explored in the next section where it is shown that a judicious selection of circuit elements can reduce this problem to manageable proportions.

Thermistors are semiconductor devices and therefore they may be expected to be susceptible to radiation damage. Bewley (1969) has reported that thermistors used in a carbon calorimeter have not shown any deterioration in performance after receiving a cumulative dose of more than 15 Mrads. In the present calorimeter the cumulative dose is less than 1 Mrad and no untoward effects have been exhibited by

the thermistors.

The above discussion has only considered thermistors and thermocouples as the possible methods of measuring small temperature differences, but some other interesting approaches have been described in the literature. In particular, Schmidt and Buck (1969) used the variation in electrical conductivity of a phosphate buffer solution to assess the temperature changes in their fluid absorber. Pettersson (1967) also used a water absorber but estimated the temperature rise by observing the expansion of the water along a calibrated capillary tube. Although Pettersson quoted a high precision (0.13%) both these methods rely rather heavily on physical data and require fluid absorbers; thus they are not suitable in the present situation.

4.3 DESIGN OF WHEATSTONE BRIDGE NETWORK

Wheatstone Bridge networks have been used for more than a century in the precision measurement of electrical resistance, and a number of papers have been published on the application of such networks to resistance thermometry. In particular, Beakley (1951) and Hyde (1971) have analysed the design of bridge networks to produce linear signals over a limited range, using thermistors as temperature sensors, but, as indicated above, such a configuration is not necessary for the small temperature differences encountered in radiation calorimetry. Numerous authors (for example Bewley, 1963; Dove and Cole, 1962; Genna et al., 1963) have described Wheatstone Bridge circuits, using thermistors, for use in radiation calorimetry. However, little detailed consideration has been given to the optimum selection of circuit elements. Laughlin and Genna (1966) have summarised some of the more commonly used circuit designs and came to the conclusion

that no clearly defined choice existed. Redpath (1967) performed a brief mathematical analysis considering voltage sensitivity and detector-normalised power sensitivity, and he came to a similar conclusion to that of Laughlin and Genna. Redpath also stated that no great difference in sensitivity existed between the configurations studied. Nevertheless, if a particular definition of system sensitivity is chosen, then an optimum design for the bridge network can be formulated. In general, the particular choice of system sensitivity will be governed by the type of detector used to analyse the output signal.

Kruglov and Lopatin (1963), Radak and Marković (1962) and Keene and Law (1963) have all used galvanometers or similar current sensing instruments to detect the out-of-balance signal and obviously the current flow in the galvanometer coil should then be maximised for optimum sensitivity. In general though, it is more convenient to detect and amplify low level signals by voltage methods. It would therefore seem essential to maximise the voltage signal appearing across the detector input. The implications of this requirement, together with the constraint of power dissipation in the thermistor, are discussed in the next section.

4.3.1 Voltage Sensitivity

Consider the circuit shown in Figure 4.1 where R_1 and R_2 are fixed resistances, hereafter referred to as the ratio arms, R_3 is the value of the variable balancing resistor, R_T the thermistor resistance and R_O is the input resistance of the voltage detector. A voltage, V_1, is applied to the bridge, and, for simplicity, it has been assumed that the voltage source has a negligible internal resistance. The out-of-

balance voltage, V_O, appearing at the detector input can be found by application of Kirchoff's network laws and is given by

$$V_O = \frac{V_1 (R_T R_2 - R_3 R_1) R_O}{R_O(R_2 + R_3)(R_1 + R_T) + R_2 R_3 (R_1 + R_T) + R_1 R_T (R_2 + R_3)} \qquad 4.2$$

To simplify this equation assume that $R_1 = R_2$ and that $\frac{R_2}{R_3} = \alpha$, then, near the position of balance, $\frac{R_1}{R_T} \simeq \alpha$. These substitutions can now be made in the denominator since it contains no difference terms and is essentially constant near the position of balance. This gives

$$\frac{V_O}{V_1} = \frac{(R_T R_2 - R_3 R_1) R_O}{R_3 R_T (1 + \alpha)(R_O(1 + \alpha) + 2R_1)} \qquad 4.3$$

Using $\Delta R = R_T - R_3$ as a measure of the deviation from balance, equation 4.3 reduces to

$$\frac{V_O}{V_1 \Delta R} = \frac{\alpha R_O}{R_T (1 + \alpha)(R_O(1 + \alpha) + 2\alpha R_T)} \qquad 4.4$$

Equation 4.4 represents the incremental voltage change per unit resistance change and may be regarded as the normalised voltage sensitivity near the position of balance. The value of the detector resistance, R_O, is usually fixed, thus the sensitivity is reduced to a function of only two variables, α and R_T. Inspection of equation 4.4 shows that the sensitivity will increase as R_T decreases. Differentiation of equation 4.4 with respect to α, keeping R_O and R_T constant, shows that amaximum sensitivity is obtained when

$$\alpha = \alpha^1 = \left(\frac{R_O}{R_O + 2R_T}\right)^{\frac{1}{2}} \qquad 4.5$$

If R_T is small compared with R_O, which is normally the case, then $\alpha^1 \simeq 1$ for maximum voltage sensitivity. This is the condition for an equal arm bridge, the only constraint being that R_O is large when voltage detection is employed, which is the standard requirement

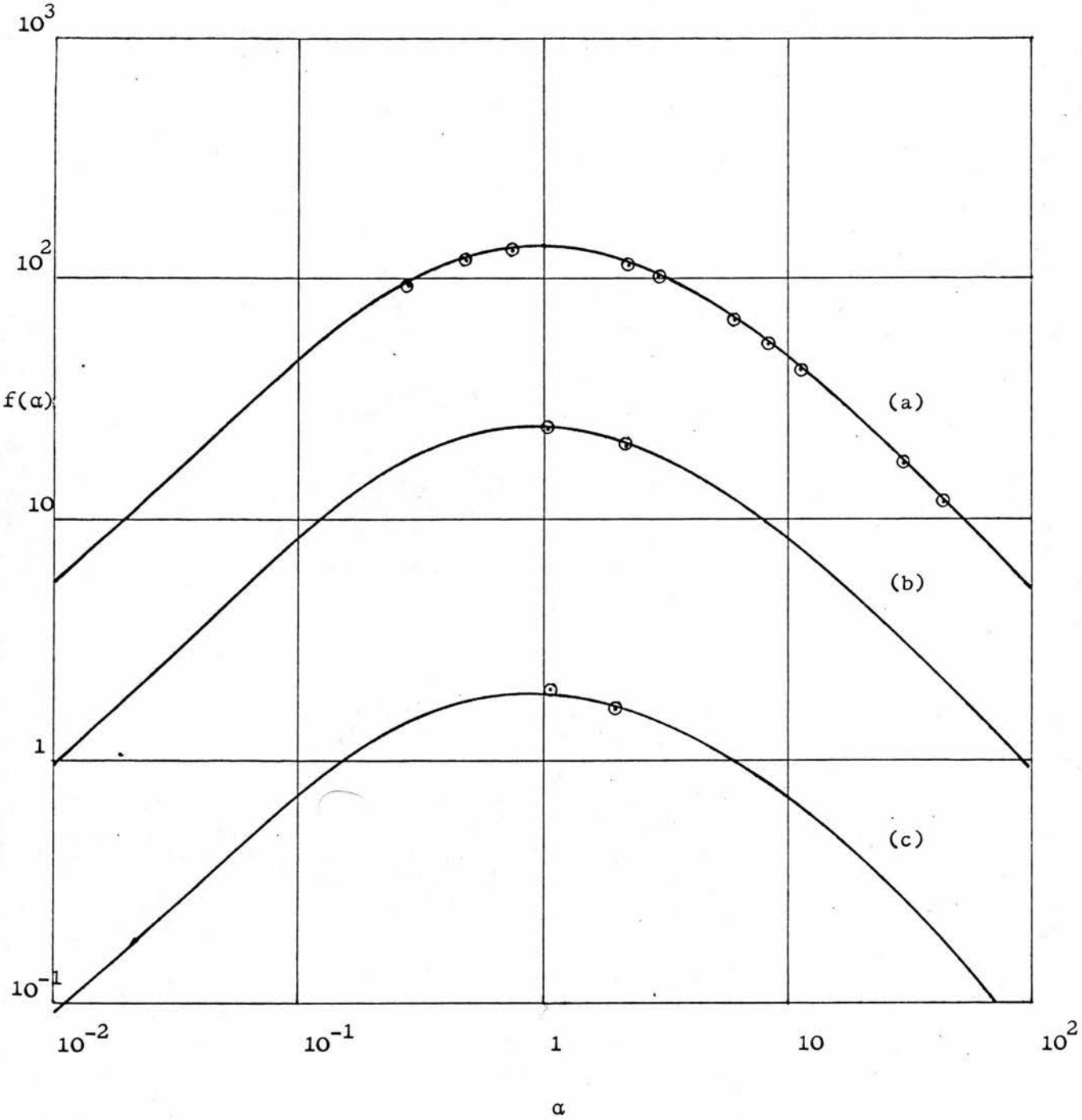

—— THEORY

⊙ EXPERIMENT

R_O = 300 kΩ

(a) R_T = 1.8 kΩ

(b) R_T = 10 kΩ

(c) R_T = 100 kΩ

FIGURE 4.2 NORMALISED VOLTAGE SENSITIVITY f(α), UNITS $\mu V.V^{-1}.\Omega^{-1}$, AS A FUNCTION OF α

for voltage measurement.

These conclusions have been plotted graphically in Figure 4.2, which also shows the experimental results of the voltage sensitivity obtained with the system described in section 4.5.

Whilst it is true that the output voltage is directly proportional to the applied voltage, and that therefore any desired output signal could be achieved by increasing the applied signal, a limit is normally set by the level of power dissipation in the thermistor. It can be argued that the level of power dissipation in the thermistor is irrelevant, since only changes in power dissipation are detected. Nevertheless, high power dissipation in the thermistor is undesirable for two reasons. In the first instance a large standing power dissipation would make it necessary to measure relatively small changes in the level of overall power dissipation. Secondly the continual dissipation of a small amount of heat inside the absorber may result in a sufficiently large temperature increase to upset the thermal equilibrium of the system. Difficulties encountered due to the first objection can be substantially reduced in a twin calorimeter system, where a second thermistor, placed in the dummy absorber, dissipates an equal amount of power. If these two thermistors are placed in opposite arms of the bridge then the resistance rise due to self heating cancels out, leaving an undisturbed out-of-balance signal. Unfortunately this approach requires not only that the temperature sensitivities of both thermistors are identical, but also that the thermal dissipation constants are equal. This latter statement may be amplified by considering the thermistors as discreet, eccentrically located heaters. Then, differences in thermal contact

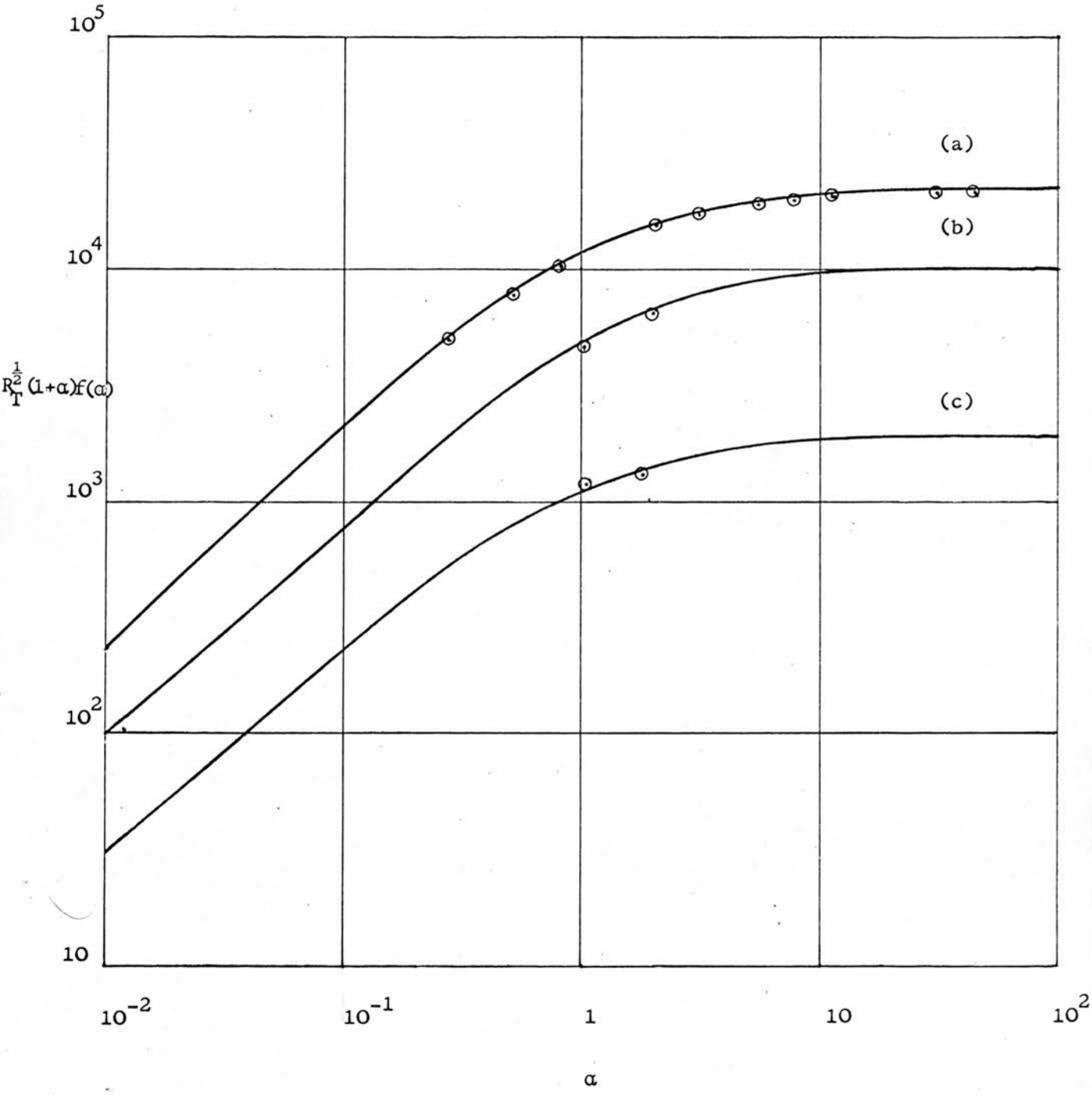

—— THEORY

⊙ EXPERIMENT

R_O = 300 kΩ

(a) R_T = 1.8 kΩ

(b) R_T = 10 kΩ

(c) R_T = 100 kΩ

FIGURE 4.3 THERMISTOR POWER NORMALISED SENSITIVITY, $R_T^{\frac{1}{2}}(1 + \alpha)f(\alpha)$, UNITS $\mu V.\Omega^{-1}.W^{-\frac{1}{2}}$, AS A FUNCTION OF α

with their respective absorbers will result in unequal temperature gradients in the two absorbers. Ultimately this will result in different heat losses from the absorbers since adiabatic conditions cannot be easily maintained for discreet heaters, the overall effect appearing as different self-heating rates. It is therefore desirable to maintain the thermistor power dissipation as low as possible and an expression for the voltage sensitivity, normalised by thermistor-power dissipation, will now be derived. Let the thermistor power dissipation be P_T. Then for an approximately balanced bridge

$$P_T = \frac{V_1^2 R_T}{(R_1 + R_T)^2} \qquad 4.6$$

rearranging and using $R_1 = \alpha R_T$ gives

$$V_1 = (R_T P_T)^{\frac{1}{2}}(1 + \alpha) \qquad 4.7$$

Substituting this expression in equation 4.4 yields

$$\frac{V_O}{\sqrt{P_T \Delta R_T}} = \frac{\alpha R_O}{\sqrt{R_T(R_O\ (1 + \alpha) + 2\alpha R_T)}} \qquad 4.8$$

Figure 4.3 illustrates this function graphically for various values of R_T with R_O = 300 kΩ. Experimental values have again been included showing very good agreement with the simple theory derived here.

The power-normalised sensitivity again shows an increased response with decreasing values of R_T similar to equation 4.4. In this case though, the function does not show a maximum value in respect of the variable α, but tends asymptotically to a limiting value as α increases.

Summarising, it has been shown that the maximum voltage sensitivity is obtained with an equal arm bridge and a high detector impedance. If a limit is applied to the thermistor power dissipation a maximum

sensitivity is obtained when a high resistance-arm ratio 'α' is employed. Physically this corresponds to a current limiting resistor in series with the thermistor. The sensitivity in either case is increased by using low values of R_T, and hence R_3, since more power is then drawn from the supply voltage.

4.3.2 Values of Circuit Elements

The theory of section 4.3 required that the thermistor resistance, R_T, was chosen to be as low as possible. In practice a lower limit is set by the effects of lead resistance and the manual resolution required in the balancing arm, R_3. Commercially obtainable precision decade resistance boxes rarely attain a resolution of better than 0.1 Ω due to contact resistance problems, although Meuller and Wenner (1935) have described a method of shunting large resistances together to achieve a device which gives arbitrarily small, equal steps in resistance, without the problem of contact resistance. The disadvantage of this method is the need to construct a large number of resistance coils which have as a result a large reactive component. The deleterious effects of reactance are examined later in this chapter.

The values of R_1 and R_2 are required to be much greater than R_3 or R_T, but inspection of Figure 4.3 shows that a law of diminishing returns is obeyed if α is increased beyond 25. It is also desirable that the values of R_1 and R_2 are kept as low as possible to reduce electronic pick-up and Johnson noise.

Values of $R_T \simeq 2k\Omega$ and $R_1 = R_2 = 50\ k\Omega$ were eventually selected as the best compromise between the conflicting requirements. In retrospect values of $R_T = 20\ k\Omega$ and R_1 and $R_2 = 100\ k\Omega$ may have proved more convenient since the 0.1 Ω decade of the balancing resistor

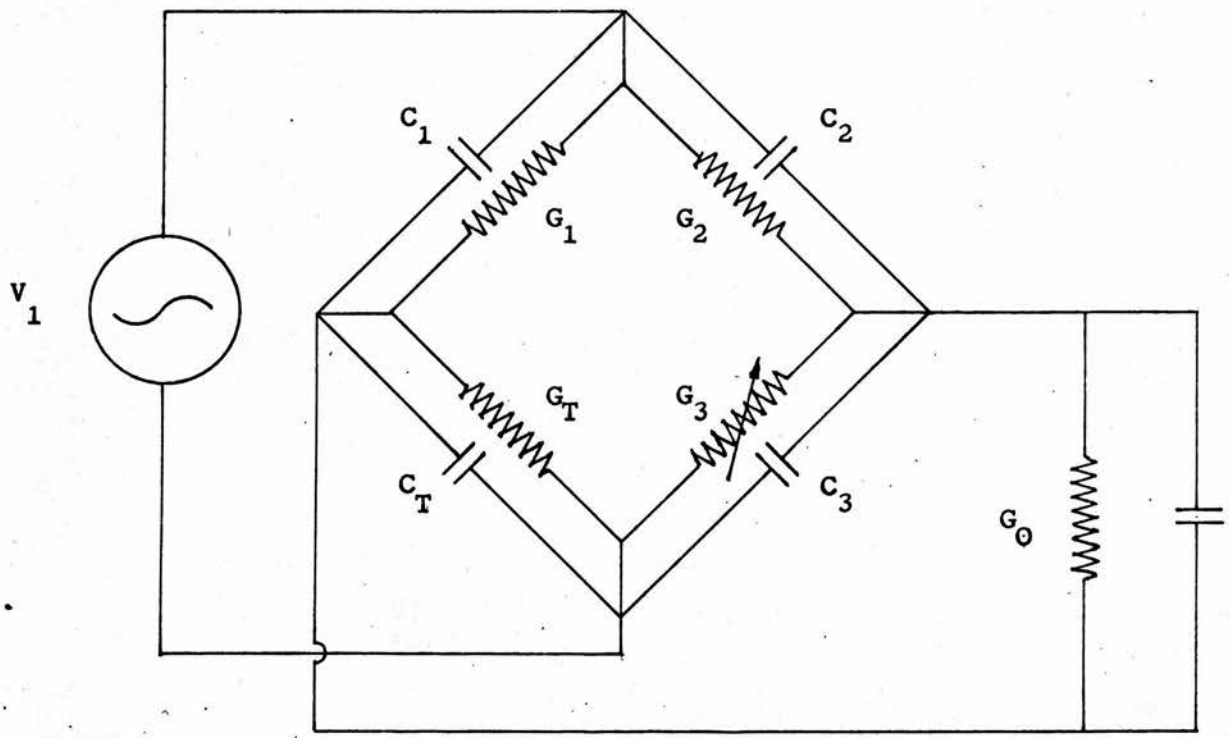

FIGURE 4.4. a.c. WHEATSTONE BRIDGE CIRCUIT

became unreliable and was eventually replaced by a parallel resistance system. (Substitution of the thermistor once incorporated into the calorimeter would have been a major undertaking and was not considered a feasible alternative.)

4.4 a.c. OPERATION OF BRIDGE NETWORKS

Genna and his co-workers (1963) and Bradshaw (1965) amongst many others have described Wheatstone Bridge networks operated in a d.c. mode, where a chopper amplifier was used as the voltage detector. Such amplifiers are rather unstable and great care must always be employed to ensure that stray thermoelectric voltages are not injected into the amplifier input. Wheatstone Bridge systems actuated by an a.c. signal are not susceptible to thermoelectric errors and amplification of small signals can be performed without recourse to chopper amplifiers. In addition, the development of Phase Sensitive Rectifiers (P.S.R.) has made it possible to extract signals submerged well below the noise level. A number of investigators have used this system, amongst them Bewley (1963), Redpath (1967) and Major (1974), and this configuration has now largely superseded the d.c. operation.

4.4.1 Effect of a.c. Operation in Bridge Output

The analysis of section 4.3 was based upon the assumption of a purely resistive circuit, but since most components will contain a reactive element, the influence of this effect will now be discussed. Figure 4.4 shows the circuit of Figure 4.1 with added capacitors to represent the stray, lead and inherent reactance of the circuit elements. Again using Kirchoff's laws it is possible to show, with some simplifying assumptions, that

$$\frac{V_O}{V_1} = \frac{(G_\alpha^2(\Delta G - \omega^2 \Delta C) + 2\omega^2 C_\alpha G_\alpha (GC)_\beta) + j\omega (G_\alpha^2 (GC)_\beta - 2C_\alpha G_\alpha (\Delta G - \omega^2 \Delta C))}{G_\alpha^4 + 4\omega^2 C_\alpha^2 G_\alpha^2} \qquad 4.9$$

where $\Delta G = (G_1 G_3 - G_T G_2)$, $\Delta C = (C_1 C_3 - C_T C_2)$, $G_\alpha = G_O + G_1 + G_T$,

$C_\alpha = C_O + C_1 + C_T$ and $(GC)_\beta = (C_1 G_3 - C_T G_2 - C_2 G_T)$

Putting $\omega = O$, $G_1 = \frac{1}{R_1}$, $G_2 = \frac{1}{R_2}$, $G_3 = \frac{1}{R_3}$ and $G_T = \frac{1}{R_T}$

equation 4.9 reduces to equation 4.2.

The significance of equation 4.9 is that it shows, not only the presence of a phase quadrature component of the out-of-balance voltage, but that even when the bridge is balanced resistively and reactively, (i.e. $\Delta G = \Delta C = O$), a residual voltage, due to the term $(CG)_\beta$, can appear at the bridge output. The presence of a large phase quadrature component will limit the gain which can be applied to the signal before the amplifier overloads or distorts. The in-phase residual voltage may have a similar effect, but, in addition, it could produce a large standing voltage at the output, causing small changes in resistive imbalance to appear as a slight perturbation in a large output signal. Equation 4.9 also requires that a reactive balance must be achieved to reduce spurious output voltages and a variable capacitor was therefore included in the bridge circuit. Equation 4.9 further shows that a low signal frequency will reduce the artifacts caused by a.c. operation. In practice it was found undesirable to operate at frequencies near 50 Hz, or multiples thereof, since the major component of noise voltage was mains hum. A frequency of 285 Hz was eventually chosen as the most suitable compromise.

FIGURE 4.5a

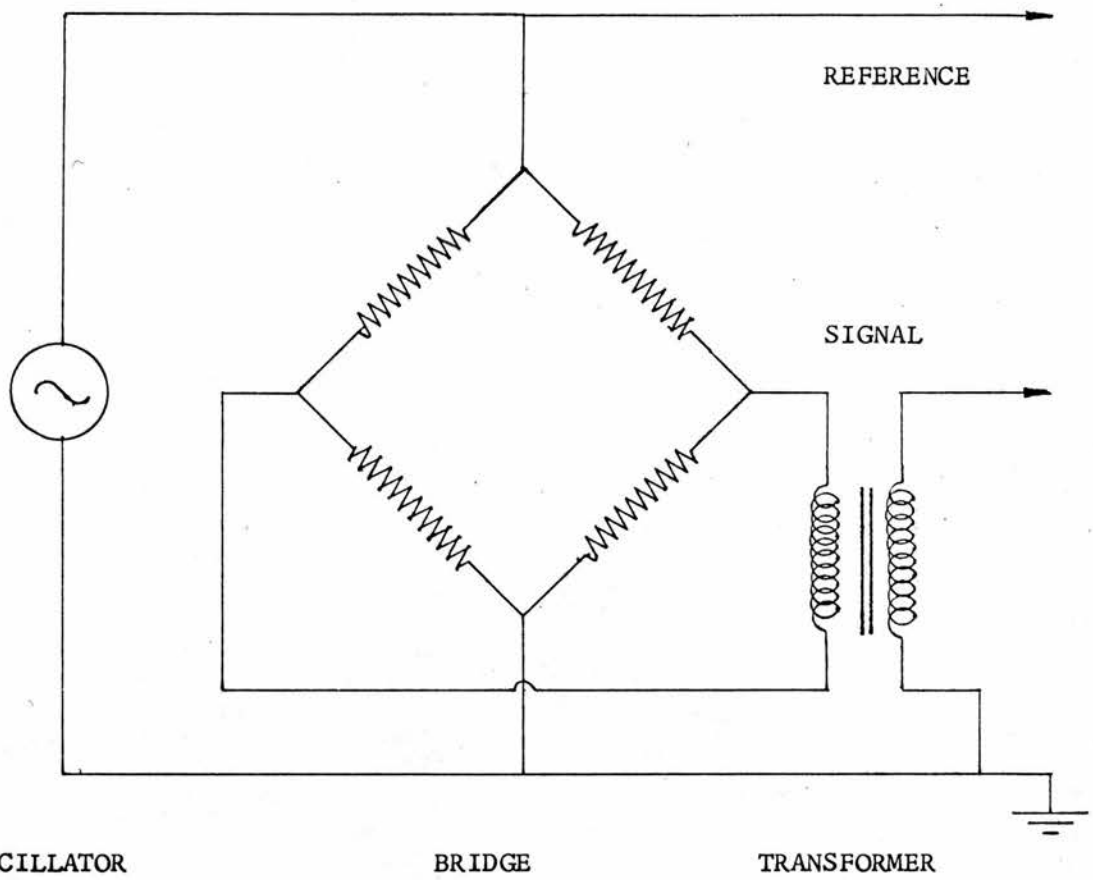

FIGURE 4.5b

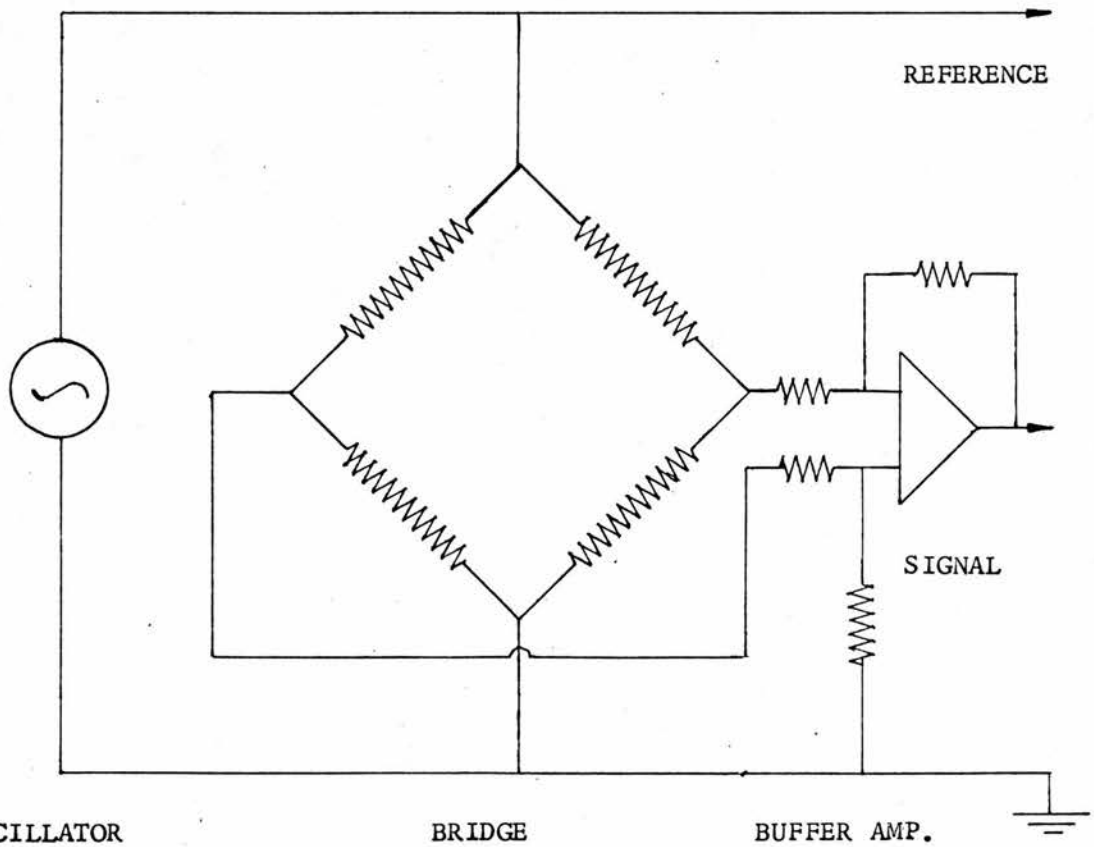

FIGURE 4.5c

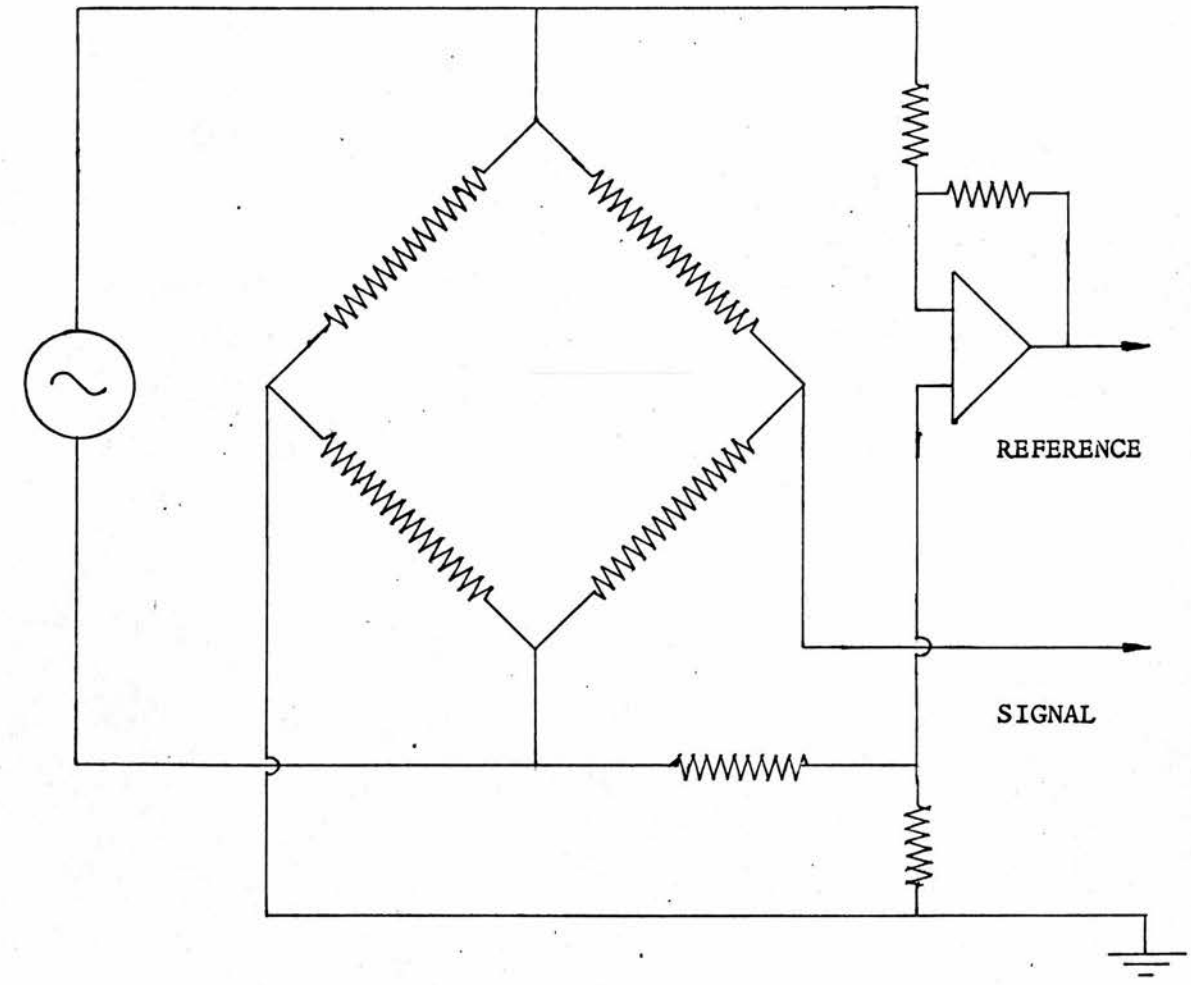

4.5 CONSTRUCTION OF WHEATSTONE BRIDGE SYSTEM

The efficient operation of the phase sensitive rectifier requires that a signal, of identical frequency to that of the bridge output, is supplied to the reference channel of the P.S.R. This requirement can readily be achieved if a single oscillator is used to supply both the bridge network and the P.S.R. reference channel. The P.S.R. reference input is single ended (i.e. one terminal is held at earth potential) and direct connection of the oscillator to both the bridge and P.S.R. uniquely determines the bridge earth point. This constraint is not serious if a differential amplifier is utilised as the bridge output detector. Unfortunately, this is rarely the case in practice since high gain, low noise amplifiers are more readily constructed with single ended inputs. Figure 4.5 illustrates some of the possible configurations that have been used to circumvent this problem. Redpath and Major have both adopted the circuit described by Figure 4.5a but it was found to be rather unsatisfactory due to the pick-up generated in the transformer, and subsequently amplified. The circuit of Figure 4.5b was an attempt to transform the single ended amplifier into a differential type using operational amplifier techniques. This circuit again introduced a significant amount of noise into the main amplifier. The circuit of Figure 4.5c provided the best compromise in the prevailing conditions and was therefore adopted. Essentially the circuit consists of a bridge network supplied by a completely floating oscillator output, the bridge output being fed directly to the low noise amplifier (Brookdeal Model LA635). The oscillator then supplies the reference signal via the differential buffer which handles a sufficiently large signal for its noise parameters to be

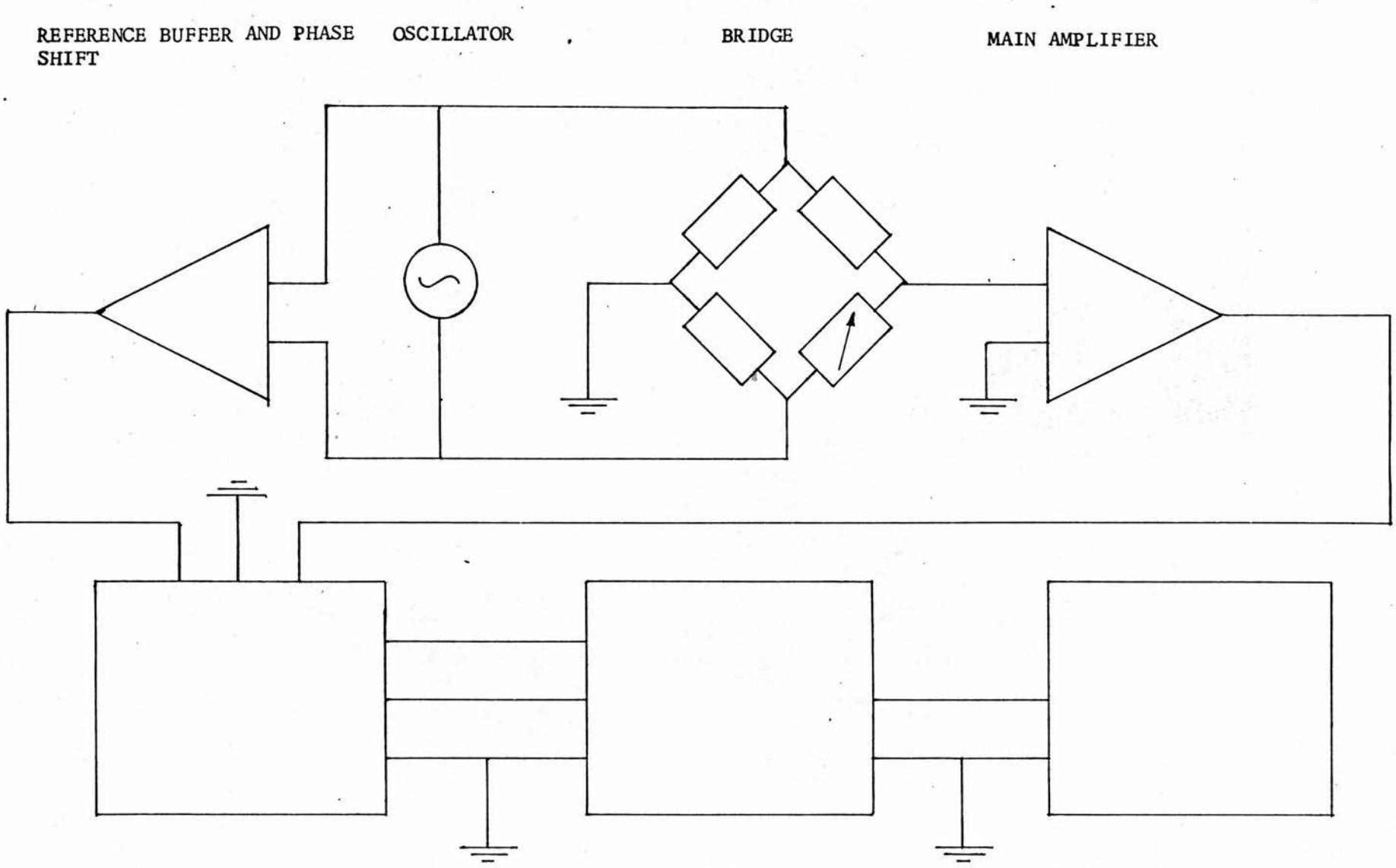

FIGURE 4.6 BLOCK DIAGRAM OF TEMPERATURE MEASURING SYSTEM

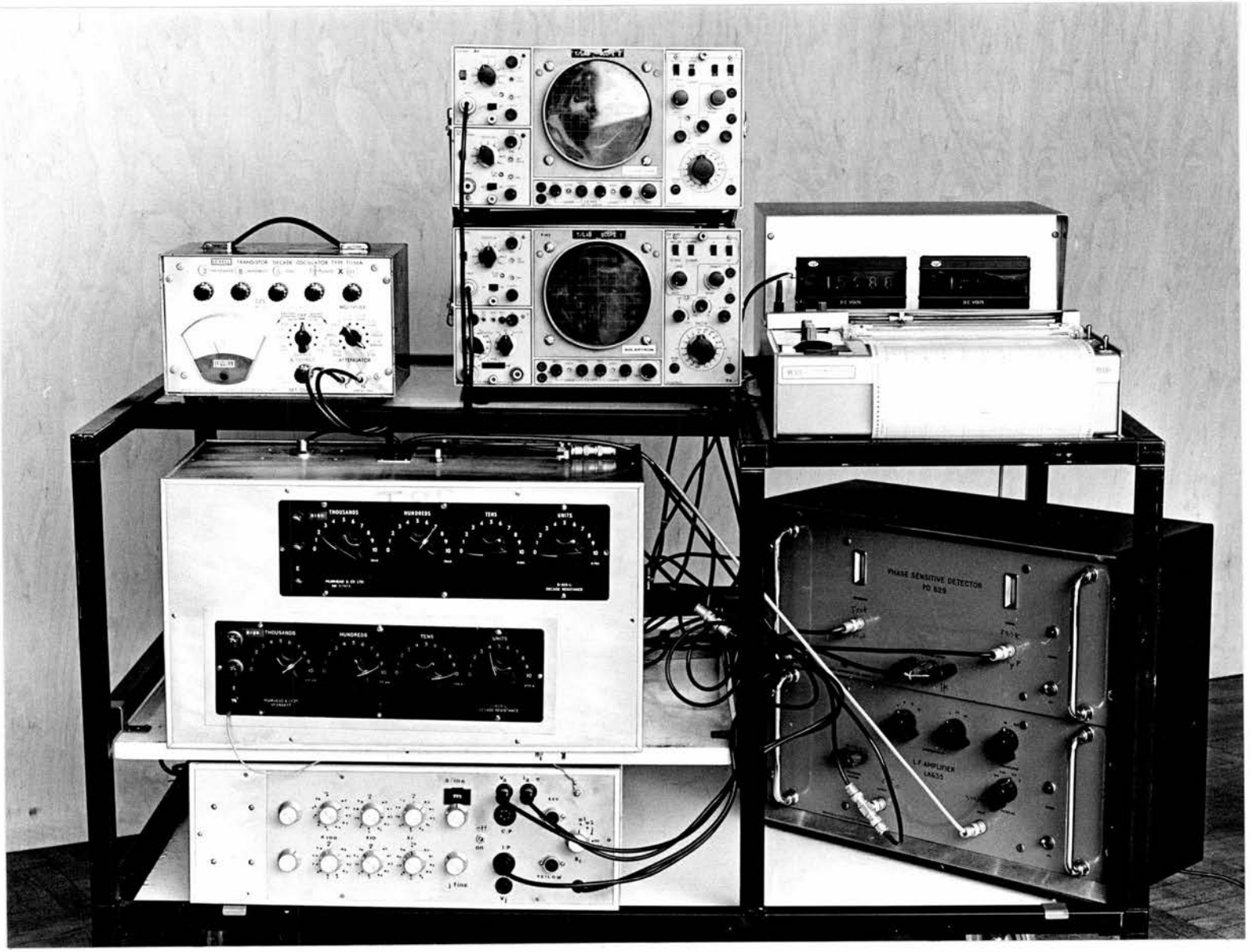

FIGURE 4.7 TEMPERATURE MEASURING EQUIPMENT

negligible, the only constraint on the buffer being that it should not shunt the resistances of the bridge arms.

A block diagram of the complete circuit is shown in Figure 4.6 and a general view of the layout in the photograph, Figure 4.7. A Levell decade oscillator, type TG66A, was specially modified to produce a floating input signal to the bridge and precision metal film resistors ($\pm$ 0.2%) (Vishay Type V53-1) were used for the bridge ratio arms. These resistors also had particularly low temperature coefficients of resistance, 10 ppm/K, since ambient temperature changes in the ratio arms could produce spurious output signals.

The balancing arm of the bridge was constructed from two decade resistance boxes, one of which was shunted by a 100 Ω precision resistor enabling the production of arbitrarily small resistance changes. Two small melinex foil trimmer capacitors were placed in parallel with one of the ratio arms to facilitate a reactive balance. The two ratio resistors together with the trimming capacitors and the differential buffer were mounted in a diecast box, which also provided a focus for the various inter-connecting leads.

It was also found necessary to introduce a phase-shifting network on the reference channel to compensate for phase changes introduced in the bridge circuit. This consisted of a simple R-C filter coupled to a compensating amplifier, resulting in a phase variation from 0 to $\frac{\pi}{2}$ radians. This assembly was mounted in a separate diecast box. The two diecast boxes were then supported inside a large aluminium case which also acted as a base for the two decade resistance boxes, the whole configuration forming a compact well shielded unit.

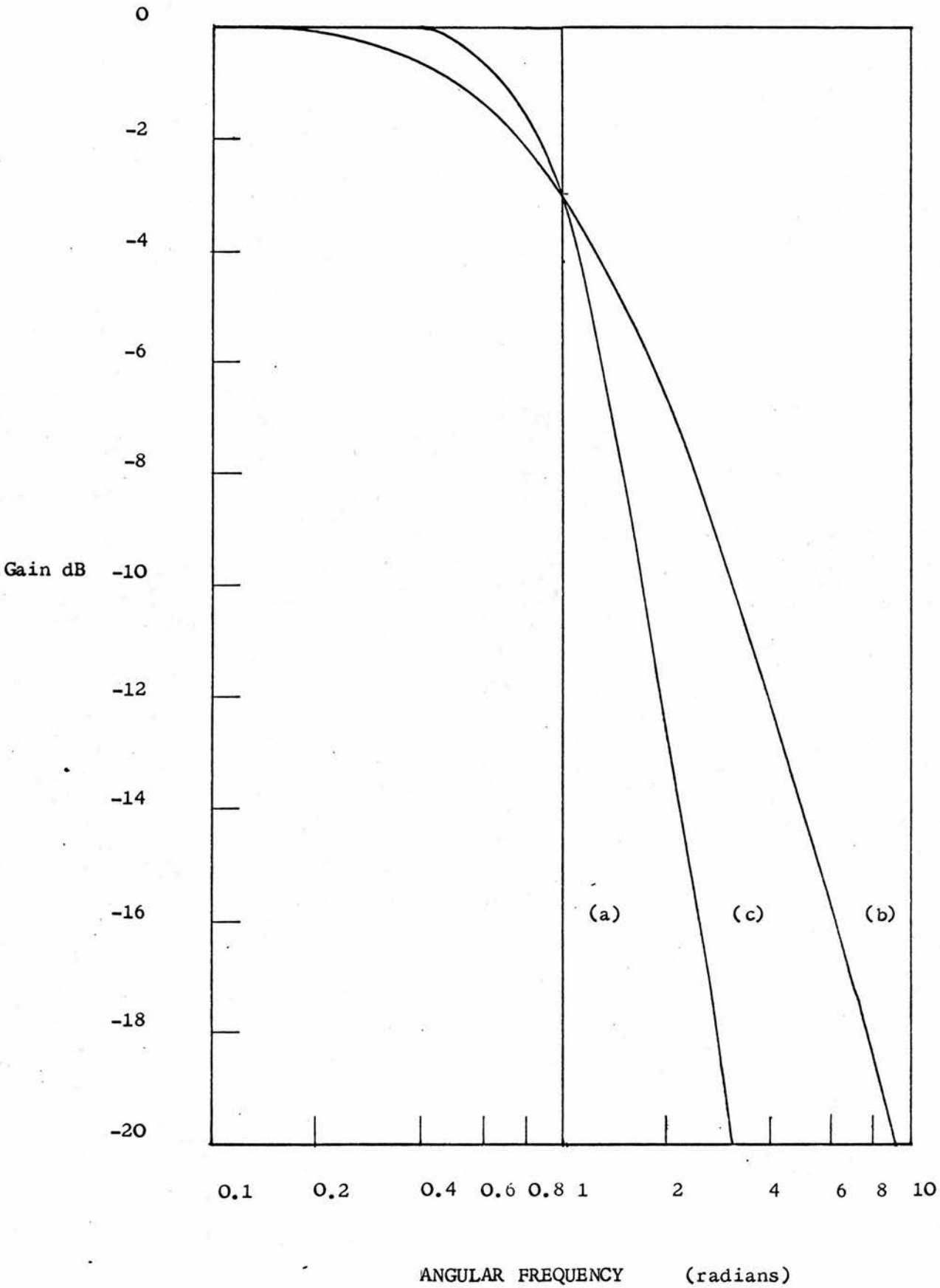

FIGURE 4.8 LOW-PASS FILTER CHARACTERISTICS

After amplification, the out-of-balance signal from the bridge was passed to the signal channel of the P.S.R. The P.S.R. acts in a similar way to a synchronous switch, the reference frequency being used to switch successive half cycles of the noisy signal to an integrating capacitor via a load resistor. If any signal, with a frequency near that of the reference, is present in the input waveform, then a voltage will eventually be integrated on the capacitor, this voltage being proportional to the amplitude of the incoming signal and its phase, θ, relative to that of the reference. All other signals which are random will eventually sum to zero. The P.S.R. thus gives an output proportional to $V_o \cos \theta$ and rejects all signals outside a bandwidth of $\frac{1}{T}$, where T is the time constant of the output integrating circuit. Ideally the bandwidth cut-off should be infinitely sharp as shown in Figure 4.8a. The frequency roll-off of a simple RC low pass filter only yields a gradient of - 6dB/octave. Faulkner et al. (1965) have described an integrating system consisting of a chain of low pass filters yielding a superior frequency response. Unfortunately though, this system achieves the superior frequency response at the expense of the output signal strength, and a more fruitful approach is to utilise an active filter network which provides an adequate frequency response, Figure 4.8c, without attenuation. The details of the design of the filter network are briefly outlined in Appendix 1, and Figure 4.9 illustrates the circuit used. Finally, the d.c. signal from the integrating network was displayed and recorded on a chart recorder, Smiths Type RE 511/20.

It was also felt desirable to monitor the progress of the signal at various points in the system and the letters A, B and C on Figure

FIGURE 4.9 LOW-PASS FILTER NETWORK

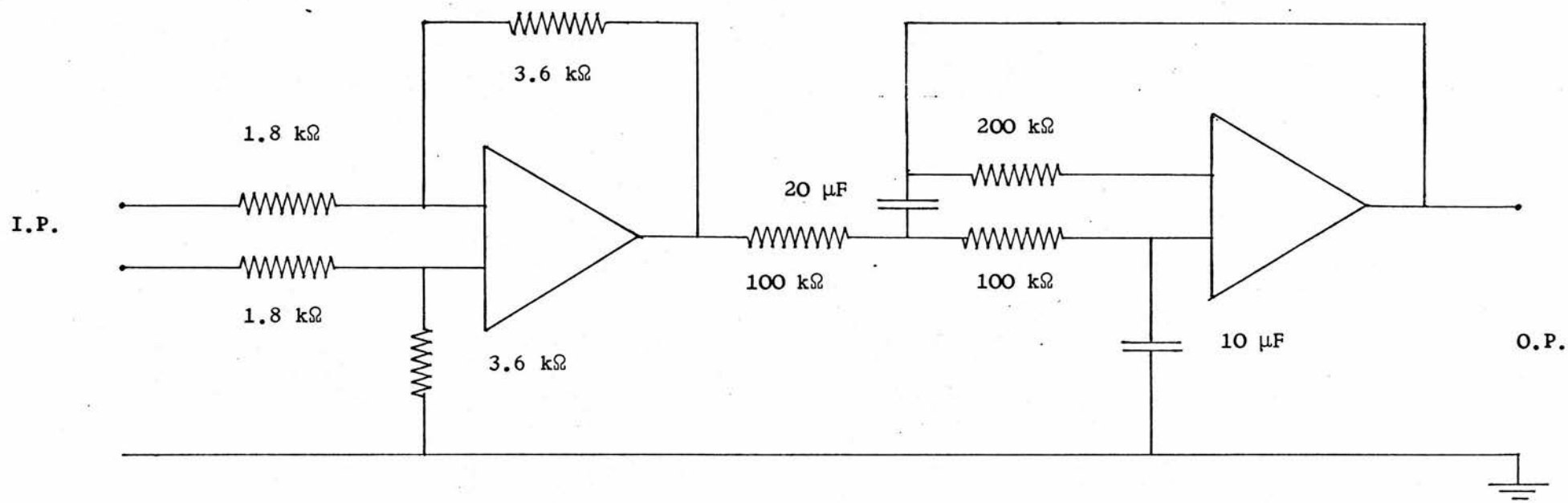

4.6 indicate the junctions where cables were introduced to display the signal on an oscilloscope.

4.6 PERFORMANCE OF THE TEMPERATURE MEASURING SYSTEM

4.6.1 Sensitivity

The overall response of the amplifier, P.S.R. and filter circuit combined was 32 mV d.c. per μV r.m.s. applied at the amplifier input, the frequency of 285 Hz being used. This corresponds to a resistance sensitivity of 680 mV d.c. per ohm change in 2000 Ω, which, expressed as a temperature sensitivity, is 54.4 V d.c./K. The resultant output noise level on the chart recorder was $\pm$ 1 mV d.c. enabling a resolution of better than 2×10^{-5} K to be obtained.

The precise position of balance varied slightly from day to day and marginal changes in phase alignment at the P.S.R. imputs resulted in a small variation in overall gain, thus the parameters quoted above have not been assigned an uncertainty and represent maximum values.

The time constant of the system, estimated as the time elapsed to achieve 99% of the final value of a resistance step impulse, was 10.0 $\pm$ 0.5 seconds. This value could be reduced by altering the values of components in the filter circuit indicating that the response of the system was limited by the instrumentation rather than any thermal barrier at the thermistor-absorber interface.

4.6.2 Stability

The evaluation of data from the Wheatstone Bridge network depended on the observation of the voltage drift rates produced on the chart recorder. These voltage drift rates were produced by the slow deviation of the thermistor resistance from its value at

the balance position. The nett result of this mode of operation is that the prime advantage of the Wheatstone Bridge network as a null instrument is lost, and the information produced by the system is critically dependent on the stability of the input voltage and the various amplification stages. This criticism appears to apply to almost all of the thermistor networks used in radiation calorimetry and only Goodwin (1959) and Kruglov and Lopatin appear to have attempted a null method. Briefly their approach consisted of pre-setting a position of bridge balance and then waiting until the output voltage fell to zero, when the time and value of the balance point were recorded. Repetition of this procedure yielded a 'resistance' drift rate when the results were plotted graphically. A similar method was attempted with the system described here. However, due to random fluctuations about the balance point, the approach did not yield superior results and, in addition, was excessively tedious.

The amplifier was quoted as stable to within $\pm$ 0.25 dB in 95 dB, with a hum level of 1 μV r.m.s. referred to a short-circuited input. Although the hum level never fell below 10 μV r.m.s. no reason was found to doubt the stability of the amplifier. Values for the stability of the P.S.R. were not quoted in the instruction manual but experiment indicated that, with both P.S.R. inputs short-circuited, the output from the combined P.S.R. and filter network gave a typical drift rate of $\pm$ 100 μV d.c./h, the noise level being insignificant. Neither the handbook nor the manufacturers of the oscillator gave details of amplitude stability, and the modifications incorporated would probably have invalidated any data available. Tests using the oscillator coupled to a potential divider network which supplied appropriate

voltage levels to the signal and reference channels of the P.S.R., yielded an output drift rate of $\pm$ 1 mV d.c./h and a similar amplitude for the noise level. Unfortunately this configuration did not simulate the working conditions, since one terminal of the oscillator was necessarily earthed. Noise levels encountered in operation were approximately $\pm$ 1 mV, similar to those obtained in the test above. However, on occasions the d.c. output signal executed large, slowly varying, random deviations. These fluctuations were often several hundreds of millivolts in size and could continue for 10 to 20 minutes at a time. Careful investigation implied that the oscillator was the source of these artifacts, and it was suspected that the modifications incorporated in the oscillator created capacitance instabilities in this instrument, resulting in misalignment of the phase at the P.S.R. input. Whilst the general performance of the temperature measuring system was adequate, this severe output instability caused a considerable loss of valuable experimental time and, in this respect, the system could not be regarded as reliable.

CHAPTER 5.

ANALYSIS OF CALORIMETER OPERATION

5.1 THE QUASI-ADIABATIC STATE AND THE EFFECT OF TEMPERATURE GRADIENTS

It was stated in Chapter 2 that the temperature behaviour of the calorimeter could be expressed by the equations

$$\frac{dT}{dt}_A = -K_A (T_A - T_J) \qquad 2.2$$

and

$$\frac{dT}{dt}_A = \frac{W_A}{M_A C_A} - K_A (T_A - T_J) \qquad 2.3$$

the first equation referring to a zero heat input and the second to a heat input of W_A. The subscripts A and J again refer to the absorber and jacket respectively. For the case of ideal adiabatic conditions the term $K_A (T_A - T_J)$ is zero, and the temperature rise of the absorber is directly proportional to the total heat input. It was observed in Chapter 2 that both these equations represent an over simplification of the true experimental conditions. It is the purpose of this chapter to examine the effects of the experimental conditions and to formulate a method for the correct interpretation of the experimental data. The treatment presented in this first section is somewhat similar to the analysis of Laughlin and Genna (1966) which itself was based upon the discussion of Genna et al. (1963). In the former of these two publications the effects of non-adiabatic conditions and thermal gradients were considered separately, but it will be shown below that a combined analysis includes some extra correction terms which must be considered when interpreting the experimental data.

Consider the situation shown in Figure 5.1 which illustrates

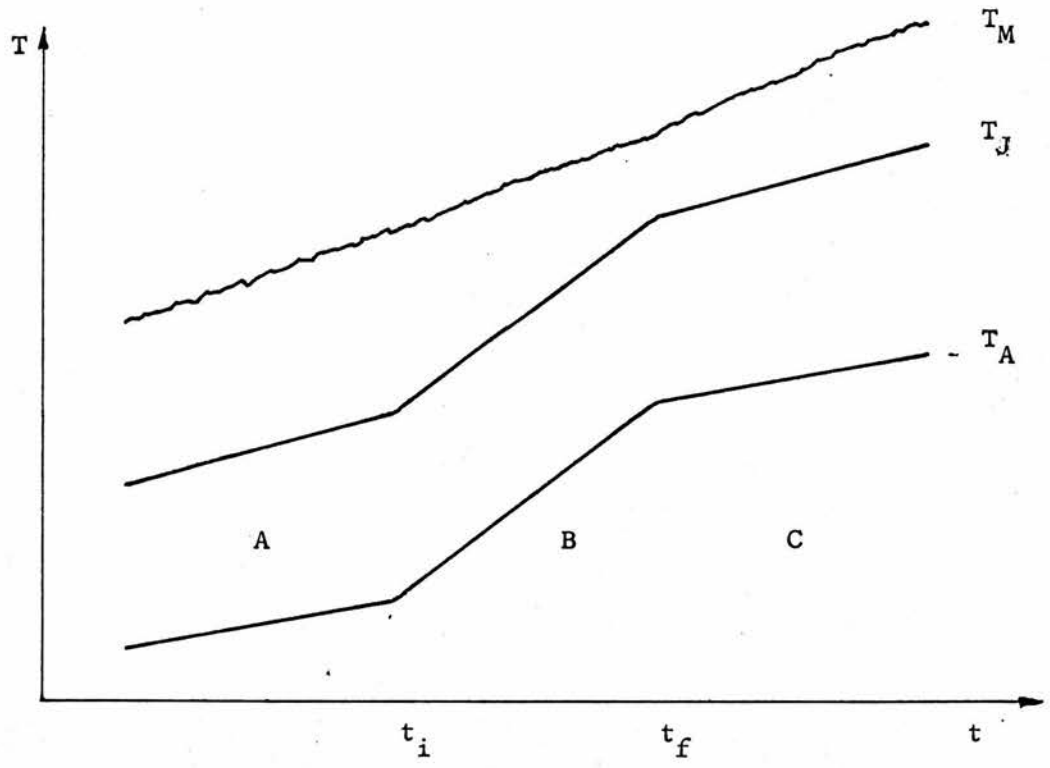

FIGURE 5.1 ABSORBER, JACKET AND MANTLE TEMPERATURE HISTORIES

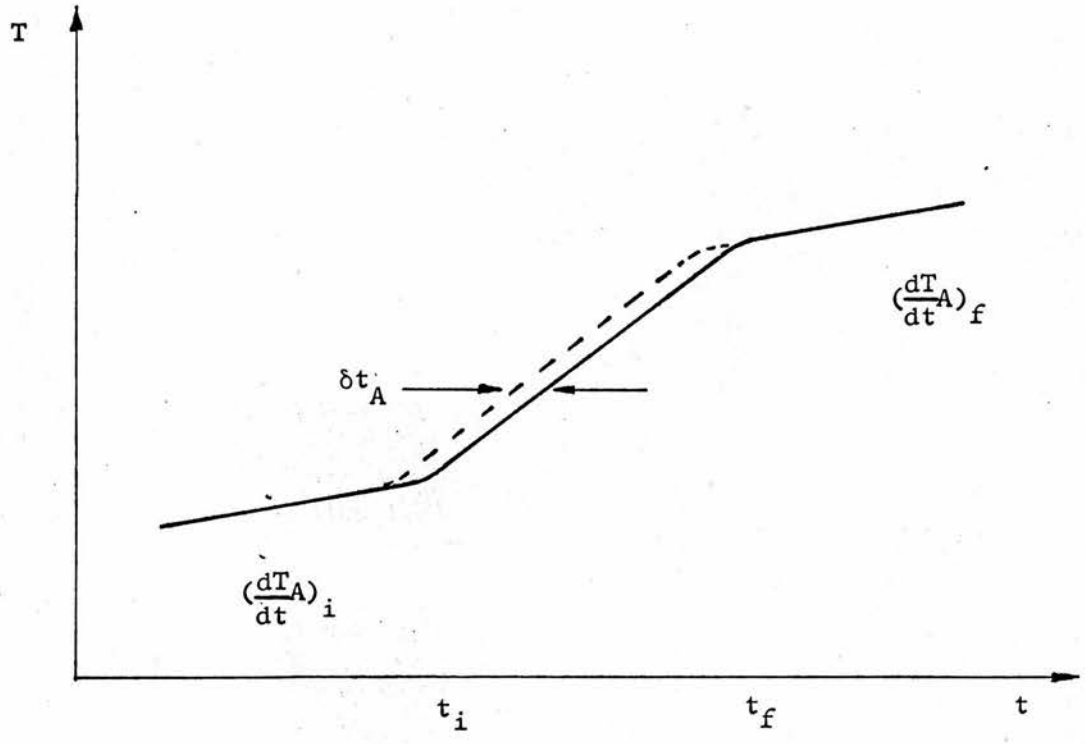

FIGURE 5.2 DEFINITION OF TIME LAG δt_A

a calibration heating experiment. The external environment is at a slightly higher temperature than the mantle which will therefore undergo a resultant heating; this has been indicated by a jagged line to depict its fluctuating nature. During the quiescent periods, marked A and C in Figure 5.1, the thermal head of the mantle over the jacket creates an upward, or positive, drift rate in this latter element and, ultimately, in the absorber as well. During the calibration period, B, thermal energy is being supplied to the absorber and jackets via their electric heaters, and this results in an increase in their upward, or positive, drift rates. Although no electrical energy is supplied directly to the mantle element during this period, it also experiences a slight increase in its positive drift rate. This is a direct result of the decrease in the thermal head of the mantle over the jacket which decreases the amount of heat leaving the mantle, dQ (M - J). The ultimate outcome of this change in the thermal head of the mantle is a slight change in the drift rate of the jacket during the final quiescent period, C, when compared with its drift rate during the initial quiescent period, A. Unless this change in the jacket drift rate is very large, the drift rates of the absorber in periods A and C will remain unchanged.

The flow of heat through the various bodies comprising the calorimeter must be associated with a temperature gradient within these bodies. Therefore, equations 2.2 and 2.3, which implicitly assume a uniform bulk temperature throughout the absorber and jacket, must be modified to account for the existence of these temperature gradients. Strictly, this alteration should apply to all the

temperature equations used in this analysis (i.e. during both the quiescent periods and the heating periods). However, to a first approximation, only equation 2.3, when applied to the calibration heating interval, need be modified. It is expected that the temperature gradients during the other periods will be much smaller than the calibration case and can thus be neglected. In this event equation 2.3 becomes, for the calibration heat input rate W_A

$$\frac{dT}{dt}A = \frac{W_A}{m_A c_A} - K_A (T_{A,S} - T_{J,S}) \qquad 5.1$$

where the extra subscript S refers to the surface temperature, since the heat transfer between the absorber and jacket is a function of the relevant surface temperatures. To relate these surface temperatures to the bulk temperatures, it can be assumed that, during the heating period, the uniform surface temperature, indicated by the solid line in figure 5.2, lags behind the bulk temperature, indicated by the broken line in Figure 5.2, by an amount δt_A. Then, at any given instant during this period

$$T_{A,S} = T_A - \frac{dT}{dt}A \cdot \delta t_A \qquad 5.2$$

for the absorber, and it may be assumed that a similar relationship exists for the jacket

$$T_{J.S} = T_J - \frac{dT}{dt}J \cdot \delta t_J \qquad 5.3$$

Furthermore, since heat is to be dissipated at a constant rate in both these elements during the calibration, it is reasonable to assume that, to a first approximation, the steady state, bulk heating rates of the absorber and jacket will be linear, and that

$$\frac{dT}{dt}A = \alpha \frac{dT}{dt}J \qquad 5.4$$

where α is a constant, which, for quasi-adiabatic conditions, must be close to unity. In the absence of all other influences, the true temperature rise due to the impressed electrical energy, is given by equation 5.5

$$\dot{\theta}_A = \frac{W_A}{m_A c_A} \qquad 5.5$$

Combining equations 5.1 to 5.5 yields

$$\frac{dT}{dt}A = \dot{\theta}_A - K_A (T_A - T_J) + K_A \frac{dT}{dt}A \, (\delta t_A - \alpha . \delta t_J) \qquad 5.6$$

which is a first order linear differential equation in T_A. Before solving this equation, T_J, which is a function of time, must be substituted. Assuming that $T_J = T_{J,i}$ at time $t = t_i$ and that, to a first approximation, $T_J = T_{J,i} + \dot{\theta}_J t$, since it has already been assumed that T_J is a linear function of time in the steady state, equation 5.5 becomes

$$\frac{dT}{dt}A = \dot{\theta}_A - K_A(T_A - T_{J,i}) + K_A \dot{\theta}_J t + K_A \frac{dT}{dt}A \, \delta t. \qquad 5.7$$

where the substitution $\delta t = (\delta t_A - \alpha \delta t_J)$ has been used. This equation may be solved using the conditions $T_A = T_{A,i}$ at $t = t_i$ (=O) and $T_A = T_{A,f}$ at $t = t_f$, where $t_f - t_i = \Delta t$, thus

$$T_{A,f} - T_{A,i} = \left[\frac{\dot{\theta}_A}{K_A} - \dot{\theta}_J \left(\frac{1 - K_A \delta t}{K_A} \right) - T_{A,i} + T_{J,i} \right] \left[1 - \exp\left(\frac{-K_A \Delta t}{1 - K_A \delta t} \right) \right] + \dot{\theta}_J \Delta t$$

Expanding the exponential term to the third order and using the approximation

$$(1 - K_A \delta t)^{-n} = 1 + n K_A \delta t + \frac{n(n + 1)}{2} K_A^2 \delta t^2$$

and the substitutions

$$\left(\frac{dT}{dt}A\right)_f = -K_A(T_{A,f} - T_{J,f}) \text{ and } \left(\frac{dT}{dt}A\right)_i = - K_A(T_{A,i} - T_{J,i})$$

derived from equation 2.2 yields

$$\dot{\theta}_A \Delta t = (T_{A,f} - T_{A,i})(1 - K_A \delta t + \frac{K_A^2}{2} \Delta t . \delta t) - \frac{\Delta t}{2} \left[(\frac{dT}{dt}A)_f + (\frac{dT}{dt}A)_i \right] + \ldots\ldots$$

$$\ldots\ldots + \frac{K_A^2}{6} \Delta t^2 \left[2(\frac{dT}{dt}A)_i + (\frac{dT}{dt}A)_f \right] \qquad 5.8$$

This equation relates the true, or ideal, temperature rise, $\dot{\theta}_A \Delta t$, during the interval Δt to the observed temperature change, $T_{A,f} - T_{A,i}$, and includes a number of additional factors to correct for the lack of ideal adiabatic conditions and the effect of temperature gradients.

To reduce this equation to more manageable proportions it is necessary to evaluate the magnitude of δt. This may be performed by solving the general equation for heat conduction in a solid, equation 5.9

$$\rho c \frac{\partial T}{\partial t} = \varkappa \nabla^2 T \qquad 5.9$$

For simple geometrical shapes and straightforward boundary conditions this equation can be solved by the separation of variables technique. The particular geometry and boundary conditions in the present case are not amenable to this technique, but, by assuming that within the cylindrical elements of the calorimeter the heat flows in a radial direction only and that the heater wire provides a uniform distribution of heat over the relevant boundary surface, the appropriate equation can be solved by transform methods. For the case of the hollow sleeve encasing the absorber core the problem reduces to an infinite hollow cylinder with a heater on the internal surface, radius a, such that $\varkappa (\frac{\partial T}{\partial r})_{r=a} = \mathcal{S}$, where $\mathcal{S}$ is the heat dissipation per unit area given by the equation

$$\frac{\beta W_A}{2\pi ah} = \mathcal{S}$$

(The factor β allows for the division of the energy supplied by the

heater between the two absorber elements.) The other boundary condition for this equation is $(\frac{\partial T}{\partial r})_{r=b} = 0$ and the initial condition is $T = T_{A,i}$ for $t = t_i (=0)$ and all values of r ($a \leq r \leq b$). The solution to this problem has been given by Luikov (1968) as

$$T(r,t) = T_{A,i} + \frac{\delta b}{\mathcal{K}} \left\{ \frac{b^2}{b^2-a^2} \left[\frac{2\mathcal{K}t}{b^2} - \frac{1}{4}(1-\frac{2r^2}{b^2}) - \frac{a^2}{b^2}(\ln\frac{r}{a} + \frac{b^2}{b^2-a^2}\ln\frac{a}{b} + \frac{3}{4}) \right] + \right.$$
$$\left. + \sum_{n=1}^{\infty} \frac{\pi}{\alpha_n b} \frac{J_1(\alpha_n a)J_1(\alpha_n b)}{J_1^2(\alpha_n a) - J_1^2(\alpha_n b)} \left[J_0(\alpha_n r)Y_1(\alpha_n a) - Y_0(\alpha_n r)J_1(\alpha_n a) \right] \times \right.$$
$$\left. \times \exp(-\alpha_n^2 \frac{\mathcal{K}t}{\rho c_A}) \right\} \qquad 5.10$$

where α_n is the n^{th} root of $J_1(\alpha a)Y_1(\alpha b) - J_1(\alpha b)Y_1(\alpha a) = 0$, J_0 and J_1 being Bessel functions of the first kind, order zero and one respectively, and Y_0 and Y_1 are Bessel functions of the second kind, again order zero and one respectively. Similar equations for the temperature distribution within a solid cylinder, with a heating element on the external surface, have been described by Dove and Cole (1962) and Kott (1967). The last term in equation 5.10 is a description of the transient temperature distribution after the initial application of electrical heat, and, whilst the time constant, τ_A, of this term is not equal to the value of δt_A referred to above, the size of τ_A does provide a good indication of the magnitude of δt_A. Evaluation of the first root, α_1, of the above equation (Abramowitz and Stegun, 1964) will give the largest value of the series of time constants, τ_A, and has a value of 0.1 s. A similar time constant will exist for τ_J, which gives, on substitution of the appropriate value of α_1, a value of $\delta t_J = 0.04$ s. Thus the magnitude of δt will be less than 0.1 s. Using this value of δt and $K_A \simeq 10^{-3}\ s^{-1}$ from Chapter 3 the first term in equation 5.10 may be simplified. Inspection of this term

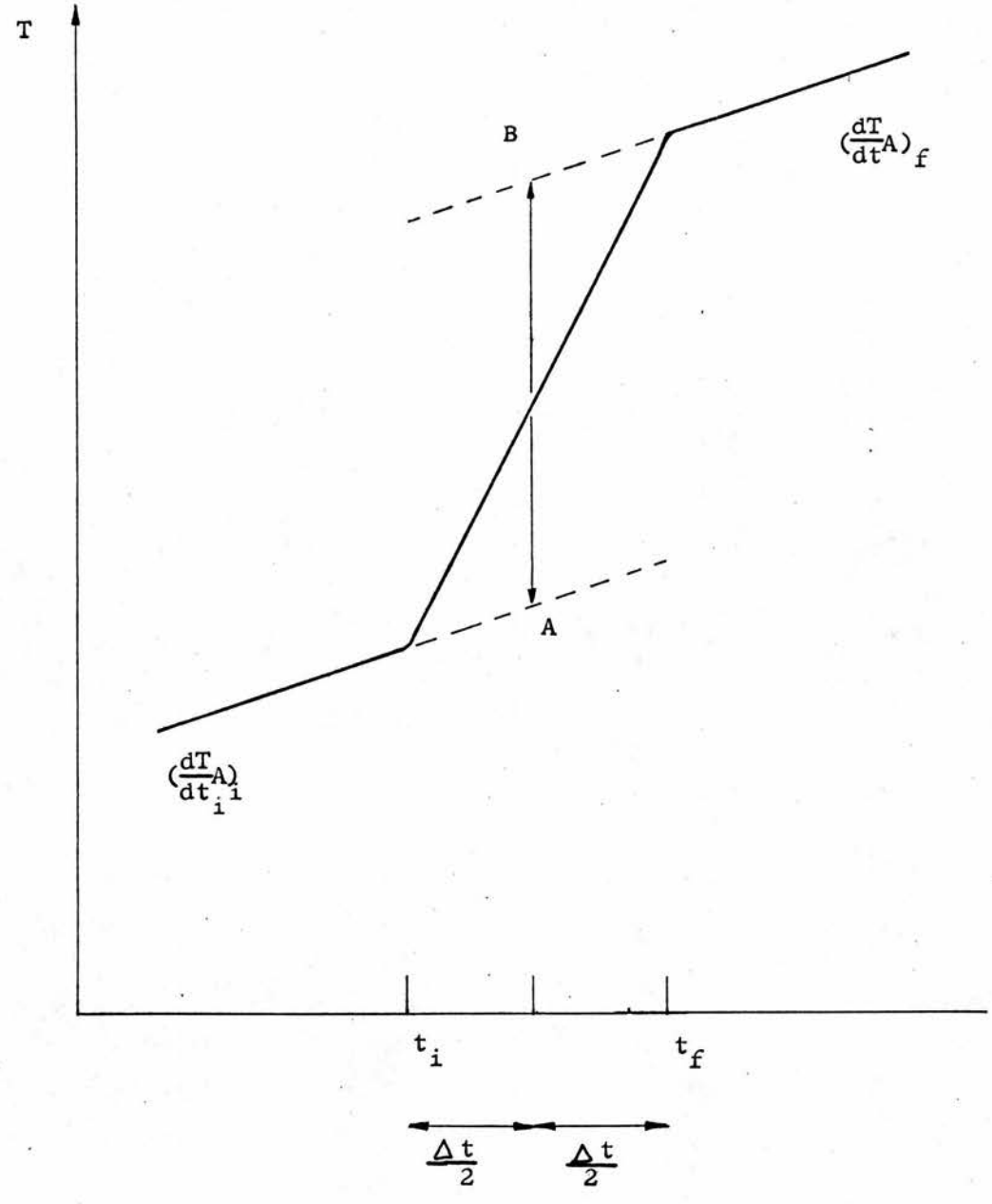

FIGURE 5.3 GRAPHICAL ANALYSIS

shows that, unless Δt is very large ($\Delta t > 10^4$), the factors $K_A \delta t$ and $\frac{1}{2} K_A^2 \Delta t \delta t$ are very much less than unity and, consequently, may be ignored.

The remaining two correction terms in equation 5.8 refer to the adjustments necessary to account for the non-zero temperature drift rates within the absorber. For the situation when the final and initial drift rates are approximately equal, it can be shown that the ratio of the second term to the third term on the right of equation 5.8 is $1 : \frac{1}{2} K_A \Delta t$. Therefore, since both terms are expected to be small correction factors applied to the observed temperature difference, the third term will be insignificant if $\frac{1}{2} K_A \Delta t \ll 1$. Equation 5.8 is then reduced to

$$\dot{\theta}_A \Delta t = T_{A,f} - T_{A,i} - \frac{\Delta t}{2} \left[\left(\frac{dT}{dt}A\right)_f + \left(\frac{dT}{dt}A\right)_i \right] \qquad 5.11$$

This expression states that the true, or ideal, temperature rise is the observed temperature change corrected by the mean drift rate during the heating period, Δt, the mean drift rate being assessed by an observation of the initial and final drift rates. This correction may be estimated graphically as shown in Figure 5.3, where the point A is equal to $T_{A,i} + \left(\frac{dT}{dt}\right)_i \cdot \frac{\Delta t}{2}$. Thus the vertical increment, B - A, at the time $t = t_i + \frac{\Delta t}{2}$ is then equal to the true temperature rise, $\dot{\theta}_A \Delta t$.

5.1.1 Calculation of Experimental Results

Before proceeding with an examination of the practical consequencies of the foregoing discussion, it will be necessary to discuss the corrections which must be applied to the experimental data produced by the temperature measuring system described in Chapter 4. It was stated in section 4.2 that the resistance-temperature relationship

of the thermistor was given by the equation

$$R_T = R_O \exp\left(\frac{B}{T} - \frac{B}{T_O}\right) \qquad 4.1$$

Differentiating this equation with respect to T and substituting the original expression yields

$$\frac{dR}{dT}T = -\frac{BR}{T^2}T \qquad 5.12$$

or

$$\Delta T = \Delta R_T \times \left(\frac{-T^2}{R_T B}\right) \qquad 5.13$$

Equation 5.13 relates the resistance change, ΔR_T, as indicated by the out-of-balance voltage produced on the chart recorder, to the change in temperature, ΔT. It will be observed that the temperature coefficient of resistance is a non-linear quantity dependent upon the variables R_T and T. Of these two parameters R_T is the most rapidly changing quantity and will have the more noticeable effect in the correct evaluation of ΔT from ΔR_T. To improve the statistical accuracy of the particular experimental situation being investigated, it was customary to perform a number of separate experimental determinations of the calorimeter response on each occasion. Since the value of R_T could change by as much as 20 Ω ($\simeq$ 1% of R_T) during the set of experimental "runs", it was necessary to normalise each experimental result by the relevant value of R_T pertaining at the time. The calorimeter response has therefore been expressed in terms of $\frac{\Delta R}{R_T}T$. The variation in the value of R_T from day to day could also be quite substantial (80 Ω). Thus, when comparing data obtained over a period of time with markedly different values of R_T, a correction for the temperature at the time of measurement was also necessary. To evaluate this factor the temperature, T, at the time

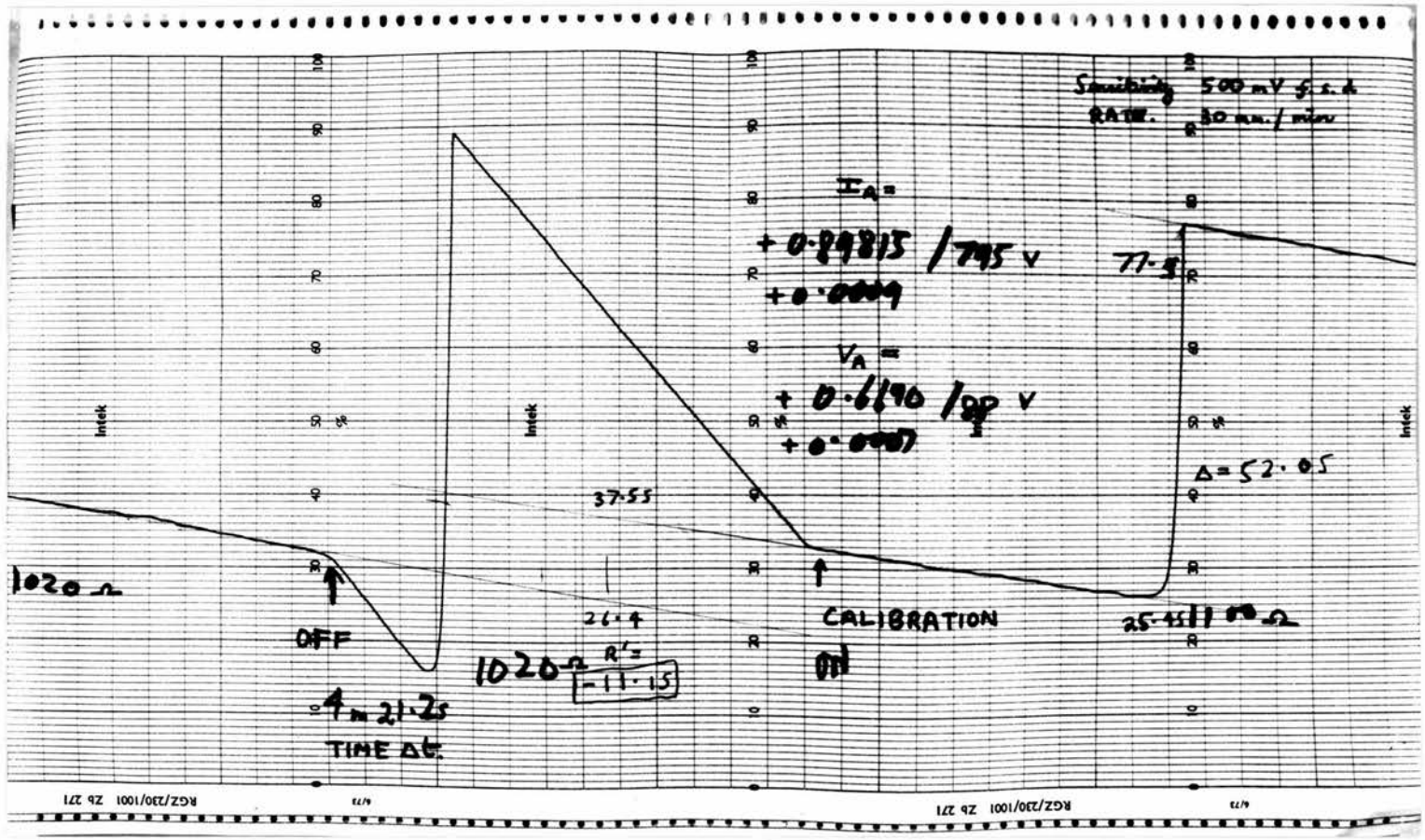

FIGURE 5.4 TEMPERATURE RECORDING, THERMISTOR A1

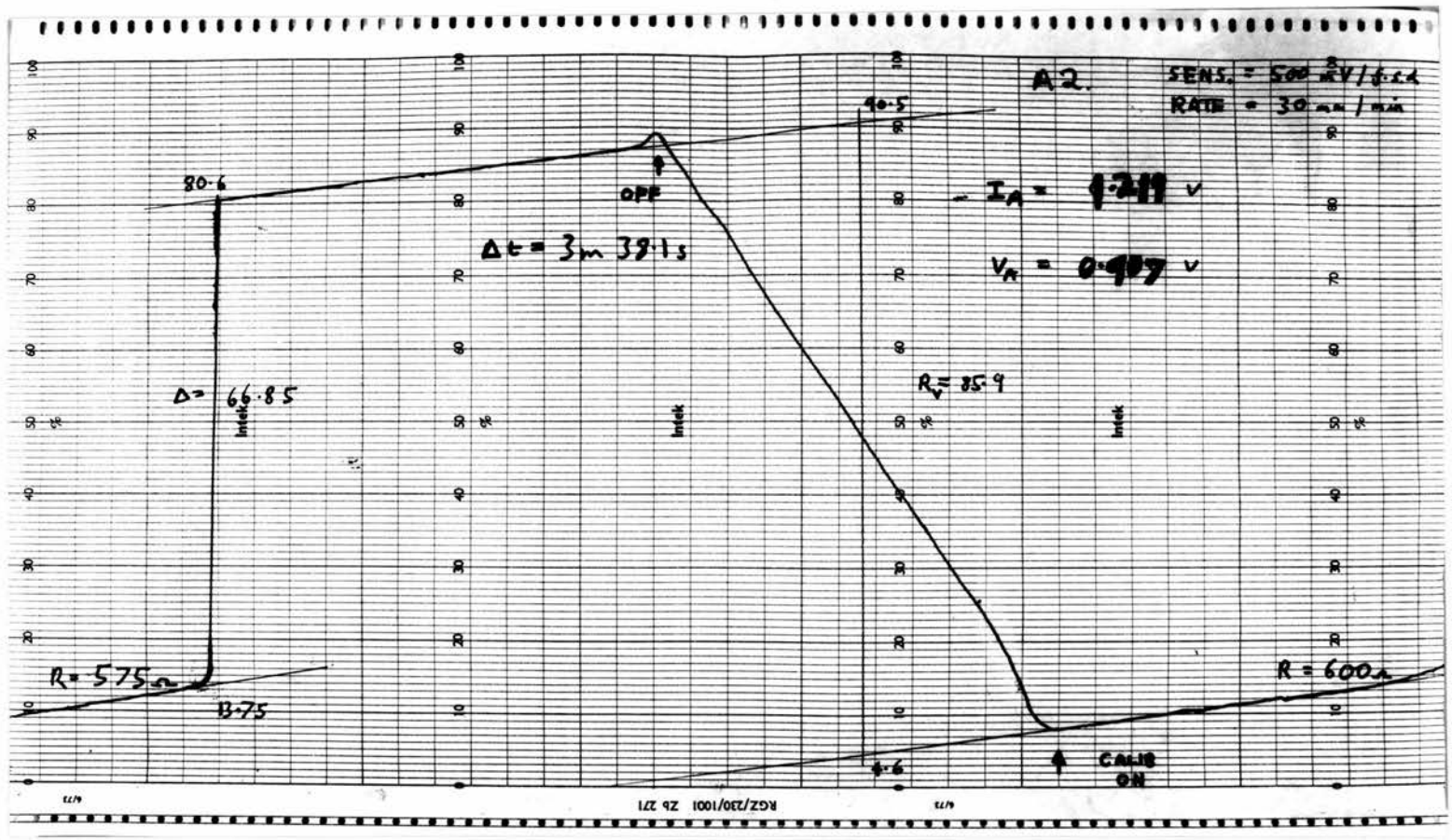

FIGURE 5.5 TEMPERATURE RECORDING, THERMISTOR A2

of measurement was found from the value of R_T and the quoted manufacturers data for the thermistor (i.e. R_T = 2KΩ and $\frac{dR}{dT}T$ = 4% K^{-1} at 293 K). The value of $\frac{\Delta R}{R_T}T$ was then corrected to a convenient reference temperature T_o by multiplying by $\frac{T^2}{T_o^2}$. No attempt was made to check the manufacturers specifications precisely, but, if the correction remains small (< 1%), no appreciable error is likely to ensue.

The actual evaluation of a calorimeter result may be described by reference to Figures 5.4 and 5.5, which illustrate two calibration runs. The sensitivity of the measuring system is found by changing the balance position of the bridge by an amount ΔR_{CALIB} and then measuring the resultant voltage swing ΔV_{CALIB}. The quotient of ΔV_{CALIB} by ΔR_{CALIB} then gives the required sensitivity or conversion factor. The total resistance change, ΔR, due to an external heat input, is calculated from the sum of ΔR_1 and ΔR_2, where ΔR_1 is the resistance change of the variable resistance arm, R_3, necessary to rebalance the bridge, and ΔR_2 is the residual change in resistance, calculated from the vertical displacement of the initial and final drift rates and the aforementioned conversion factor. Usually it was necessary to rebalance the bridge to retain the trace within the confines of the chart paper, but this practice did have two other advantages. Firstly, any miscalculation or systematic error in the conversion factor is reduced when it is applied to a small part of the total resistance change. Secondly, any serious discrepancy between the initial and final drift rates is immediately recognisable when the projections of these rates are situated beside each other.

A particular criticism of the graphical method of analysis is

the subjective assessment of the construction lines to be drawn through the actual experimental chart recordings. To estimate the possible size of the error in the voltage swing, measured from the separation of two of these lines, a given chart recording was photo-copied a number of times and the resultant identical traces were then analysed on a number of different occasions. A time interval of a few days was allowed between each analysis in the hope of avoiding any memory effects. The result of this exercise was that a given mean voltage swing of 68.6 divisions could be measured with a standard deviation of $\pm$ 0.2 divisions. This uncertainty may therefore be taken as the error in estimating any voltage change produced on the chart recorder.

5.2 EXPERIMENTAL VERIFICATION OF THE CALORIMETER OPERATION

The discussion of section 5.1 has shown that the straightforward application of equation 5.11 to the analysis of the calibration recordings is only permissible if the heating rate of the jacket closely follows that of the absorber (i.e. $\alpha \simeq 1$) and the period of electrical heating, Δt, is short. It has also been implicitly assumed that the response of the absorber to the input of electrical energy is independent of the position of temperature sampling. In order to ensure that the present calorimeter complied with these conditions, several tests were performed. The results of these tests will now be summarised.

5.2.1 Quasi-Adiabatic Conditions

It should be clearly emphasised that the condition $\alpha = 1$ does not imply ideal adiabatic conditions, since heat transfer between the absorber and jacket is not restricted by this identity. However,

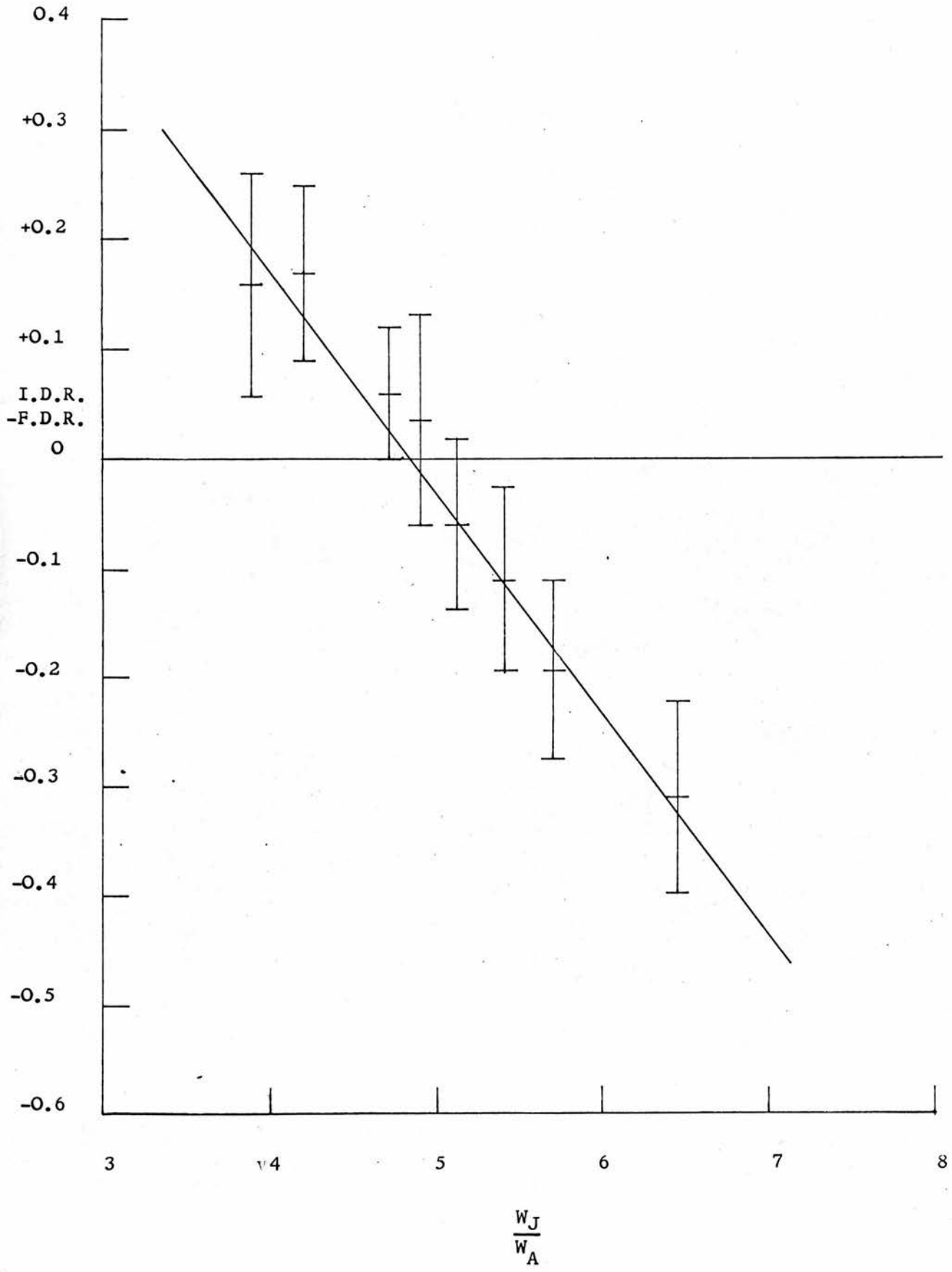

FIGURE 5.6 TEST OF QUASI-ADIABATIC CONDITIONS

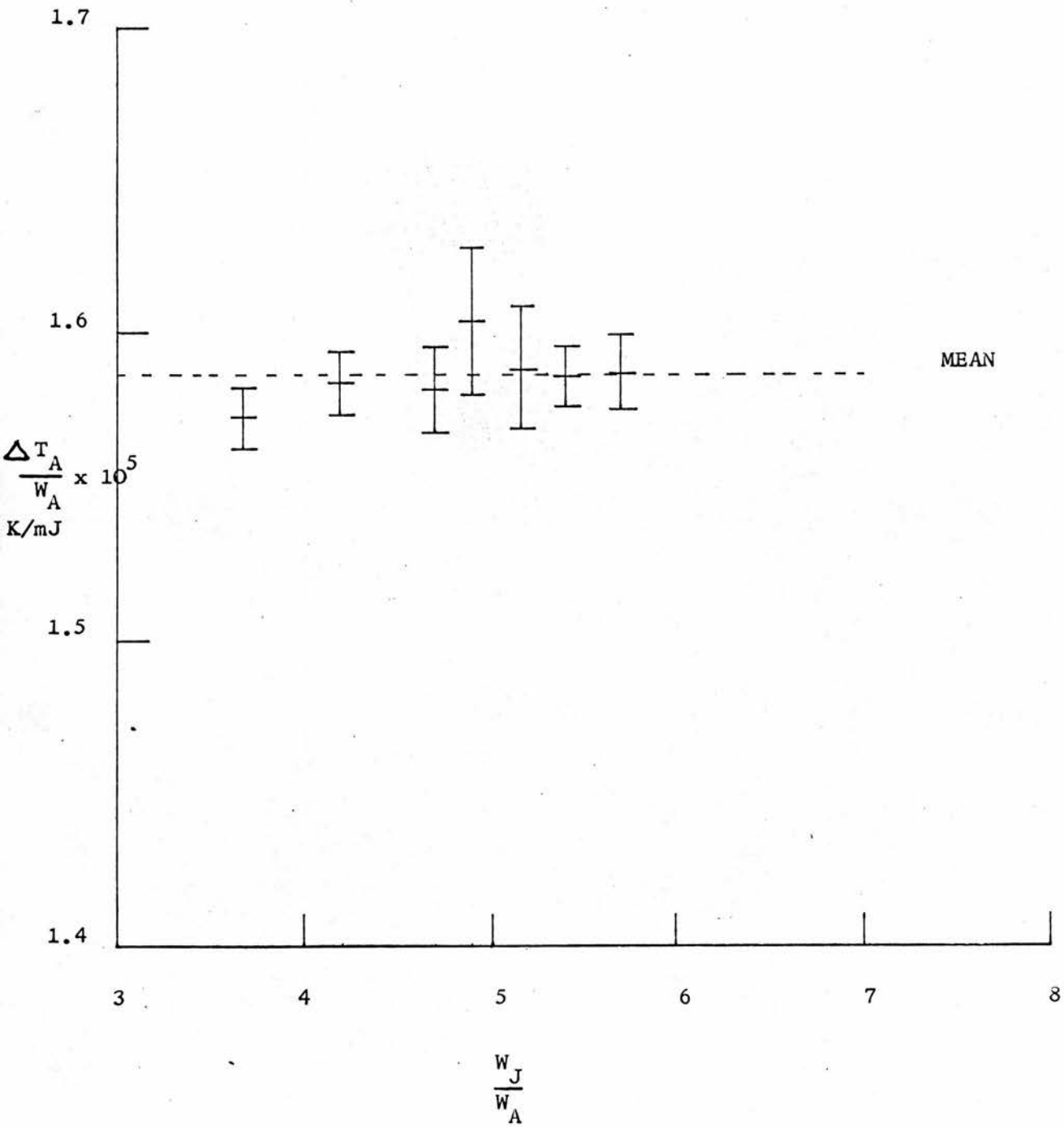

FIGURE 5.7 VARIATION OF RESPONSE FOR NON-QUASI ADIABATIC CONDITIONS

when α is unity the heating rate of the absorber and the jacket will be equal, and the quiescent heat flow before and after the calibration heating period should remain unaltered. The initial temperature drift rate, I.D.R., and the final temperature drift rate, F.D.R., will then be equal. To determine the correct value for the jacket power input, W_J, the quantity (I.D.R. - F.D.R.) was plotted as a function of the ratio $\frac{W}{W_A}J$. The results of the investigation have been depicted in Figure 5.6, which shows the linear relationship between this drift rate function and the power input ratio. A linear regression on the points plotted in Figure 5.6 gives a correlation coefficient of 98.9% and a value of $\frac{W}{W_A}J$ equal to 4.92 as the ratio for an undisturbed temperature drift rate. This value agrees quite well with the approximate theoretical value of 4.46, which was based upon the ratio of the thermal capacities of the jacket and the absorber. It is to be expected that the experimental value will be a little higher than the theoretical value since this later figure does not account for the energy which will be lost from the jacket to the mantle. In addition, the experimental value of W_J has not been corrected for the potential drop in the jacket-heater current leads, which could account for some 2 or 3% since, unlike the absorber heater, this heater was not equipped with potential leads. Although all the later experiments were performed with a ratio of the power inputs approximately equal to the experimentally determined value of 4.92, it is interesting to note that this condition is not very critical, as the graph of Figure 5.7 shows. It can be seen from this graph that, even if the input power ratio deviates from the ideal value by as much as 25%, the calorimeter response is not affected if the appropriate drift rate corrections are

FIGURE 5.8 VARIATION OF RESPONSE WITH LENGTH OF HEATING PERIOD, Δ T

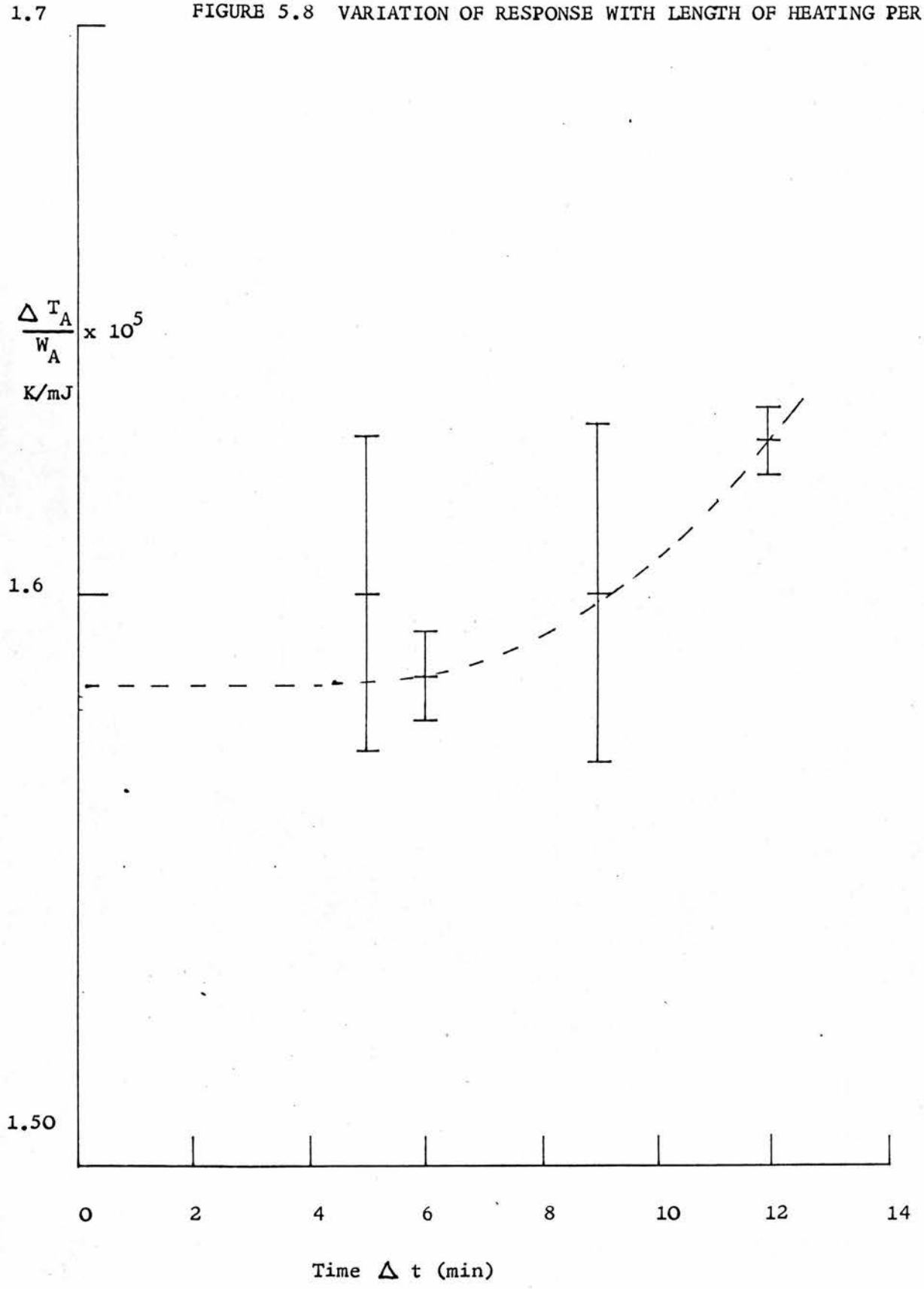

applied.

5.2.2 Length of the Calibration Heating Period

It was demonstrated in section 5.1 that the second drift rate correction term in equation 5.8

$$\frac{K_A \Delta t^2}{6} \times \left[2\left(\frac{dT}{dt}A\right)_i + \left(\frac{dT}{dt}A\right)_f \right]$$

could only be neglected if $\frac{1}{2}K_A \Delta t \ll 1$. It is to be expected therefore that a long calibration period will create a shift in the response of calorimeter. Figure 5.8 shows the calibration response, for the same total heat input, at a number of different heating intervals. The value of the response for the heating periods of 5 and 9 minutes shown on this graph both represent one set of results only, whereas the points plotted for the 6 and 12 minute heating periods are the mean responses of a number of sets of observations and therefore have correspondingly smaller uncertainties.

This graph must also be interpreted with some care, since the magnitude of this correction term is dependent on the size of the temperature drift rates as well as the value of Δt. Experimentally it was desirable to reduce these drift rates to a minimum, but, since these drifts are basically beyond experimental control, the results recorded in Figure 5.8 do not refer to a unique value of the drift rate. Therefore, the variation in response shown in the graph cannot be attributed solely to the effect of the different heating periods. Unfortunately, the data shown in Figure 5.8 are also insufficient to provide a rigorous analysis of the effect of the correction term quoted above, but it is expected that this term will be negligible for very short heating periods and will only become important when very

long heating periods are used. As an indication of the possible influence of this term a broken line has been drawn in Figure 5.8. It cannot be emphasised too strongly though, that without a greater degree of control over the drift rates and a decrease in the uncertainties, this line must remain rather tentative.

All subsequent experiments, both calibration and irradiation, were performed with heating periods of less than 4 minutes and no obvious variation with the length of heating period was observed with these periods. The possible error associated with neglecting the above term can therefore be assumed to be insignificant.

5.2.3 Point of Measurement

The temperature profile within the absorber during electrical heating is given by a combination of equation 5.10 and the relevant equation for the temperature distribution within the core of the absorber. Neglecting the transient term of equation 5.10, which has already been shown to be of short duration, the temperature profile of the absorber is of the form

$$T_A(r,t) = T_{A,i} + \frac{W_A}{m_A c_A} \cdot t + f(r,a,b.) \qquad 5.14$$

Comparing this equation with the temperature profile during irradiation heating

$$T_A = T_{A,i} + \frac{W_A'}{m_A c_A} \cdot t \qquad 5.15$$

it would appear that the position of the transducer is specified by the roots of the function f(r,a,b.). This condition is only important though, if the temperature is to be measured during the calibration heating period, such as the isothermal method of Dove and Cole. Since it has already been shown that only the final and initial temperatures

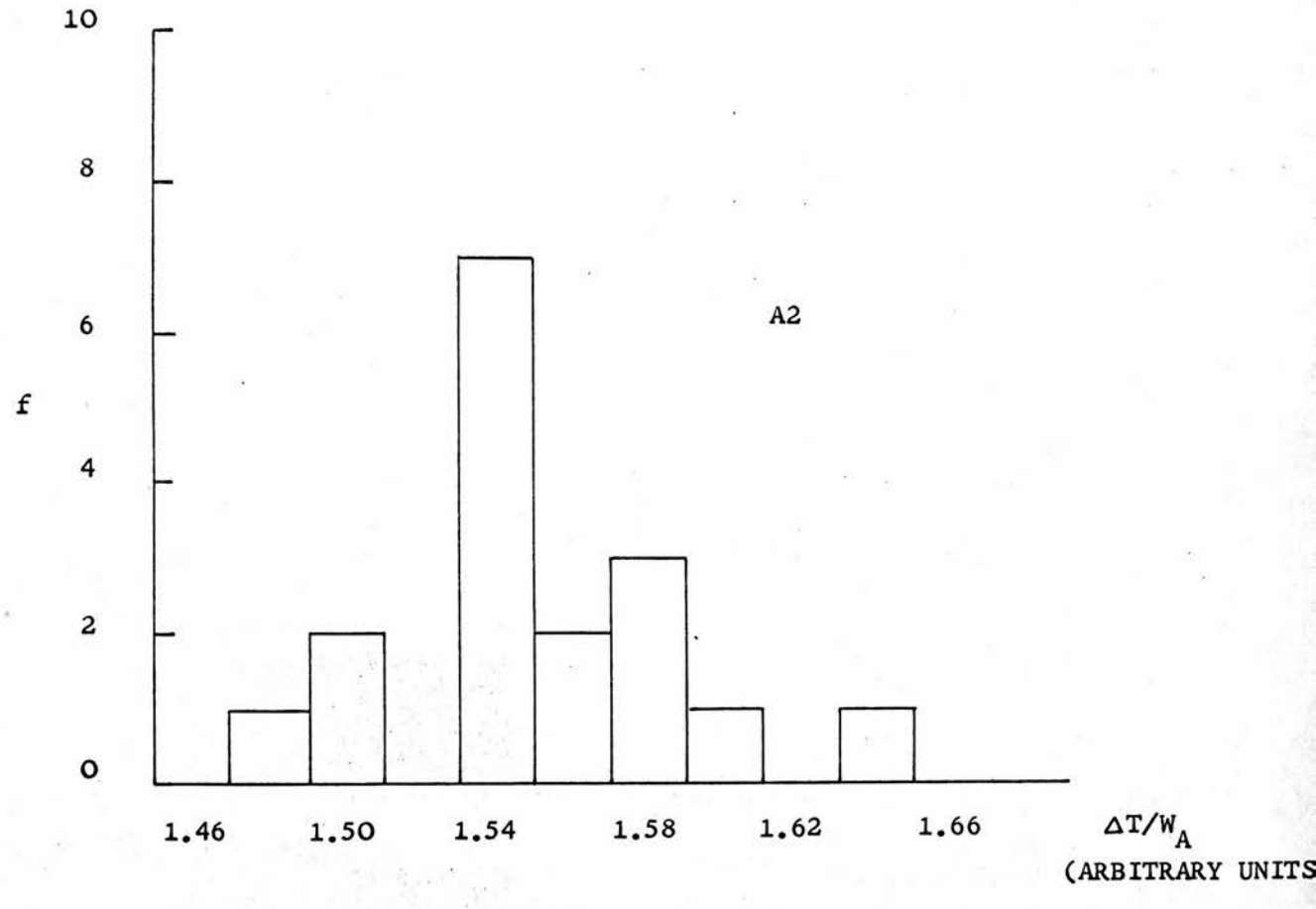

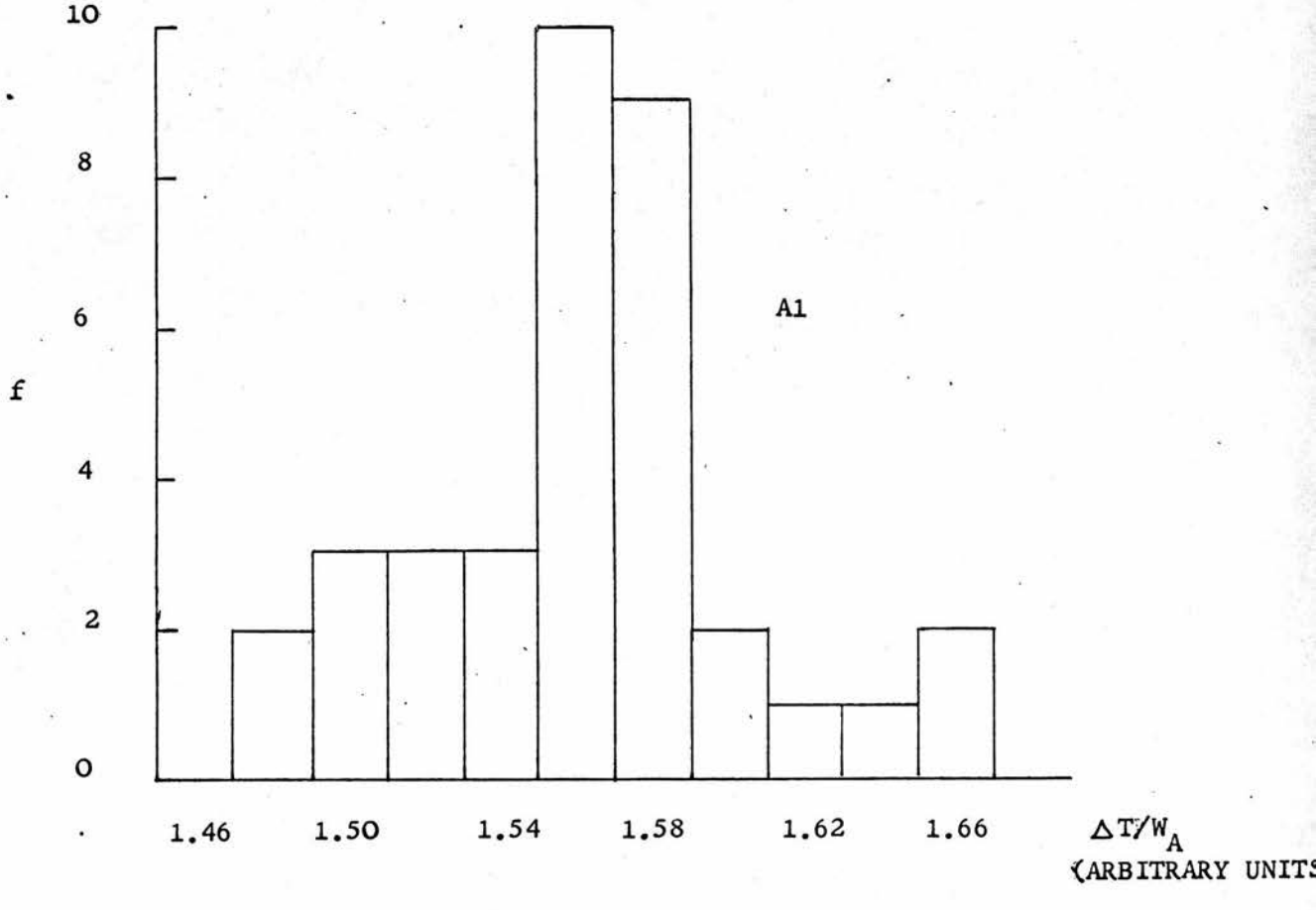

FIGURE 5.9 CALIBRATION RESPONSE OF THERMISTORS

and the relevant drift rates are involved in the calculation of the temperature rise, it is unnecessary to measure the temperature during the heating period. The thermistor position is therefore not specified by the roots of f(r,a,b.) (which is fortunate since the roots of f(r,a,b.) do not lie within the region $0 < r < b$).

It would be erroneous to assume though, that the response of the calorimeter is independent of the point of temperature measurement without experimental proof and, as the absorber was provided with two thermistors, it was possible to make a partial investigation of this problem. Reproductions of the calibration response for each thermistor, designated A1 and A2, are shown in Figures 5.4 and 5.5. It will be observed that the recording produced by thermistor A2 shows an initial sharp rise at the beginning of the heating period followed by an overshoot at the end of this period. The most probable explanation for this phenomenon was that the thermistor was placed too close to the heater wire and was thus directly influenced by this heating element. It is also interesting to note that, although the time constant of the output filter attached to the P.S.R. was 2.5 s, this overshoot effect was still observable. This would appear to indicate that the relaxation time of the temperature gradients within the absorber may be much larger than predicted in section 5.1. Nevertheless, since it is only the difference between the time lags in the jacket and the absorber which is important, and assuming that the jacket time constant is in error by a similar amount, the deductions of section 5.1 still remain valid.

The results of the calibration responses for the two thermistors are shown in Figure 5.9. The experiments summarised by these two

histograms were performed before various improvements in the measuring technique were evolved, and also at a time when the bridge lacked some of its later refinements. These two facts may help to explain the rather large spread of results. Nevertheless, well defined mean values are exhibited by both histograms, the values being $1.573 \pm 0.040 \times 10^{-5}$ units/mJ for thermistor A1 and $1.560 \pm 0.041 \times 10^{-5}$ units/mJ for A2. The uncertainties quoted with these results are the standard deviations of one result from the respective means. Thermistor A2 was situated in the upper cylindrical surface of the absorber whilst A1 was positioned on the plane end face of the absorber. These two positions will represent the extreme variation in response of the calorimeter and the true response may be taken as the mean of these two values (Engelke and Hohlefeld, 1971b). As the analysis of the temperature recordings was complicated by the overshoot artifact mentioned above, all later experiments were performed with thermistor A1. A correction of - 0.42% was therefore applied to the response given by this thermistor to allow for the temperature gradients and the point of measurement. As insufficient data is available from only two thermistors to estimate this correction with absolute certainty a systematic uncertainty of 0.42% has been attached to this correction factor.

5.2.4 Summary

It has been demonstrated that the data produced by a calibration heating experiment can be correctly interpreted by the use of equation 5.11 if the external heating period remains short and the jacket absorber power input ratio is 4.92, although this last condition is by no means critical. In addition, a correction of $- 0.42 \pm 0.42\%$

must be applied to the results provided by thermistor A1 to account for the slight variation in response with the point of temperature measurement.

This chapter has been almost entirely concerned with the performance of the calorimeter during calibration heating since this operation provides the most critical test of the calorimeter's ability. Similar attempts were made to check the calorimeter's performance during irradiation. Unfortunately though, due to the difficulty in estimating the precise quantity of radiation deposited in the calorimeter (the monitor unit problem discussed in Chapters 7 and 8) the tests comparing thermistors A1 and A2 were inconclusive. Also, the result of varying the accelerator dose rate was to completely swamp any effects dependent upon the time of irradiation. The only unambiguous result of these investigations, which did not depend on the accuracy of the monitor chamber, was that the difference between the initial and final drift rates was always negligibly small. A not unexpected result.

CHAPTER 6.

SECONDARY DOSIMETRIC SYSTEMS

6.1 INTRODUCTION

It was stated in Chapter 1 that the aim of this project was the experimental calibration of the more commonly encountered secondary dosimetric systems. The design and construction of the calorimeter, which formed the major part of this work, has already been described in the preceding chapters. It will be apparent from this description that, because of its construction, the calorimeter cannot be readily removed from its phantom and replaced by a secondary dosimetric system. Consequently, these systems must be irradiated in a separate phantom which reproduces, as far as possible, the geometry of the calorimeter. In the case of the commercial secondary dosimeters, such as the Farmer-Baldwin chamber or the ferrous sulphate cells, this simulation constraint provides the basic criterion for the design of the secondary phantom. The construction of these phantoms is therefore quite straightforward and will only be very briefly mentioned at the end of this chapter.

Apart from the aforementioned secondary dosimeters it was also decided to construct a small air ionization chamber for use within a carbon phantom. Provided that this chamber is sufficiently small, it will conform to the restrictions of the simple cavity theory discussed in Chapter 1 and the Bragg-Gray relation

$$D_C = D_{AIR} \cdot s_{C/AIR} \cdot p_{C/AIR} \qquad 6.1$$

can be applied. As the value of D_C, the absorbed dose in carbon, has already been measured calorimetrically, equation 6.1 can be

used to evaluate the mass stopping power ratio for carbon to air, $s_{C/AIR}$. This quantity cannot be regarded as a direct calibration factor for a routine secondary dosimeter since the complexity of construction and operation of such cavity chambers usually precludes their use in routine work. Nevertheless, this quantity is used in many of the theoretically determined conversion factors (e.g. C_E) for other secondary dosimeters and is therefore of considerable importance.

Since this carbon-walled ionization chamber had to be specially constructed in accordance with the geometrical design of the calorimeter, the bulk of this chapter has been devoted to a description of this instrument and its attendant circuitry.

6.2 DESIGN AND CONSTRUCTION OF THE CAVITY IONIZATION CHAMBER

The correct application of equation 6.1 requires that the dose measured by the calorimeter is equivalent to the dose measured by the ionization chamber. Therefore, the effective point of measurement for each instrument must be the same, and, in addition, the radiation spectrum, both in energy and spatial distribution, at this point must also be the same. Obviously the difference in the composition of the probe material and the contrasting methods of conveying the signal away from the sensitive region will create some dissimilarity in the geometries of the two systems. Nevertheless, to attach any degree of confidence to these measurements, these differences must be minimal.

Chronologically the calorimeter was built first; thus, the ionization chamber design had to be modelled on this geometry. Since the shape of the absorber was that of a short cylindrical rod, the

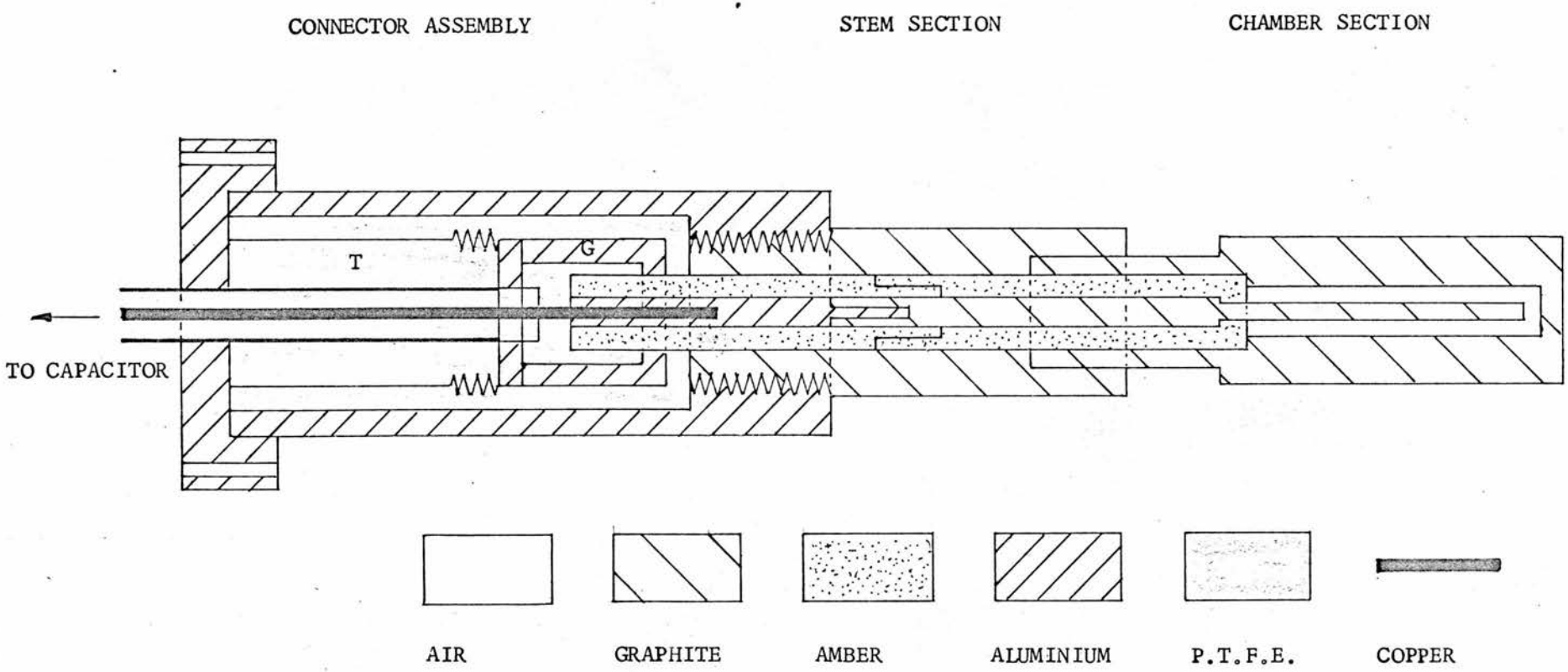

FIGURE 6.1 SECTION THROUGH CARBON-WALLED IONIZATION CHAMBER

most convenient chamber geometry was also that of a short cylinder, with an axial collecting electrode, mounted at the end of a cylindrical stem. This stem could be used to locate the chamber in the main block of graphite which formed the phantom or extended irradiated medium (i.e. a design almost identical to a Farmer-Baldwin chamber). The precise details of this chamber design can most easily be explained by reference to Figures 6.1 and 6.2, which show a section through the assembled chamber and a photograph of the component parts respectively.

Two of the most important considerations when designing an ionization chamber are the production of a uniform electric field within the collecting volume and the elimination of charge leakage across the insulators. Taking the former of these two factors first, it can be seen from Figure 6.1 that the only regions where a non-uniform field might occur are the corners of the cylindrical chamber and the tip of the collecting electrode. Originally, it was felt that the tip of this electrode should be hemispherical, thereby reducing the possibility of the high field gradients which could be created at the corners of a plane end. Also, to remove the weak field region at the internal corners of the chamber, it was proposed to construct the end of the outer electrode as a plug, such that the corners could be shaped or contoured to increase the field strength. Practically it was very difficult to machine the long, thin central electrode, and it would have been almost impossible to construct a true hemispherical end with any precision. Also, unless the end plug was a very close fit, a greater uncertainty in the actual air volume could have been produced than the uncertainty which it was

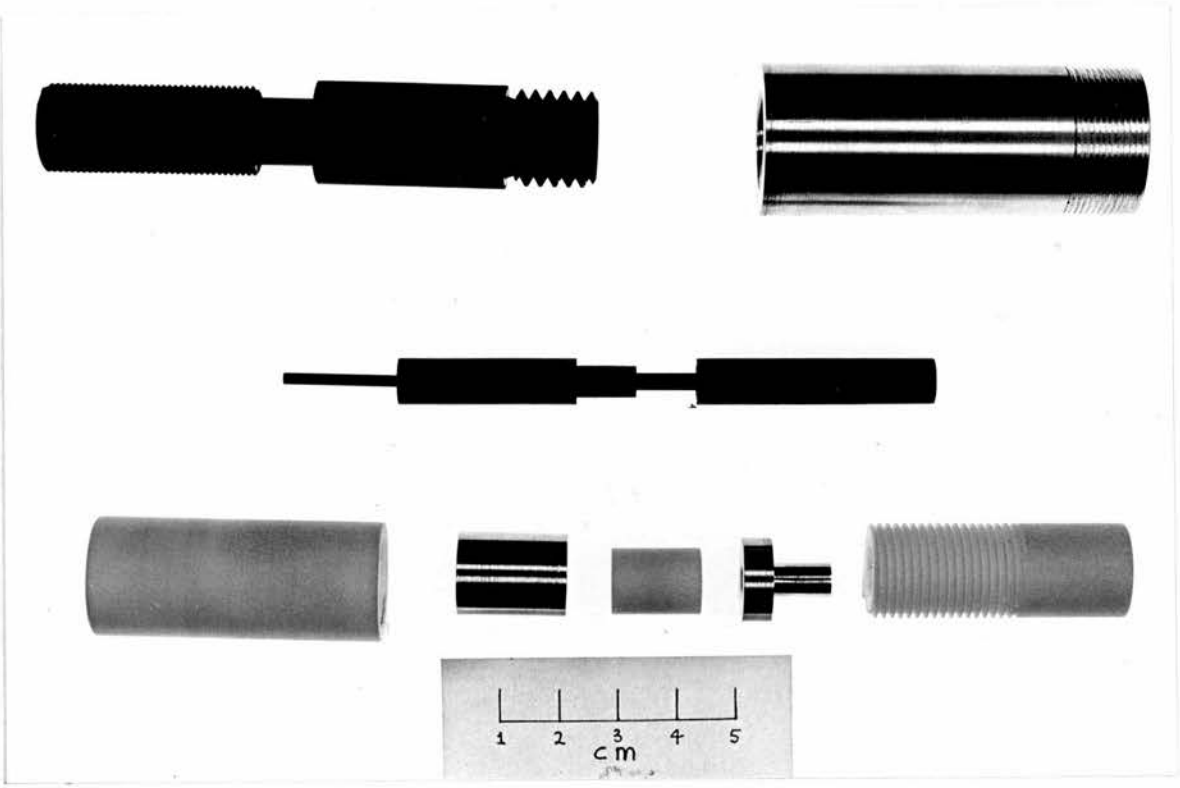

FIGURE 6.2 IONIZATION CHAMBER COMPONENTS

hoped to remove. Ultimately though, the main reason for rejecting these modifications was one of mensuration. The usual method of measuring the volume of small chambers is to weigh the chamber empty and then full of mercury, the volume can then be calculated from these weighings and the tabulated density of mercury. However, since graphite is slightly porous, the possibility exists that some of the mercury could be absorbed onto the inner walls of the ionization chamber and this layer of impurity could severely distort the desired secondary electron equilibrium at the carbon-air interface (I.C.R.U., 1972). Therefore, the volume of the chamber had to be determined by a direct observation of its dimensions and its geometrical shape. Consequently, any irregularities in the geometry would introduce a large uncertainty into these measurements.

Returning to the problem of charge leakage, inspection of the bulk resistivitues of the more common insulating materials indicates that, in the unirradiated state, almost all would be suitable. In ionization chambers of this design though, it is virtually impossible to avoid exposing part of the insulator to the radiation beam. Therefore, the insulator must retain a high resistance during irradiation. Although polymers such as P.T.F.E. and P.T.C.F.E. are now thought to be suitable insulators under these conditions (Farmer and Aird, 1972), the more proven material of amber was used in this instance. An alternative type of design, which obviates the need for a high grade insulator, is the use of a guard electrode to surround the irradiated portion of the stem containing the collecting electrode. This guard electrode is maintained at the same potential as the collecting electrode, and will intercept any charge flowing

from the high tension (H.T.) electrode to the collector. The major difficulty with this system is the point of termination of the guard electrode. If it does not extend to the stem-chamber interface, then a small portion of the insulator will still form a direct path between the H.T. and collecting electrodes. Alternatively, if the guard electrode terminates at the stem-chamber interface, part of the geometric volume of chamber may be excluded from the collecting volume. It was therefore felt that the inclusion of this component would add an unnecessary constructional complication without improving the performance of the chamber. Nevertheless, an earthed screen, running from the instrumentation screen to the connecting region of the stem, was included.

Returning to Figure 6.1 it is now possible to discuss the construction of the chamber in more detail. The outer, or H.T., electrode was fabricated from graphite and constructed in two separate sections. These two sections were joined on a push-fit principle, the precision and reproducibility of this fit being tested by direct measurements and a series of X-ray photographs. This procedure indicated a satisfactory and reproducible fit. The collecting electrode was made from graphite and the dimensions of the actual portion protruding into the chamber were 29 mm long by 2 mm diameter, the chamber dimensions being 31 mm by 5 mm diameter. This central electrode was expanded to a diameter of 3 mm inside the hollow, cylindrical, amber insulator. Unfortunately, the two billets of amber (for which I am indebted to Dr. L. A. W. E. Kemp of the N.P.L.) were not large enough to construct the insulator in one continuous unit. This component therefore had to be joined as shown in Figure 6.1. The 'stepping' in this joint increased the

length of surface path between the H.T. and collecting electrodes, thus reducing any surface conduction. A small aluminium tongue was inserted into the space in the amber insulator just behind the carbon electrode. This component served as a link between the copper wire protruding from the connecting cable and the carbon electrode. The function of this tongue was to reduce the wear on the soft graphite electrode produced by the chafing of the copper wire, which would have resulted in a loose contact. The connecting assembly, shown on the left of Figure 6.1, consisted of a series of interlocking aluminium and P.T.F.E. components. This connector assembly was designed so that any charge, leaking from the H.T. electrode to the collecting electrode, would be intercepted by the guard screen, G. The whole assembly was locked together by the threaded tube, T, which ensured that the shoulder of the carbon central electrode was pressed tightly against the end face of the amber insulator. Finally, the outer carbon electrode was screwed into the outer aluminium shield, which also provided the connection to the H.T. supply, ensuring that the end face of the amber insulator was pressed home against the stem-chamber shoulder.

To locate the ionization chamber at a depth in the carbon medium similar to that of the calorimeter absorber a graphite block was machined to the same dimensions as the calorimeter block. A circular hole was cut in the upper surface of this block to accommodate a cradle identical to the one used to locate the calorimeter mantle assembly. A hollow cylinder, of dimensions identical to that of the calorimeter mantle, was located inside this cradle by a series of pins using a similar principle to the one described in Chapter 3 for locating the calorimeter mantle aasembly within its cradle. To

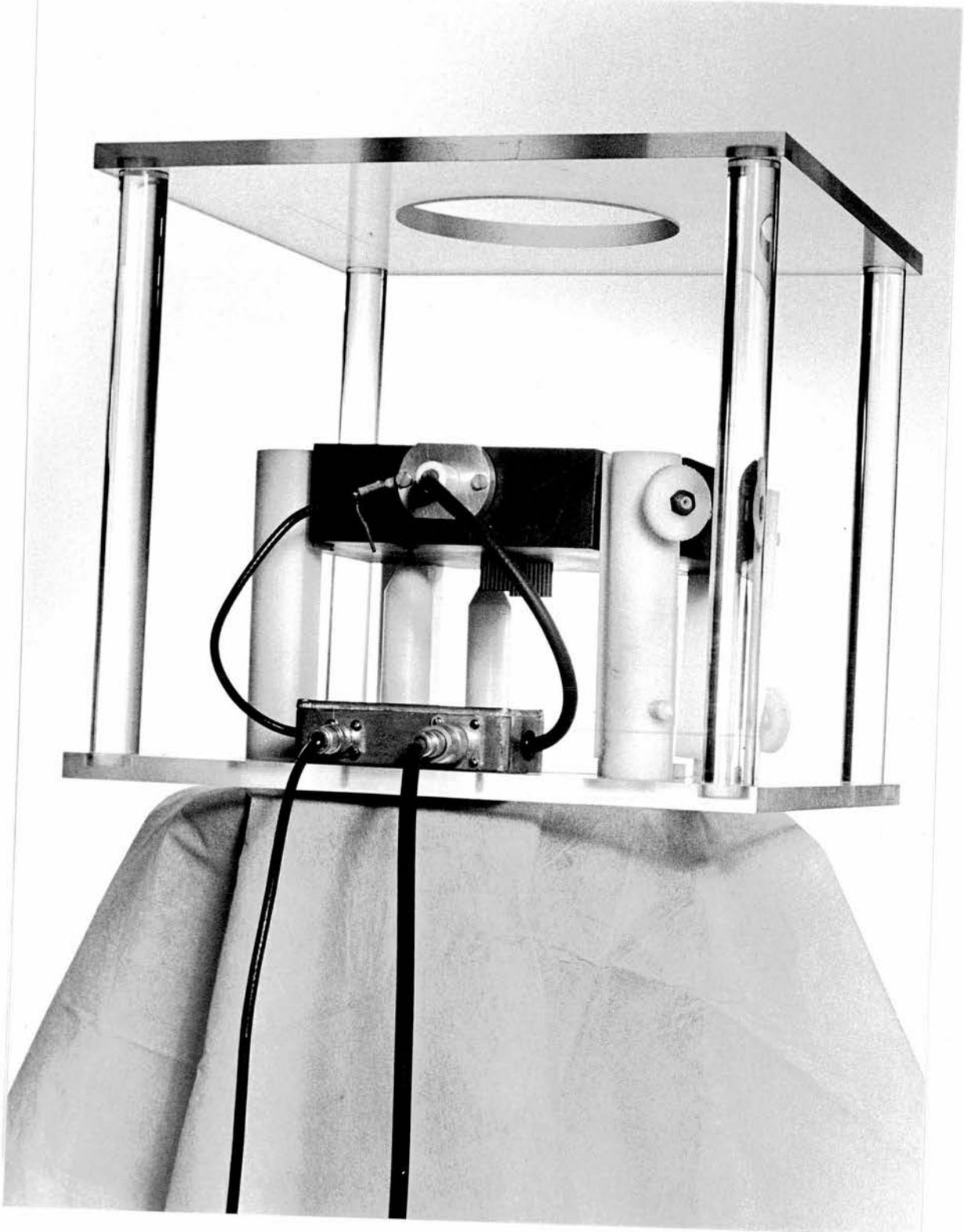

FIGURE 6.3 IONIZATION CHAMBER PHANTOM LOCATED IN PERSPEX IRRADIATION JIG

complete the simulation of the mantle geometry, two printed circuit boards were attached to the protruding ends of these pins. The only departure from the calorimeter geometry was that the simulated mantle had only one closed end, and one of the printed circuit boards had a hole cut in its centre to allow for the insertion of the ionization chamber.

Unfortunately, because of the difference in design between the ionization chamber and the calorimeter absorber, this was the limit of the exact phantom simulation. In an attempt to recreate the jacket geometry though, a thread was cut on the outer surface of the H.T. electrode and a 2 mm thick sleeve was then placed over this surface. To locate the ionization chamber and its attached stem in the phantom block, a hole was cut in one of the sides of this block such that the axis of this hole coincided with the simulated mantle axis. A perspex sheath was used to line this hole so that the potential applied to the outer electrode did not make the whole phantom 'live'. With the exception of the chamber stem and the differing geometries of the sensitive elements, these two phantoms were as closely matched as possible. The major part of the stem, containing the aluminium and P.T.F.E. sections, was outwith the irradiation field and therefore did not influence the radiation spectrum at the point of measurement. The exact definition of this point of measurement and its evaluation are discussed in Chapter 8, as are the slight differences in phantom geometry. A view of the assembled ionization chamber, located in its phantom and positioned on its perspex irradiation jig, is shown in Figure 6.3.

6.2.1 Measurement of Chamber Volume

As noted above, the measurement of the chamber volume was made

by the direct observation of the dimensions of the relevant components. Although this measurement was relatively straightforward, the technique used and the uncertainties involved are worthy of a brief mention.

The length and diameter of the central electrode were measured by a travelling microscope, using an illuminated white perspex sheet as the background to improve the definition of the electrode edges. The measurement of the hollow chamber presented rather greater difficulties, since it was impossible to illuminate the chamber and focus the microscope on the chamber walls at the same time. Therefore, the actual length of the chamber was found from a series of dial guage measurements made upon the chamber section of the outer electrode. Basically, these observations consisted of measuring the total length of this electrode section and then subtracting the thickness of the end face of the chamber together with the length of the entrance bore which accommodated the amber insulator. The determination of the chamber diameter was more indirect, since it was impossible to apply internal calipers to this recessed volume. To circumvent this problem, several small cylinders were constructed. The smallest of these cylinders was arranged to have a diameter rather less than the internal diameter of the chamber. Each successive cylinder in the series was then machined to have an increase in diameter of 1.27×10^{-3} cm ($\frac{1}{2}$ "thou") over the preceding one. From this series of cylinders it was possible, not only to measure the diameter of the chamber, but the slight taper in this diameter could also be investigated. This was found to be equal to a decrease of 2.54×10^{-3} cm over the length of the chamber. As a result of this taper, and the indirect method of measurement, a systematic uncertainty of 2.52×10^{-3} cm was included in the diameter of this element. The total effective

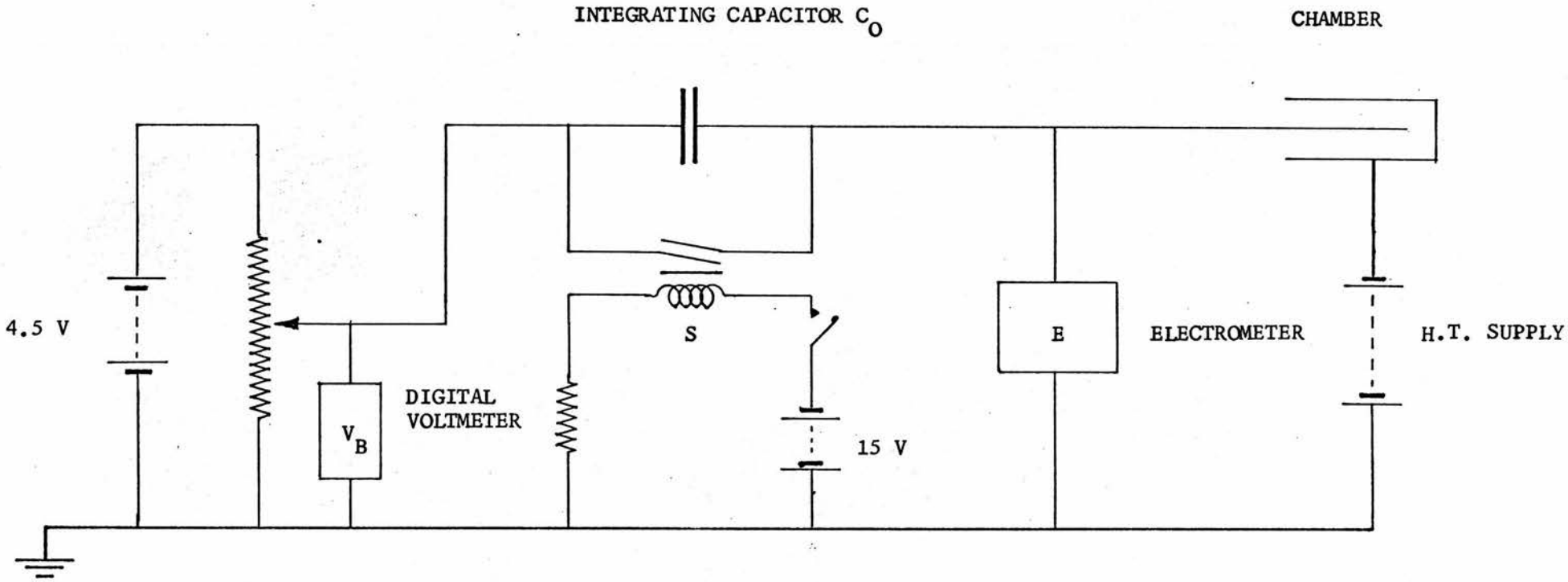

FIGURE 6.4 TOWNSEND BALANCE CIRCUIT

volume of the chamber, found from a subtraction of the central electrode volume from the chamber volume, was 0.5177 cm^3 with a standard error of the mean of $\pm$ 0.0016 cm^3 and 9 effective degrees of freedom. Unfortunately the fragile central electrode was broken after the series of X-ray measurements and had to be replaced. This gave the effective volume of the 'second' chamber as 0.5204 $\pm$ 0.0021 (SEOM) with 8 degrees of freedom.

6.2.2 Measurement of Charge

All ionization chambers, especially those with small collecting volumes, produce rather small amounts of charge which are consequently rather difficult to measure accurately. The circuit used to measure the charge collected by the central electrode is shown in Figure 6.4. This circuit is the well known Townsend Balance which has the advantage of employing a very high impedance electrometer as the null indicator. The cycle of operation of this balance starts by closing the switch, S, and adjusting the backing-off voltage, V_B, to indicate a null on the electrometer, E. The switch, S, is then opened and the current from the chamber proceeds to charge the capacitor, C_O. As the voltage across this capacitor increases, the backing-off voltage is adjusted to keep the electrometer balanced. Thus, when the ionization current ceases, the voltage across the capacitor is just equal to V_B, which is indicated by the digital voltmeter. Although the operation of this circuit is basically quite simple the correct choice of the circuit components is very important.

An approximate calculation shows that a total charge of about 75 nanocoulombs could be expected from an absorbed dose of 500 rads deposited in the air volume. This very small charge could be converted into any desired voltage by using an appropriate value of

the integrating capacitor and, from the aspect of voltage measurement, the larger the voltage the better. Therefore, a very small capacitor would be required. However, two factors set a lower limit to the size of this component. In the first instance the capacitor should be large enough to reduce any slight variations in stray (cable) capacitance to negligible proportions. Secondly, if capacitor voltages of the same order of magnitude as the polarising voltage are produced, the collection efficiency of the chamber might not remain constant throughout a given measurement. The digital voltmeter used to measure the back-off voltage had a range of $\pm$ 3.9999 V. Thus, a value of C_o in the region of 50000 pF would produce a capacitor voltage of 1.5 V, which could be accurately measured by this digital voltmeter. Also, this value of capacitor voltage allows the back-off voltage to be derived from three 1.5 V "Mallory" cells and a standard potential divider box.

The choice of capacitor dielectric is also very important, since internal charge leakage and dielectric absorption must be avoided. This latter effect will be discussed further in Appendix 2 which describes a method for the absolute d.c. measurement of capacitance. Considering the phenomenon of dielectic leakage, a short calculation shows that a charge loss of 0.2%/s would be obtained at a capacitor voltage of 1.5 V and an insulation resistance of $10^{10}\Omega$. Such a leakage rate would create great difficulties in the accurate measurement of the capacitor voltage. Therefore, a capacitor with a minimum insulation resistance of $10^{12}\Omega$ was used. This capacitor had a polystyrene dielectric and a nominal value of 46000 pF yielding a precise d.c. capacitance of 46840 $\pm$ 20 pF.

The comments regarding charge leakage also apply to the switch,

S, which is in parallel with the capacitor, C_o. Also, this switch should generate a negligible amount of charge when opened at the beginning of each measurement. To fulfil this condition a coil-operated reed relay, with an insulation resistance of greater than $10^{15}\Omega$ and charge generation of less than 10^{-14} C, was used. (Values: Kemp and Woodall, 1965). To reduce surface conduction this reed switch was mounted inside a P.T.F.E. sleeve placed inside the coil former. The current supply to operate this coil was derived from a 15 V transistor power supply and this circuit could be interrupted by a manual toggle switch.

The integrating capacitor, C_o, together with the switch, S, and the measuring circuit described in Appendix 2 were all placed in a screened aluminium box, and C_o was connected to the chamber by a screened co-axial cable. A separate cable was used to convey the H.T. voltage to the outer electrode, as shown in Figure 6.3.

6.3 FARMER-BALDWIN CHAMBER

The size and geometry of this instrument was very similar to that of the carbon-walled ionization chamber described in the preceding section. Therefore, the same graphite block, cradle and mantle components could be used as the basis of the Farmer-Baldwin phantom. To locate the Farmer-Baldwin chamber within this block, a graphite sheath was used to reduce the dimensions of the carbon ionization chamber hole in the side of the block to the size of the Farmer-Baldwin probe. The end of this sheath, which surrounded the active volume of the Farmer-Baldwin probe, was again threaded and covered with a thin graphite sleeve to reproduce the jacket geometry. A cross-section of this geometry is shown in Figure 8.1c, where the

precise depth of measurement and the difference between this phantom geometry and that of the calorimeter is also discussed.

The circuitry for measuring the charge produced by the Farmer-Baldwin chamber was the standard Townsend Balance type supplied with the instrument and requires no further description.

6.4 FERROUS SULPHATE CELLS

The previous two secondary dosimetric systems attempted, as far as possible, to reproduce the calorimeter geometry. The situation with the ferrous sulphate cells was rather different. Initially, it had been hoped to construct small tubular irradiation vessels to simulate the dimensions of the absorber. Unfortunately, the volume of dosimeter solution which would have been contained by these vessels would have been insufficient to fill the spectrophotometer cells, which were necessary in the measurement of the ferric ion concentration. Although larger tubular vessels could have been constructed, thereby retaining the rod-shaped geometry, it was decided to employ the readily available flat, disc-shaped, polythene irradiation vessels. Accordingly, the mantle and cradle components were removed from the central hole in the graphite block and replaced by three flat graphite discs. These discs positioned the ferrous sulphate irradiation cells at the required depth below the phantom surface and simulated the effective number of layers of graphite and air present in the calorimeter geometry. A cross-section of this phantom is shown in Figure 8.1d which also indicates the effective depth of measurement for this dosimeter. The method of determining the absorbed dose received by the ferrous sulphate solution is also discussed in Chapter 8 together with the results of this investigation.

CHAPTER 7.

X - R A Y M E A S U R E M E N T S

7.1 INTRODUCTION

It was noted in Chapter 2 that, whilst a number of calorimetric determinations of the product $\bar{W}\, s_{C/AIR}$ have been made at ^{60}Co energies, the only extensive set of experimental measurements of this quantity for artificially produced high energy photon beams was the work of Bewley (1963). Although his results were in reasonable agreement with the theoretical values published by the I.C.R.U. (1969), very little evidence has been forthcoming to verify these experimental results. Therefore, although the calorimeter and carbon-walled ionization chambers were primarily designed for use with electron beams, it was felt that a useful preliminary exercise would be the evaluation of $\bar{W}\, s_{C/AIR}$ for a 4 MV X-ray beam. The experimental measurements and the calculations necessary to derive this quantity are presented in this chapter.

7.2 THE MONITOR UNIT PROBLEM

In the calibration of the ionometric and chemical dosimeters it is of critical importance to expose all the dosimetric systems to the same radiation flux. Chapter 6 described the design and construction of the secondary dosimeter phantoms where particular attention was devoted to the exact reproduction of the calorimeter geometry. The extent to which this objective was achieved in practice will be discussed in Chapter 8. However, even if the phantoms are identical, it will be impossible to irradiate, simultaneously, any two dosimeters in the same beam. Consequently, no two dosimeters can receive exactly the same flux of radiations. Therefore, the

alternative procedure of consecutive irradiations of each dosimeter must be employed. When utilising this method it is obviously important to ensure that each dosimeter receives an equal, or precisely known, quantity of radiation energy during each experiment.

Most clinical linear accelerators measure the quantity of radiation emanating from the machine by inserting a small transmission ionization chamber near the source of the beam. In this position the chamber will intercept the complete cross-section of the beam and will produce a signal proportional to the integration of the energy fluence over the total beam cross-section. This signal is normally displayed on the control panel of the machine. The dose delivered in any given situation is then found from the reading of this panel meter and the appropriate conversion factor. As this method forms the basis for the clinical estimation of the absorbed dose, it appeared reasonable to use the transmission ionization chamber to quantify the output of the accelerator. Thus, the irradiation response of the calorimeter was normalised by the relevant reading of the panel-unit meter.

The results of the initial series of X-ray measurements have been displayed in Figure 7.2, which shows the frequency distribution of the calibration and irradiation responses. Inspection of these diagrams shows that, whilst the histogram of the calibration response approximates to the expected normal experimental distribution and has a well defined mean, the irradiation response is widely distributed and does not exhibit an obvious peak value. Since the mode of operation of the calorimeter and the method of calculating the results were the same, irrespective of the source of energy, some untoward variation must have been occurring in the X-ray beam. To investigage

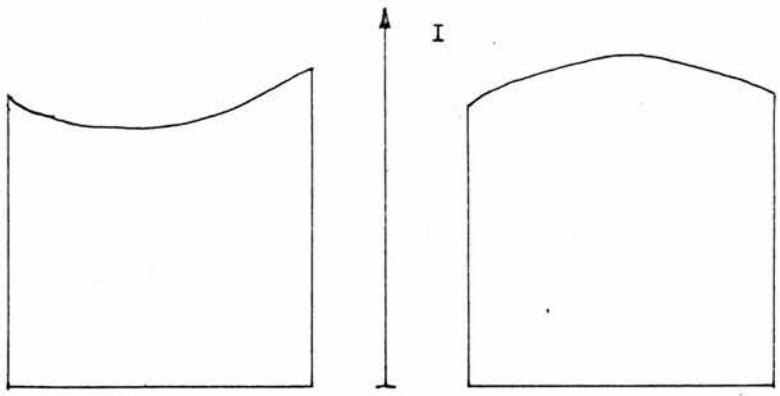

BEAM PROFILE AT TRANSMISSION CHAMBER

TOTAL AREA UNDER CURVE = A A

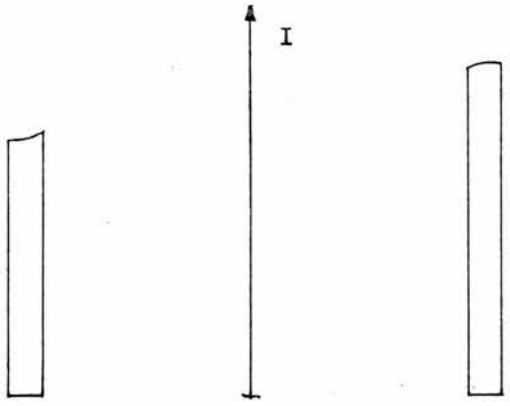

BEAM PROFILE

TOTAL AREA UNDER CURVE SAMPLED BY AREA α a b

$a \neq b$

FIGURE 7.1 THE MONITOR UNIT PROBLEM

this effect an Ionex chamber was positioned, together with its 8 mm thick build-up cap, at a point in the beam similar to the position which would have been occupied by the calorimeter absorber. Measurements with this chamber indicated that, for a fixed value of the panel-unit reading, P, the dose received by the Ionex chamber could change by as much as 8%. It was also observed that an increased Ionex reading was associated with a fall in the output dose-rate of the accelerator. Although recombination effects in the transmission-ionization chamber at the different dose rates cannot be completely excluded, the most promising explanation of this phenomenon may be described by reference to Figure 7.1. Since the reading of the panel unit meter is the result of an integration over the total beam cross-section, it can be readily appreciated that two totally different beam-fluence profiles may integrate to give the same measured output, A. However, for this given output, A, the dose received by a device sampling only a small area, α, of the beam cross-section may vary substantially. Thus the panel meter cannot be relied upon to monitor accurately the dose received by the calorimeter. Obviously the only reliable method of monitoring the beam is to use a small transmission ionization chamber placed directly above the sensitive area. Unfortunately, this approach requires the introduction of a larger amount of scattering material into the path of the beam, which may significantly disturb the energy spectrum and spatial distribution of the beam. To avoid this problem an alternative approach was adopted. This consisted of positioning the Ionex chamber just above the surface of the entrance window in the calorimeter heat shield, but at the periphery of the 10 cm x 10 cm applied radiation field. This configuration permits the Ionex chamber to monitor part of the central

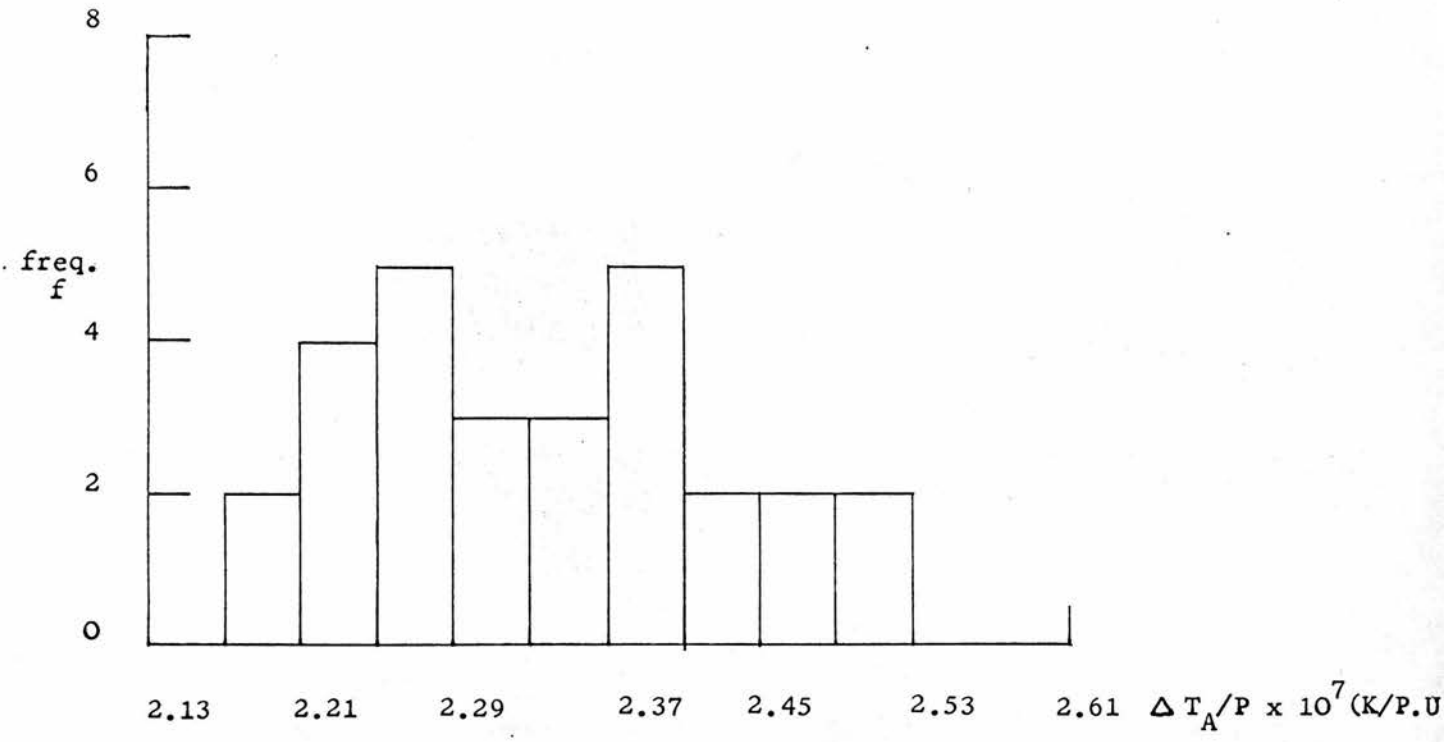

FIGURE 7.2b IRRADIATION RESPONSE (THERMISTOR A1)

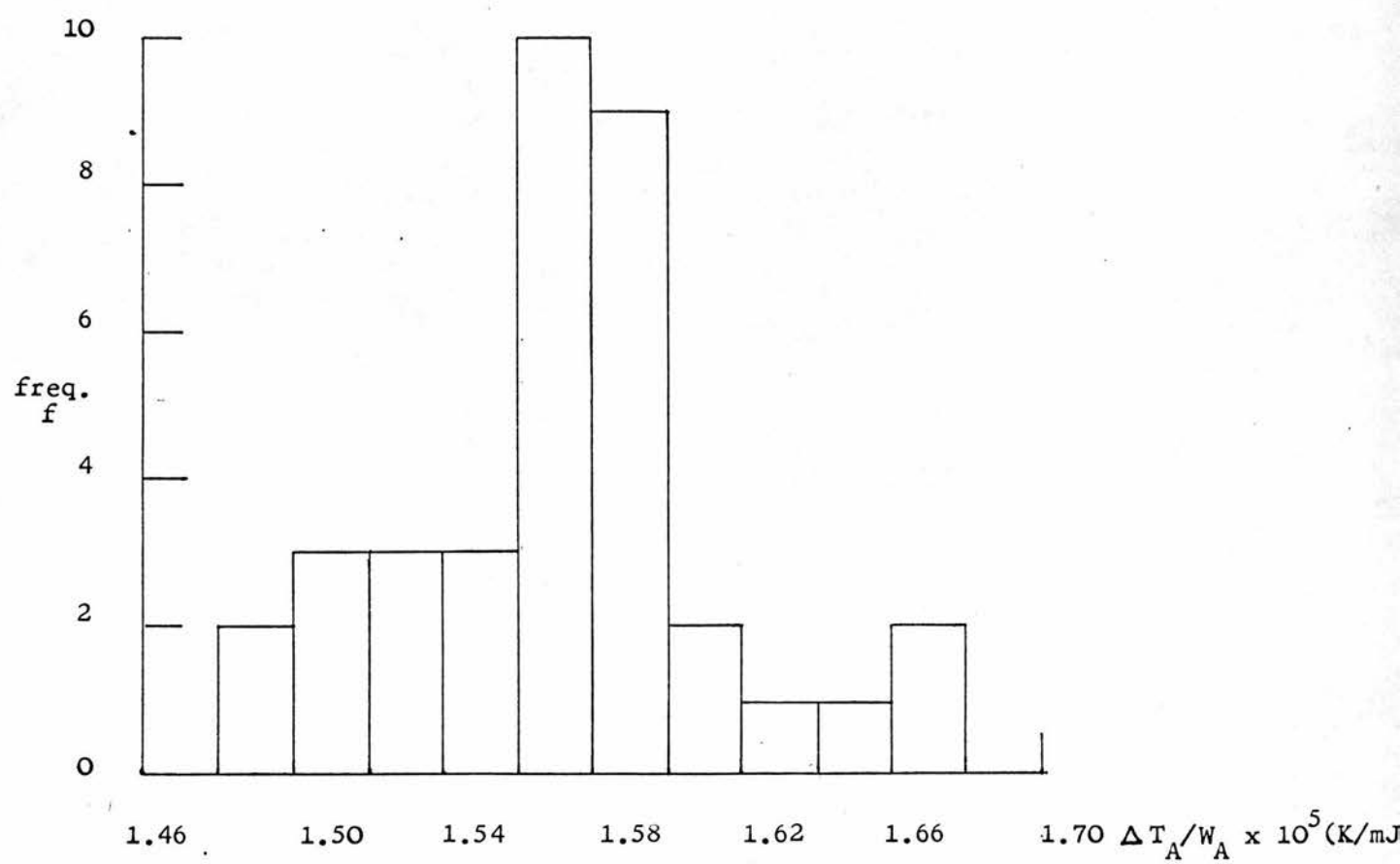

FIGURE 7.2a CALIBRATION RESPONSE (THERMISTOR A1)

region of the beam without actually disturbing the radiation flux impinging upon the absorber. If the ratio of the dose absorbed by the Ionex chamber, I, when placed at the edge of the field, to the dose received at the centre of the field is constant, then the value of I may be used to normalise the irradiation response of the calorimeter. A study of the depth-dose data for the particular accelerator in question indicated that the depth-dose profile in the central region of the beam was reasonably flat, and presumably reproducible. To check the Ionex ratio, and the possible errors associated with its repositioning, a series of measurements was undertaken. The results of these tests indicated that, on a given occasion, the ratio was constant to within $\pm$ 0.4% (standard deviation of one result from the mean of ten results) including possible positional errors. Regrettably, this ratio was not checked on each occasion when the calorimeter or ionization chamber was used and later evidence was adduced to show that this ratio could change by 1.3% from day to day. This occurrence of reasonable consistency on any one day, but a marked variation from day to day, may help to explain the shape of the histogram inFigure 7.2b. If it is postulated that two, or more, metastable states of machine operation exist, and that these states can only interchange when the accelerator is switched off and restarted. Then the agglomeration of measurements taken on different days will yield the super-position of a number of experimental normal distributions. Inspection of Figure 7.2b shows that there is some evidence of a bimodal distribution, lending some credibility to this hypothesis.

Whilst the Ionex technique of monitoring the beam showed a marked improvement compared with the panel-unit meter, it must be emphasised that the method is still indirect and, for beams of poor stability or

TABLE 7.1

CALORIMETER RESULTS

DATE	THERMISTOR RESISTANCE	CALIBRATION RESPONSE	IRRADIATION RESPONSE	RATIO
	R_T	$\frac{\Delta R_T}{R_T} / W_A$	$\frac{\Delta R_T}{R_T} / I_A$	W_A / I_A
	Ω	Ω/Ω.mJ	Ω/Ω.Ionex Volt	mJ/Ionex Volt
		x 10^5	x 10^4	x 10
28.1.74	1861 ± 2	1.581 ± 0.008 (9)	2.608 ± 0.014 (9)	1.650
29.1.74	1859 ± 1	1.575 ± 0.009 (11)	2.556 ± 0.036 (9)	1.623
30.1.74	1853 ± 1	1.575 ± 0.007 (8)	2.618 ± 0.017 (9)	1.662
11.2.74	1763 ± 2	1.554 ± 0.005 (8)	2.510 ± 0.013 (11)	1.614
14.2.74	1743 ± 2	1.540 ± 0.004 (8)	2.564 ± 0.012 (11)	1.664
15.2.74	1753 ± 2	1.544 ± 0.006 (7)	2.504 ± 0.012 (11)	1.611
		MEAN VALUE		1.637 ± 0.010

or reproducibility, the only safe technique is direct monitoring. Nevertheless, the difficulties encountered in these measurements did serve to highlight the practical problems involved in the irradiation measurements, and provided useful background experience for the electron measurements.

7.3 EXPERIMENTAL RESULTS

7.3.1 Calorimeter

The X-ray measurements were performed with a 4 MV beam produced by a Vickers Series 1 linear accelerator and the results of these experiments, together with the relevant calibration responses, have been listed in Table 7.1. This table has been split into two sections according to the date of measurement. It can be seen that those results quoted for late January are characterised by values of R_T approximately equal to 1857 Ω, whilst the results of mid-February are characterised by a value of R_T approximately equal to 1753 Ω. Whilst the change in the value of R_T may be indicative of a shift in the operating temperature of the calorimeter, the simple correction for the variation in the temperature at the time of measurement, as detailed in Chapter 5, cannot be applied in this situation for two reasons. Firstly, during the intervening period between these two groups of measurements, the cable connecting the calorimeter to the instrument trolley was lengthened in preparation for the electron measurements. The increased capacitance of this cabling resulted in a shift of the reactive balance point of the temperature measuring system and caused a slight decrease ($\simeq$ 1%) in the sensitivity of the system (see Chapter 4). Secondly, as explained earlier, the temperature correction was based upon the un-checked manufacturer's

data, and, for corrections greater than 1 K, could introduce a not insubstantial error. Therefore, instead of adjusting all the results, the ratio of the irradiation response to the calibration response for each pair of results has been tabulated in the last column of the table.

The values of the calorimeter response entered in Table 7.1 refer to the arithmetic mean of a number of separate experimental determinations performed on each occasion. The number of experiments performed on each day has been indicated by the figure in parenthesis following each entry. The values of the calibration response, shown in column 3, have been corrected for the loss of energy in the absorber heater leads (2.5%, Chapter 3) and the variation in response due to the temperature gradients within the absorber during calibration (0.42%, Chapter 5). These values therefore represent the corrected or "true" calibration response of the absorber. In accordance with normal statistical practice the experimental uncertainty associated with each measurement has been taken as the standard error of the mean (SEOM), and the uncertainties quoted in the table refer to this quantity. The number of degrees of freedom associated with each SEOM may be taken as n-1, where n is the number in parenthesis (i.e. one degree of freedom is lost when assuming that the sample mean represents the true, or population, mean). In the case of the calibration response the systematic uncertainties associated with the correction factors mentioned above have not been included in the uncertainties quoted in the table. Thus, these tabulated uncertainties refer to the experimental sources only. These systematic uncertainties will be considered, together with all other systematic uncertainties, at the end of this chapter. The final, or overall, response of the

calorimeter has been taken as the mean of the ratios listed in column 5. It should be stated at this juncture that, unless otherwise specified, all the experimental results reported in this thesis have been assumed to be derived from a normal population distribution, and the treatment of the results, together with the related uncertainties, have been based upon this premise. In the majority of cases the amount of data pertaining to one particular set of conditions was insufficient to permit a rigorous test for normality. Nevertheless, a visual inspection of the data usually indicated that an embryonic normal distribution was present, and it was taken that this was sufficient to justify the above assumption. Returning to the above case, an inspection of the figures in column 5 of Table 7.1 does not justify the assumption of normality, and it would appear that some systematic effect may be influencing these results. A study of the individual calibration responses reveals that, in both sets of results, the reproducibility of the calibration response is very good and, within the limits of the experimental uncertainties, the individual values are in close agreement. In contrast, the values of irradiation response are rather scattered and the individual uncertainties are much larger and more variable than the corresponding calibration values. The explanation for this phenomenon almost certainly lies with the monitoring problem discussed above. Although one explanation for the variation in the irradiation results has already been suggested, much more data would be required to conclusively prove any hypothesis concerning the behaviour of the beam and its monitor chambers. Therefore, in the absence of any firm evidence to the contrary, the irradiation results were assumed to be derived from a normal distribution

and have been treated accordingly.

7.3.2 Ionization Chamber

Upon completion of the calorimetric experiments the calorimeter was replaced by the ionization chamber, the position and orientation of this dosimetric system reproducing as precisely as possible the physical set-up of the calorimeter. The possible error due to the slightly different orientations is difficult to estimate, especially for beams with poor profile reproducibility, but the tolerance associated with the vertical positioning of the phantom, at a Source-Surface Distance (S.S.D.) of 1.106 m, is $\pm$ 1mm (0.18%). The error in positioning the phantom should be random and, therefore, this uncertainty will be reflected in the total experimental uncertainty, as will any slight inconsistencies in the orientation of the phantom. In preparation for the ionization measurements the Ionex monitor chamber was again placed in its position near the periphery of the beam cross-section, simulating its station during the calorimeter measurements.

A particular problem common to all gaseous ionization dosimeters is the recombination of the charged ions produced by the passage of the radiation beam. Of the two possible types of recombination, general and initial, only the former is of importance for the low L.E.T. photon and electron beams. For general recombination the efficiency, f, of charge collection by a cylindrical ionization chamber, when exposed to a pulsed radiation beam, has been given by Boag (1966) as

$$f = \frac{\nu}{e^{\nu} - 1} \qquad 7.1$$

where $\nu = \mu p d^2 V_p^{-1}$. The symbol μ refers to a function of the recombination rate and mobility of the ions, p is the charge collected

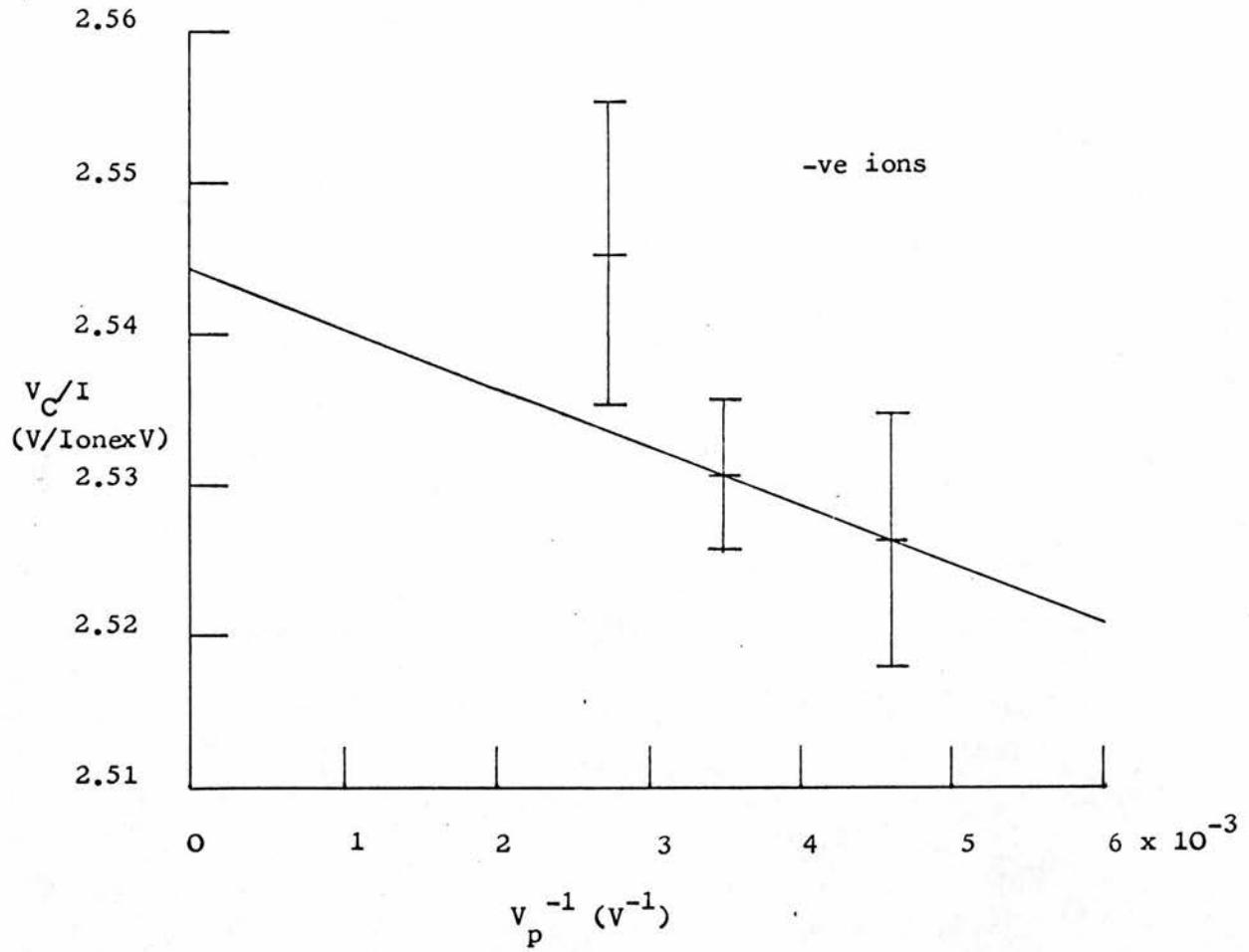

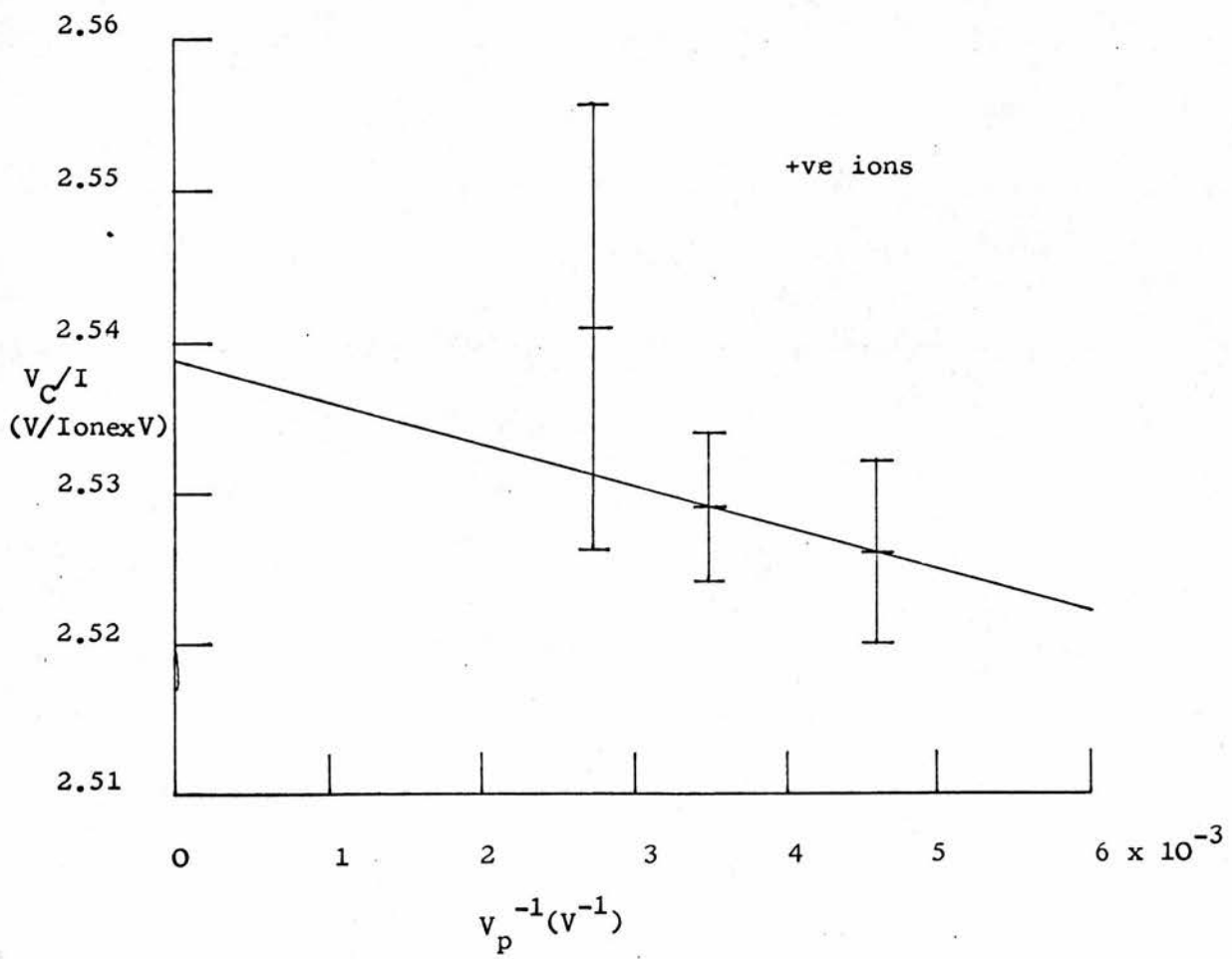

FIGURE 7.3 SATURATION CHARACTERISTICS OF IONIZATION CHAMBER

per pulse, d is a geometrical factor relating to the electric field strength and V_p is the polarising voltage applied to the electrodes. In the present case d is 0.160 cm which, for a polarising voltage of 200 V, gives an efficiency of 99.90% using the appropriate values of μ and p. This value of f has been deduced on the assumption of perfectly uniform radial electric field width in the collecting volume. This is unlikely to be the case in practice, especially near the corners of the collecting volume which will distort the field, and a practical determination of the true charge liberated per pulse, r, must be made. It is possible to show from Boag's analysis that the charge collected, p, is related to r by the equation

$$p = r\left(1 - \frac{\mu r d^2}{2V_p}\right) \qquad 7.2$$

(this equation is based on the assumption that $\frac{1}{x} \ln (1 + x) = 1 - \frac{x}{2}$ where $x = \frac{\mu r d^2}{V_p}$. For the voltages used here, x is approximately 10^{-3} and therefore the use of this approximation will involve an error of less than 0.05%.) Equation 7.2 shows that, if r is constant, the charge collected, p, is a function of V_p^{-1} only. It is perhaps interesting to compare this result with the one obtained for continuous radiation beams, where the charge collected is a function of V_p^{-2}. Accordingly, the value of V_C, the voltage integrated on the Townsend balance capacitor, C_O, normalised by the Ionex reading, I, has been plotted as a function of V_p^{-1} (Figure 7.3). The normal practice of converting the Ionex reading to the value obtaining at 291 K and 760 mm Hg was omitted in this case, since a similar correction factor would also have to be applied to V_C. However, all the values of the calorimeter Ionex readings were corrected to this thermodynamic point, and, therefore,

the values recorded in Figure 7.3 may be taken as referring to the charge produced at 291 K and 760 mm Hg. To ascertain whether the charge upon the ions influenced the measured value of V_C, observations were made with both positive and negative voltages applied to the central electrode, which was always maintained near earth potential. The results of these measurements are shown in Figure 7.3 and 7.3b. Each point plotted in these graphs is the mean of seven or eight separate determinations of the charge collected per Ionex monitor unit. The uncertainties attached to each point are, as usual, the standard errors of the relevant means. It will be observed that, whilst the values of V_C/I measured at the lower polarising potentials are in close agreement, the values at the highest polarising potential show some discrepancy. Furthermore, if a linear regression (least squares fit) is performed upon the individual results, the slopes of regression lines differ markedly from one another and the correlation coefficients for both sets of data are very poor. Also, the collection efficiency deduced from the intercept of these regression lines with the V_C/I axis is only 98.0%, well below the theoretical value of 99.9%. Conversely, a linear regression performed upon the data obtained at the two lower polarising voltages yields two almost identical slopes, much better correlation coefficients and an efficiency of 99.0%. The field strength at the highest polarising voltage was, on average, 2400 volts/cm, and it is not inconceivable that at such field strengths ionization by collision could occur, especially at the tip of the probe which was not bevelled. In view of these facts it was felt justifiable to neglect the upper voltage points. The intercept of the linear regression lines, based upon the lower voltage data, with the V_C/I axis was taken as the value

of the charge liberated. This gives a value of 2.5441 $\pm$ 0.0328 volts/Ionex volt for the collection of negative ions and 2.5389 $\pm$ 0.0519 volts/Ionex volt for the collection of positive ions. These two values are in very close agreement and the slight difference is insignificant in view of the quoted experimental uncertainties. A mean value of 2.5415 volts/Ionex volt has been taken as the response of the ionization chamber.

The uncertainties in the value of V_C/I at $V_p^{-1} = 0$ quoted above were derived from equation 7.3 (Parl, 1967), which gives the combined estimated standard error in Y_2 at the corresponding abcissa X_2

$$\hat{\sigma}_{(x.y)} = \left(\hat{\sigma}_{x.y}^{2} \left[1 + \frac{1}{n} + \frac{(X_2 - \bar{X})^2}{n \hat{\sigma}_x^2} \right] \right)^{\frac{1}{2}} \qquad 7.3$$

In equation 7.3 X is the independent variable representing V_p^{-1}, whilst Y is the dependent variable equivalent to V_C/I. The term $\hat{\sigma}_{x.y}$ in equation 7.3 is the standard estimate of error for the regression and is defined by equation 7.4

$$\hat{\sigma}_{x.y} = \left(\frac{\sum (Y_c - Y)^2}{n - k} \right)^{\frac{1}{2}} \qquad 7.4$$

where Y_c is the regression value corresponding to the point (X,Y), n is the number of points and k is the number of degrees of freedom lost, which for a linear regression is 2. The term $\hat{\sigma}_x$ is the estimated variance of the X population defined in a similar way to equation 7.4, but with the proviso that k is unity.

The precision of ionization dosimetry is often presented as one of its major advantages, but it is apparent here that the experimental uncertainties encountered in the ionization measurements are much larger than the calorimetric values. This result is almost certainly

the outcome of the monitoring problem, since a small uncertainty in the ionization data will result in a large uncertainty in the regression intercept. Undoubtedly this is the most insidious effect of the inability to monitor the beam accurately.

Charge leakage effects were studied by observing the stability of the integrating capacitor voltage before, and immediately after, irradiation. In the absence of any radiation impinging upon the ionization chamber this voltage was found to remain steady, irrespective of the sign and magnitude ($\leq$ 450 V) of the H.T. voltage applied to the outer electrode. For the case of radiation induced leakage, the conductivity of the insulator takes some time to return to its nominal value after being exposed to a radiation beam (Boag, 1966). Therefore, the observation of a steady capacitor voltage at the end of an ionization measurement indicates, not only the absence of quiescent leakage, but also the absence of radiation induced leakage as well.

In an attempt to verify this latter statement, small sections of the stem region were exposed to the radiation beam whilst the actual collecting volume remained outwith the radiation field. The charge produced on the integrating capacitor by these irradiations varied between 0.2 and 1% of the total charge which would have been collected for a similar irradiation of the active air volume. The smaller figure was obtained when this section was well removed from the stem-chamber interface. Since the sign of the charge collected was always the same as that which would have been derived from an irradiation of the collecting volume, the evidence would suggest that this extra charge collection is the result of photons being

scattered into the collecting volume and producing a few ions, rather than the leakage of charge across the insulator. However, in view of the inconclusive nature of this investigation, a value of 0.2% has been included in the list of systematic uncertainties under the heading of charge leakage.

7.4 CALCULATION OF MASS STOPPING POWER RATIO

The value of mass stopping power ratio is given by the Bragg-Gray relationship introduced in Chapter 1

$$D_C = J_g \bar{W} s_{C/AIR} p_{C/AIR} \qquad 7.5$$

where $J_g.\bar{W}$ corresponds to the absorbed dose in Air, $D_V(AIR)$. The value of D_C to be substituted in this equation is obtained from the mean ratio of column 5 in Table 7.1 which is 16.37 m J/Ionex volt (@ 291 K and 760 mm Hg). For an absorber mass of 2.5118 g (Table 3.2) the absorbed dose received by the central element is 6.517×10^{2} rads/Ionex volt. J_g, the ionization per unit mass of gas, is obtained from the product of the voltage integrated upon the capacitor and the capacitance of this element, divided by the mass of gas in the chamber at 291 K and 760 mm Hg. This gives

$$J_g = \frac{2.5415 \times 4.684 \times 10^{-8}}{0.5177 \times 1.208 \times 10^{-3}} \quad \text{C/g.Ionex volt}$$

i.e. $J_g = 1.9035 \times 10^{-4}$ C/g.Ionex volt

The perturbation of the 4 MV X-ray beam by the small air chamber within the carbon phantom is expected to be slight and the value of $p_{C/AIR}$ may thus be equated to unity (Bewley, 1963). Substituting the relevant values into equation 7.5 yields the product $\bar{W} s_{C/AIR} = 34.373$ eV ion pair. Using the value of the mean energy expended per ion pair, $\bar{W}$,

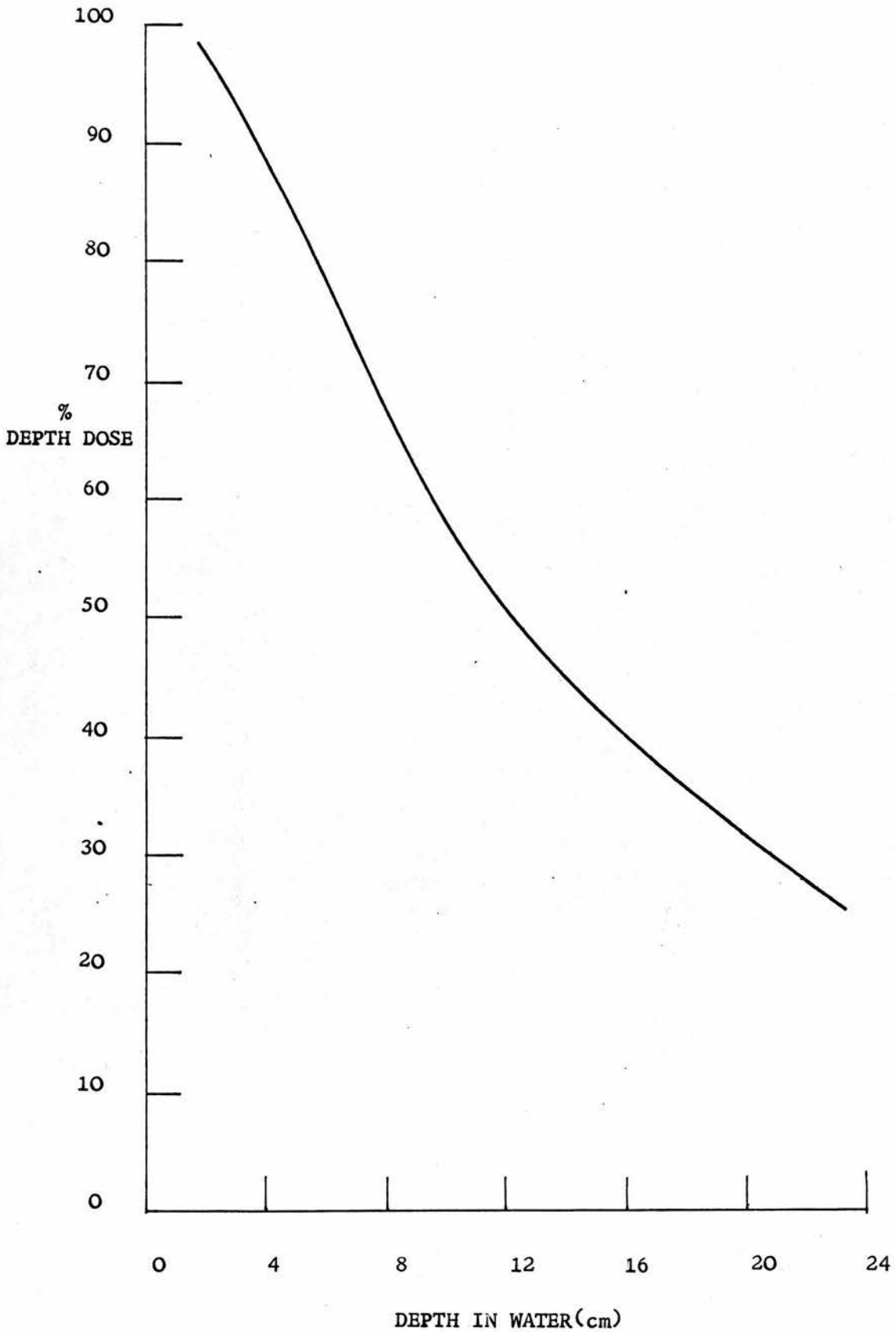

FIGURE 7.4 DEPTH DOSE CURVE FOR 4 MV X RAYS (WATER PHANTOM, 10 cm x 10 cm FIELD, 1 m S.S.D.)

as 33.73 $\pm$ 0.15 (I. C.R.U., 1969) yields the result $s_{C/AIR} = 1.019$.

It has been assumed for the purpose of this calculation that the point of measurement, and the radiation spectrum at this point, are identical for each dosimetric system. A full discussion of the depth of measurement is presented in Chapter 8, but, for the present purposes, it will be sufficient to state that the depth of measurement for the calorimeter is 12.21 $\pm$ 0.01 mm of graphite, (36), whilst the depth of measurement for the ionization chamber is 12.69 $\pm$ 0.01 mm of graphite, (27). The uncertainties are the SEOMs and the numbers in parenthesis indicate the effective degrees of freedom. To correct for this slight discrepancy in the point of absorbed dose measurement Figure 7.4 has been used. This figure shows the depth-dose curve for a 10 cm x 10 cm field at 1 m S.S.D. in a water phantom. Using a value of 1.7 g/cm^3 as the density of graphite, the percentage of the peak dose at the centre of the calorimeter is 96.0% whilst the equivalent value of this quantity for the ionization chamber is 95.7%. The uncertainty in the value of the depth dose resulting from the uncertainty in the point of measurement is negligible. Nevertheless, to allow for the possible differences between a carbon depth-dose curve and the water one, a systematic uncertainty of 0.2% has been included in Table 7.3. The result of the discrepancy in the point of measurement is that the value of J_g should be increased by 0.3%, thus the final value of the mass stopping power ratio is

$$s_{C/AIR} = 1.016$$

7.4.1 Estimation of Uncertainties

The sources of the experimental uncertainties have been displayed

TABLE 7.2

EXPERIMENTAL UNCERTAINTIES

SOURCE	SEOM %	$a_i \times 10^4$	DEGREES OF FREEDOM
Calorimeter response	0.610	0.377	5
Mass of Absorber	0.004	Negligible	9
Extrapolated value of V_C/I + ve	1.290	1.679	12
- ve	2.044	4.246	12
Time Const. of $C_O\left[t(\ln\frac{V}{V_O})^{-1}\right]$	0.018	Negligible	Large
Leakage Resistance of $C_O(R)$	0.086	0.007	9
Volume of Chamber	0.309	0.696	9
Mean Energy/ Ion Pair $\bar{W}$	0.445	0.197	Large
TOTAL	-	6.603	11.4

in Table 7.2. As an illustration of the relative magnitude of each uncertainty the SEOM has been tabulated as a percentage of its appropriate mean value. These uncertainties have been combined according to equation 7.5 (Campion et al., 1973)

$$S^2(\bar{Y}) = (\frac{\partial \bar{Y}}{\partial a})^2 \times S^2(\bar{a}) + (\frac{\partial \bar{Y}}{\partial b}) \times S^2(\bar{b}) + (\frac{\partial \bar{Y}}{\partial c}) \times S^2(\bar{c}) \qquad 7.5$$

$$\text{or} \quad S^2(\bar{Y}) = \sum_i \alpha_i \quad \text{where} \quad \alpha_i = (\frac{\partial \bar{Y}}{\partial b}) \times S^2(\bar{b}) \quad i = a,b,c \ldots\ldots$$

In these equations a,b,c, etc. are the parameters involved in deriving the required result $\bar{Y}$ (i.e. $s_{C/AIR}$) and $S^2(\bar{a})$ etc. are the population variances for the relevant parameters. The final experimental uncertainty in the value of $s_{C/AIR}$ is the SEOM given by $S(\bar{Y})$ and, from the quantities shown in Table 7.2, is $\pm$ 0.026. The effective number of degrees of freedom for this SEOM can be calculated from equation 7.6

$$\frac{1}{\nu_{eff}} = \frac{\sum_i \alpha_i^2/\nu_i}{(\sum_i \alpha_i)^2} \qquad 7.6$$

(This equation usually results in ν_{eff} being a non-integer, and thus the result must always be rounded down to the nearest whole number). Referring to Table 7.2 again, the value of ν_{eff} is found to be 11.

The systematic uncertainties have been listed according to source in Table 7.3. The total systematic uncertainty of 0.79% was obtained by taking the root of the sum of the squares of the separate quantities. The mean experimental value of the mass stopping power ratio for carbon to air, derived from a 4 MV X-ray beam, can now be stated as 1.016 with a standard error of the mean of $\pm$ 0.026 and 11 degrees of freedom. The systematic uncertainty is not expected to exceed $\pm$ 0.008.

TABLE 7.3

SYSTEMATIC UNCERTAINTIES

SOURCE	MAGNITUDE %
Absorber Heater End Effect	0.50
Absorber Temperature Gradients	0.42
Ionization Chamber Volume	0.26
Stem "Leakage"	0.20
Capacitor Leakage Resistance	0.09
Depth Dose Curve	0.20
TOTAL	0.79

This result is in excellent agreement with the experimental result of Bewley (1963), 1.015 $\pm$ 0.008, and assuming a value of $\overline{W}$ = 33.73, it is also in close agreement with the result for ^{60}Co γ-rays, 1.013 $\pm$ 0.006, determined by Engelke and Hohlfeld (1971a). In addition the present result is well within the range of the theoretical calculation of this quantity, 1.007 (estimated uncertainty $\pm$ 0.02), (I.C.R.U., 1969). However, it is to be regretted that the experimental uncertainty is so large that it is in excess of the systematic uncertainty, and in this light the excellent agreement must be regarded as slightly fortuitous.

CHAPTER 8.

E L E C T R O N M E A S U R E M E N T S

8.1 ELECTRON BEAM PARAMETERS

This chapter describes the measurement of absorbed dose for three different electron beam energies. The precise electron energy at the surface of the phantom, and at the point of measurement, will be discussed in section 8.1.3, but, throughout this chapter, these beams have been referred to by their nominal accelerator energies, E_a, (= 11, 9 and 6 MeV). All three beams were produced by the same linear accelerator, an M.E.L. SL75, using an applicator size of 10 cm diameter and a S.S. D. of 134.3 $\pm$ 0.05 cm. Whilst this particular machine was expected to yield a more reproducible beam profile than the X-ray accelerator mentioned in the last chapter, the comments of section 7.2 concerning the monitor unit variation still apply and the approach to this problem will now be discussed.

8.1.1 Beam Monitoring

The lessons recounted in Chapter 7 indicated that the only reliable method of monitoring a small sample of the beam cross-section was to introduce a second transmission ionization chamber immediately above this area. Unfortunately, even a small amount of foreign material placed in the path of the electron beam will cause a marked distortion or attenuation of the electron flux. For this reason it was considered even more undesirable to introduce a second monitor chamber and another alternative approach was pursued. Measurements with a Farmer-Baldwin chamber, centered 1 cm deep in a large perspex block, showed that, for a particular energy on any given occasion, the central axis dose delivered by the beam was

TABLE 8.1

DAILY VARIATION OF FARMER-BALDWIN MONITOR CHAMBER

DATE	ENERGY E_a MeV	RESPONSE OF FARMER-BALDWIN B rads(in water)/Panel Unit
28.2.74	11	1.0383 ± 0.0027
1.3.74	11	1.0355 ± 0.0027
9.3.74	11	1.0126 ± 0.0050
11.3.74	11	1.0182 ± 0.0050
17.3.74	11	1.0446 ± 0.0027
2.3.74	9	1.0250 ± 0.0050
3.3.74	9	1.0172 ± 0.0027
4.3.74	9	0.9930 ± 0.0027
9.3.74	9	1.0126 ± 0.0050
12.3.74	9	1.0007 ± 0.0027
6.3.74	6	0.8627 ± 0.0050
7.3.74	6	0.8314 ± 0.0027
8.3.74	6	0.8410 ± 0.0050
13.3.74	6	0.8258 ± 0.0027
14.3.74	6	0.8432 ± 0.0027
15.3.74	6	0.8504 ± 0.0027

constant. Furthermore, measurements on either side of the beam axis (2.5 cm) indicated that the beam profile also remained con stant on the given occasion. However, as Table 8.1 demonstrates, the central axis depth dose could vary markedly from day to day. Considering these results it was concluded that the simplest, and least disruptive, method of monitoring the beam would be to check the central axis depth dose with the Farmer-Baldwin chamber in its perspex phantom before, during and after each set of experimental results. The product of the Farmer-Baldwin response for that day and the number of panel units indicated on the machine console then gave the appropriate number of monitor units, M, which could be used to normalize the response of the dosimeter in question. This system, which performed tolerably well in practice, was a definite improvement over the Ionex chamber system, although to what extent the difference in profile reproducibility for each machine was responsible for this improvement is not known. Nevertheless, problems were still encountered with the monitoring arrangements especially during the ionization chamber measurements, and, in retrospect, a transmission ionization chamber may have improved matters (see Chapter 9.)

It is perhaps worthwhile to note that the I.C.R.U. (1972) have advocated a policy of a second special transmission ionization chamber, but, with very few exceptions, little explicit attention has been paid to this problem. An early acknowledgement of this problem was by Bewley (1963), who continued to use the internal or machine monitor chamber but included an uncertainty of 0.4% to allow for the variation in beam profile and the recombination effects within the monitor chamber. Pinkerton (1969) did not specifically mention the monitoring

problems in the text of his article but an illustration of a small transmission ionization chamber, placed directly above the sensitive volume, did appear in the diagram of his calorimeter. Perhaps one of the most cogent reasons for the lack of appreciation of this problem is that, until recently, most of the precise calorimetric measurements have been performed with radionuclide γ-ray beams (Dove and Cole, 1962; Keene and Law, 1963; Engelke and Hohlfeld, 1971a). With such radionuclides, apart for half-life corrections, the stability and reproducibility of the beam is not in question.

8.1.2 Position of Measurement Within the Phantom

So far this thesis has placed considerable emphasis upon the problem of measuring the amount of radiation impinging upon the phantom. The related problem of verifying that each dosimetric system receives the same flux of radiation at its point of measurement has not yet been fully investigated. In the majority of calorimeters discussed in Chapter 2 a coin-shaped absorber geometry was adopted. In this situation the depth of measurement below the phantom surface is usually quite unambiguously defined as the centre of the absorber disc, since the extent of the absorber in the direction of the incident beam is a constant. Similarly, if the radiation beam is normally incident upon the plane face of a coin-shaped ionization chamber, the point of measurement is normally defined as being slightly above the axis of this chamber. Provided that reasonable precautions have been taken in the construction of the phantoms, the uncertainty involved in comparing these two measurements will be negligibly small. As explained in Chapter 3, the present situation is rather different and, to elucidate the discussion of the point of measurement, Figures 8.1a, b, c and d, representing vertical sections through each dosimeter,

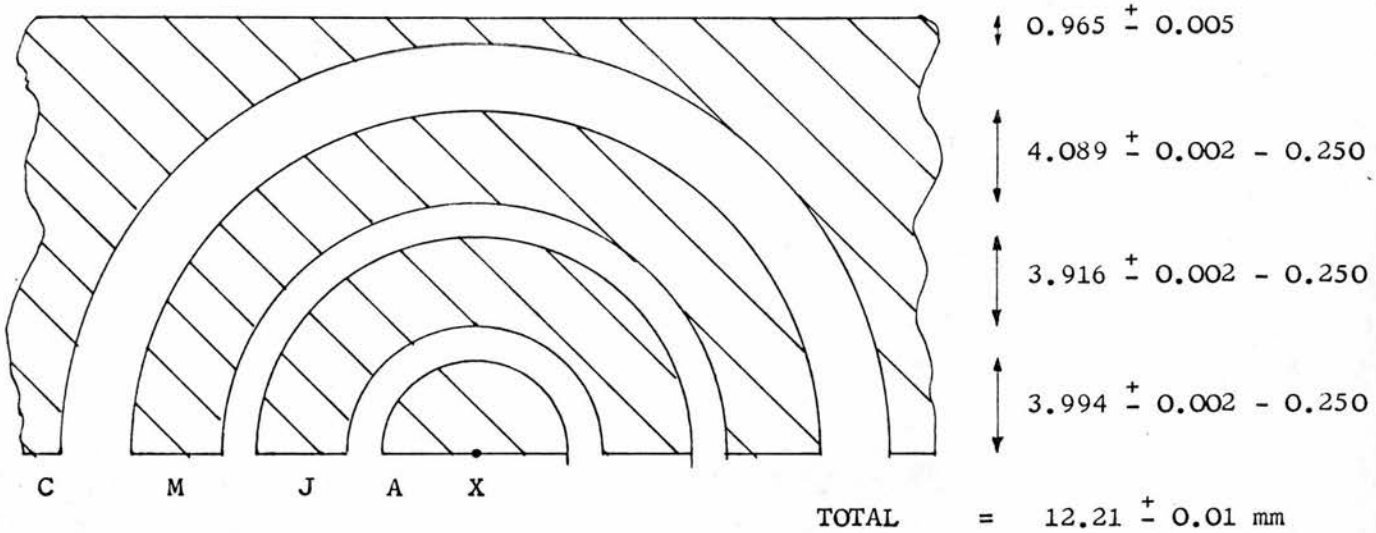

FIGURE 8.1a SECTION THROUGH CALORIMETER

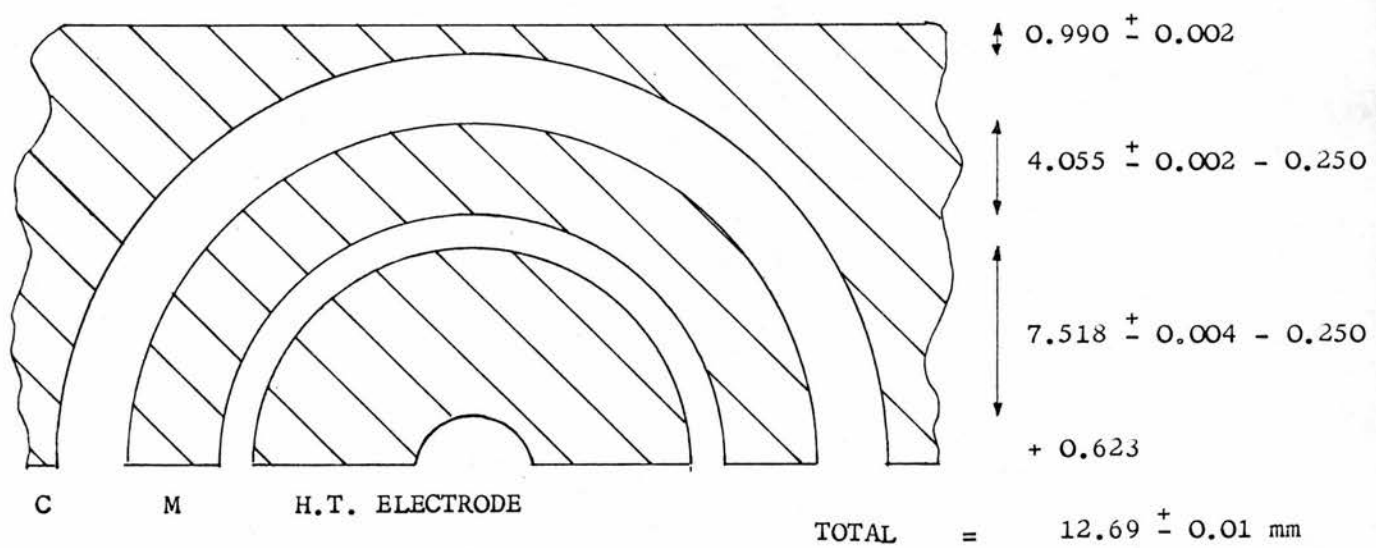

FIGURE 8.1b SECTION THROUGH IONIZATION CHAMBER

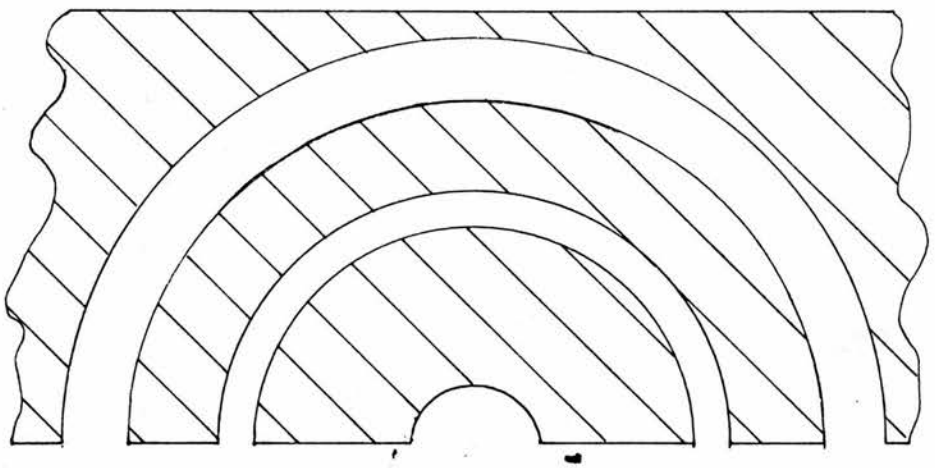

0.990 ± 0.002

4.055 ± 0.002 - 0.250

6.879 ± 0.002 - 0.250

+ 0.750

TOTAL 12.17 ± 0.01 mm

FIGURE 8.1c SECTION THROUGH FARMER-BALDWIN PHANTOM

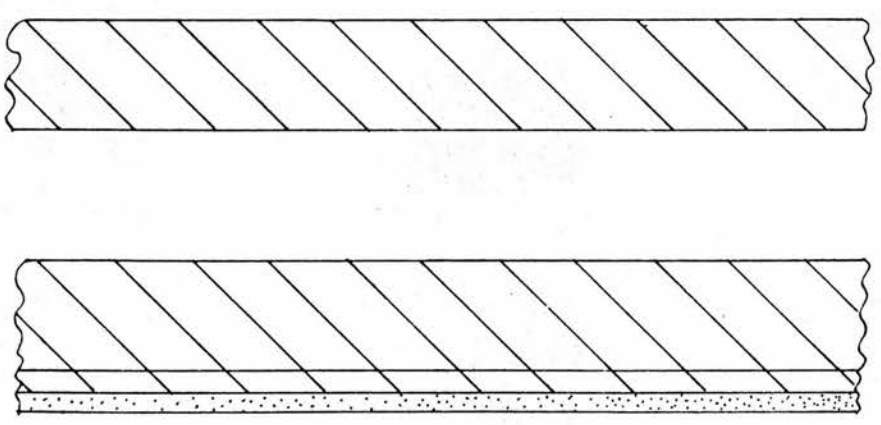

5.002 ± 0.002

5.002 ± 0.002

0.541

1.028

TOTAL = 11.57 ± 0.01 mm

FIGURE 8.1d SECTION THROUGH FERROUS SULPHATE PHANTOM

have been included. Reviewing the case of the calorimeter first, Figure 8.1a, it may be stated that, if a linear absorbed dose gradient exists in the region of the central absorber, the point of measurement will be the horizontal axis of the absorber, X. There is no a priori reason for this statement but, considering the symmetry of the design, any other position would seem unjustifiable.

The approximate depth dose profile may be ascertained by reference to Figures 8.2, 8.3 and 8.4 which show the depth percentage-ionization curves for each of the three beam energies. These graphs were constructed from measurements made with a small end-window chamber and a collection of plane, rectangular graphite slices of different thicknesses. It must be emphasised that these curves are not true depth dose curves since the rads to roentgen conversion factor for the end-window chamber varies with depth, but, for the sake of convenience, this factor may be assumed to be constant. In addition, although the same beam applicator, windows and S.S.D. used during the calorimetric measurements were recreated for the depth dose measurements, the phantom geometries for the depth ionization curves and the other measurements were not identical. Nevertheless, the use of an end-window chamber and thin slices of graphite did allow measurements to be made at very shallow depths with an unambiguous point of measurement. Both of these conditions would have been impossible to obtain with the calorimeter and very difficult to ahcieve with either of the ionization chambers. The depth of the axis of the cylindrical absorber below the plane surface of the phantom may be found by reference to Figure 8.1a. The measurements recorded in this figure relate to the thicknesses of each cylindrical shell surrounding the absorber and were obtained from the measured internal and external diameters of these

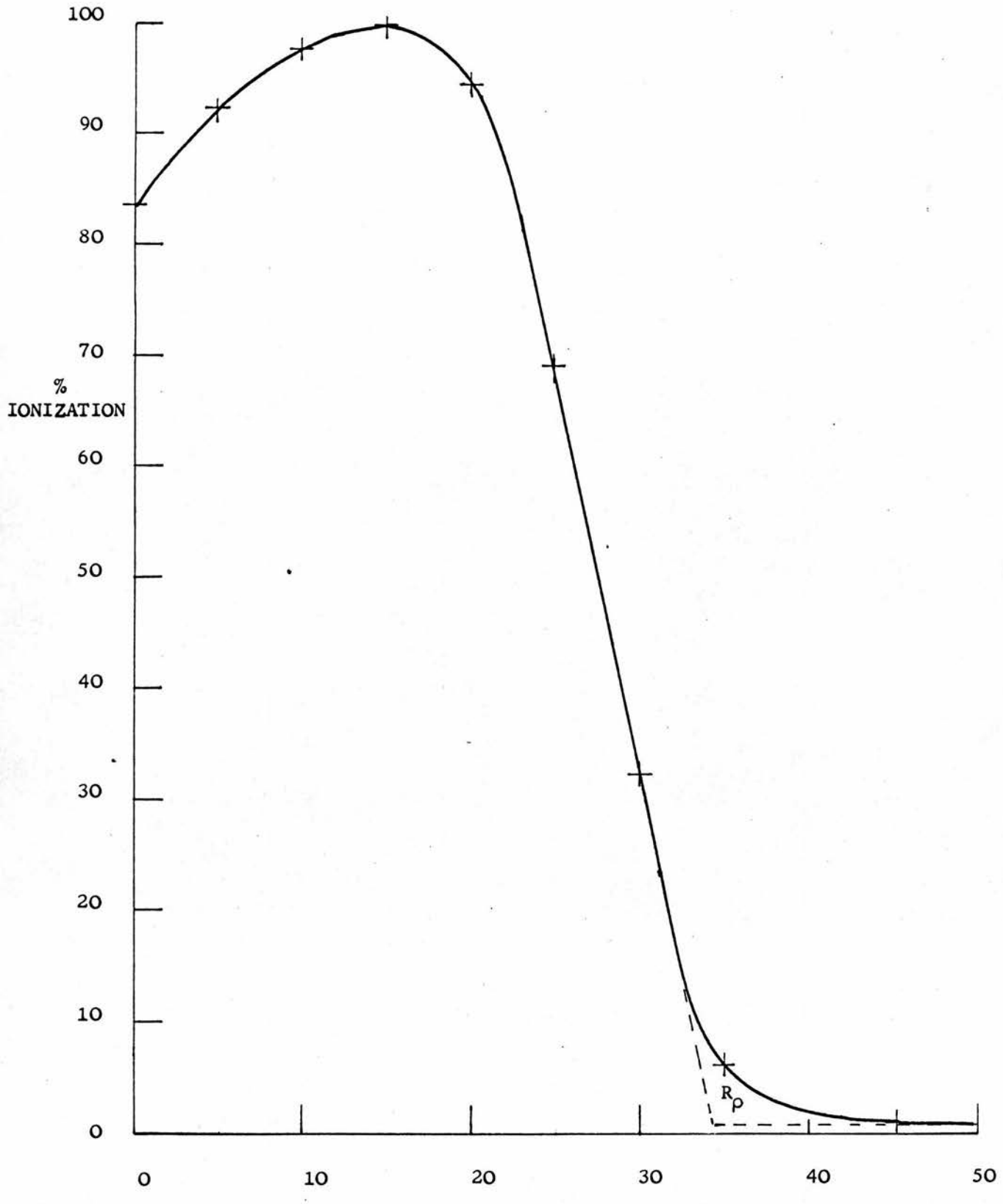

FIGURE 8.2 DEPTH IONIZATION CURVE FOR 11 MeV ELECTRONS (CARBON)

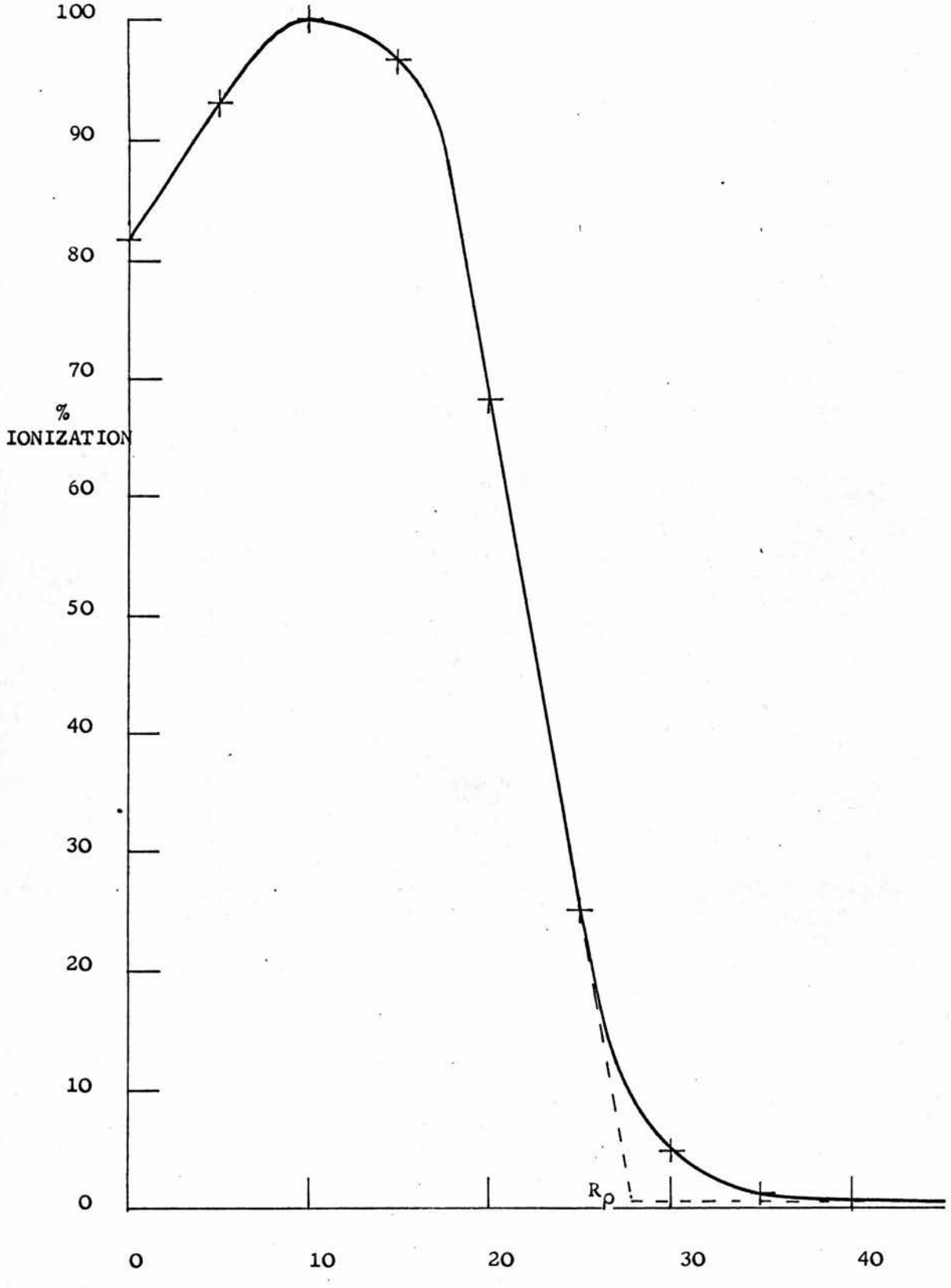

FIGURE 8.3 DEPTH- IONIZATION CURVE FOR 9 MeV ELECTRONS (CARBON)

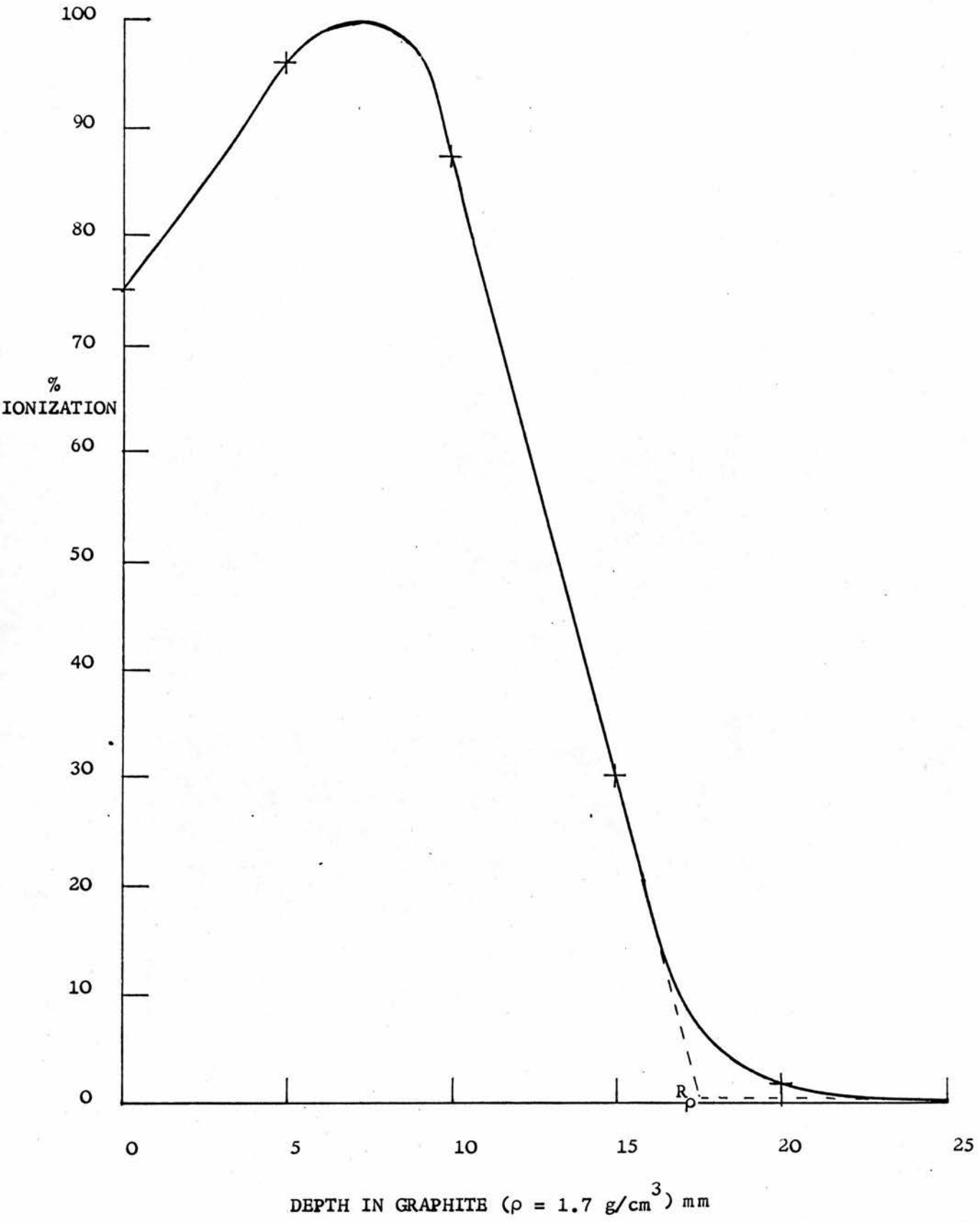

FIGURE 8.4 DEPTH IONIZATION CURVE FOR 6 MeV ELECTRONS (CARBON)

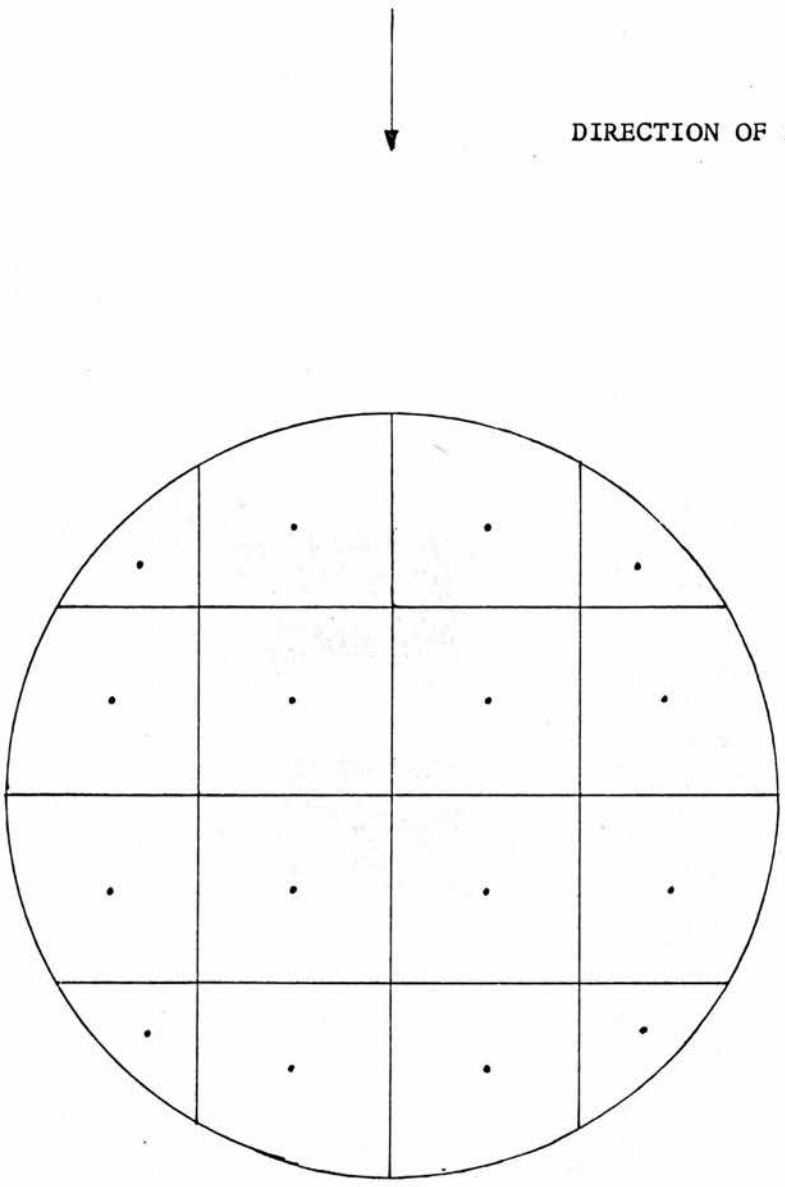

FIGURE 8.5 SECTION ILLUSTRATING DIVISION OF CALORIMETER ABSORBER

elements. A number of measurements were performed on each element and the uncertainties refer to the appropriate standard error of the mean. In the case of the absorber, jacket and mantle a value of 0.25 mm was subtracted from the thickness of each shell to allow for the graphite lost from each shell when the threads were cut into the convex surfaces of these elements. The systematic uncertainty in this correction, estimated from engineering tolerances, was $\pm$ 0.03 mm per thread. This value is insignificant when compared to the total depth involved. The total depth of the axis of the absorber is thus 12.21 $\pm$ 0.01 mm (ν_{eff} = 36). Returning to Figures 8.2 to 8.4 it can be seen that only in the case of the 6 MeV beam is the depth-ionization curve linear in the region encompassed by the absorber. In order to assess the dose which would have been produced in the absorber if all the mass had been concentrated in an infinitesimally small region around the axis, the circular cross-section of the absorber was divided into sixteen units, Figure 8.5, each of these units being assigned a weighting factor proportional to its size. The extent of each of these units, in the direction of the dose gradient, was sufficiently small to assume that the dose gradient was linear in each segment. Therefore, the dose at the centre of the unit could be taken as the representative value for that unit. The total percentage depth-ionization, integrated over the whole absorber, was then found from the summation of percentage ionization at the centre of each segment multiplied by the appropriate weighting factor. The result of this exercise is shown in column 2 of Table 8.2. The very small experimental uncertainty in the depth of the absorber axis produces a negligible uncertainty in the percentage ionization. However, to allow for the possible differences in the depth-ionization curves due to the

TABLE 8.2

PERCENTAGE IONIZATION AT THE RESPECTIVE DEPTHS OF MEASUREMENT

FOR EACH DOSIMETRIC SYSTEM

DOSIMETER	CALORIMETER	IONIZATION CHAMBER	FARMER-BALDWIN	FERROUS SULPHATE
DEPTH (mm)	12.21	12.69	12.17	11.57
BEAM ENERGY (MeV)	PERCENTAGE IONIZATION			
11	98.8	99.4	99.6	96.7
9	99.5	99.9	100.0	99.7
6	60.0	54.5	60.3	66.0

non-identical phantoms and the lack of experimental data in the region of interest, a systematic uncertainty of 0.3% has been associated with each value of the percentage-ionization for the 11 and 9 MeV beams. This uncertainty was increased to 3% for the 6 MeV case since very slight changes in the shape of the depth-ionization curve could produce very large changes in the value of the percentage ionization. In examining the effective point of measurement of the ionization dosimeters a further complication is added by the low density nature of the collecting volume. It has been shown by Dutreix and Dutreix (1966) that the true, or effective, point of measurement for a cylindrical ionization chamber is displaced towards the direction of the incident beam by an amount 3r/4, where r is the radius of the chamber. Assuming that this result holds for the present geometry, the effective point of measurement for the carbon ionization chamber is 12.69 $\pm$ 0.01 mm (ν_{eff} = 27) and 12.17 $\pm$ 0.01 mm (ν_{eff} = 27) for the Farmer-Baldwin chamber. (The Farmer-Baldwin wall thickness of 0.5 mm of Tufnol, ρ = 1.2 g/cm^3, was considered to be equivalent to 0.376 mm of graphite). As above 0.25 mm was allowed for the thickness of graphite removed when cutting the threads on the cylindrical elements (see Figure 8.1). The resultant depth-ionization, obtained from Figures 8.2 to 8.4 has been recorded in Table 8.2.

The situation with regard to the ferrous sulphate vessels is rather different. Here, the position of measurement may be confidently stated to be the centre of the ferrous sulphate solution. However, inspection of Figures 8.1a and 8.1d shows that the differences in phantom geometry are quite gross. The reason for this particular phantom geometry, as explained in Chapter 6, was the necessity to irradiate sufficient ferrous sulphate solution to fill the

spectrophotometer cells. The depth of measurement, in equivalent mm of carbon, is 11.57 $\pm$ 0.01 mm (ν_{eff} = 18) and the percentage ionization, recorded in Table 8.2, has been based upon this value. It must be stated though, that, because of this geometrical mismatch, a large error could be involved in relating the absorbed dose measured by the calorimeter to the absorbed dose calculated from the yield of Fe^{3+} ions.

8.1.3 Electron Beam Energies

There are a number of different parameters which may be employed to specify the electron beam produced by an accelerator (I.C.R.U., 1972), and the choice of parameter to be used in any particular situation is governed by the nature of the beam spectrum and the method of measuring the electron energy. The most precise techniques for measuring electron energies of this magnitude rely on either the initiation of a nuclear reaction (Lanzl, 1969) or the emission of Cerenkov radiation (Svensson, 1971). Both of these methods require a considerable expenditure in time and materials which is only justifiable when an accurate determination of the electron energy is required. A more straightforward, though less accurate, approach has been recommended by the I.C. R.U. (1972). Basically this method relies on the application of equation 8.1 (Katz and Penfold, 1952)

$$\rho R_p = k_1^* \bar{E}_0 - k_2^* \qquad 8.1$$

to relate the extrapolated range, R_p, as defined in Figures 8.2 to 8.4, to the mean electron energy at the phantom surface, $\bar{E}_0$. The constants k_1^* and k_2^* in this equation are specific to a given medium and can only be used if the practical range is measured in this medium. To circumvent this restriction the more general equation

TABLE 8.3

RANGE - ELECTRON ENERGY DATA FOR CARBON AND PERSPEX

NOMINAL BEAM ENERGY E_a (MeV)	CARBON ρ = 1.7 g/cm^3		PERSPEX ρ = 1.19 g/cm^3		ENERGY AT POINT OF MEASUREMENT $(E_p)_z$ (MeV)
	RANGE Rp(cm)	INCIDENT ENERGY $\bar{E}_o$(MeV)	RANGE Rp(cm)	INCIDENT ENERGY $\bar{E}_o$(MeV)	
11	3.42	10.67	4.55	10.70	6.85
9	2.78	8.77	3.69	8.77	4.91
6	1.73	5.64	2.38	5.82	1.66

$$\rho R_p \left(\frac{Z}{A}\right)_{eff} = k_1 \bar{E}_0 - k_2 \qquad 8.2$$

has been proposed by Markus (1961), where the factor $\rho(Z/A)_{eff}$ adjusts the practical range according to the relative electron density. The value of this factor is given by equation 8.3:

$$\left(\frac{Z}{A}\right)_{eff} = \frac{1}{\sum a_i} \left(a_1 \frac{Z_1}{A_1} + a_2 \frac{Z_2}{A_2} \ldots\ldots a_r \frac{Z_r}{A_r}\right) \qquad 8.3$$

where a_r is the mass in grammes of the r^{th} component of atomic weight A_r and mass number Z_r. From experiments in water, perspex and tissue-equivalent wax (M 3) Markus evaluated the constants k_1 and k_2 to be 0.285 and 0.137 respectively. Applying equation 8.2 to the practical ranges derived from Figures 8.2 to 8.4 and using a value of $(Z/A)_{eff}$ = 0.4996 (98.9% carbon 12, 1.1% carbon 13; Kaye and Laby, 1966) yields the mean energy of the incident electrons (Table 8.3). As noted above the depth-ionization curves illustrated in these figures were derived from rather few experimental points and, consequently, the practical range may have a considerable error. Fortunately, a second set of depth-ionization curves, measured in a perspex medium, were available. Whilst not conforming to the same experimental conditions as the calorimetric measurements in respect of the S.S.D. and the extra scattering foils, these curves were constructed from a great many observations at a large number of different depths. It may therefore be assumed that the practical ranges derived from these curves will be more accurate than the corresponding 'carbon' values. The incident electron energies for the perspex curves, calculated from equation 8.2 and using a value of $(Z/A)_{eff}$ = 0.538 for perspex (Markus, 1961) have been listed in column 4 of Table 8.3. Apart from a slight increase in magnitude, which might be expected from the absence of the extra scattering foils, these results are in excellent agreement with the

previously derived values.

The quantities $s_{C/AIR}$ and $p_{C/AIR}$ derived later in this chapter are both functions of electron energy. Therefore, whilst the mean energy of the incident electrons is of prime importance, a more useful parameter is the most probable electron energy, $(E_p)_z$, at the depth of measurement, z. This energy, $(E_p)_z$, can be related to the mean electron energy at the surface, $\bar{E}_o$, by equation 8.4 (Harder, 1966)

$$(E_p)_z = \bar{E}_o (1 - z/R_p) \qquad 8.4$$

Substituting z = 1.221 cm (i.e. the depth of the calorimeter axis below the surface) and using the appropriate values of R_p and $\bar{E}_o$ from the carbon depth-ionization curves (Table 8.3) the most probable electron energy at the centre of the calorimeter has been calculated. These figures are shown in the last column of Table 8.3. Although the depths of measurement for the two ionization chambers are slightly different from that of the calorimeter, the difference between the most probable energy of the electrons crossing the gas filled cavities and the electron energy at the centre of the calorimeter will be negligible. A much larger discrepancy in the depth of measurement exists between the calorimeter and the ferrous sulphate ampoules. Fortunately, the response of the ferrous sulphate dosimeter is substantially independent of the incident electron energy in the region under consideration here (Shalek and Smith, 1969). In addition, the calorimeter is energy independent and therefore this discrepancy will be of no consequence. The values of $(E_p)_z$ calculated from equation 8.4 have been expressed to three significant figures which is consistent with the 1% accuracy normally attainable with this method (I.C.R.U., 1972).

TABLE 8.4

CALORIMETER RESPONSE

DATE	BEAM ENERGY	THERMISTOR RESISTANCE	IRRADIATION RESPONSE	CALIBRATION RESPONSE
	E_a	R_T	$\frac{\Delta R_T}{R_T}/M \times \frac{T^2}{293.15^2}$	$\frac{\Delta R_T}{R_T}/W_A \times \frac{T^2}{293.15^2}$
	MeV	Ω	Ω/Ω.Monitor Units x 10^7	Ω/Ω.mJ x 10^5
28.2.74	11	2070 ± 15	2.049 ± 0.004 (13)	1.639 ± 0.007 (10)
1.3.74	11	2030 ± 10	2.041 ± 0.010 (12)	1.628 ± 0.004 (9)
9.3.74	11	2040 ± 5	2.035 ± 0.006 (15)	1.629 ± 0.004 (10)
2.3.74	9	2010 ± 5	1.946 ± 0.005 (13)	1.612 ± 0.024 (11)
3.3.74	9	2035 ± 5	1.933 ± 0.005 (12)	1.624 ± 0.026 (11)
4.3.74	9	2070 ± 5	1.929 ± 0.008 (12)	1.640 ± 0.005 (12)
9.3.74	9	2040 ± 5	1.901 ± 0.005 (8)	1.629 ± 0.004 (10)
6.3.74	6	2030 ± 5	1.074 ± 0.005 (15)	1.635 ± 0.008 (9)
7.3.74	6	2010 ± 5	1.066 ± 0.003 (14)	1.626 ± 0.003 (10)
8.3.74	6	2000 ± 5	1.081 ± 0.009 (18)	1.635 ± 0.004 (9)
	ALL	2000	Mean -	1.630 ± 0.0026 (8)
	11	2000	2.042 ± 0.004 (3)	-
	9	2000	1.927 ± 0.009 (4)	-
	6	2000	1.074 ± 0.004 (3)	-

8.2 CALORIMETER RESULTS

The response of the calorimeter to the energy deposited by the electron beams and the impressed electrical energy has been recorded in Table 8.4. This table follows the format of Table 7.1 where each entry refers to the mean of a number of experimental observations made on each day. The precise number of experiments has again been indicated by the figure in parenthesis. The uncertainty associated with each entry is the standard error of the mean. The complete series of measurements reported in Table 8.4 was taken with the same physical set-up of the calorimeter and its temperature measuring system and, therefore, the day to day change in the mean value of R_T is a direct result of the shift in the temperature of measurement. The total change in the value of R_T was less than 4% (i.e. $< 1K$) and thus the temperature correction discussed in Chapter 5 may be applied. As the headings of columns 4 and 5 show this adjustment has already been included in the data displayed in the table. In addition, the calibration response, column 4, has also been corrected for the absorber heater 'end effect' which decreases the measured value of W_A by 2.5%, and the temperature gradient effect (Chapter 5) which reduces the response by 0.42%. The systematic uncertainties associated with these correction factors have not been included in the uncertainties quoted in Table 8.4 which, as stated above, represent the random experimental variations only. These systematic uncertainties will be dealt with later in this chapter. Inspection of Table 8.4 shows that, with the exception of the last 9 MeV result, the agreement amongst each set of data is very good and within the quoted experimental uncertainties. The arithmetic mean value for each of the four sets of results has been indicated in the latter half of

TABLE 8.5

CALORIMETER SENSITIVITY

BEAM ENERGY E_a MeV	IRRADIATION RESPONSE / CALIBRATION RESPONSE mJ/Mon.Unit	ABSORBER MASS g	ABSORBED DOSE rads/ M.U
11	1.2528×10^{-2}	2.5118	0.4988
9	1.182×10^{-2}	2.5118	0.4706
6	0.6589×10^{-2}	2.5118	0.2632

Table 8.4. The uncertainty is again the SEOM and the figures in brackets refer to the effective number of degrees of freedom. Finally the sensitivity of the calorimeter, for each beam energy, has been expressed as the ratio of the calibration response to the irradiation response (Table 8.5). For the purposes of later calculations this sensitivity has been divided by the absorber mass to yield the sensitivity in rads per monitor unit.

8.3 IONIZATION RESULTS

In order to reproduce the irradiation conditions encountered during the calorimetric measurements, the calorimeter and its vacuum tank were removed from the heat shield and replaced by the jig holding the ionization phantom. To simulate the S.S.D. used in the calorimeter experiments, the upper surface of this phantom was placed at 134.3 cm from the source of the beam. The tufnol window was removed from the vacuum tank and placed over the aperture in the top of the perspex jig, Figure 6.3. The lid of the heat shield was then replaced and the electrical leads attached to the ionization chamber were led away from the heat shield via the redundant vacuum port. To investigate the effects of general recombination and the possibility of appreciable numbers of primary electrons accumulating in the central collecting electrode, ionization chamber measurements were again carried out at a number of polarising voltages of either sign. The results of these investigations are shown in Figures 8.6, 8.7 and 8.8, where the voltage integrated upon the Townsend capacitor, C_o, has again been plotted as a function of the reciprocal of the polarising voltage, V_p^{-1}. It must be noted that equation 7.2, on which figures 8.6 to 8.8 and the graphs of Figure 7.3 are based, is only true if the transit time of the ions produced by the radiation is short when compared to the

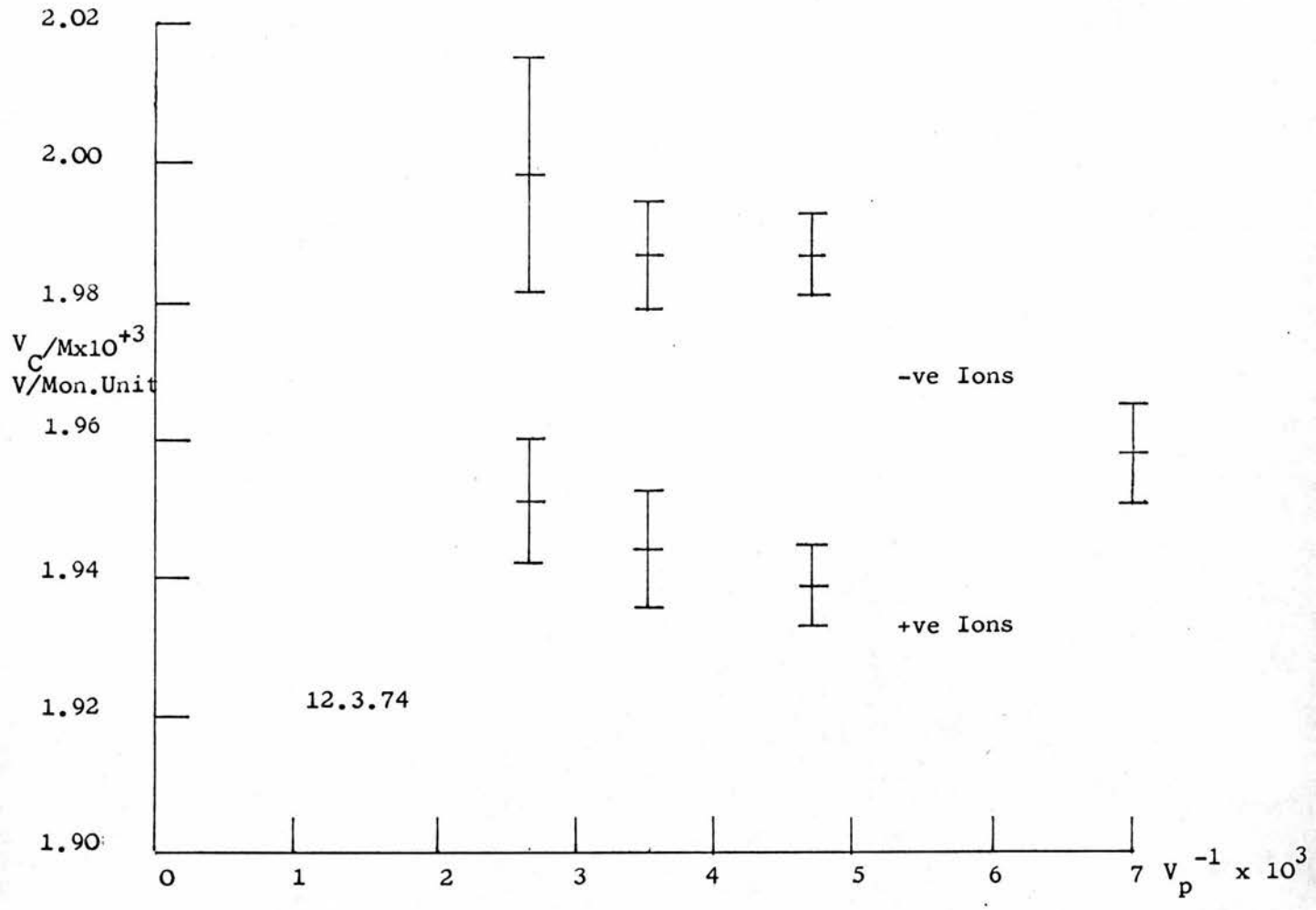

FIGURE 8.7 SATURATION CHARACTERISTICS 9 MeV BEAM

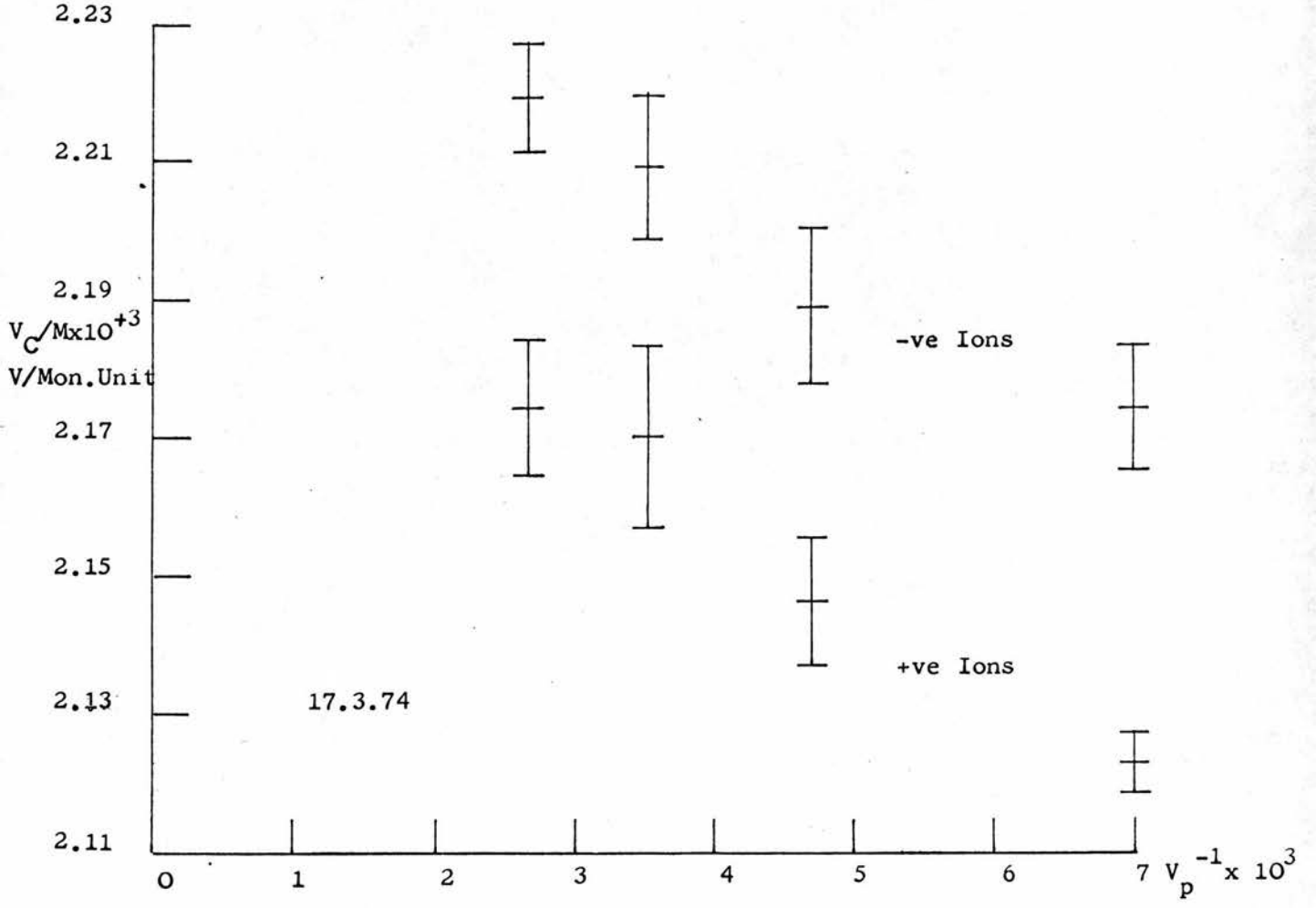

FIGURE 8.6 SATURATION CHARACTERISTICS 11 MeV BEAM

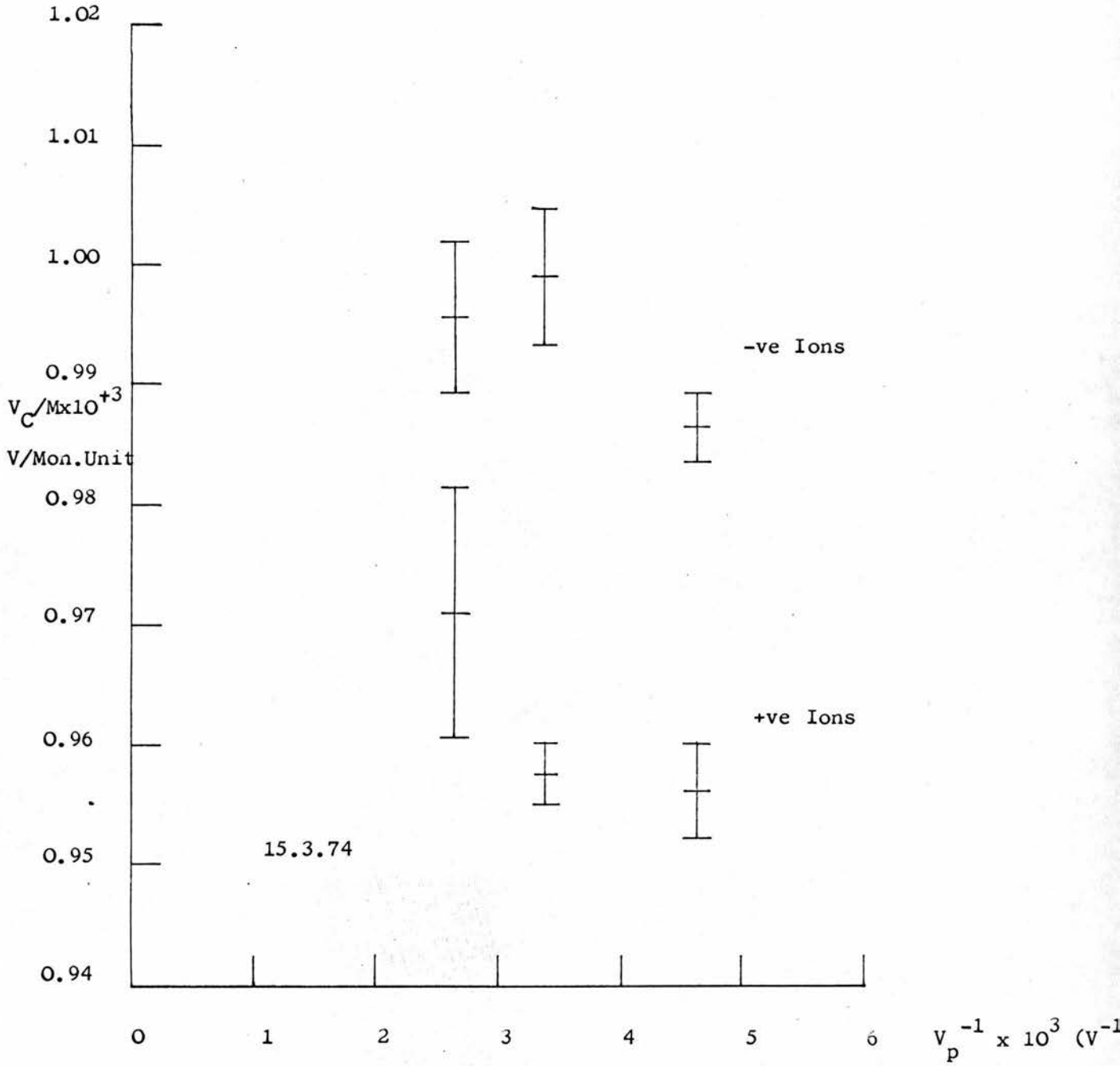

FIGURE 8.8 SATURATION CHARACTERISTICS 6 MeV BEAM

time which elapses between pulses. At the field strengths and chamber sizes used here the transit time is approximately 30 μs, very much less than the duty cycle of the accelerator. The values of V_C were corrected to 293.15 K and 760 mm Hg since the value of M, the monitor unit, was calculated at this temperature and pressure. The points plotted in Figures 8.6 to 8.8 are the mean values of a number of separate determinations for each voltage setting. The uncertainties associated with these points are the standard errors of the relevant means calculated from the experimental data. Each of these graphs indicates that the true value of the charge liberated by the radiation beam must again be found by performing a linear regression on the original data. The results of this manipulation are shown in Table 8.6, where the relationship $Y = AX + B$ has been assumed. The value of X is again the independent variable, $= V_p^{-1}$, and Y is the dependent variable, $= V_C/M$. The value of A then denotes the intercept with the Y axis, which is the desired result, and B is the slope of the regression line. It can be seen from this table that, in each set of results, the slope of the regression line is smaller for the negative polarising voltages. This phenomenon may possibly indicate two different collection efficiencies depending upon the sign of the ion gathered. However, since the errors are large and the value of the slope varies from energy to energy little useful information can be gained from this parameter. In contrast to the X-ray measurements the most striking feature of Figures 8.6 to 8.8 is the consistently higher yield of charge when negative ions are collected. This phenomenon is consistent with the accumulation of stopped, primary electrons in the central electrode. The magnitude of the effect

TABLE 8.6

SUMMARY OF LINEAR REGRESSION RESULTS FOR IONIZATION CHAMBER MEASUREMENTS

DATE	ENERGY E_a	POLARISING VOLTAGE	NUMBER OF POINTS N	INTERCEPT ON Y AXIS A $\times 10^3$	SLOPE B	ESTIMATED COMBINED ERROR (x,y) $\times 10^3$
11.3.74	11	+ve	19	2.2157	- 0.0078	$\pm$ 0.0103
17.3.74	11	+ve	24	2.2067	- 0.0120	$\pm$ 0.0125
	11	-ve	29	2.2453	- 0.0106	$\pm$ 0.0111
12.3.74	9	+ve	16	1.9811	- 0.0093	$\pm$ 0.0112
	9	-ve	23	2.0050	- 0.0040	$\pm$ 0.0127
14.3.74	9	-ve	21	2.0013	- 0.0064	$\pm$ 0.0130
13.3.74	6	+ve	15	0.9894	- 0.0082	$\pm$ 0.0098
15.3.74	6	+ve	14	0.9901	- 0.0087	$\pm$ 0.0056
	6	-ve	12	1.0200	- 0.0072	$\pm$ 0.0091

varies from 0.75% of the total charge collected for the 11 and 9 MeV measurements, taken near the peaks of the respective depth dose curves, to 1.5% for the 6 MeV beam in the 50% depth dose region. For each beam energy one set of measurements, of either sign of the polarising potential, was repeated to check the results of the paired values. As indicated in Table 8.6 these additional values of A_+ and A_- agree quite well with the paired values of A. The calculation of the true charge liberated, described in the next section, was based upon the mean value of the paired result. This procedure eliminates the extra electrons deposited in the collecting electrode, whether this phenomenon occurs in the chamber or stem region of this component.

Owing to difficulties in obtaining very small field sizes, the small stem section of the ionization chamber irradiated during the normal course of measurements was not separately exposed. The effect of the excess deposition of electrons in the stem has already been dealt with, therefore only charge leakage effects remain to be considered. In the absence of the radiation beam a negligible charge leakage from the capacitor occurred even when the highest polarising voltages were applied to the chamber and its leads. Also, the capacitor voltage remained steady after each irradiation indicating that radiation induced leakage, as well as inherent leakage, was negligibly small in these experiments. Nevertheless, since the evidence for these statements is rather indirect a systematic uncertainty of 0.2% (based on the figure derived in Chapter 7) has been included to allow for the possibility of charge leakage.

8.3.1 Calculation of the Ionization per Unit Mass

The product of the mean corrected value of the paired results, $(A_+ + A_-)$ and the value of the integrating capacitor and its leads

TABLE 8.7

CALCULATION OF CARBON/AIR MASS STOPPING POWER RATIO

$(E_p)_z$ MeV	J_g C/g.M.U.x10^7	$p_{C/AIR}$ -	$\bar{W}$ eV/Ion pair	D_C rads/M.U.	$s_{C/AIR}$ -	D.I.Corr. -	$s_{C/AIR}$ -
6.85	1.670	0.988	33.73	0.4988	0.897	1.006	0.902
4.91	1.498	0.984	33.73	0.4706	0.947	1.005	0.952
1.66	0.7551	0.961	33.73	0.2632	1.075	0.908	0.977

(C_o = 46840 pF) yields the charge, Q, liberated in the ionization chamber per monitor unit. The volume of this chamber was given in Chapter 6 as 0.5204 cm^3 and, since the value of Q was corrected to 293.15 K and 760 mm Hg, the appropriate density for the air within this volume is 1.199 x 10^{-3} g/cm^3 (Value, Kaye and Laby, 1966, Ambient air containing 0.04% of CO_2 by volume and 50% relative humidity). The mass of gas within the chamber is thus 6.240 x 10^{-4}g. The required value of J_g (ionization/unit mass) was found from the ratio Q/m for each beam energy and is shown in column 2 of Table 8.7.

8.3.2 Calculation of Mass Stopping Power Ratios

The calculation of the mass stopping power ratio for carbon to air is again based upon equation 1.4 which, in this instance, becomes

$$D_C = J_g . \bar{W} . s_{C/AIR} \cdot p_{C/AIR}$$

In contrast to the X-ray situation the perturbation factor, $p_{C/AIR}$, cannot be equated to unity and must be evaluated for the specific electron energy at the point of measurement. For a cylindrical ionization chamber, orientated with its axis perpendicular to the direction of the incident beam, a theoretical evaluation of this perturbation factor has been given by Harder (1968) (equation 8.5)

$$p_{C/AIR} = 1 - \frac{2b}{5\pi} \cdot r^{\frac{1}{2}} \qquad 8.5$$

where r is the radius of the chamber and the factor b is given by equation 8.6:

$$b = \frac{0.318\ E_S\ (E + \mu)}{X_o^{\frac{1}{2}}\ E\ (E + 2\mu)} \qquad 8.6$$

where E_S is a constant (= 21 MeV), X_o is the radiation length, μ is the electron rest mass in MeV (= 0.511), and E is the kinetic energy of the electrons traversing the chamber. Taking the most probable energy

TABLE 8.8

EXPERIMENTAL UNCERTAINTIES IN $s_{C/AIR}$

SOURCE		SEOM %	DEGREES OF FREEDOM
Irradiation Response	11 MeV	0.20	2
	9 MeV	0.47	3
	6 MeV	0.37	2
Calibration Response		0.16	8
Mass of Absorber		0.004	9
Charge Liberated	11 MeV A_+	0.57	24
	A_-	0.49	27
	9 MeV A_+	0.57	14
	A_-	0.63	21
	6 MeV A_+	0.57	11
	A_-	0.89	10
Capacitor Time Constant		0.02	12
" Leakage Resistance		0.09	5
Chamber Volume		0.40	8
D.I.Correction		0.00	-
Energy Required per Ion Pair ($\bar{W}$)		0.44	∞

TABLE 8.9

SYSTEMATIC UNCERTAINTIES IN $s_{C/AIR}$

SOURCE		MAGNITUDE %
Calorimeter:	Absorber Heater End Correction	0.50
	Temperature Gradients	0.42
Ionization Chamber:	Volume of Chamber	0.26
	Capacitor Resistance	0.09
	Charge Leakage	0.20
Others:	Perturbation factor	0.10
	D.I. Curve 9 and 11 MeV	0.30
	D.I. Curve 6 MeV	2.00

TABLE 8.10

SUMMARY OF MASS STOPPING POWER RESULTS

ENERGY MeV	$s_{C/AIR}$	SEOM	ν_{eff}	SYSTEMATIC UNCERTAINTY
6.85	0.902	$\pm$ 0.009	94	$\pm$ 0.007
4.91	0.952	$\pm$ 0.011	50	$\pm$ 0.008
1.66	0.977	$\pm$ 0.012	30	$\pm$ 0.021

of the electrons at the depth z, $(E_p)_z$, to be equivalent to E, the value of the perturbation co-efficient at the point of measurement can be evaluated for each beam. The results of this calculation are shown in column 3 of Table 8.7. Using the recommended value of $\overline{W}$ (column 4) and the appropriate calorimeter response, D_C, (column 5) the mass stopping powers have been listed in column 6. From the discussion of section 8.1 a further correction must be applied to these results to account for the slight discrepancy between the two points of measurement. The magnitude of this factor is shown in column 7 and the final corrected value of the mass stopping power ratio for carbon to air has been tabulated in the last column.

8.3.3 Uncertainties in the Value of $s_{C/AIR}$

A complete list of the experimental quantities involved in the determination of $s_{C/AIR}$ is presented in Table 8.8. This table follows the style of Table 7.2 where the SEOM was recorded as a percentage of the appropriate value and the experimental uncertainties have been combined according to equation 7.5. As before, the major component in the experimental uncertainty was due to the ionization measurements. The total random experimental uncertainty has been shown in Table 8.10 as the SEOM and the associated effective number of degrees of freedom. A compilation of the systematic uncertainties is presented in Table 8.9. With the exception of the correction for the point of measurement for the 6 MeV beam, the major systematic uncertainty derives from the absorber heater 'end effect' correction. As before the total systematic uncertainty was obtained by taking the square root of the sum of the squares of the individual uncertainties. The results of this calculation together with the final values of $s_{C/AIR}$ have been recorded in Table 8.10.

FIGURE 8.9 CARBON/AIR MASS STOPPING POWER RATIO ($s_{C/AIR}$) AS A FUNCTION OF ELECTRON ENERGY $(E_p)_z$

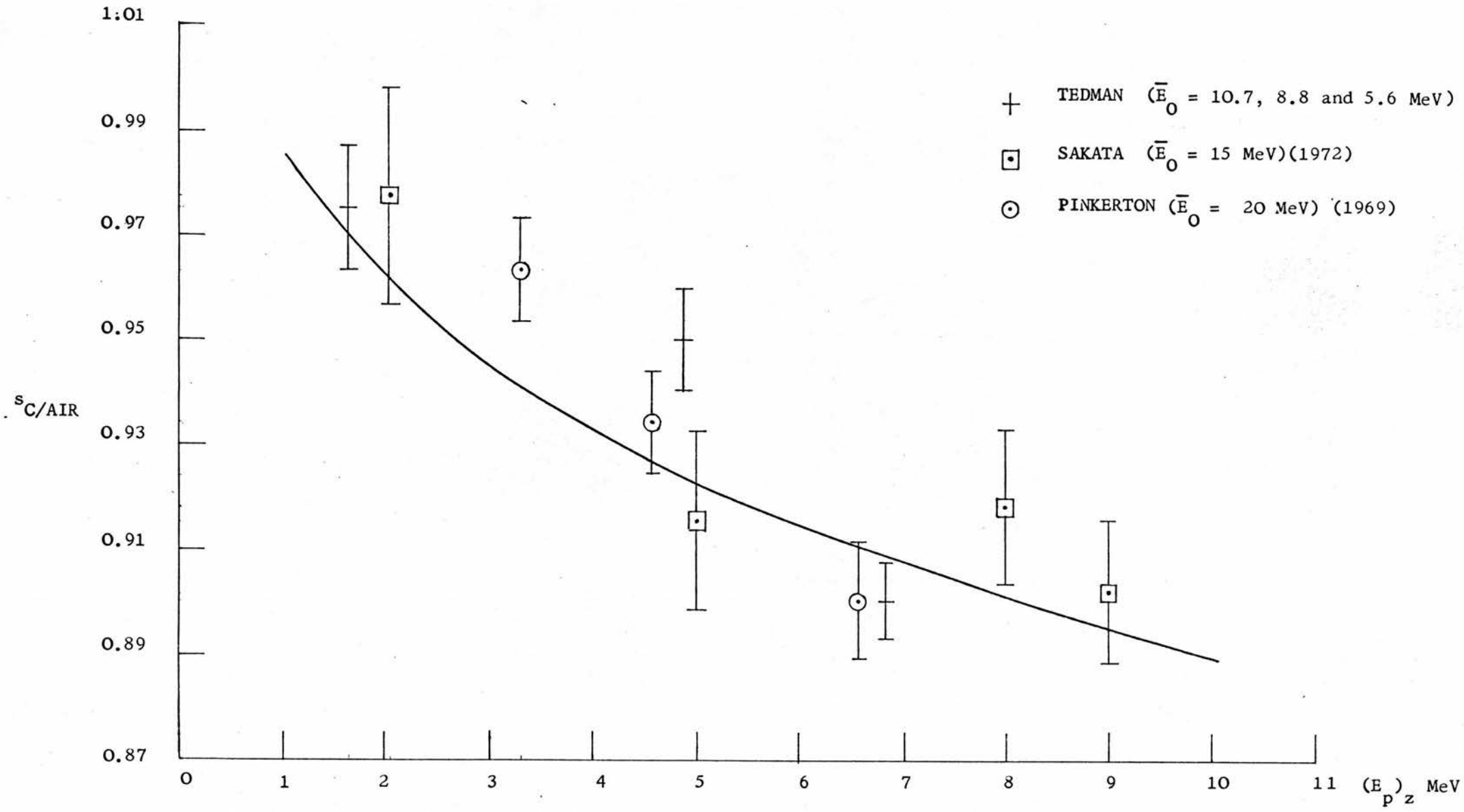

8.3.4 Comparison with other Values

The values of $s_{C/AIR}$ shown in Table 8.10 have been plotted in Figure 8.9, where the error bars shown in this graph refer to the SEOMs. Two other sets of experimental data have been displayed in this figure, namely the results of Pinkerton (1969) and Sakata (1972). In both of these cases several experimental determinations were performed at different depths within the phantom and only one incident beam energy was used (Pinkerton 20 MeV, Sakata 15 MeV). For the purposes of comparison with the present measurements Harder's formula, relating the most probable energy at a depth z to the incident beam energy, has been used to transform these authors' experimental data to the format illustrated in Figure 8.9. The solid curve shown in this figure refers to the mass stopping power for carbon to air derived from the theoretical tables of Berger and Seltzer (1964, 1966). It must be emphasised that these theoretical values were obtained with a beam of monoenergetic incident electrons, whereas all the experimental values are derived from electron fluxes with a finite, and possibly variable, spectral width. Nevertheless, if this energy spectrum is sufficiently narrow and is approximately symmetrical in the region of the peak energy, the mass stopping power ratio is a sufficiently slowly varying quantity to be represented by the mean, or most probable, energy of the electron spectrum. It will be observed that, in all cases, the experimental values are quite widely scattered and the only points which are in close agreement with the theoretical data are the presently determined 1.6 MeV value and Sakata's 9 MeV value. (It should be remembered that the actual electron energy for the present measurements has a probable systematic uncertainty of $\pm$ 0.1 MeV and this has been indicated by the length of the horizontal

TABLE 8.11

FARMER-BALDWIN RESULTS

Beam Energy E_a (Mev)	11	9	6
Farmer-Baldwin Readings at 293 K and 760 mmHg per Monitor Unit	0.6081 ± 0.0018 0.5981 0.6035 0.5987 0.6084	0.5579 ± 0.0017 0.5494 0.5577 0.5590	0.2965 ± 0.0009 0.3019 0.2937 0.2972
Mean SEOM	0.6034 ± 0.0022	0.5560 ± 0.0022	0.2973 ± 0.0017

TABLE 8.12

CALCULATION OF CARBON/AIR C_E VALUES

$(E_p)_z$ MeV	R Reading/ Mon.Unit	N_4 R/Reading	D_C rads/Mon. Unit	D-I Corr.	C_E rads/R
6.85	0.6046	1.06	0.4988	1.008	0.785
4.91	0.5571	1.06	0.4706	1.005	0.801
1.66	0.2972	1.06	0.2632	1.005	0.840

error bars). In general, it must be concluded that, until much more information becomes available and the uncertainties in each individual value are decreased, no categoric conclusion can be drawn between the theoretical and experimental values. However, from the data presented in this graph there is some evidence to indicate that the theoretical data may be systematically undervalued.

8.4 FARMER-BALDWIN MEASUREMENTS

The Farmer-Baldwin chamber measurements were performed with essentially the same phantom and window arrangements used in the carbon ionization chamber measurements, the only variation being that a different sheath was used to locate the Farmer-Baldwin chamber. The results of these experiments are displayed in Table 8.11. Each entry is the mean of 7 readings corrected to 293 K and 760 mm Hg and normalised by the appropriate monitor unit reading. On any given occasion the response of this instrument was found to be highly reproducible and the uncertainties accompanying the figures in Table 8.11 represent the reading error of the Farmer-Baldwin scale. The mean value of the Farmer-Baldwin response for each of the three energies has been tabulated at the foot of the appropriate column. The uncertainties in these figures are represented by the standard error of the mean for each group of results.

In routine measurements with the Farmer-Baldwin chamber the direct scale reading of the instrument, corrected for temperature and pressure, is usually sufficiently accurate. When a more precise determination of the charge collected by the Farmer-Baldwin chamber is required consideration must be given to the effects of the ionic recombination, charge accumulation in the collecting electrode and stem irradiation. The theoretical efficiency of the Farmer-Baldwin

chamber, calculated from equation 7.1, at a dose rate of 0.014 rads/pulse (9 and 11 MeV beams) is 99.79%. and at a dose rate of 0.007 rads/pulse (6 MeV beam) it is 99.89%. In effect, these figures represent the upper limits of the collection efficiency which can only be achieved when a perfectly uniform radial field is preset. The Hospital Physicists Association (H.P.A., 1971) have recommended that the efficiency of the Farmer-Baldwin chamber should be taken as 99.5% at a dose rate of 0.017 rads/pulse and a collecting voltage of 160 V. For these parameters the ideal efficiency is 99.7%, therefore, an adjustment of -0.2% has been applied to this ideal value to allow for the non-realisation of a perfect electric field and other effects. Applying this same adjustment to the ideal collection efficiencies for the present conditions yields a true efficiency of 99.6% for the 9 and 11 MeV beams and 99.7% for the 6 MeV beam. In the absence of a rigorous experimental verification for the collection efficiencies it would seem prudent to include a systematic uncertainty of $\pm$ 0.2% in these estimated values (i.e. equal to the difference between the true and ideal efficiencies). The mass of the aluminium collecting electrode inside the Farmer-Baldwin chamber is almost four times less than the carbon electrode used in the ionisation chamber measurements described in the previous section. As the mass stopping power ratio for carbon to aluminium is approximately 1.09 at the two upper energies and 1.08 at the lower energy, it may be concluded that the total charge deposited by the primary electron flux in the collecting electrode will be some 3.66 times lower than the corresponding accumulation of charge in the carbon ionization chamber. The Farmer-Baldwin chamber in question collected negative ions, thus the total charge accumulated must be reduced by 0.20% in the 11 and 9 MeV cases, and 0.34% in the

case of the 6 MeV beam. These correction factors are again unproven and consequently systematic uncertainties of the same order of magnitude as the correction factors must be included.

In common with all previous experiments the volume of the chamber stem exposed to the radiation beam was kept to a minimum. However, because of the difficulty in irradiating the desired portion of the stem alone, no direct information is available to predict the behaviour of the stem during irradiation. The alternative procedure of shielding the stem with a lead block was not a feasible approach for two reasons. Firstly, the presence of the lead block could distort and scatter the electron flux in the region of the sensitive measuring volume, leading to a false result. Secondly, even if no distortion was present, it would be very difficult to detect accurately such a small change (0.2 - 0.35%) in the reading of the Farmer-Baldwin.

In the absence of any radiation striking the chamber the scale reading remained constant indicating that no inherent leakage was occurring. Also, since the scale reading remained constant at the end of each exposure, radiation induced leakage in the stem of the Farmer-Baldwin chamber has been assumed to be negligible, although a systematic uncertainty of 0.2% has been included under the heading of charge leakage in Table 8.14.

Table 8.12 has been constructed according to the variables comprising equation 8.7:

$$D_C = R\ N\ C_E \qquad 8.7$$

The values of R recorded in this table have been corrected for the lack of total charge collection and the charge deposition in the central electrode as discussed above. The values of D_C were derived from Table 8.5 and the value of N.P.L. calibration factor, N, was 1.06

TABLE 8.13

EXPERIMENTAL UNCERTAINTIES IN C_E (CARBON/AIR)

SOURCE		SEOM %	ν_{eff}
Calorimeter: Irradiation Response	11 MeV	0.20	2
	9 MeV	0.47	3
	6 MeV	0.37	2
Calibration Response	-	0.16	8
Absorber Mass		0.004	9
Farmer-Baldwin Measurements:	11 MeV	0.36	4
	9 MeV	0.40	3
	6 MeV	0.57	3

TABLE 8.14

SYSTEMATIC UNCERTAINTIES IN C_E (CARBON/AIR)

SOURCE	MAGNITUDE %
Calorimeter: Absorber Heater "End Effect"	0.50
Temperature Gradients	0.42
Farmer-Baldwin Chamber:	
Ionization collection efficiency	0.20
Charge Leakage	0.20
Electrons stopped in Collecting Electrode (9 and 11 MeV)	0.20
Electrons stopped in Collecting Electrode (6 Mev)	0.34
Depth Ionization Correction (9 and 11 Mev)	0.30
" " " (6 Mev)	2.00
N.P.L. Calibration Factor	1.00

TABLE 8.15

SUMMARY OF C_E (CARBON/AIR) VALUES

ENERGY (Mev)	C_E	RANDOM UNCERTAINTY (SEOM)	ν_{eff}	SYSTEMATIC UNCERTAINTY
6.85	0.785	$\pm$ 0.003	3	$\pm$ 0.010
4.91	0.801	$\pm$ 0.005	3	$\pm$ 0.010
1.66	0.840	$\pm$ 0.006	3	$\pm$ 0.020

for the chamber used in these experiments. The correction factors to allow for the differing positions of measurement between the two dosimeters have been shown in column 5, and the final, corrected C_E values for a carbon phantom have been recorded in column 6. The value of the N.P.L. calibration factor, N, is only quoted to three significant figures, therefore, it may be deduced that the uncertainty in this factor will not be less than 1%. The major portion of this uncertainty is expected to be the result of systematic effects (Barnard, 1964; Barnard et al., 1964). Consequently, a value of 1% has been entered in the table of systematic uncertainties under this heading. A complete list of the various uncertainties has been shown in Tables 8.13 and 8.14 whilst the final results have been recorded in Table 8.15.

8.4.1 Comparison of C_E Results

The comparison of the C_E values, calculated in the previous section, with other experimental and theoretical results is complicated by the variety of ways in which various authors have displayed their data. The meaning of this statement can best be illustrated by an example. The experimental C_E values quoted by Harder (1965) were derived from measurements made at the peak of the depth dose curve for three different initial electron energies. The C_E values were then displayed as a function of the incident energy, having previously specified the depth of measurement. In contrast, the theoretical data of Kessaris (1970b) was displayed in the form of a curve showing the variation of C_E with the depth in the phantom, or the average primary energy at that depth. Whilst the former method has the advantage of excluding assumptions concerning the electron spectrum at the point of measurement, all comparative measurements must be made under the same specified conditions. A further complication encountered when comparing C_E

FIGURE 8.10 CARBON/AIR C_E VALUES AS A FUNCTION OF ELECTRON ENERGY $(E_p)_z$

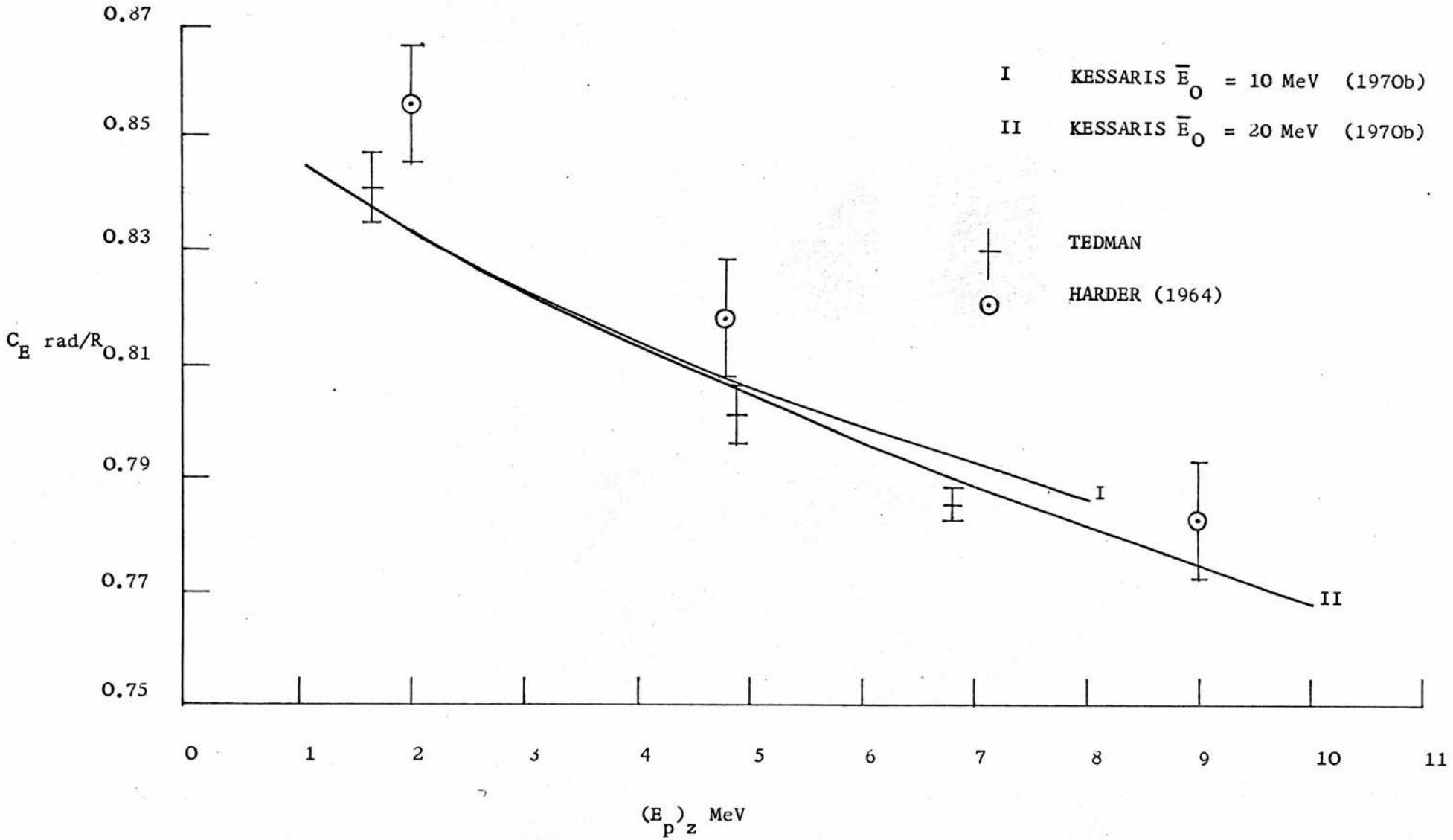

values is the variation in the choice of absorbing medium. Many experimental C_E results, in particular those derived from calorimetric investigations as well as much of the theoretical data, refer to a carbon absorbing medium. In contrast, many other experimental C_E values, and the majority of routine measurements, relate to a water medium. If it is assumed that the C_E value is predominantly a function of the mean energy of the primary electrons at the point of measurement, it would seem logical to display the C_E values as a function of this energy. The plausibility of this assumption is examined in Figure 8.10, where curves I and II represent the theoretical C_E values obtained by Kessaris (1970b) for 10 and 20 MeV incident electron energies respectively. These C_E values have been plotted as a function of the mean electron energy at the point of measurement. Apart from a small difference at higher energies these two curves show very close agreement. It can therefore be deduced that the shape of the energy spectrum is largely immaterial, and the C_E values can be well defined by a measurement of the mean primary electron energy at the point of interest. Accordingly, the C_E factors shown in Table 8.15 have been reproduced in Figure 8.10 as a function of the mean, primary electron energy. In addition, invoking the use of equation 8.4, the experimental C_E values of Harder (1965) have been converted to this format and are shown in Figure 8.10. The experimental uncertainties shown in this figure represent the standard error of the relevant mean. It can be seen that quite good agreement exists between the present experimental values and the theoretical data of Kessaris (1970b). The experimental results of Harder (1965) were derived from measurements with a scintillation spectrometer and cannot therefore be considered an absolute measurement. Whilst it would be pure conjecture

FIGURE 8.11 WATER/AIR C_E VALUES AS A FUNCTION OF ELECTRON ENERGY $(E_p)_z$

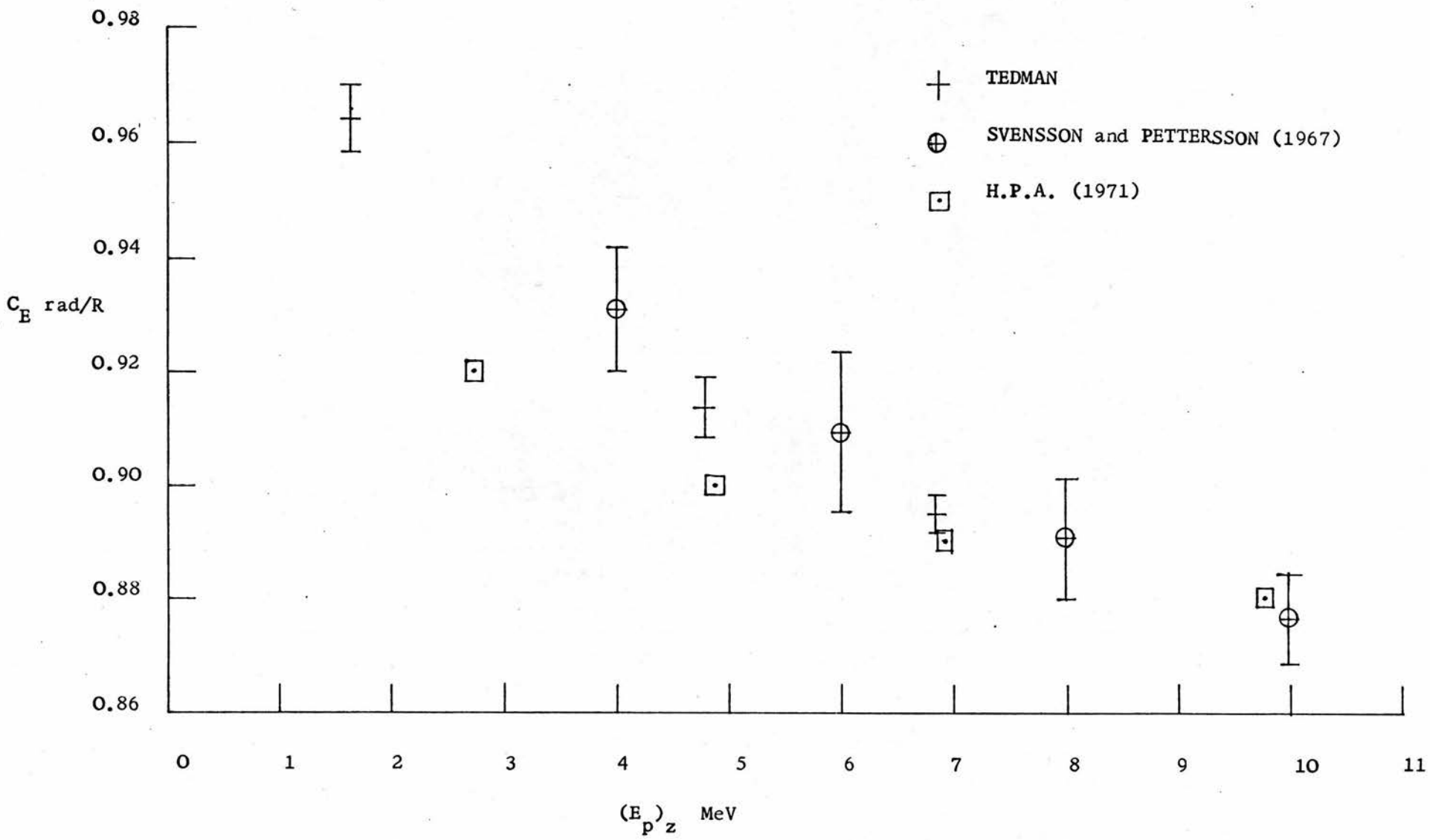

to speculate to what extent the difference in reference systems may be responsible for this discrepancy between the C_E values of Harder and the present results, a true appreciation of Figure 8.10 should include this consideration.

It should also be remembered that the theoretical data of Kessaris (1970b) refer to an infinitesimally small chamber with a perturbation factor of unity. Thus, it is to be expected that the curves I and II in Figure 8.10 will be greater than the practical values. Using the relationship shown in equation 8.8 (Svensson and Pettersson 1967; Almond, 1967) the C_E value for water can be calculated by multiplying the present C_E results by the appropriate mass stopping power ratio for water to carbon

$$C_E = A\, s_{C/AIR}\, p_{C/AIR}\, \frac{\overline{W}}{e} \qquad 8.8$$

A further small correction is also necessary to convert the carbon-air perturbation factor to a water-air perturbation factor. This correction may be evaluated from equations 8.5 and 8.6. Using the relevant mass stopping power ratio calculated from the tables of Berger and Seltzer (1964, 1966) and the above-mentioned perturbation adjustment factor, the carbon-air C_E values have been converted into the water-air C_E values and the results of these calculations have been shown in Figure 8.11. Also shown in this figure are the experimental results of Svensson and Pettersson (1967) and the C_E values recommended by the Hospital Physicists Association (H.P.A., 1971). The former of these two sets of values was derived using a ferrous sulphate dosimeter ($G = 15.56$, 0.4 M H_2SO_4) and may thus be subject to a systematic uncertainty. The C_E values recommended in the H.P.A. guide were tabulated as a function of the incident electron energy and a specified depth of measurement. To convert these data into a format

suitable for inclusion in Figure 8.11 equation 8.1, which related the range in water to the incident electron energy, and equation 8.4, which gave the mean electron energy as a function of the depth, were used. Values of k_1 = 0.521 and k_2 = 0.376 (Markus, 1961) were substituted in equation 8.1. Although no uncertainties have been included in the H.P.A. figures, the accuracy is expected to be approximately $\pm$ 3%. It can be seen that the agreement between all the sets of data is quite close, especially at the higher energies. However, in view of the better agreement between the two sets of experimental data, there is some indication that the low energy H.P.A. C_E values are too small. It should be remembered though, that an additional systematic uncertainty is involved in converting the carbon-air C_E figures to water-air values and, without further experimental verification, the last statement must remain unsubstantiated.

8.5 FERROUS SULPHATE RESULTS

The polythene irradiation cells containing the ferrous sulphate solution were placed in the phantom described in Chapter 6. In common with the previous ionmetric measurements these cells were irradiated with the same beam geometry and entrance windows used in the calorimetric experiments. The dosimeter solution contained 10^{-3} Moles/l of ferrous ammonium sulphate and 10^{-3} Moles/l of sodium chloride dissolved in 0.4 Molar sulphuric acid. All the chemicals used in the preparation of this solution were analar grade reagents and the water used in the dilution of the concentrated acid was obtained by redistilling a solution of alkaline potassium permanganate solution and distilled water. Six cells were irradiated at each beam energy, and, on each occasion, a further six were left un-irradiated to act as controls.

TABLE 8.16

CALCULATION OF FERROUS SULPHATE G VALUE

ENERGY (E_a) MeV	OPTICAL DENSITY O.D.U./Mon.Unit x 10^9	MASS-STOPPING POWER RATIO (Carbon/Water)	DEPTH-IONIZATION CORR.	ABSORBED DOSE rads/Mon.Unit	G Fe^{3+}/100 eV
11	94.11 $\pm$ 0.21	0.878	1.022	0.4988	15.1
9	88.54 $\pm$ 0.17	0.876	0.998	0.4706	14.7
6	55.57 $\pm$ 0.16	0.871	0.909	0.2632	14.7

The irradiations were performed at temperatures varying between 292 K and 295 K. Both sets of cells were then returned by post from the irradiation site in Sheffield to the processing laboratory in Edinburgh (Transit time 1-2 days). The yield of ferric ions was measured by observing the change in optical density, Δ A, between the irradiated and un-irradiated control solutions. These measurements were made with a Pye Unican SP 500 series 2 spectrophotometer using cells having an optical path length of 5 cm in the dosimeter solution. The relationship between the change in optical density and the absorbed dose, in eV/g, received by the solution is given by equation 8.9:

$$D_{FeSO_4} = \frac{\Delta A \,.\, N_A}{\rho.1.\ \varepsilon_m.G} \qquad 8.9$$

In this equation N_A refers to Avogadros number, ρ is the density of the dosimeter solution (= 1.024 g/cm^3, Svensson and Pettersson, 1967), 1 is the optical path length in the dosimeter solution (cm), ε_m is the Molar extinction coefficient for the ferric ions (=2122 $\pm$ 9 litre/mole.cm at 293 K, (Law, 1970) and G is the yield of ferric ions per 100 eV of energy absorbed.

The measured optical densities are shown in Table 8.16 and the uncertainties associated with these figures represent the SEOMs for 5 degrees of freedom. It was noted above that equation 8.9 yielded the absorbed dose in the dosimeter solution. It is expected that the absorbed dose in water will be 0.4% higher than this value. (Svensson and Pettersson, 1967). However, for the purposes of comparing the dose received by the ferrous sulphate dosimeter with the calorimetric measurements, it is the energy absorbed in carbon and not water which is important. Consequently the value of D_{FeSO_4} must be multiplied by the factor 1.004 x $s_{C/WATER}$ to give the required

dose. The values of the mass stopping power ratio to be substituted in this factor were evaluated at the relevant electron energy at the depth of measurement for the ferrous sulphate cells. The mass stopping power ratios were again taken from the tables of Berger and Seltzer (1964, 1966). It may be argued that the mass stopping power ratio should be evaluated at the depth of measurement for the calorimeter, but, since this ratio is such a slowly varying function of energy, this difference is immaterial. Finally a depth-dose correction must be included to account for the differing points of measurement between the two systems. This factor has been shown in column 4, whilst the appropriate calorimetric dose has been recorded in column 5 of Table 8.16.

8.5.1 Calculation of Uncertainties

The experimental uncertainties involved in the calorimetric measurements have already been summarised in Tables 8.8 and 8.13. The additional experimental uncertainties encountered in the calculation of the G value are derived from the measurements of the optical density, shown in column 2, Table 8.16, and the uncertainty in the molar extinction coefficient (0.43%). For the purposes of evaluating the total uncertainty it has been assumed that any uncertainties in the values of ρ, 1 and N_A are negligible. The total random uncertainty has been displayed in Table 8.17 as the SEOM and the effective number of degrees of freedom. In addition to the systematic uncertainties involved in the calorimetric measurements and the depth-dose corrections, Tables 8.9 and 8.14, a further 1% must be included in the total systematic error, Table 8.17, to allow for the possible error in the mass stopping power ratio of Berger and Seltzer used to convert the measured dose into the dose in carbon.

TABLE 8.17

COMPARISON OF FERROUS SULPHATE G VALUES

SOURCE	INCIDENT ELECTRON ENERGY (MeV)	G	UNCERTAINTY		
			EXPERIMENTAL		SYSTEMATIC
			SEOM	ν_{eff}	
Tedman	10.7	15.1	$\pm$ 0.08	5	$\pm$ 0.19
	8.8	14.7	$\pm$ 0.10	5	$\pm$ 0.18
	5.6	14.7	$\pm$ 0.10	5	$\pm$ 0.34
Geisselsoder et al. (1963)	10	15.17	$\pm$ 0.28*	-	-
	20	15.32	$\pm$ 0.34*	-	-
Pettersson and Hettinger (1967)	20$^{\Phi}$	15.56	$\pm$ 0.12	-	-
Almond (1967)	13.25	15.35**	$\pm$ 0.40$^{\theta}$	-	-
	15.9	15.25**	$\pm$ 0.40$^{\theta}$	-	-
	24.0	15.20**	$\pm$ 0.40$^{\theta}$	-	-
Anderson (1962)	15	15.2	$\pm$ 0.40$^{\theta}$	-	-
Pinkerton (1969)	20	15.52	$\pm$ 0.22$^{\theta}$	-	-
I.C.R.U. (1972)	-	15.7	$\pm$ 0.6	-	-

* Standard Deviation.

$^{\theta}$ Definition of Uncertainty not Given.

** Using extinction coefficient of 2196 1/mole.cm (I.C.R.U. 1972).

$^{\Phi}$ Estimated Mean Primary Energy.

No allowance has been made for the difference between the phantom geometries of the calorimeter and the ferrous sulphate cells but a figure of 3% would not be unreasonable.

8.5.2 Comparison of G. Values

To facilitate a comparison with the present G value results several other G value determinations, derived from calorimetric experiments, have been listed in Table 8.17. For electron energies in the million electron volt region the yield of ferric ions per unit of absorbed energy is thought to be constant. Therefore no attempt has been made to specify the G value as a function of the electron energy at the point of measurement, although incident beam energies have been recorded. In most papers very little information has been given concerning the systematic uncertainties. However, the calorimeters of Geisselsoder, Almond, and Pinkerton all require the mass stopping power conversion factor described above, and it can thus be assumed that the systematic uncertainty in these results will be at least 1%. In comparison to the other values listed in this table the present G values are rather low, particularly for the 9 and 6 MeV beams. To what extent the difference in phantom geometries may be responsible for this discrepancy is difficult to ascertain, and without this knowledge the present results must be treated with some degree of caution. Nevertheless, it would appear quite significant that, in all cases, the calorimetric determination of the yield of ferric ions is lower, and in some cases much lower, than the G value recommended by the I.C.R.U. (1972). Whilst the uncertainty attached to this recommendation is sufficiently large to encompass most of the experimental results, it would appear that a lower G value might be more appropriate.

CHAPTER 9.

C R I T I C I S M

The performance of the calorimeter and the calibration of the various secondary dosimeters has been described in the preceding chapters. Before concluding this thesis however, it would seem pertinent to present an appraisal of the calorimetric method and the difficulties involved. In this respect it will be useful to classify the problems encountered under three general headings, namely (a) Design and Construction, (b) Temperature Stability and Measurement, and (c) Beam Monitoring.

(a) Design and Construction

The technical problems involved in the design and construction of the calorimeter were fully examined in Chapter 3, but it is worth emphasising that many of the difficulties are directly attributable to the scale, or small size, of the components. This particular problem will be inherent in all calorimeters and can only be reduced by improvement in handling techniques, such as the use of micro-manipulators. A further problem, which was vividly demonstrated in Chapter 3, is the gulf between what is practically possible and that which is theoretically desirable. An excellent example of this confrontation was the modification of the absorber geometry from the initial coin-shaped design to the cylindrical rod-shaped design. Although factors were later adduced to correct for the extent of the absorber cross-section in the direction of the beam, the coin-shaped geometry would have provided a more localised position of measurement and this type of design is to be recommended wherever possible.

The problems relating to the calibration of the absorber, which were intimately related to the reasons for modifying the design, were responsible for the two major systematic uncertainties in the calorimetric measurements. Firstly, since a considerable portion of the heater wire was not in direct contact with the absorber, it was difficult to measure accurately the amount of heat deposited within the absorber. This source of uncertainty will always be present to a greater or lesser extent with discrete heaters, but with exceptional care, its magnitude could probably be decreased fourfold. The second, and far more intractable problem , concerns the temperature gradients which arise during calibration with a discrete heater. In the present case every effort was made to distribute the heating wire as evenly as possible throughout the absorber, but a correction of 0.42% still appeared necessary to correct for the ensuing temperature gradients. A similar correction factor, of magnitude 0.2%, was obtained by Engelke and Hohlfeld (1971b) in their coin-shaped calorimeter absorber. It would therefore seem likely that such values represent the lower limits of the uncertainties attainable by this method of heating. The development of a bulk heating material with a minimal heat defect by the National Physical Laboratory (Kemp, 1971) offers the hope of a considerable improvement in both of these sources of uncertainty and, provided that the use of such a material proves practicable, its use is to be recommended in the future.

(b) Temperature Stability and Measurement

The problem of temperature stability, which is of fundamental importance in all calorimeters, has already been discussed at some length. Whilst the choice of a multi-jacket system in the present

calorimeter performed tolerably well in practice and circumvented the extra constructional problems necessitated by other approaches, its use is more suitable to laboratory situations where the temperature variation of the environment may be controlled to some extent. In other situations, when the ambient temperature cannot be constrained, a twin absorber system or a thermostatically controlled mantle, or even a combination of both these systems, is clearly desirable.

There is a limit beyond which further improvements in temperature stability will only be of use if the temperature sensitivity of the measuring system can be increased proportionately. However, the introduction of low noise, high gain, differential-input amplifiers together with improvements in oscillator stability characteristics and low pass active filters will make a significant improvement on the ultimate sensitivity attainable in a system such as that described in Chapter 4. It therefore seems unlikely that future calorimeters will be limited by instrumentation considerations.

(c) Beam Monitoring

In contrast to the problems outlined above, which were peculiar to the design and construction of the calorimeter, the difficulty in accurately measuring the quantity of radiation energy impinging upon the phantom is common to all dosimetric systems, not to mention clinical treatments. That this is in fact so can be amply demonstrated by considering the ionization chamber results, which are usually renowned for their accuracy and reproducibility but in the present case yielded the largest experimental uncertainties. Although one particular theory describing the variation of the beam profile for the 4 MV X-ray generator has been advanced, in the absence of any firm evidence to the contrary it must be assumed that profile variation

is a purely random event. Hence the internal monitor chamber readings should vary in a totally random way and the mean value of a series of experiments should converge to the true population mean as the sample size is increased. Therefore, there is no necessity to introduce a second monitor chamber. Unfortunately though, the size of the sample which may be required to yield an acceptably small experimental uncertainty may be prohibitively large, and recourse must then be made to the introduction of a second monitor chamber which will sample the desired field. Although such a chamber may distort the field, this complication may not be important if the same irradiation geometry is used for every exposure, whether of the calorimeter or a secondary dosimeter. Such exposures may not then correspond directly to the beams used in clinical practice but this will be of secondary importance.

In addition to beam monitoring problems the differences in phantom geometry can also create systematic uncertainties in the reproduction of irradiation conditions. Inevitably the different types of sensitive volume will create differences in the phantom geometries, but, as long as particularly gross dissimilarities are avoided and the position of measurement is known, this particular problem should not present great difficulties.

In conclusion it may be stated that, whilst micro-calorimetry will remain technically difficult and rather complex, provided due care and consideration are exercised in the areas outlined above, definite improvements in the calibration factors of secondary dosimeters should be obtained, thereby opening the door to improved methods of treatment.

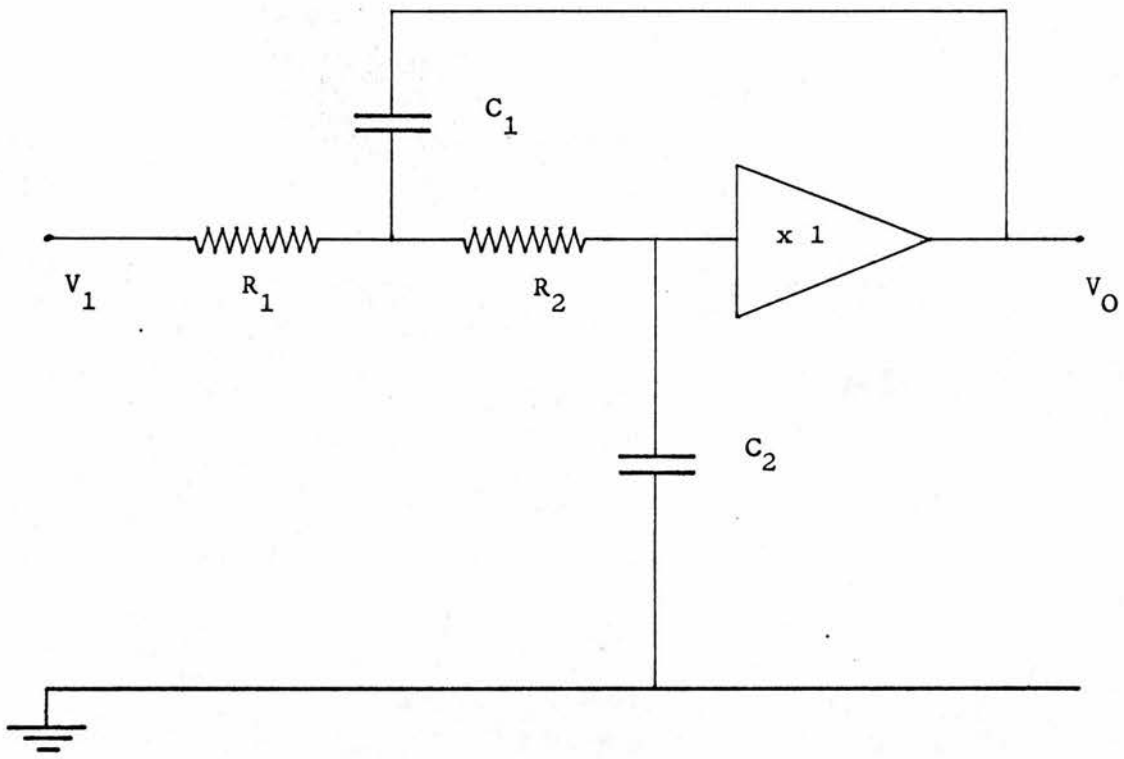

FIGURE A1.1

APPENDIX I

THE DESIGN OF LOW PASS BUTTERWORTH FILTERS

Consider Figure A1.1 which illustrates two RC circuits coupled to a unity gain amplifier.

The transfer function of this circuit may be derived as follows: The output voltage V_O is given by

$$V_O = V^* \frac{1}{1 + s R_2 C_2} \qquad \text{A.1.1}$$

where s denotes a complex frequency.

Using Kirchoffs law of current summation at the node V^* gives

$$\frac{V_1 - V^*}{R_1} + \frac{V_O - V^*}{1/sC_1} - \frac{V^*}{(R_2 + 1/sC_2)} = 0 \qquad \text{A.1.2}$$

Substituting for V^* in equation A.1.2 yields, on rearranging,

$$\frac{V_O}{V_1} = \frac{1}{1 + sC_2(R_1 + R_2) + s^2 R_1 R_2 C_1 C_2} \qquad \text{A.1.3}$$

which is the desired transfer function. The transfer function for a second order Butterworth filter with a frequency cut off of $\omega_O = \frac{1}{\tau}$ (- 3dB point) is given by (Kuo, 1966)

$$\frac{V_O}{V_1} = \frac{1}{1 + s\sqrt{2}\,\tau + s^2 \tau^2} \qquad \text{A.1.4}$$

Thus if

$$\sqrt{2}\,\tau = C_2(R_1 + R_2)$$

$$\text{and} \qquad \tau^2 = R_1 R_2 C_1 C_2 \qquad \text{A.1.5}$$

then the circuit of Figure A.1.1 will produce a second order Butterworth response. Using $R_1 = R_2 = R$ and $\tau^2 = \tau_1 \tau_2$ the conditions of equation A.2.5 can be satisfied by

$$\tau_1 = \frac{\tau}{\sqrt{2}} = \frac{R\,C_1}{2} \qquad \text{A.1.6}$$

and $$\tau_2 = \sqrt{2}\,\tau = 2\,R\,C_2 \qquad \text{A.1.7}$$

Values of R = 100 kΩ and C_1 = 20 μF and C_2 = 10 μF were used in the circuit shown in Figure 4.9 yielding a cut-off frequency of approximately 1.4 radians per second or 0.2 Hz.

To create a unity gain operational amplifier illustrated in Figure 4.9 a feedback signal was applied to the inverting input of the amplifier via a 200 kΩ resistor. The purpose of this resistor was to balance the offset currents flowing into the amplifier terminals and thus reduce any d.c. offset voltage appearing at the output.

APPENDIX II

ABSOLUTE MEASUREMENT OF CAPACITANCE

Section 6.2.3 described the Townsend balance circuit used for measuring the charge liberated in the air volume of the carbon-walled ionization chamber. The value of this charge, Q, is determined solely by the measured back-off voltage V_B, and the size of the integrating capacitor, C_O. The digital voltmeter used in these measurements had a precision of 0.01% for a reading of 2.0000 volts and it was therefore felt desirable to measure the capacitance to an accuracy of at least 0.1%.

Usually a capacitance measurement of this precision would be carried out on a ratio transformer bridge such as the Wayne Kerr Model B 221, the desired uncertainty being attained by performing a sufficient number of observations. Unfortunately, such a measurement would yield the a.c. capacitance at the frequency of measurement, normally 1 kHz. In the present case the capacitor is operated in the d.c. mode and, therefore, it is the d.c. capacitance which is the required parameter. (Strictly, the capacitor is used in an a.c. mode with a bandwidth of 0 to 1/t, where t is the time for the integration of the ion-chamber charge upon the capacitor, but, since t is of the order of 150 → 300 s, this bandwidth is sufficiently narrow to be approximated to d.c.).

Owing to the phenomena of dielectric absorption and polarisation, the dielectric constant of a medium changes with the frequency of the applied voltage (Bleaney and Bleaney, 1965; Renne, 1968). Consequently the value of capacitance may be expected to change with frequency.

For a very few dielectics this variation has been studied in the frequency range between a few k Hz and d.c. and thus the ratio between the d.c. capacitance and the a.c. capacitance at 1 kHz can be found. (e.g. Air 1.000 $\pm$ 0.001; P.T.F.E. 1.001 $\pm$ 0.001; Source Ferranti Standards Laboratory, Ferranti Ltd., Edinburgh). In the case of the polystyrene dielectric used in the integrating capacitor incorporated in the Townsend Balance, this ratio is expected to be 1.002, but, since this result is rather uncertain, a d.c. measurement of the capacitance is required.

The most direct method of measuring the d.c. value of capacitance, C_O, is to discharge the capacitor through a leakage resistor of known value, R, for a given period, t. The voltages before and after discharge, V_O and V respectively, are then given by equation A.2.1.

$$V = V_O \exp(-t/C_O R) \qquad \text{A.2.1}$$

In order to measure the capacitance under the same conditions encountered in practice, the dielectric should be stressed to the same extent. Thus, the charging voltage, V_O, should not exceed a few volts. Also to measure V with the same precision as V_O, the discharge period should not exceed 2 $C_O R$. If t is to be measured with a stopwatch, the period of discharge would need to be greater than 100 s to achieve an accuracy of better than 0.1%. For a 50,000 pF capacitor this requires a leakage resistance of greater than 10^9 Ω. Such resistance values are not common and it would be very difficult to measure the resistance accurately, except by a reverse of the above process using a standard 50,000 pF capacitor. The largest stable resistor which was readily available had a value of approximately 10^8 Ω, thus a discharge period of less than 10 s was required. To measure such a

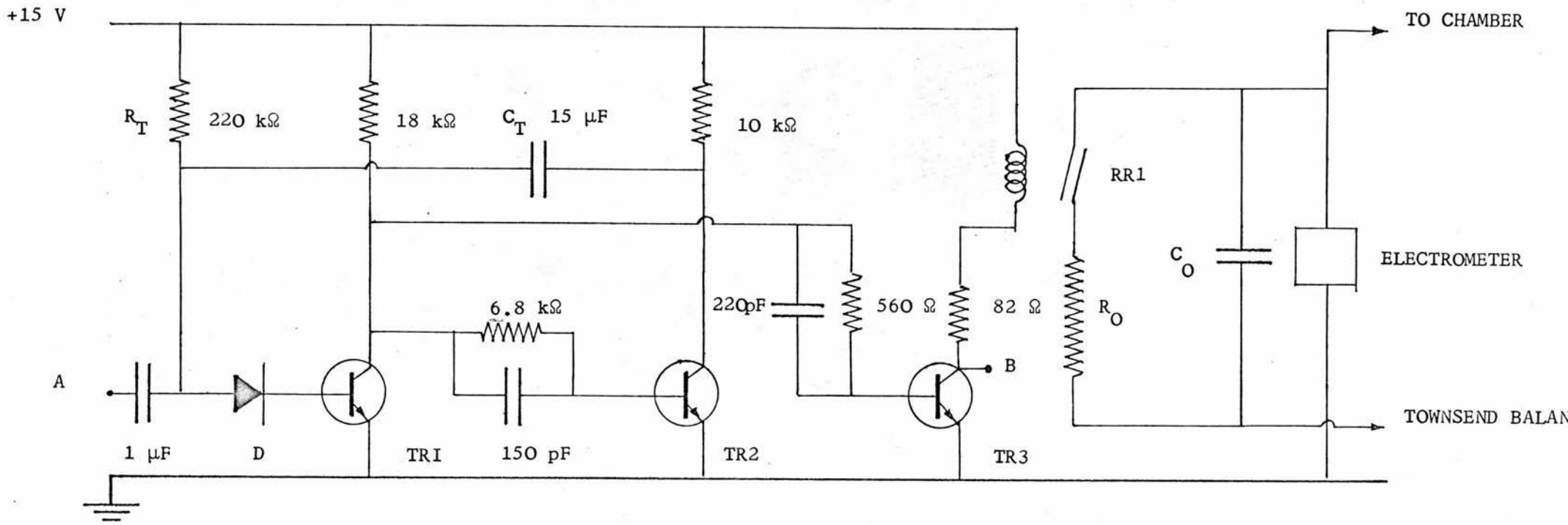

FIGURE A.2.1 MONOSTABLE DISCHARGE CIRCUIT FOR CAPACITOR C_O

period of time to better than 0.1% requires a switch, with a bounce time of less than 5 ms, coupled to an electronic timer. Since this bounce time represents the very lowest limit attainable by conventional manual switches, a high speed electronic switch is preferable. Initially a device using fast field effect transistors (F.E.T.s) was constructed, but since the insulation resistance of the source-drain junctions was comparable to the leakage resistance, R, this device was unsuitable. The solution to this problem is shown in the circuit figure A.2.1, where a high insulation ($> 10^{15}$ Ω) reed switch is activated by the monostable circuit.

The monostable cycle is initiated by a negative pulse injected at the point A. This causes transistor TR1 to become non-conducting and transistor TR2, and hence transistor TR3, to start conducting, or turn 'on'. In this on state TR3 draws its collector current through the reed relay coil, RR1, creating a magnetic field in the region of the reed switch. When this relay closes the capacitor C_O discharges through the leakage resistance, R, and the sudden drop in the potential at the point B, due to the conduction of TR3, is used to initiate an electronic timer. After a time approximately equal to the product $C_T R_T$, the base of TR1 conducts. This in turn causes TR2 and TR3 to switch off, and the current flowing in RR1 ceases. The reed relay then opens terminating the discharge of C_O, and the change in potential at B interrupts the electronic timer, which thus indicates the time, t, for which the reed relay coil was activated. The voltage, V, after discharge can then be measured in the normal way by the Townsend Balance circuit. The mean value of the quantity $t/\ln(V_O/V)$ for ten observations was 5.452 $\pm$ 0.002 (SEOM) and the resistance of R was 116.4 $\pm$ 0.1 MΩ (SEOM; $\nu_{eff} = 9$). Thus the value

of the capacitor, C_o, was 46,854 pF, this agrees very well with the a.c. capacitance measured at 1592 Hz of 46,882 $\pm$ 20 pF (ν_{eff} = 9). The value of the total capacitance of the system, including the cable and chamber capacitance, was found to be 46,840 $\pm$ 40 pF SEOM (ν_{eff}). This value was checked on numerous occasions to investigate the temperature and other stability factors. No significant variation was found.

The systematic uncertainties involved in these calculations can arise from three sources. Firstly, the bounce time of the reed relay may decrease the actual period of discharge as indicated above. This effect was investigated by applying a voltage directly to the reed relay, via a ballast resistor, and observing the waveform on a high-speed oscilloscope. A total bounce time of less than 200 μs was observed which is in close agreement with the values of 160 μs reported by Kemp and Woodall (1965). For a total discharge period of 2.5 s this bounce time is insignificant and has therefore been neglected. Secondly, the inductance of the reed relay coil may cause a time delay between the actuation of the electronic clock, which was designed to trigger on the initial slope of the voltage change, and the closing of the relay, which would not operate until the current approached its maximum value. The rise and fall time of the voltage waveform was found to be less than 20 μs, thus this effect can also be neglected. The third source of systematic uncertainty was the value of the leakage resistance, R. This was measured on a d.c. bridge at applied voltages of 100 V and 10 V. These results indicated that the resistance increased from 115.8 MΩ at 100 V to 116.3 MΩ at 10 V, thus assuming a linear relationship the

resistance at 1-2 V should be 116.4 MΩ. To allow for the uncertainty in this correction, a value of 0.1% has been included in the appropriate list of systematic uncertainties.

A C K N O W L E D G E M E N T S

I should firstly like to express my gratitude to the University of Edinburgh and the Faculty of Medicine of the University of Edinburgh for their financial support during this project. Of the many people whom I should like to thank for their help and advice throughout this project I should like to especially mention my Supervisor, Professor J. R. Greening, Dr. J. Law and Dr. A. Murray. My thanks are due to the staffs of the mechanical workshops of the Medical Physics Departments at the Royal Infirmary of Edinburgh and the Western General Hospital, and my fellow research students, of whom Alan Nahum deserves a particular mention. I should also like to express my sincere thanks to Professor H. Miller and the staff of the Weston Park Hospital, Sheffield, especially Mr. C. K. Bomford and Mr. A. R. Robinson, who made the electron measurements possible. Finally, I should like to thank Mrs. H. D. McKinna, Miss L. S. Gilliat and my mother for typing this manuscript.

REFERENCES

ABRAMOWITZ, M. and STEGUN, I. A. (1964). Handbook of Mathematical Functions p 415. Pub. by National Bureau of Standards, Washington D.C.

ALMOND, P. R. (1967). Phys. Med. Biol. 12, 13.

ALMOND, P. R. (1968). Phys. Med. Biol. 13, 285.

ANDERSON, A. R. (1962). J. of Phys. Chem. 66, 180.

ARYA, A. P. (1966). Fundamentals of Nuclear Physics Ch. IX, Pub. Allyn and Bacon Inc., Boston, U.S.A.

BARNARD, G. P. (1964). Phys. Med. Biol. 9, 287.

BARNARD, G. P.; ASTON, G. H.; MARSH, A. R. S. and REDDING, K. (1964) Phys. Med. Biol. 9, 333.

BEAKLEY, W. R. (1951). J. of Sci. Instr., 28, 176.

BERGER, M. J. (1965). Nat. Bur. Stand. Report 8678. N.B.S. Washington D.C.

BERGER, M. J., and SELTZER, S. M. (1964). National Aeronautics and Space Administration Report No. NASA-SP-3012.

BERGER, M. J. and SELTZER, S. M. (1966). National Aeronautics and Space Administration Report No. NASA-SP-3036.

BERGER, M. J. and SELTZER, S. M. (1969). Annal. N.Y. Acad. of Sci. 161, Art 1, 8.

BEWLEY, D. K. (1963). Brit. J. Radiol. 36, 865.

BEWLEY, D. K. (1969). Annal. N.Y. Acad. of Sci. 161, Art 1, 94.

BEWLEY, D. K.; McCULLOUGH, E. C.; PAGE, B. C. and SAKATA, S. (1971). Phys. Med. Biol. 16, 95.

BILLINGTON, D. S. and CRAWFORD, J. H. (1961). Radiation Damage in Solids. Pub. by Princeton Univ. Press, Princeton, N.J., U.S.A.

BLEANEY, B. I. and BLEANEY, B. (1965). Electricity and Magnetism. 2nd Edition Ch. 17, Pub. by Oxford Univ. Press.

BOAG, J. W. (1966). Radiation Dosimetry Vol. II Ch. 9. Ed. by Attix, Roesch and Tochilin. Pub. by Academic Press N.Y., U.S. A.

BOSWORTH, R. C. L. (1952). Heat Transfer Phenomena. Pub. John Willey and Sons Inc., N.Y., U.S.A.

BRADSHAW, A. L. (1965). Phys. Med. Biol. 10, 355.

BURLIN, T. E. (1968). Radiation Dosimetry Vol. I Ch. 8. Ed. by Attix, Roesch and Tochilin. Pub. Academic Press, N.Y., U.S.A.

BURLIN, T. E. (1970). Manual on Radiation Dosimetry, Part I Ch. A.2. Ed. by Holm and Berry, Pub. Marcel Dekker Inc., N.Y., U.S.A.

BURLIN, T. E. and SNELLING, R. J. (1969). Proc. of the 2nd Symp. on Microdosimetry, Stresa, Italy. Pub. E.A.E.C. p 455.

CALVET, E. and DUQUESNE, R. (1964). J. Chimie Physique 61, 303.

CAMPION, P. J.; BURNS, J. E. and WILLIAMS, A. (1973). A Code of Practice for the Detailed Statement of Accuracy. Pub. by H.M.S.O. London.

CURIE, P. and LABORDE, A. (1904). Comp. rend. Acad. de Sci. Paris, 138, 1150.

DIENES, G. J. and VINEYARD, G. H. (1957). Radiation Damage in Solids, Ch. 4.C. Pub. by Interscience Inc., N.Y., U.S.A.

DOMEN, S. R. (1969). J. of Res. of the Nat. Bur. Stand. 73C, 17.

DOMEN, S. R.; PETREE, B. and LAMPERTI, P.J. (1970). Paper presented at 12th Annual Conf. of the Amer. Assoc. of Phys. in Med. Washington D.C.

DOVE, D. B. and COLE, B. G. (1962). Atomic Energy Research Establishment Report No. AERE-R-3063.

DUTREIX, J. and DUTREIX, A. (1966). Biophysik 3, 249.

ENGELKE, B. A. and HOHLFELD, K. (1971a). PTB-Mitteil-ungen, 5, 336.

ENGELKE, B. A. and HOHLFELD, K. (1971b). PTB-Mitteil-ungen, 3, 185.

FARMER, F. T. and AIRD, E. G. A. (1972). Phys. Med. Biol. 17, 169.

FAULKNER, E. A.; STUBLEY, D. and McGLASHAN, M. L.(1965). J. of Chem. Soc. 510, 2837.

FLEMING, D. M. (1970). Health Phys. 18, 135.

FLEMING, D. M. and GLASS, W. A. (1969). Rad. Res. 37, 316.

FREGENE, A. O. (1967). Rad. Res. 31, 256.

FRICKE, H. and MORSE, S. (1927). Amer. J. Roentgen 18, 430.

GENNA, S.; JAEGER, R. G.; NAGL, J. and SANIELEVICI, A. (1963). Atomic Energy Review 1, No. 4, 239 I.A.E.A., Vienna.

GIESSELSODER, J.; KOEPKE, K. and LAUGHLIN, J.S. (1963). Rad. Res., 20.3, 423.

GINNINGS, D. C.; BALL, A. E. and VIER, D. T. (1953). J. of Res. of the Nat. Bur. of Stand. 50 (2), 75.

GOLDSTEIN, N. (1968). U.S.N. R.D.L. Report No. TR.-68-52.

GOODWIN, P. N. (1960). Radiol. 75, 112.

GOODWIN, P. N. and ADAIR, H. W. (1963). Radiol. 81, 320.

GUNN, S. R. (1964). Nucl. Instru. and Methods, 29, 1.

GUNN, S. R. (1970). Health Phys. 11, 829.

HARDER, D. (1965). Symp. on High Energy Electrons, Montreaux, 1964, p 40, Ed. by Zuppinger and Poretti, Springer Verlag Berlin.

HARDER, D. (1966). Biophysical Aspects of Radiation Quality. I.A.E.A. Tech. Rep. No. 58, p 140, Pub. by I.A.E.A., Vienna, Austria.

HARDER, D. (1968). Biophysik, 5, 157.

HOCHANADEL, C. J. and GHORMLEY, J. A. (1953). J. Chem. Phys. 21, 880.

H.P.A. (1971). A Practical Guide to Electron Dosimetry (5-35 MeV) H.P.A. Report Series No. 4. Pub. by the Hospital Physicists' Association, London.

HYDE, F. J. (1971). Thermistors, Ch. 8. Pub. by Illiffe, London.

I.C.R.U. (1969). I.C.R.U. Report 14. Pub. by I. C.R.U., Washington D.C.

I.C.R.U. (1971). I.C.R.U. Report 19. Pub. by I.C.R.U., Washington D.C.

I. C.R.U. (1972). I.C.R.U. Report 21. Pub. by I. C.R.U., Washington D.C.

KATZ, L. and PENFOLD, A. S. (1952). Rev. Mod. Phys. 24, 28.

KAYE, G. W. C. and LABY, T. H. (1966). Tables of Physical and Chemical Constants. Pub. by Longmans, Green and Co. Ltd., London.

KEENE, J. P. and LAW, J. (1963). Phys. Med. Biol. 8, 83.

KEMP, L. A. W. E. (1971). N.P.L. Note 101-1971. Nat. Phys. Lab. Teddington, Mddx.

KEMP, L. A. W. E. and WOODALL, J. E. (1965). Elec. Engin. 40, p 236.

KENNARD, E. H. (1938). Kinetic Theory of Gases, Pub. by McGraw-Hill, N.Y., U.S.A.

KESSARIS, N.D. (1964). Rad. Res. 23, 630.

KESSARIS, N. D. (1966). Phys. Rev. 145, 164.

KESSARIS, N. D. (1970a). Rad. Res. 43, 281.

KESSARIS, N. D. (1970b). Rad. Res. 43, 288.

KOTT, J. (1967). Tech. Digest 8, 537.

KRUGLOV, S. P. and LOPATIN, I. V. (1963). Translation from Pribory i Tekhnika Eksperimenta 4, 53.

KUO, F. F. (1966). Network Analysis and Synthesis, Ch. 13. Pub. by John Wiley and Sons Inc., N.Y., U.S.A.

LANZL, L. H. (1969). Ann. New York Acad. Sci. 161, Art 1, 101.

LAUGHLIN, J. S. and GENNA, S. (1966). Radiation Dosimetry Vol. II Ch. 16, Ed. by Attix, Roesch and Tochilin, Pub. by Academic Press, N.Y., U.S.A.

LAW, J. (1970). Phys. Med. Biol., 15, 301.

LILLICRAP, S. C. and ROSENBLOOM, M. (1972). Brit. J. Radiol. 45, 229.

LINACRE, J. K. and THOMAS, R. B. (1965). Atomic Energy Research Establishment Rep. No. AERE-R-4805.

LOEVINGER, R., KARZMARK, C. J. and WEISSBLUTH, M. (1961). Radiol. 77, 906.

LUIKOV, A. V. (1968). Analytical Heat Diffusion Theory, pp 197-200, Pub. by Academic Press, Inc., N.Y., U.S.A.

McADAMS, W. H. (1942). Heat Transmission. Pub. by McGraw-Hill, N.Y., U.S.A.

MAJOR, D. (1973). Part of Thesis for M.Sc. Univ. of Leeds.

MARKUS, B. (1961). Strahlentherapie 116, 280.

MEULLER, E. F. and WENNER, F. (1935). J. of Res. of the Nat. Bur. of Stand. 15, 477.

MILVY, P.; GENNA, S.; BARR, N. and LAUGHLIN, J. S. (1955). Proc. of 2nd Inter. Conf. on Peaceful uses of Atomic Energy. Geneva. p 142.

MYERS, I. T.; Le BLANC, W. H. and FLEMING, D. M. (1961). Rev. Sci. Instr., 32(9), 1013.

N.B.S. (1962). Nat. Bur. Stand. Handbook 84, Pub. by U.S. Govt. Printing Office, Washington D.C.

PARL, B. (1967). Basic Statistics, Pub. Doubleday and Co. Inc., N.Y., U.S.A.

PETREE, B. and LAMPERTI, P. (1967). J. of Res. of the Nat. Bur. of Stand. 71C, 19.

PETREE, B. and WARD, G. (1962). Nat. Bur. of Stand. Tech. Note No. 163.

PETTERSSON, C. (1967). Arkiv. för Fysik, 34, 385.

PINKERTON, A. P. (1969). Annals of the N.Y. Acad. of Sci., 161, Art 1, 63.

PRUITT, J. S. and DOMEN, S. R. (1962). J. of Res. of Nat. Bur. of Stand. 66A, 371.

RASE, S. and POHLIT, W. (1962). Strahlentherapie 119, 226.

RADAK, B. and MARKOVIC, V. (1962). Int. J. of Applied Rad. and Isotopes, 13, 287.

RADAK, B. and MARKOVIC, V. (1970). Manual on Radiation Dosimetry, Ch. B.3. Ed. by Holm and Berry. Pub. by Marcel Dekker Inc., N.Y., U.S.A.

REDPATH, A. T. (1967). Ph.D. Thesis Edinburgh University.

REID, W. B. and JOHNS, H. E. (1961). Rad. Res. 14, 1.

RENNE, V. T. (1968). Electronic Components, August 1968, 911.

RUMP, W., (1927), Physik, 44, 396.

SAKATA, S. (1972). Nippon Acta. Radiol. 32, 619.

SCHLEIGER, E. R. and GOLDSTEIN, N. (1964). Rev. Sci. Instr. 35, 890.

SCHMIDT, K. and BUCK, W. (1969). Rad. Res. 40, 473.

SEGRE, E. (1953). Experimental Nuclear Physics Vol. I. Part II. Pub. by John Wiley and Sons Inc., N.Y., U.S.A.

SHALEK, R. J. and SMITH, C. E. (1969). Annals of the N.Y. Acad. of Sci., 161, Art 1., 44.

SHONKA, F. R.; ROSE, J. E. and FAILLA, G. (1958). Proc. of 2nd Inter. Conf. on Peaceful Uses of Atomic Energy. Vienna. Art. 21, 184.

SKARSGARD, L. D.; BERNIER, J. P.; CORMACK, D. V. and JOHNS, H. E. (1957). Rad. Res. 7, 217.

STERNHEIMER, R. M. (1952). Phys. Rev. 88, 851.

STERNHEIMER, R. M. (1956). Phys. Rev. 103, 511.

SVENSSON, H. (1971). Acta. Radiol. Ther. Phys. Biol., N.S.10., 631.

SVENSSON, H. and PETTERSSON, C. (1967). Arkiv. för Fysik, 34, 377.

TIAN, A. (1922). J. de Chimie Physique, 20, 132.

WEST, E. D. (1963). J. of Res. of the Nat. Nur. of Stand., 67A, 331.